THE UNIVERSITY *of* EDINBURGH

Femtosecond Laser Studies of Fullerenes and Nanotubes

Gordon Henderson

Degree of Doctor of Philosophy
University of Edinburgh
2012

Abstract

This work concerns the interaction of intense, ultrashort laser pulses with fullerenes and carbon nanotubes. This includes the excitation and ionisation dynamics of gas phase fullerenes and the response of carbon nanotubes to intense ultrashort laser pulses.

When ionising C_{60} with laser pulses of duration between 50 fs up to a few hundred fs, the ionisation mechanism has been proposed to be thermal in nature, with the electronic subsystem 'hot' and the vibrational system 'cold' at the time of ionisation. Recent results show an anisotropy in the photoelectron angular distribution which may suggest more direct mechanisms at work. Velocity-Map Imaging photoelectron spectroscopy results are presented for the ionisation of C_{60} and C_{70} at various wavelengths, pulse durations and intensities and the results are compared to theoretical models. The results are described well by a thermal ionisation mechanism in which a significant number of electrons are emitted during the laser pulse. Electrons may gain a momentum 'kick' from the electric field of the laser which results in an anisotropy in the photoelectron angular distributions.

Peaks are observed, superimposed on the thermal background, in the photoelectron kinetic energy spectra of fullerenes ionised by ultrashort laser pulses which were previously assigned as Rydberg peaks. Photoelectron angular distributions of these peaks are presented for C_{60} and C_{70} ionised with laser pulses of various wavelengths. The binding energies and anisotropy parameters fitted to the peaks suggest that they are due to the population and one-photon ionisation of superatom molecular orbitals (SAMOs). The results rule out a direct multiphoton population mechanism for these states and show many similarities with Rydberg fingerprint spectroscopy.

The fusion of carbon nanotubes has been observed under high energy electron beams and fullerene molecules have been shown to fuse together after irradiation with ultrashort laser pulses. Results are presented for experiments where fusion of carbon

nanotubes with ultrashort laser pulses was attempted. Thin carbon nanotube films are analysed via Raman spectroscopy after irradiation by single laser pulses. A number of low frequency radial breathing mode peaks were observed which suggest that fusion may have taken place at certain areas of the sample.

Declaration

I declare that the work presented in this thesis is my own unless otherwise stated by reference.

Gordon Henderson

Publications

J.O. Johansson, J. Fedor, M. Goto, M. Kjellberg, J. Stenfalk, G.G. Henderson, E.E.B. Campbell and K. Hansen, *Anisotropic hot electron emission from fullerenes*, Journal of Chemical Physics, **136** (2012) 164301.

J.O. Johansson, G.G. Henderson, F. Remacle and E.E.B. Campbell, *Angular-resolved Photoelectron Spectroscopy of Superatom Orbitals of Fullerenes*, Physical Review Letters, **108** (2012) 173401.

The experimental work and data collected for the gas phase fullerene results presented in this thesis was carried out together with Olof Johansson, who designed, installed and tested the experimental setup. All the results presented were analysed using the GPOP inversion program (Appendix C), written by myself, based on the POP inversion program. The theoretical model used to compare with the experimental results presented in Chapter 6, is a slightly modified version of a program written by Olof Johansson, based on the model written by Juraj Fedor which, in turn, is based on the earlier work by Klavs Hansen. The model used for the results presented here takes into account the electronic excitation energy when modelling the dissipation of energy into vibrational modes rather than solely being based on a time dependency.

The experimental work for the nanotube fusion experiments presented in this thesis was partly carried out together with Devin Dunseith. Devin prepared and characterised the nanotube samples, carried out the irradiation experiments, together with myself, and carried out some initial Raman spectroscopy on the irradiated samples.

Acknowledgements

The last four years have been challenging but also very rewarding and enjoyable (though maybe not all at the same time, all of the time). So many people have contributed to making this a good experience, whether it's been help and advice with lasers, LabVIEW and Raman or playing football, getting a pint and having (toy) gun fights in the office. The people I'd like to thank especially are…

Eleanor Campbell for giving me the oppertunity to work in this group and all the help and advice you've given me. I don't think I've ever left your office thinking things were more complicated or hopeless than when I walked in.

Olof Johansson for having the patience to teach me an incredible amount about so many things.

All the members of the Campbell group, past and present; Andrei Gromov, Oleg Nerushev, Johan Ek Weis, Andrew Gray, Chaweewan Sapcharoenkun and Kirsten Strain. As well as all the project students I've worked with; Darren Smith, Andreas Molle, Matthew Robinson and Devin Dunseith. You've all helped make this a great group to be a part of.

And, finally, my mum and dad. Your encouragement and support right from the start means so much to me. Thank you.

Table of contents

Chapter 1 – Introduction

Since the early 20th century, when the quantisation of light was introduced to explain the photoelectric effect and the Bohr model considered quantised electronic energy levels in atoms to explain the discrete lines in atomic emission and absorption spectra, scientists have used light as a powerful tool to probe the structure and behaviour of matter and even to drive, direct and control chemical and physical processes.

The development and widespread use of femtosecond (10^{-15} s) pulsed lasers has opened up many more possibilities in the field of light-matter interactions. The high intensities available with such short pulses allow many direct processes to be probed, which would otherwise be unobservable. The high photon flux makes coherent absorption of multiple photons possible and the electric field strength becomes comparable to or even higher than the Coulomb potential of atoms and molecules. To gain information on physical processes which take place on very short timescales, it is necessary to use probes on similar timescales. This was demonstrated by Zewail [1], for which he won the 1999 Nobel Prize for chemistry and effectively founded the field of 'femtochemistry'. The pulse durations available have become comparable to the timescale of many processes in atoms and molecules such as the orbital period of electrons in atomic orbitals (10^{-16} s), molecular vibration (10^{-15} s) and the energy relaxation in large molecules and bulk solids (10^{-12} s). To put these kinds of timescales in perspective, the typical kind of pulse duration used in the work presented in this thesis, 120 fs, is to 1 second what 14.5 hours is to the age of the universe.

The excitation and ionisation mechanisms which take place when ultrashort laser pulses interact with atoms and small molecules can be well understood with a simple direct ionisation model. However, the ionisation dynamics of complex systems such as large organic molecules and clusters are less well understood. With the addition of many more atoms and electrons, comes a large increase in the number of degrees of freedom within the molecule. Ultrafast internal energy redistribution and

dissipation makes explaining the ionisation mechanism much more complicated than in the case of a single atom.

Fullerenes, particularly C_{60}, are commonly used as model systems to study the excitation and ionisation dynamics of both complex molecules and clusters. It is well known that when ionising C_{60} with relatively long laser pulses (from a few picoseconds upwards), statistical excitation, ionisation and fragmentation mechanisms are observed [2], where the excitation energy is regarded as being fully distributed among all degrees of freedom. In this sense, the fullerene molecule can be thought of as behaving in a similar manner to a bulk solid. With very short laser pulses (below 50 fs) there are signs of a direct ionisation mechanism, such as strong above threshold ionisation (ATI) peaks in the photoelectron spectrum [3]. In this sense, the fullerene molecule can be thought of as behaving in a similar manner to an atom. In the intermediate pulse duration range (from 50 fs up to a few hundred fs) there is evidence for a statistical, thermal ionisation mechanism [4, 5], where the electrons are highly excited and vibrations remain cold, but also signs that point towards a direct mechanism, namely peak structure and an anisotropic photoelectron angular distribution [6]. It is therefore interesting to study the ionisation mechanisms of these molecules to understand the processes involved, under what conditions might ionisation be considered direct or statistical, on what timescales these processes take place and what the limits of applicability are. Answering these questions will hopefully lead to as much understanding and possibly control of the ionisation mechanisms of large molecules and clusters as for atoms and small molecules.

Recently, evidence has been found, using scanning tunnelling microscopy, for the existence of hydrogen atom-like molecular orbitals in C_{60} molecules adsorbed on a copper surface [7]. The existence of these orbitals was supported by theoretical calculations. These were termed superatom molecular orbitals (SAMOs) and are thought to be exclusive to hollow, symmetrical molecules with a central potential. Previous work on C_{60} has identified reproducible peaks in the photoelectron spectra which were attributed to the population and ionisation of Rydberg states [8]. It is of interest to study C_{60} in the gas phase to determine if peaks corresponding to SAMOs can be seen and identified in photoelectron spectra and to see if conclusions can be drawn about the population and ionisation mechanism.

Carbon nanotubes are members of the fullerene family. Their structure consists of a long cylinder (similar to a rolled sheet of graphene) with the ends capped by the hemispheres of a spherical fullerene. They are known to have many interesting and potentially useful properties [9]. It is the goal of much work to transfer the properties of individual molecules to composite materials and to manipulate carbon nanotubes so that they may form the building blocks of future nanotechnology applications. One method which may facilitate this is by fusing individual nanotubes together. This has been observed for nanotube samples under irradiation by high energy electron beams [10] and the fusion of fullerene molecules has been observed when fullerene clusters have been exposed to intense laser pulses [3]. It would be interesting to see if ultrashort laser pulses could be used to fuse individual carbon nanotubes, in a sample, together.

Chapter 2 of this thesis will present a background to the excitation and ionisation mechanisms of C_{60} subjected to ultrashort intense laser pulses as well as a background on what is known about Rydberg and SAMO states of the molecule. Chapter 3 will present a background on the fusion of carbon nanotubes with electron beams and the fusion of gas phase fullerene molecules with ultrashort, intense laser pulses. Chapters 4 and 5 will present the experimental techniques and equipment used for experiments involving gas phase fullerenes and fusion of carbon nanotubes, respectively. Chapter 6 will present results concerning thermal electron emission from fullerenes in strong laser fields. Angle-resolved photoelectron spectroscopy results of fullerenes ionised with laser pulses of varying wavelength, intensity and pulse duration will be presented and the effect of energy redistribution within the molecule and the role of the laser electric field in the ionisation mechanism will be discussed. Chapter 7 will present results concerning superatom molecular orbitals (SAMOs) in fullerenes. Angle-resolved photoelectron spectroscopy results will be presented for C_{60} and C_{70} over a range of laser wavelengths and peaks in the spectrum which correspond to SAMOs will be identified and discussed. Chapter 8 will present results concerning the fusion of carbon nanotubes with ultrashort intense laser pulses. Resistance measurements on buckypaper, irradiated with ultrashort laser pulses, will be presented as well as Raman spectra of thin carbon nanotube films, irradiated with ultrashort laser pulses, and the effectiveness of the methods attempted to fuse nanotubes together will be discussed.

Chapter 2 – Background: Excitation and ionisation dynamics of atoms and molecules irradiated with ultrashort laser pulses

This chapter will provide a background to excitation and ionisation dynamics of atoms and molecules irradiated with ultrashort laser pulses. An introduction to fullerenes is given followed by an introduction to the ionisation mechanisms of atoms in ultrashort, intense laser pulses which are compared to the ionisation mechanisms observed in C_{60} and other large molecules and clusters. The observation of superatom molecular orbitals in C_{60} molecules adsorbed on solid surfaces is discussed as well as the previous observation of peaks in photoelectron spectra and their identification as Rydberg peaks.

2.1 Fullerenes: C_{60}

Fullerenes, particularly C_{60}, are commonly used as model systems to study the excitation and ionisation dynamics of both complex molecules and clusters. The fullerenes are large, hollow cage-like molecules, containing only carbon atoms and were first discovered in 1985 [11]. C_{60} was originally named Buckminsterfullerene due to the similarity of its structure to the domes made up of pentagons and hexagons designed by the architect Richard Buckminster Fuller. The C_{60} molecule is a truncated icosahedron made up of 20 hexagons and 12 pentagons in a fused-ring structure with a carbon atom at each vertex. The smallest possible fullerene molecule is C_{20} and C_{60} is the smallest structure possible without neighbouring pentagons and is the most stable of the fullerenes. They make particularly good model systems as they are relatively easy to handle in the lab and high quality, mass-selected samples are commercially available. The fact that they are highly symmetric, homonuclear and contain a relatively simple bond structure means that they also lend themselves to theoretical modelling. Since they contain carbon, they can also be compared to

complex organic molecules. The carbon atoms in the C_{60} molecule are held together by distorted sp^2 hybridised bonds and contain 240 valence electrons; 180 σ electrons forming the localised carbon-carbon bonds and 60 delocalised π electrons which lie just below the Fermi level and define the electronic properties of the molecule [12]. The large number of delocalised electrons means that electron-electron interactions can take place as a means of redistributing energy throughout the electronic subsystem.

2.2 Photoionisation of atoms in strong laser fields

When ionising atoms with intense laser pulses, the coupling of the laser electric field and the atom is so strong that it can affect the mechanism by which the atom is ionised. This coupling results in a shifting up of atomic energy levels known as the A.C. Stark shift. In the intensity and wavelength ranges used for these experiments, the Stark shift can be approximated by the ponderomotive energy, U_p [13], which is the energy gained by a free electron in a time varying electric field and can be expressed as

$$U_p[\mathrm{eV}] = \left(\frac{E_0}{2\omega}\right)^2 = 9.34\times10^{-20}\times\lambda(\mathrm{nm})^2\times I\,, \tag{2.1}$$

where E_0 is the amplitude of the laser electric field, ω is the angular frequency of the laser electric field, λ is the laser wavelength and I is the laser intensity. For this reason, the Stark shift is also known as the ponderomotive shift. The ponderomotive energy for laser pulses of a certain wavelength and intensity, as well as the ionisation potential of the atom, combine to determine the ionisation mechanism for atoms in strong laser fields [14]. When the photon energy is much smaller than the ionisation potential, there are three distinct ionisation mechanisms and the transition between these mechanisms can be described by the Keldysh parameter [15],

$$\gamma = \sqrt{\frac{\Phi}{2U_p}}\,, \tag{2.2}$$

where Φ is the ionisation potential of the atom.

For relatively low intensities, $\gamma > 1$ and the ionisation mechanism is direct multiphoton ionisation (MPI). Here an electron coherently absorbs the number of photons needed to overcome the ionisation potential. High lying states are Stark shifted by U_p whilst more strongly bound states are not which reduces the kinetic energy, E_k, carried away by the photoelectron,

$$E_k = nhv - \Phi - U_p, \tag{2.3}$$

where hv is the photon energy and n is the number of photons needed to overcome Φ. Multiphoton ionisation is depicted in Figure 2.1. It is possible for the electron to absorb more photons than are necessary to overcome Φ. This is called above threshold ionisation (ATI) and results in equidistant peaks in the photoelectron kinetic energy spectrum, separated by the photon energy [16]. Where intermediate resonances are involved, the ionisation probability is significantly increased as the full number of photons needed to overcome Φ, does not need to be absorbed coherently. This is called resonance-enhanced multiphoton ionisation (REMPI). Where no intermediate resonances are involved, the ionisation probability scales with I^n, where I is the laser intensity and n is the number of photons needed to overcome Φ.

When the laser intensity is increased, so that $\gamma \approx 1$, the magnitude of the electric field becomes comparable to the binding potential of the electron and so a suppression of the ionisation barrier takes place. This means the electron can tunnel through the barrier, resulting in ionisation. This is known as tunnelling ionisation and is depicted in Figure 2.1. In a static field, the barrier suppression will be constant. In an oscillating field, the suppression oscillates according to the period of the laser field. If the tunnelling period is long compared to the period of the laser field, the electron may not have time to tunnel through the barrier before the field changes sign.

When the laser intensity is increased further, so that $\gamma < 1$, the field is so strong that the electron can escape, classically, from the potential well as the

confining potential is weaker than the energy of the escaping electron. This is known as over-the-barrier ionisation and is depicted in Figure 2.1. In tunnelling ionisation and over-the-barrier ionisation, the electron is, effectively, 'pulled off' the atom by the strength of the electric field and so the mechanism in these regimes is known as field ionisation. The transition from an MPI mechanism to field ionisation is characterised by a change in the photoelectron kinetic energy spectrum from ATI peaks, to a smooth, structureless spectrum. The Keldysh parameter can also be thought of as the ratio between the laser period and the tunnelling time, so when $\gamma \leq 1$, the laser field can be treated as quasistatic. For this reason, the above model is often referred to as the quasistatic model. In the ionisation regimes discussed above, for atoms, it is assumed that ionisation takes place via the excitation of a single active electron (SAE).

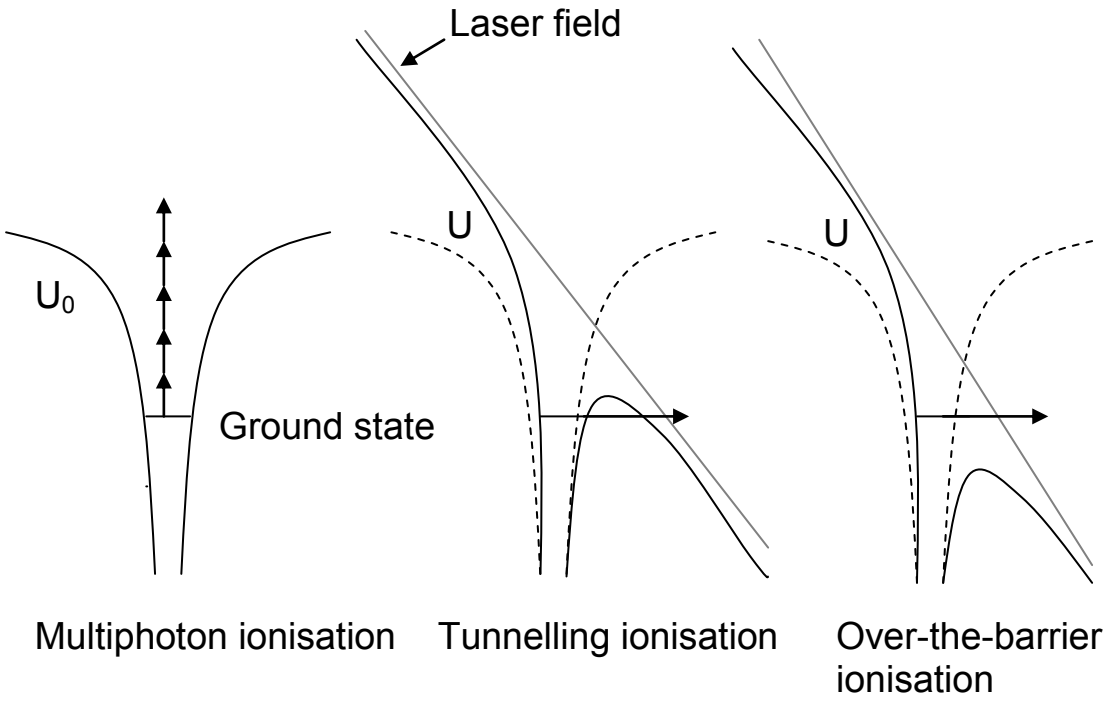

Figure 2.1: Diagrams depicting (from left to right) direct multiphoton ionisation, tunnelling ionisation and over-the-barrier ionisation. U_0 represents the Coulomb potential and U represents the Coulomb potential coupled to the laser electric field.

2.3 Photoionisation of complex molecules and clusters with ultrashort laser pulses

2.3.1 Photoionisation of C_{60}

When gas phase fullerenes are irradiated with ultrashort, intense laser pulses and reach a highly excited state, that is to say the molecules have more internal excitation energy than the energy needed to remove one electron, they can decay by C_2 evaporation, electron emission or photon emission. Ionisation and fragmentation are the dominant decay mechanisms and photon emission is usually disregarded (although it has been shown to be significant under certain circumstances [17]). In laser excitation of bulk metals, the two-temperature model is used to describe the energy equilibration [18]. The initial energy is absorbed by the electronic subsystem, leaving the system in a state of non-equilibrium. Over time, the absorbed energy is equilibrated amongst the electronic subsystem through electron-electron interactions and eventually redistributed to the vibrational system via electron-phonon interactions. This is analogous to excitation of C_{60}. The mechanism by which ionisation and fragmentation of the molecule takes place is dependent on the rate at which energy is absorbed by the molecule and so depends on laser pulse duration.

When the laser pulse duration is on the order of a nanosecond, the photoionisation of C_{60} can be explained by thermionic emission from a vibrationally excited molecule [4]. The molecule absorbs a large number of photons, incoherently, and the total energy gained is equilibrated over electronic and vibrational degrees of freedom until the molecule is vibrationally hot enough to eject an electron. The electron emission and fragmentation of the molecule can be described by statistical models [19], which assume that the energy is equilibrated over all degrees of freedom, and the process is not direct with respect to the laser pulse, with ionisation occurring up to microseconds after the interaction. There is evidence for this in the tail on the high mass side of the C_{60}^+ molecular ion peak, seen in mass spectra (Figure 2.2). The mass spectra show only singly charged ions and extensive fragmentation with a bimodal pattern. Multiple ionisation channels are suppressed as the energy couples to

molecular vibrations before sufficient energy can accumulate in the electronic subsystem to cause multiple ionisation. The ions on the high mass side of the bimodal distribution are produced by sequential C_2 evaporation from the excited parent ion and the ions on the low mass side are the result of the catastrophic break up of the fullerene molecules subjected to high laser fluences at the centre of the beam focus, producing smaller carbon rings and chains. C_2 evaporation is characteristic of fullerene fragmentation. Evaporation of odd numbered carbon fragments would destabilise the cage structure. The statistical nature of the fragmentation is highlighted by the metastable emission of C_2 from ions produced in the field-free region of a reflectron Time-of-Flight (TOF) mass spectrometer. This phenomenon can lead to the appearance of small peaks on the lower mass side of each fullerene ion peak. The photoelectron spectra produced by thermionic electron emission (Figure 2.2d) are structureless and can be described by a Boltzmann distribution [20],

$$S(\varepsilon)d\varepsilon = \exp(-\varepsilon / k_{\mathrm{B}}T_{\mathrm{a}})d\varepsilon, \tag{2.4}$$

where ε is the electron kinetic energy, k_{B} is the Boltzmann constant and T_{a} is the apparent temperature of the emitted electrons, a measure of their average energy which can be extracted from the slope of the photoelectron kinetic energy distribution. Typical apparent temperatures for thermionic ionisation are around 3,000-4,000 K (0.26-0.34 eV) [3]. The apparent temperature is related to the kinetic energy of the delocalised electrons and, as such, apparent temperatures are commonly given in units of eV. The relation between energy (eV) and temperature (K) is

$$1\mathrm{eV} = 1.160\mathrm{x}10^{4}\,\mathrm{K}.$$

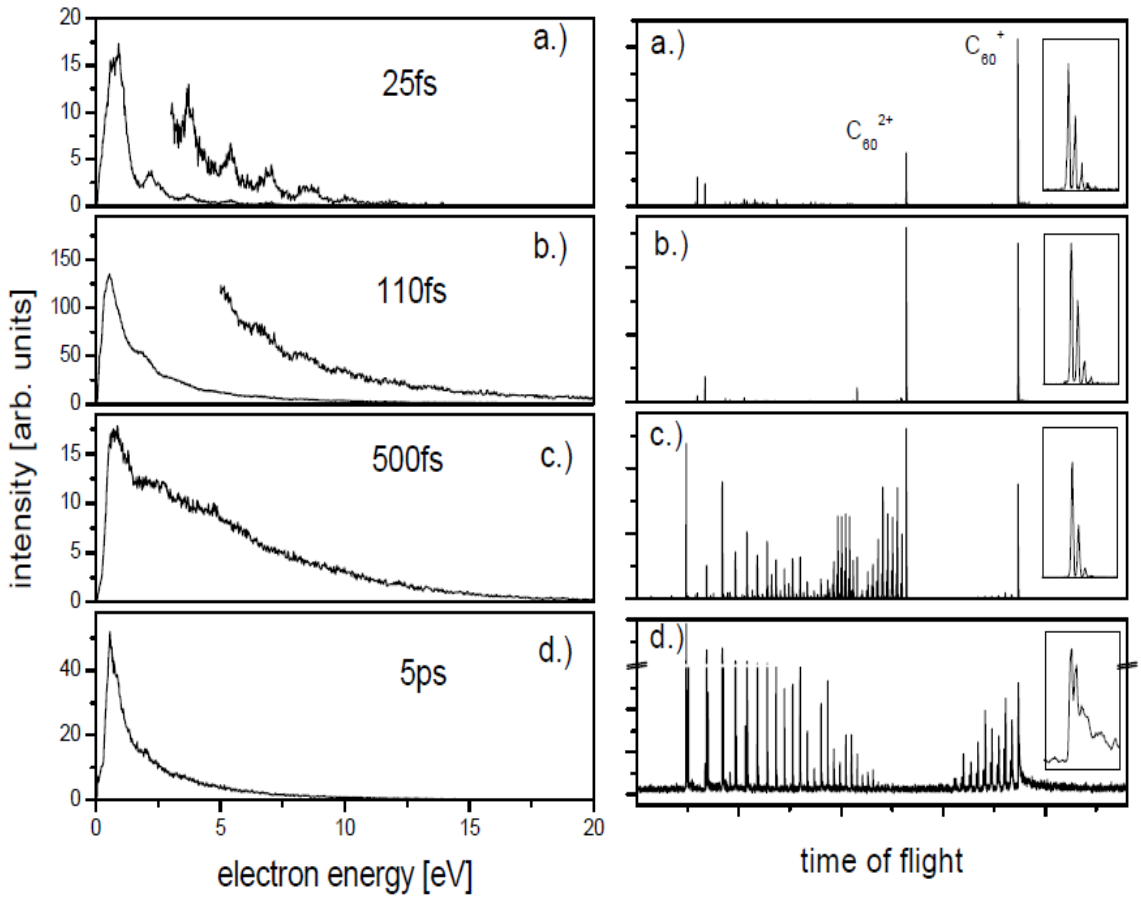

Figure 2.2: PES and mass spectra depicting pulse duration dependence of ionisation and fragmentation of C_{60} ionised by 790 nm laser pulses of intensity a) – c) 8 x 10^{13} W/cm^2 and d) 5 x 10^{12} W/cm^2. The cut-off at low energies is an artefact due to the time-of-flight PES technique used. Figure from ref [21].

As the pulse duration is decreased to between 1 ps and 50 fs, the characteristic signs of thermionic emission disappear. On this timescale, enough energy can be accumulated in the electronic system to induce thermal ionisation from the hot electron cloud before coupling to vibrations takes place, leaving a vibrationally cold molecule [5]. This results in multiply charged species and less fragmentation appearing in the mass spectra. Multiple electrons are excited and energy is equilibrated among electronic degrees of freedom by electron-electron interactions. The large amount of energy equilibrated amongst the delocalised valence electrons results in multiple ionisation and much higher apparent temperatures, on the order of 10,000 to 40,000 K (0.86 to 3.45 eV), resulting in smaller gradients in the PES than

for longer pulses and photoelectron distributions stretching to higher energies (Figure 2.2b,c). Since the ionised electrons carry away such a large amount of energy, the vibrational system is left much colder than in the thermionic emission case. Ionisation is relatively prompt, with no detectable delay and also produces a Boltzmann distribution in the photoelectron kinetic energy distribution, similar to thermionic emission. Simulations have shown that, for C_{60}, the cooling of the electronic subsystem due to coupling to vibrational degrees of freedom is accounted for by introducing an exponential decay with a time constant of around 240 fs [5]. The electron-electron thermalisation timescale has been estimated to be less than 50 fs [22]. In bulk metals, the timescale for electron-electron thermalisation is around 10 fs [23]. Structure can often be seen superimposed on the thermal background in the PES. This was thought to be due to population and single-photon ionisation of Rydberg states [8]. Small ATI peaks can be seen in spectra taken with higher laser intensity.

For pulse durations on the order of 50 fs or less, there is evidence that more direct ionisation mechanisms come into play [4]. The PES obtained for sub-50 fs pulses show evidence of transitions between different ionisation regimes, according to the Keldysh parameter, with ATI peaks observed at lower intensities and structureless spectra dominating at higher intensities (Figure 2.3). There is also evidence that in the long wavelength limit, fragmentation is dominated by a re-collision mechanism which is indicative of a tunnelling ionisation mechanism [24]. Under these conditions, high charge states are seen and very little fragmentation, compared to longer laser pulses [25]. It is thought that on such short timescales, there is not time for energy to be equilibrated amongst the electronic or vibrational degrees of freedom before ionisation occurs and so more direct ionisation mechanisms are responsible, similar to the situation with atoms. Metastable ion peaks have also been observed for C_{60} ionisation with sub-50 fs pulses, indicating that the fragmentation pattern can be described by statistical models and that energy is finally equilibrated amongst vibrational degrees of freedom on a timescale shorter than the μs mass spectrometer timescale [25].

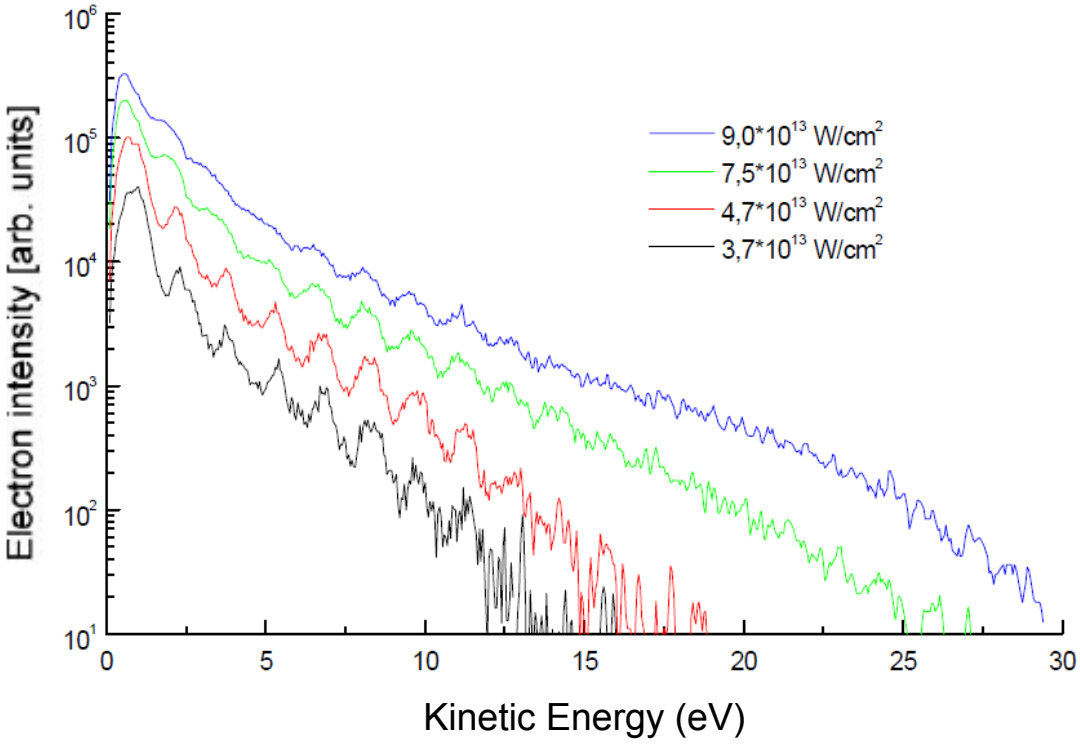

Figure 2.3: PES of C_{60} ionised with 25 fs, 800 nm laser pulses of varying intensity. At lower intensities, ATI peaks are visible, indicative of a multiphoton ionisation mechanism. As intensity is increased, the ATI structure is less obvious. Figure from ref. [26].

In atoms, a single active electron (SAE) model is used to describe ionisation although it is not certain whether, at pulse durations below 50 fs, the same can be said for C_{60} or if multiple active electrons (MAE) are excited during the laser pulse. Although ATI peaks are indicative of a SAE mechanism in atoms, theoretical studies have shown that it is possible to observe ATI for multi-electron processes [27]. Likewise, ion yields displaying an I^n power law dependency, as is the case with C_{60} [25], are not necessarily indicative of a SAE MPI process and can also arise through thermal ionisation mechanisms [3]. An indication that ionisation of C_{60} with sub-50 fs pulses does not fit the quasistatic model is the increased saturation intensity of C_{60} compared to atoms with a similar ionisation potential [28, 29]. According to the quasistatic model, the value of the saturation intensity should be decided by laser parameters and the ionisation potential of the atom/molecule alone. Contrasting theoretical models prompt suggestions as to how this may fit with the SAE picture or the MAE picture, citing destructive interference from electron waves originating from

the finite cage structure of the molecule [29] and multi-electron excitation which can result in the screening of the electric field [28], respectively. This 'screening effect' brought about by multiple excited electrons has been proposed elsewhere, by Zhang *et al*., to explain dynamical electron correlation effects in C_{60} [30]. The same authors attribute the apparent shortening of the lifetime of quasiparticle excitation in C_{60} to electron-electron interactions suppressing the charge fluctuations within the molecule [31].

Several studies advocate the role of nonadiabatic multielectron (NME) dynamics [32, 33] in the ionisation mechanism of C_{60} with short laser pulses. This involves the excitation of multiple electrons into a quasi continuum (QC) through a 'doorway state' [34], thought to be the LUMO+1 t_{1g} state in C_{60}. From the QC, rapid absorption of energy can occur and internal conversion between electronic and vibrational degrees of freedom, leading to ionisation and fragmentation. Hertel *et al*. studied the ellipticity dependence of ion yields at different wavelengths [35] and concluded that the coherent excitation into the QC was effectively a bottleneck to ionisation and that after this step, incoherent excitation of multiple excited electrons takes place. The proposed doorway state, LUMO+1, can be reached by absorption of one 400 nm photon or two 800 nm photons. Shchatsinin *et al*. found that C_{60} fragmentation can be greatly increased in pump-probe experiments when a strong 800 nm probe pulse follows a weaker 400 nm pump pulse [36]. This was attributed to the particularly efficient 1-photon population of the doorway state by 400 nm photons. Laarman *et al*. proposed that the $a_g(1)$ radially symmetric breathing mode can be excited directly by exciting multiple electrons through the QC [37]. Excitation of up to 31 electrons leads to a repulsive force which could double the size of the molecule, leading to a fast conversion of electronic excitation energy to vibrational modes. It seems that multiple electrons may be excited even with laser pulses below the electron thermalisation timescale although elements of a SAE model exist.

2.3.2 Photoionisation of clusters and organic molecules

Thermionic emission, where absorption energy is equilibrated over electronic and vibrational degrees of freedom, has been observed in various strongly bound metal cluster systems [38], which can be heated to sufficient temperatures to observe electron emission without undergoing fragmentation. The transient thermal emission model used to describe the ionisation of C_{60} with laser pulses of intermediate duration, where the electronic subsystem is excited and the vibrational system is cold, has been used to describe ionisation in sodium clusters [39, 40] and various transition metal clusters [23]. Studies on palladium clusters [41] have shown that the electron thermalisation time-constant, for clusters ranging from three to seven atoms, is between 25-91 fs and is dependent on cluster size. Generally, the time taken for thermalisation decreases with increasing cluster size as the density of states is increased. This results in an increase in the inelastic scattering rate of electrons, the method by which energy is equilibrated among the electronic subsystem. The palladium clusters, although much smaller than C_{60}, display more bulk-like time constants due to the larger valence electron density associated with open d-shell transition metals, which leads to a greater inelastic scattering rate for electrons.

Perhaps unsurprisingly, the ionisation dynamics of large organic molecules displays significant structure dependence. DeWitt *et al*. studied photoionisation of benzene, naphthalene and anthracene with identical laser pulses and observed that ATI peaks were present for benzene but structureless spectra were obtained for the larger molecules [42]. The authors concluded that field ionisation was responsible for the structureless spectra and that the Keldysh parameter, γ, is structure-dependent for large molecules. Lezius *et al*. presented mass spectra of unsaturated linear hydrocarbons ionised with laser pulses of varying intensity and wavelength and concluded that the ionisation mechanism makes a transition from field ionisation to a nonadiabatic multielectron excitation mechanism at lower intensities and shorter wavelengths [32]. The point at which this transition occurs is dependent on the length of the molecule. It is possible, however, that thermal ionisation was mistaken for field ionisation in the above studies. Kjellberg *et al*. studied the ionisation of anthracene, coronene and benzo[GHI]perylene [43]. Based on fluence and pulse duration

dependence measurements, the two larger molecules were shown to ionise via a thermal emission process. Anthracene displayed ATI peaks in the PES but showed signs of thermal ionisation at longer pulse durations. In a follow up study, Goto *et al*. described how direct MPI and thermal ionisation channels compete in anthracene [44]. They report that thermal ionisation dominates at higher intensities as rapid internal conversion from a quasi continuum of states suppresses MPI from the ground state.

2.4 Population of highly excited states in fullerenes

2.4.1 Rydberg states

Superimposed on the thermal background of photoelectron spectra produced during ionisation of C_{60}, using laser pulses of duration up to around 5 ps, is a reproducible peak structure below the electron kinetic energy corresponding to the energy of one photon. This structure was attributed to the population of and subsequent, one-photon, ionisation of Rydberg states [8] (Figure 2.4). Rydberg states are highly excited electronic states with large orbitals compared to the inner core electrons. A Rydberg series exists for each angular momentum quantum number, *l*, with a progression of principal quantum number, *n*. The energy levels are described by the equation,

$$E_{\mathrm{n}} = \Phi - \frac{R}{(n-\delta)^2}, \tag{2.5}$$

where *R* is the Rydberg constant (13.6 eV) and δ is the quantum defect.

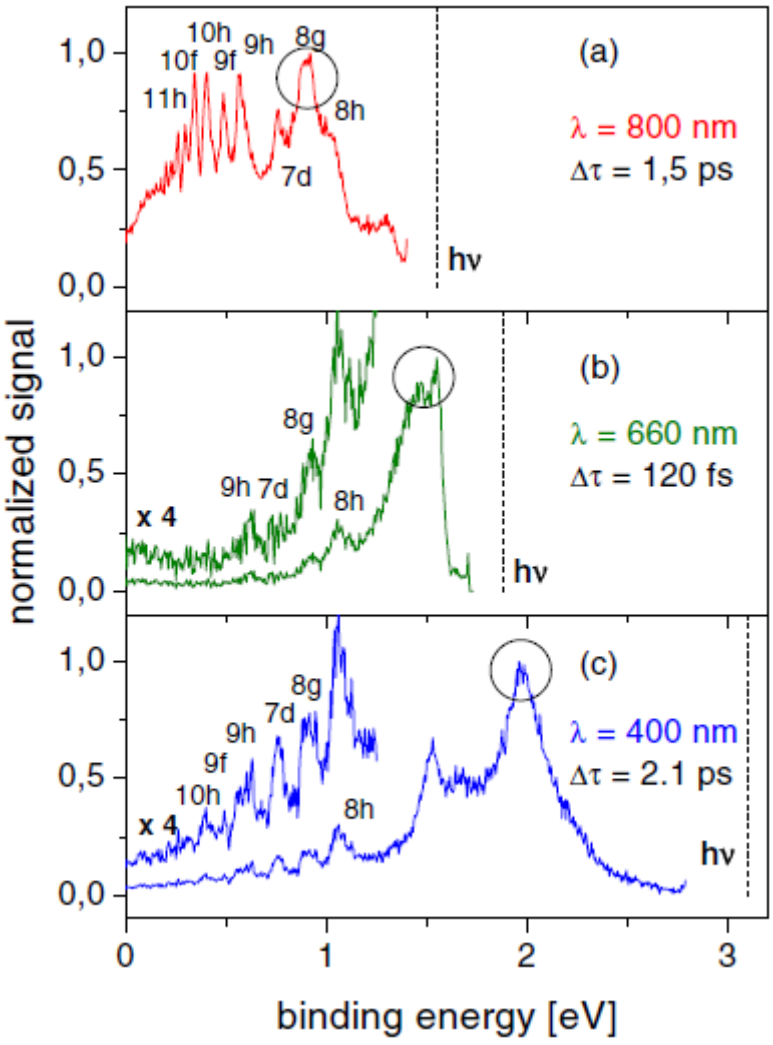

Figure 2.4: Photoelectron spectra of C_{60} plotted versus the electron binding energy obtained for different laser wavelengths and pulse durations. The same peaks can be seen in different spectra, suggesting that the same states are responsible for the peaks and that these states are one-photon ionised. Figure from Ref. [45].

When changing the wavelength of the photons used to excite the molecule, the peaks observed converge to the corresponding photon energy. The peaks appearing at the lower energy end of the spectrum show the same binding energy, regardless of the wavelength used and by changing the chirp on the pulse, the peaks in the spectrum can be shifted. When the pulse is negatively chirped, so that the red wavelengths lag behind the blue wavelengths, the peaks are shifted to lower kinetic energies. These results indicate that the ionisation step is a one photon process and that the Rydberg states are populated, independently of the wavelength, in the first part of the pulse and

ionised by the latter part of the pulse. The peak structure can be observed for a range of pulse durations from 30 fs to 5 ps and neither varying the pulse duration nor the laser intensity changes the peak position or the relative intensity of the peaks, although the relative intensities of the peaks change at different wavelengths. This suggests that the Rydberg excitation mechanism is fast but not overly dependent on pulse duration in the range under 5 ps. However, at shorter pulse durations, the Rydberg peaks appear smeared out compared to longer pulses. This is due to the shorter pulses having a larger bandwidth.

The excitation mechanism of these excited states is not known. Originally, a direct MPI process from the ground state was proposed although this fails to account for the spread in energy of the Rydberg peaks of 1-2 eV [46]. Freeman *et al*. explained the structure observed in xenon ATI peaks [47] by suggesting that different Rydberg peaks are shifted into resonance by the varying ponderomotive shift across the intensity profile of the laser beam. However, the ponderomotive energy and the bandwidth of the laser used in C_{60} experiments were too small to account for the observed energy range. Wesdorp *et al*. observed the population of Rydberg states in neutral molecules when C_{60}^{+} cations were bombarded by electrons, in the presence of a weak electric field [48]. They proposed that a laser electric field may act in a similar way by creating a 'saddle point' in the Coulomb potential and capturing an electron in a highly excited state. The observation of Rydberg peaks in phenol has been linked with nonradiative decay of superexcited states in the molecule [49].

An interesting observation was that Rydberg peaks are only observed for 'hot' C_{60} molecules. Results were compared for C_{60} at temperatures of 770 K and 80 K, produced by 'hot' and 'cold' molecular sources respectively; with only the hotter, vibrationally excited molecules producing Rydberg peaks in the photoelectron spectrum [46]. The authors accounted for this by suggesting that Rydberg states are populated by direct multiphoton excitation from a doorway state around 3 eV above the ground state where coupling of electronic and vibrational energy can occur. The first step in the mechanism is nonadiabatic multielectron excitation from the HOMO to the LUMO+1 doorway state, from which electronic thermalisation and coupling to vibrational modes takes place. Rydberg states are then populated in a direct multiphoton process and finally one-photon ionised. Vibrationally pre-excited

molecules would have a much higher density of populated vibrational states and might therefore experience a more efficient coupling between electronic and vibrational energy, through an improved Frank-Condon overlap, allowing more efficient population of the doorway state. The doorway state is proposed to be a broad quasi continuum of mixed states thought to span around 1 eV in energy. This would account for the spread in energy of observed Rydberg peaks. Another interpretation of the internal energy dependence involves the mixing of electronic and vibrational energy states at low principal quantum numbers, *n*. The inverse Born-Oppenheimer (IBO) approximation states that at high *n*'s the period of the electron is much longer than any period of the rovibrational motions of the molecular core [50]. This means that any vibrational state of C_{60} can be regarded as having a complete set of excited electronic states. However, for low *n*'s the separation of electronic and vibrational motion is not exact which implies that states of the same total energy are mixed. This could imply that molecules with pre-existing vibrational energy may be able to access a range of Rydberg states as wide as the range of vibrational energy.

Pump-probe experiments were carried out with a relatively weak 400 nm pump and a more intense 800 nm probe [46]. It was found that the electron yields for individual Rydberg states were greatly increased when the red probe followed the blue pump (Figure 2.5). Since the doorway state is reached by the absorption of just one 400 nm photon, this was seen to provide evidence that efficient population of the doorway state is crucial to the Rydberg population mechanism. However, it is possible that the weak 400 nm pump is much more efficient in exciting the molecule in general. The recorded signal depends almost linearly on the pump pulse intensity. Calculations suggested that the time evolution of the electron density in the LUMO+1 state also increases linearly with the pump intensity. The fast relaxation at short time delays is attributed to a thermalisation of the multiple excited electrons.

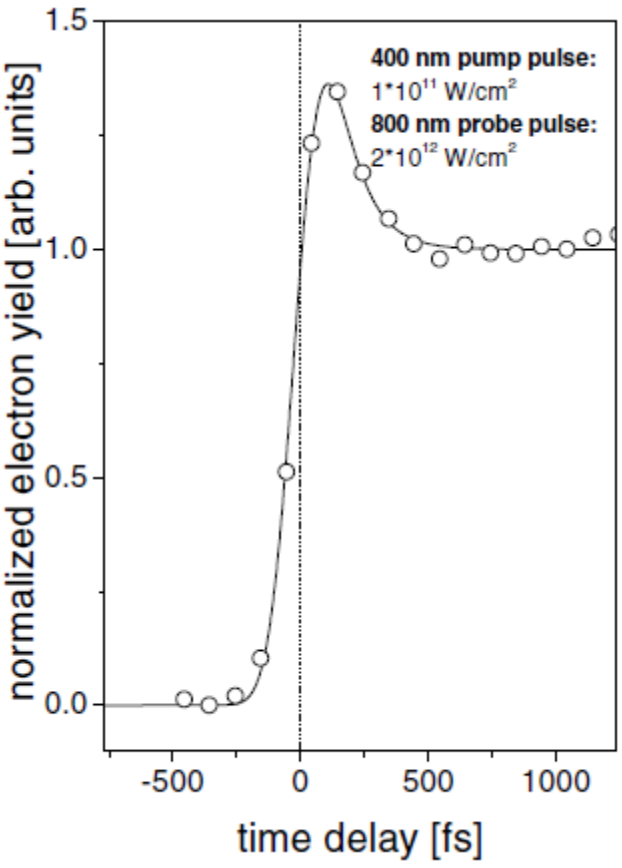

Figure 2.5: Normalised photoelectron yield from 8*g* Rydberg state as a function of pump-probe time delay. Figure from Ref. [46].

Similar Rydberg structure is seen in molecules besides C_{60}. Other fullerenes, such as C_{70} (Chapter 7) and endohedral fullerenes, such as La@C_{82} [51], as well as the polycyclic aromatic molecule anthracene [44] display peak structures in PES attributed to Rydberg peaks. Rydberg peaks are not observed, however, in metal clusters such as sodium [39]. The observation and analysis of this peak structure is similar to Rydberg fingerprint spectroscopy [52]. It has been shown that the Rydberg structure observed when ionising large molecules is very sensitive to the structure of the molecule and individual molecules display unique peak structures in the photoelectron kinetic energy spectra.

2.4.2 Superatom molecular orbitals

Recently, evidence has been reported of large atom-like hollow-core-bound molecular orbitals in C_{60} [7]. The local density of states of the orbitals were imaged using low-temperature scanning tunnelling microscopy on a sample of C_{60} molecules adsorbed on a copper surface (Figure 2.6). Their similarity to atomic orbitals led to them being named superatom molecular orbitals (SAMOs). The SAMOs assume the radial and angular distributions of spherical harmonic functions and are large and diffuse with significant electron density found inside the fullerene cage. They are thought to be unique to hollow shell molecules derived by wrapping of molecular sheets, with a central potential, which is where the similarity with atoms arises. The orbitals are attached to the hollow core of the molecule, rather than the carbon cage. The origin of the central potential can be traced to the short-range exchange-correlation effect between electrons with overlapping wavefunctions and the long-range Coulomb potential. In 2-D molecular sheets, such as graphene, these effects give rise to a series of hybridised image potential (IP) states on either side of the sheet [53]. Wrapping a 2-D sheet into a 0-D molecule stabilises the inner IP state with respect to the outer one, giving rise to the central potential of the molecule. In this sense they are different to Rydberg states in which a weakly bound electron is found far from the molecular core and interacts via a long-range Coulomb potential. The SAMOs are the lowest members of a series of states that should converge in a Rydberg series to the vacuum level [54].

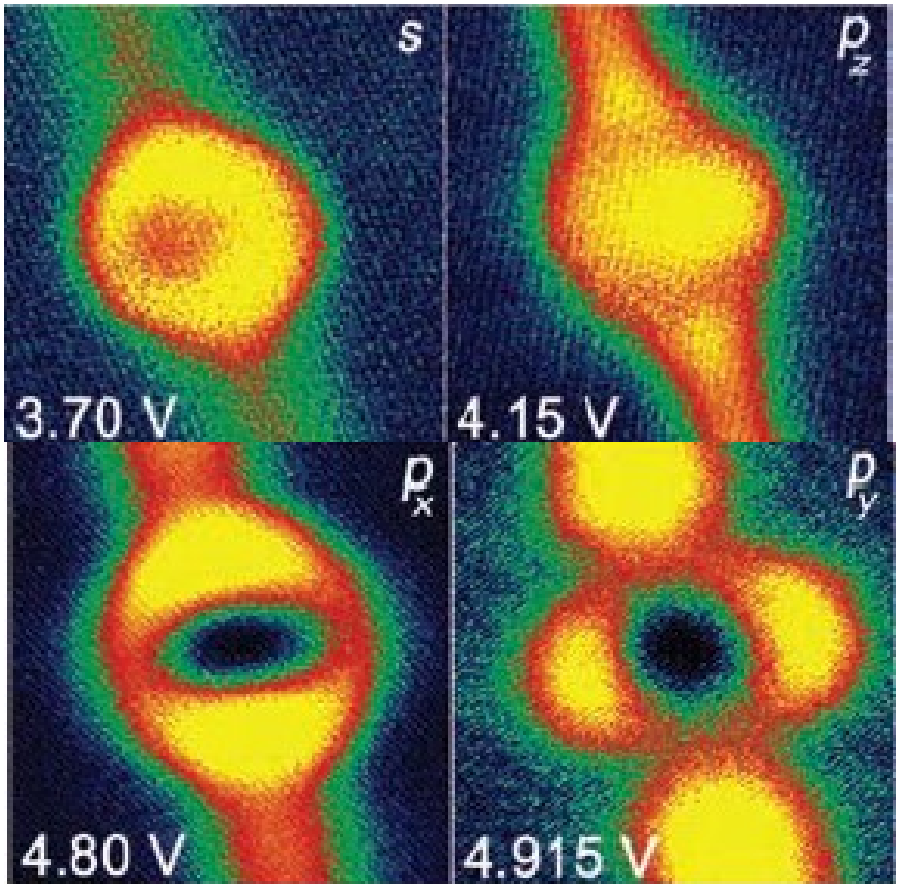

Figure 2.6: STM images of a single C_{60} molecule adsorbed on a copper surface. As the voltage is increased (as highlighted in the bottom left corners), excited states are populated and imaged. Above are shown the s, p_z, p_x, and p_y SAMOs. Figure adapted from ref [7].

DFT calculations were carried out and the wave functions and binding energies of the observed SAMOs were calculated [7]. The calculated wave functions for the s, p and d SAMOs are shown in Figure 2.7. The calculated binding energies are shown in Figure 2.8.

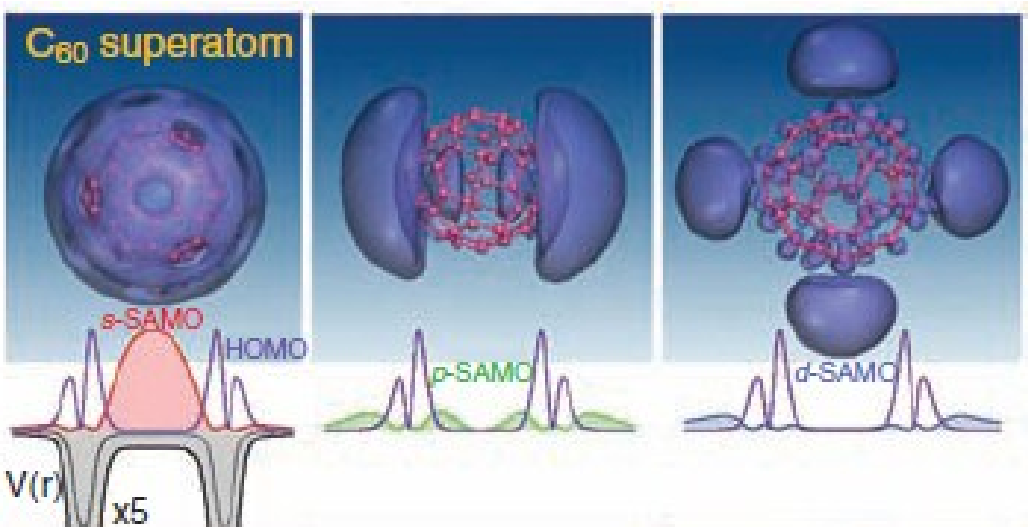

Figure 2.7: Wavefunctions for s, p and d SAMOs obtained by plane-wave DFT calculations. Figure adapted from ref [7].

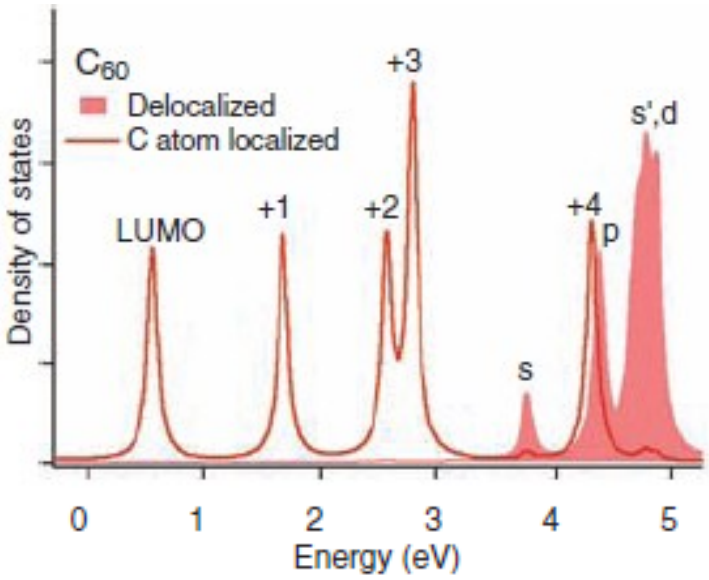

Figure 2.8: Density of states calculations carried out for C_{60}, showing the density of states associated with the SAMOs and their energies, relative to the LUMO. Figure from ref [7].

Since SAMOs are a property of hollow-shell molecules derived from the wrapping of molecular sheets, carbon nanotubes and endohedral fullerenes are also predicted to posses them. Calculations for the molecule Li@C_{60} suggest that the SAMOs are stabilised by the presence of the endohedral Li atom [54]. When C_{60} molecules are placed next to each other in 1-D, 2-D and 3-D assemblies, the SAMOs

were shown to combine, producing σ and π type delocalised orbitals of nearly free-electron like character. This raises the prospect of achieving metal-like conduction in fullerene assemblies if the SAMO orbitals can be adequately reduced in energy, for applications in areas such as molecular electronics and optoelectronics [55].

Chapter 3 –Background: Fusion of nanocarbon materials

This chapter will present a brief introduction to carbon nanotubes as well as a background to previous experiments where nanotubes have been fused or welded using electron beams. Since the fullerenes are from the same family as carbon nanotubes, a background to C_{60} fusion using ultrashort laser pulses is also presented.

3.1 Carbon nanotubes

Carbon nanotubes are members of the fullerene family. Since they first came to the widespread attention of the scientific community in 1991 [56], a great deal of work has been focussed on them. Single-walled carbon nanotubes (SWNT) can be thought of as 2-D sheets of graphene, rolled into a cylinder and capped at either end. The main body of the cylinder consists purely of hexagons whilst the end caps correspond to half of a fullerene molecule and are made from hexagons and pentagons. Like the spherical fullerenes, the bonds between carbon atoms are strong sp^2 bonds, which give the tubes incredible mechanical strength. Weaker van der Waals bonding exists between nanotubes. Multi-walled carbon nanotubes (MWNT) consist of concentric shells of tubes of increasing diameter, they possess many interesting and potentially useful properties. They display incredible mechanical strength [57] and are very good conductors of electricity [58] and heat [59]. Depending on the chirality of their structure, nanotubes can also be either metallic or semiconducting and because of their high aspect ratios, can be thought of as a quasi-one-dimensional material. These properties make them potentially useful materials as the building blocks for future applications in nanotechnology. If their incredible mechanical strength can be harnessed effectively, carbon nanotubes could form the basis for new, large-scale, technologies ranging from sporting and military equipment to space elevators [60]

. 3.2 Fusion of carbon nanotubes with electron beams

Studies have shown the apparent fusion and welding of multi and single-walled carbon nanotubes subjected to the high energy electron beams used in tunnelling electron microscopy (TEM) and scanning electron microscopy (SEM). Chen *et al*. reported the fusion of multi-walled nanotubes into amorphous nanorods under SEM conditions [61]. After 2 minutes of electron irradiation, a 50% expansion of tube diameter was recorded, with a 500% expansion at the tip. In this study, SEM pictures show a solid amorphous structure with an increased diameter, with respect to the original multi-walled tubes. This process is illustrated in Figure 3.1.

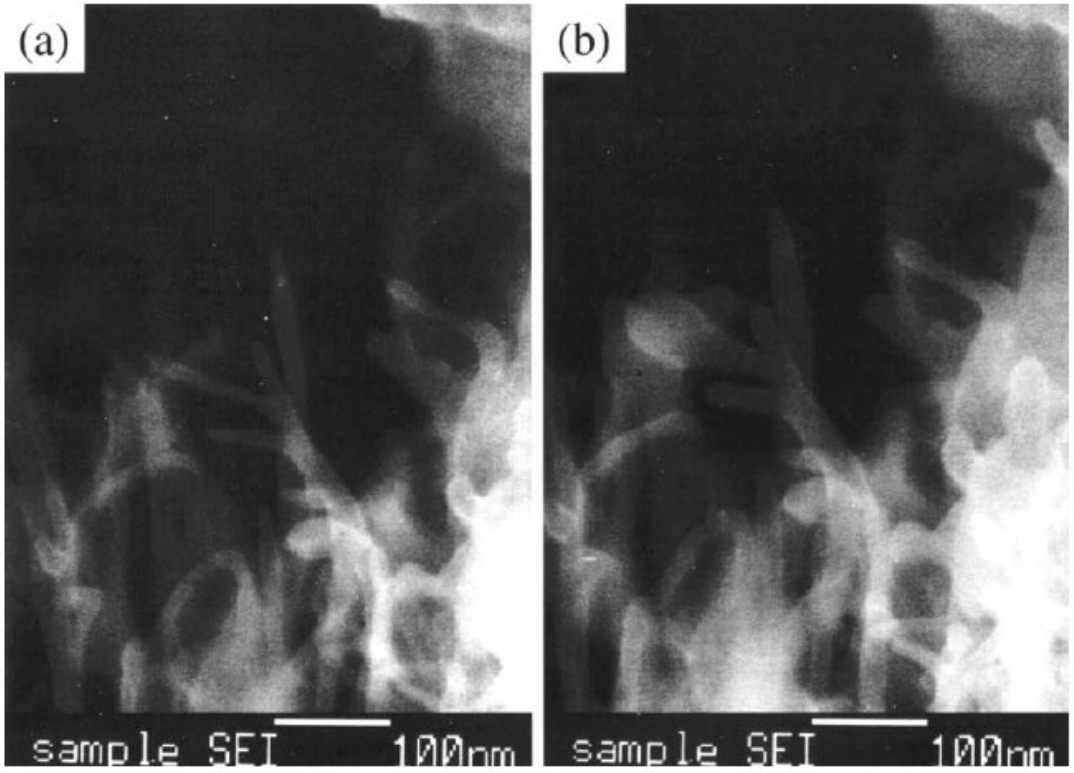

Figure 3.1: Comparison of (a) initial SEM image of multi- walled carbon nanotubes and (b) nanotubes after 2 minutes of electron beam irradiation in SEM. Figure from ref [61].

Ho *et al*. presented evidence of nanojunction structures in MWNT arrays after application of high electric fields [62] (Figure 3.2). They report that the electric field

resulted in carbon-carbon bond breaking and deposition leading to nanojunction formation where the carbon atoms at two adjacent tips chemically react and fuse.

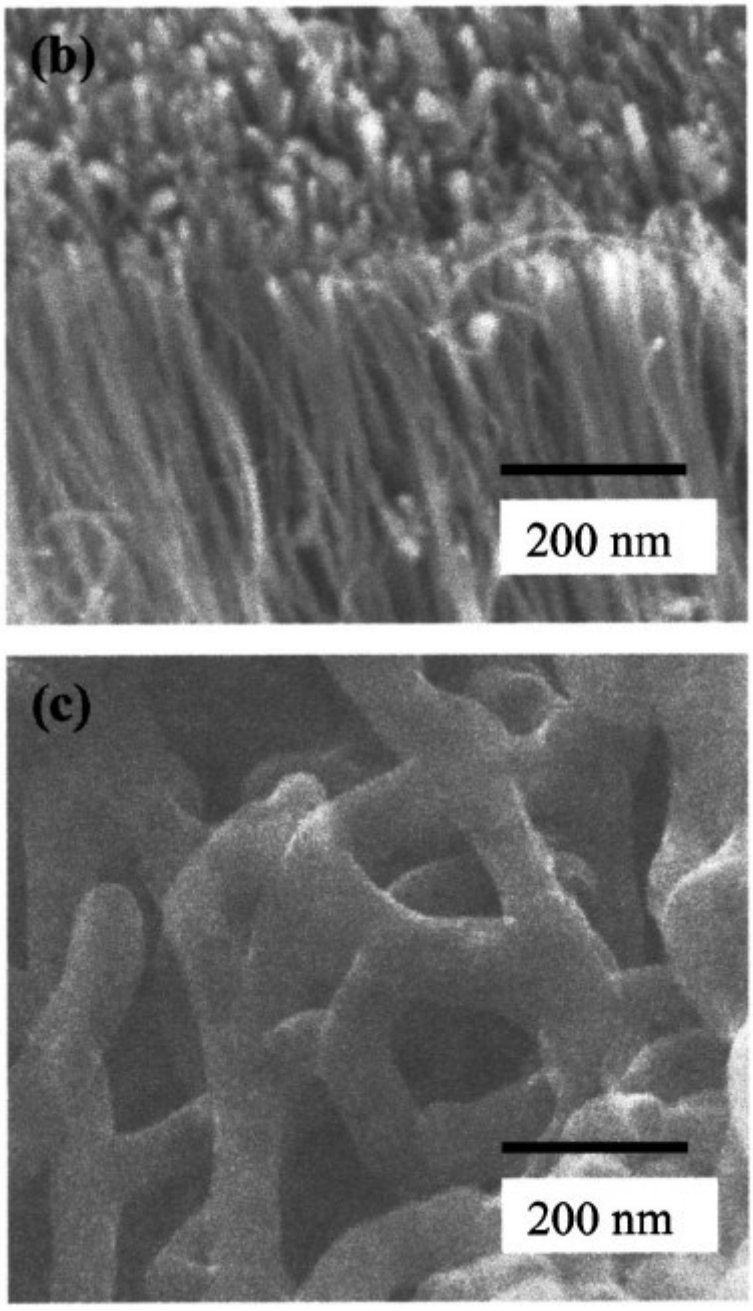

Figure 3.2: Comparison of top) SEM image of MWNT array before application of electric field and bottom) MWNTs after 6 hours of exposure to high electric fields. Figure from ref [62].

Zou *et al*. reported various transformations of the structure of single-walled nanotubes subjected to the high energy electron beam in TEM, including the welding

of aligned tubes [10]. Nanotubes with defects, introduced by chemical oxidation, were compared with tubes with few or no defects. It was observed that an increased level of structure transformation, such as amorphism, was observed for tubes with defects. This can be rationalised by the increased strain in the carbon network structure at defect sites. The carbon-carbon bonds at defect sites then become particularly susceptible to breaking under irradiation by the electron beam. This causes carbon atom sublimation, leading to sublimed carbon deposition on the walls of nearby nanotubes, increasing the thickness of these tubes. The welding of two aligned tubes was also observed. The electron beam can open the end of each tube, leaving dangling bonds. These bonds can connect, forming bonds with carbon atoms from another nanotube, which satisfy a continued nanotube structure. Figure 3.3 shows this process taking place under TEM conditions.

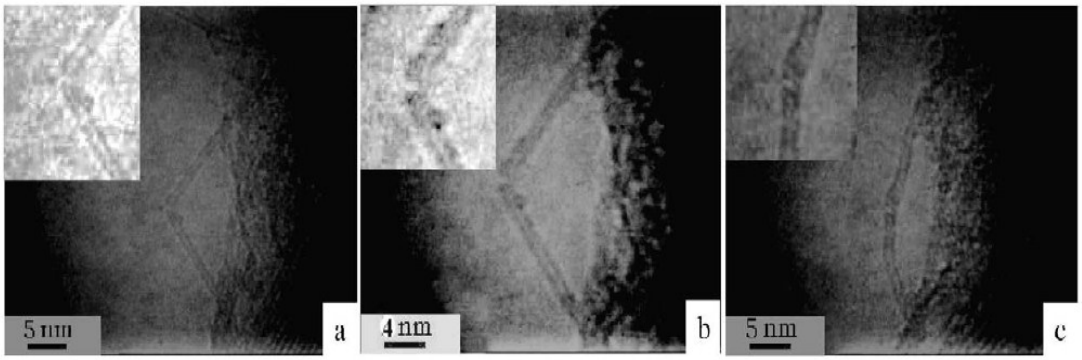

Figure 3.3: High resolution TEM images, taken at 1 minute intervals, showing (a) two aligned, capped nanotubes, (b) contact between tubes and (c) fusion of nanotubes at tips. Figure from ref. [10].

Terrones *et al*. reported that crossed SWNTs can be welded together to form molecular junctions by irradiation with electron beams in TEM [63]. The experiments were carried out at high temperatures and the authors conclude that this, along with the electron bean irradiation, induces structural defects which promote the joining of tubes via cross-linking of dangling bonds. This is depicted in Figure 3.4.

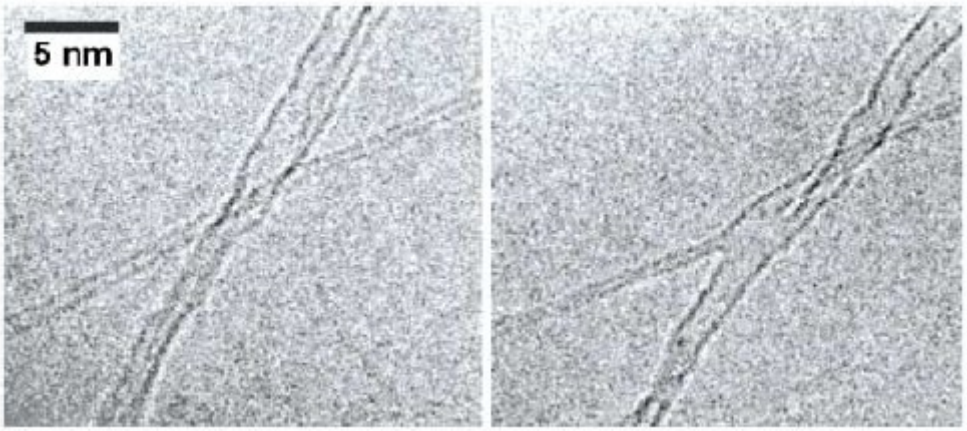

Figure 3.4: Left) two crossed carbon nanotubes. Right) the same picture but after 60 seconds irradiation with an electron beam, showing fusion of the tubes at the point they cross. Figure from ref [63].

In all these studies, the energy deposited in the carbon nanotubes, either by electron irradiation or exposure to high electric fields, appears to cause defects in the tube structure which then facilitates carbon-carbon bond breakage. The dangling bonds from nearby nanotubes can then link, fusing the tubes together.

Romo-Herrera *et al*. published a theoretical study on the properties of covalently bonded 2-D and 3-D networks of carbon nanotubes, formed by the creation of molecular junctions between tubes [64]. It was predicted that these networks could display a range of interesting properties such as high mechanical strength, good electrical conductivity, low mass densities and high surface areas. This makes these materials potentially very useful as nanoelectronic circuits, catalysts, sensors, filters or as molecular stores.

3.3 Fusion of C_{60} clusters with ultrashort laser pulses

Studies have shown that molecular fusion of fullerenes can be observed when fullerene clusters are subjected to intense femtosecond laser pulses [65]. Large clusters of $(C_{60})_N$,which are held together by relatively weak van der Waals bonds, can be produced from a gas aggregation source with cluster size of up to N = 250

recorded. The mass spectrum produced when C_{60} clusters are irradiated with 775 nm, 150 fs laser pulses shows groups of peaks which are associated with parent molecules of differing size, with the peaks within each group separated by C_2 units (Figure 3.5). This result can be explained by the fullerene molecules undergoing a fast rearrangement and fusion to form larger fullerene molecules. The fused molecule undergoes sequential emission of C_2 fragments to lose the excess energy after fusion. Fusion of fullerene molecules is only observed when the laser pulse is short enough (in the femtosecond range). This is because enough energy must be present in the electronic subsystem to overcome the fusion barrier which is around 80 eV. As described in Chapter 2, only with relatively short pulses can a large amount of energy build up in the electronic system before transfer into the vibrational modes occurs.

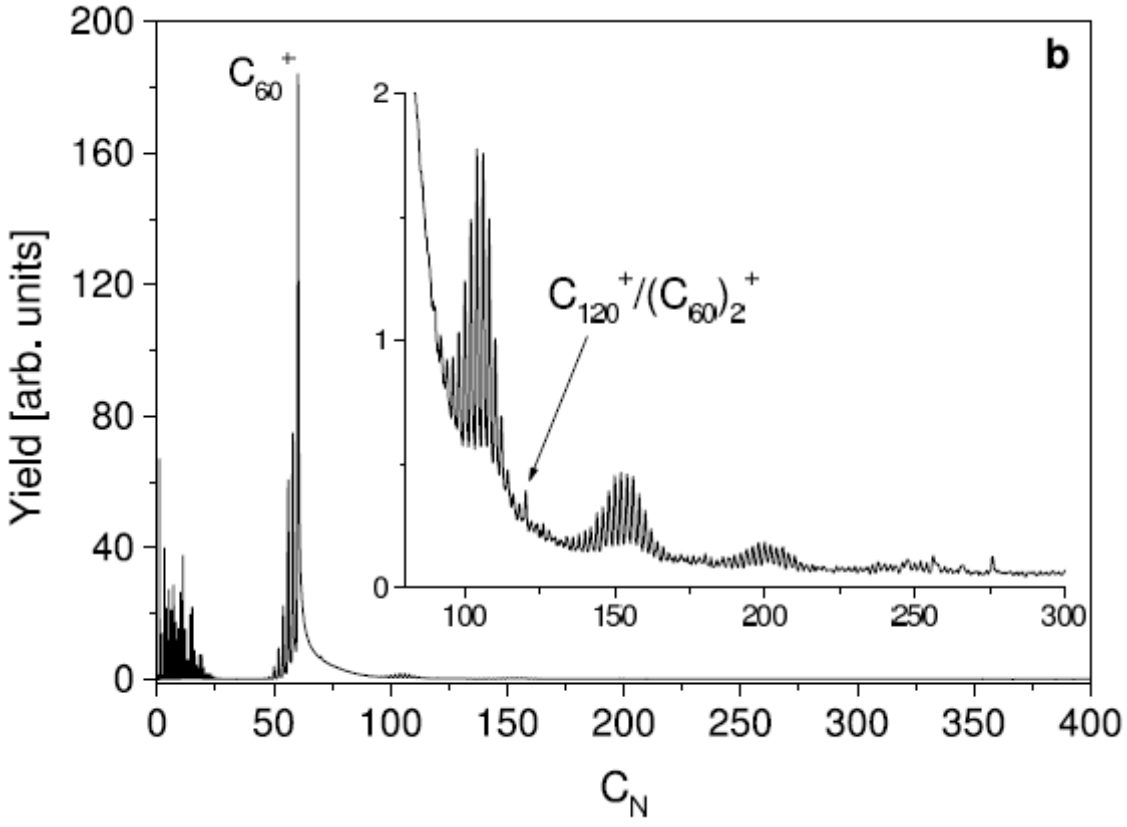

Figure 3.5: Mass spectrum from $(C_{60})_N$ ionised by 150 fs, 775 nm laser pulses. Figure from ref. [66].

Chapter 4 – Experimental setup and techniques: Gas phase experiments

This chapter describes the experimental setup, equipment and techniques used to obtain the results presented in Chapters 6 and 7 of this thesis. The vacuum chamber where the laser-fullerene interaction takes place is described, as well as the molecular beam source and the electrodes used to steer the appropriate photoproducts to their detectors. The Velocity-Map Imaging (VMI) setup and the Time-Of-Flight (TOF) mass spectrometer are described. A description of the lasers used in the lab is given, as well as the techniques used to characterise the laser pulses.

4.1 Vacuum chamber, beam source and ion optics

The interaction of fullerene molecules with laser pulses, as well as the detection of the photoelectrons and positive ions produced, takes place in a vacuum chamber (interaction chamber). A diagram, showing the main features of the vacuum chamber can be seen in Figure 4.1. Laser pulses, after passing through a focussing lens, enter and leave the chamber, travelling horizontally, through two windows, situated at either side of the chamber, attached to flanges. The laser beam intersects with a gaseous C_{60} molecular beam, travelling vertically upwards, produced in an effusive oven, situated below the interaction chamber, in a separate vacuum chamber (oven chamber). At one end of the interaction chamber, a Velocity-Map Imaging (VMI) photoelectron detector is mounted to a flange, to detect the photoelectrons produced. At the opposite end, a Time-Of-Flight (TOF) mass spectrometer is situated, with the ion detector on an identical flange, to detect positive ions. Voltages can be applied to electrodes on either side of the region where the laser-C_{60} interaction takes place, creating an electric field, so that the photoelectrons are sent towards the VMI detector or so that the positive ions are sent towards the mass spectrometer.

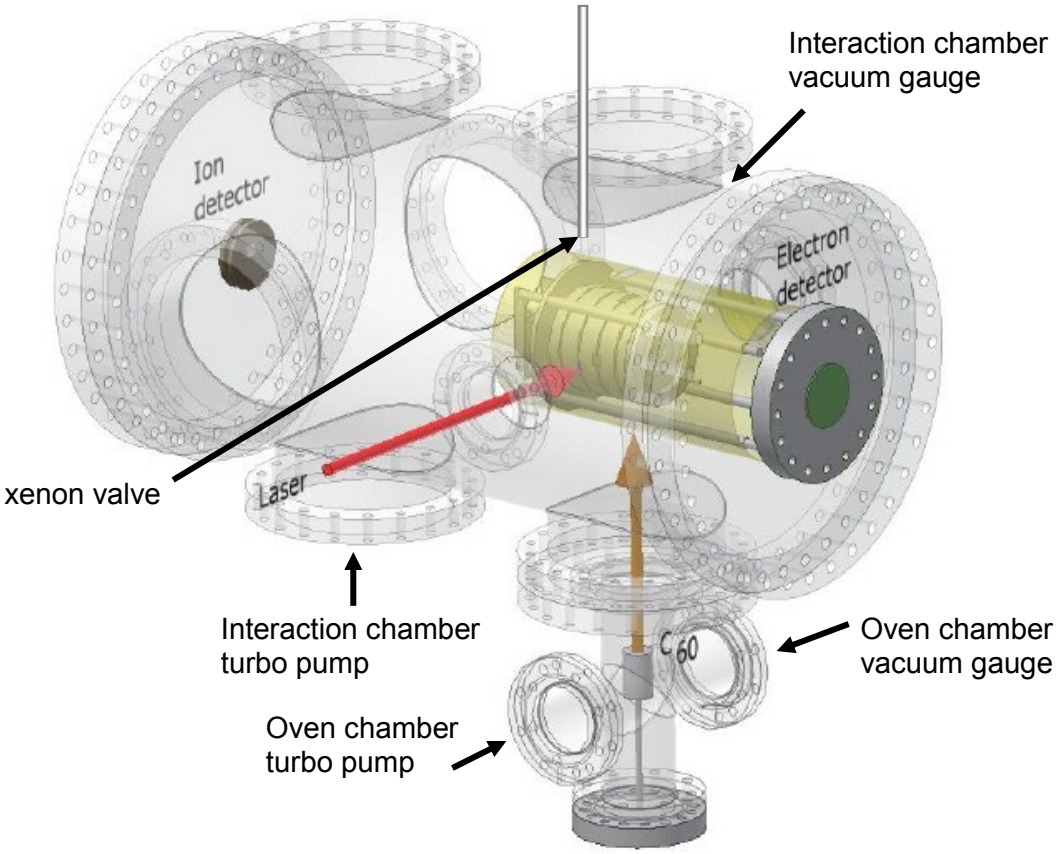

Figure 4.1: A sketch showing the interaction chamber, oven chamber, ion optics, photoelectron detector, ion detector, location of turbomolecular pumps, location of vacuum gauges, xenon needle valve and the experimental geometry. Sketch made by Olof Johansson.

The interaction chamber was custom built by CVT Ltd. and is pumped by a 300 l/s turbomolecular pump (Edwards, STP-301C) which is backed up by an oil-free scroll pump (Edwards, XDS10). The oven chamber is pumped by a 60 l/s turbomolecular pump (Edwards, EXT 75DX) and backed by an identical backing pump as the interaction chamber. Inverted magnetron vacuum gauges (Edwards, AIM-S) are installed in both chambers and the lowest pressure which can be measured with these gauges is 1.0×10^{-8} mbar. Pressures of 1.0×10^{-8} mbar are measured in the interaction and oven chambers, both when the effusive oven is off and when it is set at temperatures typically used in experiments. Xenon can be introduced to the interaction chamber through a needle valve, shown in Figure 4.1. This is used to calibrate the VMI detector (section 4.2.4) and the laser intensity

(section 4.4.7). Typical pressures used when measuring with Xe are in the 10^{-6} mbar range.

The C_{60} molecular beam is produced by heating a solid sample of 99.95% purity commercial C_{60} powder (SES Research) to temperatures of 450 – 500 ^{o}C. This is achieved in an effusive oven, inside the oven chamber (Kurt Lesker, part no. C-0450). A quartz ampoule, containing a sample of the powder, is placed inside a molybdenum cylinder. This is surrounded by a NiCr (80/20) heating wire which is resistively heated to the required temperature. A thermocouple is placed inside the Mo cylinder to allow the temperature to be recorded. A stainless steel nozzle is attached to the oven, with an orifice diameter of 3 mm. This gives a C_{60} molecular beam of Gaussian cross section and FWHM of 11-12 mm at the point where it intersects with the laser pulses [67]. After a fresh sample has been placed in the oven, the temperature is slowly increased over a number of hours to allow out-gassing of any impurities, before measurements are taken. The C_{60} sample can be replaced with a commercial C_{70} sample when needed. The oven chamber and the C_{60} molecular beam are represented in the diagram in Figure 4.1. The effusive oven is depicted in Figure 4.2.

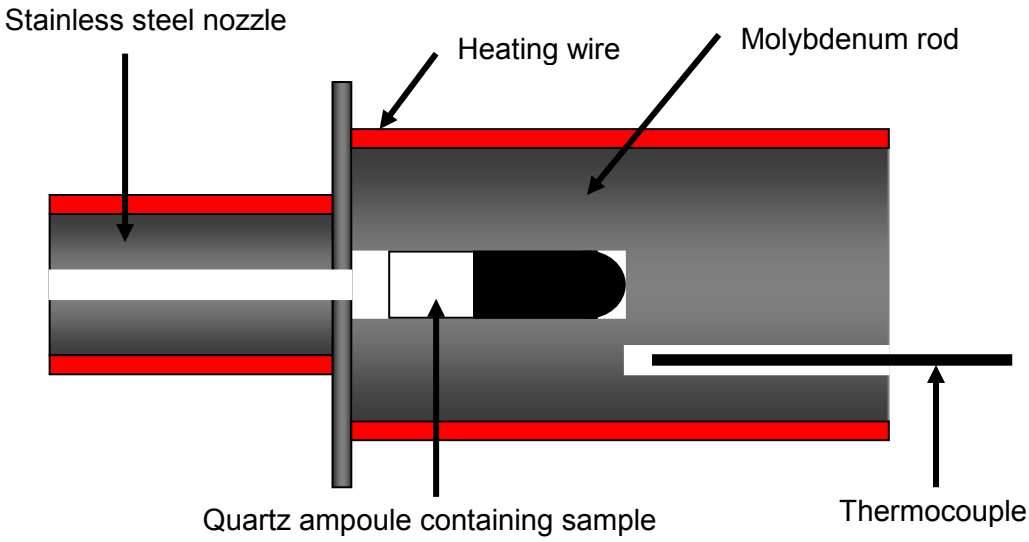

Figure 4.2: Diagram depicting the effusive fullerene oven. The molybdenum rod has a diameter of 25 mm and length 50 mm. A hole of diameter 4.2 mm and length 25 mm is drilled through to hold a quartz ampoule of length 25 mm and inner diameter 2 mm which contains the fullerene sample. The stainless steel nozzle has length 25 mm, outer diameter 12 mm and inner diameter 3 mm.

The series of electrodes which surround the laser-molecular beam interaction region are known as the ion optics. These consist of five stainless steel plates, mounted to the same flange as the VMI detector. Voltages, called the extraction voltages, can be applied to the electrodes labelled as HV_1, HV_2 and $HV_2/2$ (Figure 4.3) via electrical feedthroughs. The voltages applied create an electric field that extracts the desired photoproducts (either photoelectrons or positive ions) towards the appropriate detector (VMI detector or mass spectrometer, respectively). The electrodes labelled G_1 and G_2 are grounded to create field-free regions between the ion optics and the detectors. To avoid focussing effects in the ion trajectories, a 90% transmitting wire mesh is fitted to the electrodes HV_2, $HV_2/2$ and G_2, on the mass spectrometer side of the ion optics. The electrode assembly and field-free region between the grounded electrode, G_1, and photoelectron detector is surrounded by a cylinder of μ-metal which prevents external magnetic fields affecting the trajectories of the photoelectrons. An accurate depiction of the position of the ion optics, relative to the other components of the experimental setup can be seen in Figure 4.1. A sketch showing the electrode configuration can be seen in Figure 4.3.

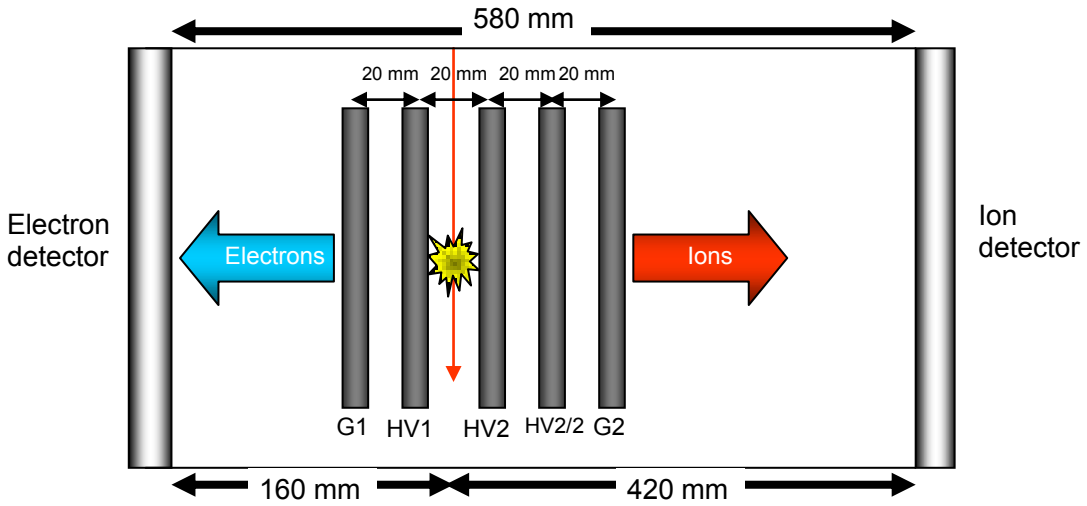

Figure 4.3: A sketch (not to scale) of the electrode configuration of the ion optics. The thin red arrow represents the laser beam and the yellow marker represents the intersection of the laser beam and fullerene molecular beam, at the laser focal spot, where the electrons and ions are created.

4.2 Velocity-Map Imaging

4.2.1 Introduction

Conventional photoelectron spectroscopy (PES) techniques involve ionizing an atom or molecule with light and measuring the intensity of the outgoing photoelectrons as a function of their kinetic energy. The kinetic energy of the photoelectrons in a direct multi-photon ionisation (MPI) mechanism is given by the equation

$$E_k = nhv - \Phi, \tag{4.1}$$

where n is the number of photons absorbed, hv is the photon energy and Φ is the ionisation potential of the electron in a given molecular orbital. This technique allows us to study the kinetic energy distribution of photoelectrons and thus gain information on the energy level structure of electronic orbitals. However, this gives limited

information regarding the angular distribution of the photoelectrons as only electrons ejected at a certain angle, with respect to the detector, are detected. Techniques, such as magnetic bottle photoelectron spectroscopy, allow electrons emitted over a 2π steradian angle to be detected but again, do not provide information on angular distributions [68]. Photoelectron angular distributions (PADs) contain much important information and a large amount of work has been done over recent years, utilising them to gain insight into the structure and behaviour of atoms and molecules [69]. PADs contain information on the angular momentum of the outgoing electrons and therefore the angular momentum of the orbitals from which they are ionised. They also contain information about physical phenomena which can affect the angular distributions of ionised electrons such as the repulsive Coulomb barrier peaked around the negative charges of dianions [70].

Velocity-Map Imaging (VMI) is a technique which allows the measurement of the kinetic energy distribution of ionised electrons as well as their angular distribution, with respect to the polarisation of the ionising laser pulse over a 4π steradian angle [71]. If one were to view a field-free photoionisation event in Cartesian coordinates, with the photoelectrons being created at the origin, with linearly polarised light travelling along the x-axis and the polarisation being parallel with the z-axis, all electrons with initial kinetic energy E_k would be found on the surface of a sphere, called a Newton sphere, after time t. The magnitude of the initial velocity vector, $|\boldsymbol{v_0}| = \sqrt{(2 \times E_k / m)}$, where m is the electron mass, for each electron of initial kinetic energy E_k, would be identical and the direction of emission would be different for electrons with different initial momentum vectors. The radius of the sphere, R, is the product of v_0 and t and the position of individual electrons on the Newton sphere surface can be described by the polar and azimuthal angles, θ and φ, respectively, giving the distribution of electrons $F(R, \theta, \varphi)$. The Newton sphere is depicted in Figure 4.4.

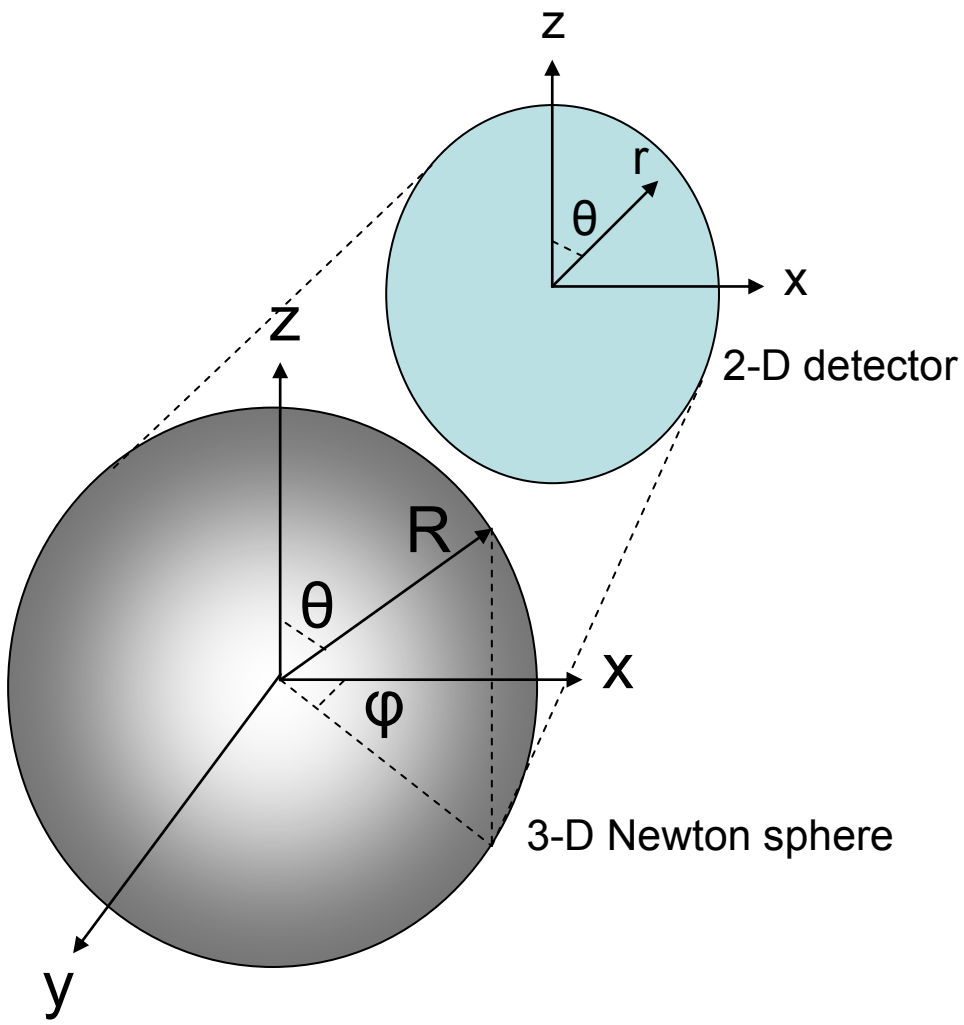

Figure 4.4: A sketch showing the geometry of the Newton sphere in Cartesian coordinates and the photoelectron distribution *F(R, θ, φ)* as well as the collapse of the 3-D distribution onto the 2-D detector. In the diagram, *R* does not have the same value as *r* as the radial distance of an electron arriving at the detector will depend on the focussing conditions. *r* is proportional to *R*.

In the presence of an electric field anti-parallel to the y-axis, the electrons are accelerated towards a position sensitive detector, with its plane coinciding with the x/z plane. The electric field is achieved by applying appropriate voltages to the electrodes HV_2 and HV_1, with a field-free region between the grounded electrode, G1 and the detector (see Figure 4.3). The electrodes act as an electrostatic lens and are left open, with no metallic meshes. This results in spatial focussing which implies that photoelectrons with the same initial momentum, whether or not they are created at the

same point in space, will arrive at the same point on the detector [72]. This process is depicted in Figure 4.4. By this method, the initial 3-D distribution of photoelectrons is collapsed and captured on a 2-D detector.

The optimum focussing conditions are found by keeping the HV_2 voltage constant and measuring the width of peaks in the Xe photoelectron spectrum for a range of different HV_1 voltages. Optimum focussing conditions are achieved when the xenon peak is narrowest, meaning the spectrometer is operating at highest resolution. An example of the spectra taken to optimise the voltages is given in Figure 4.5. By keeping the HV_2/HV_1 ratio constant and varying the absolute values, the 'strength' of focus can be tuned, effectively zooming in or out on an image. Examples of xenon images taken at different focussing 'strengths' are shown in Figure 4.6.

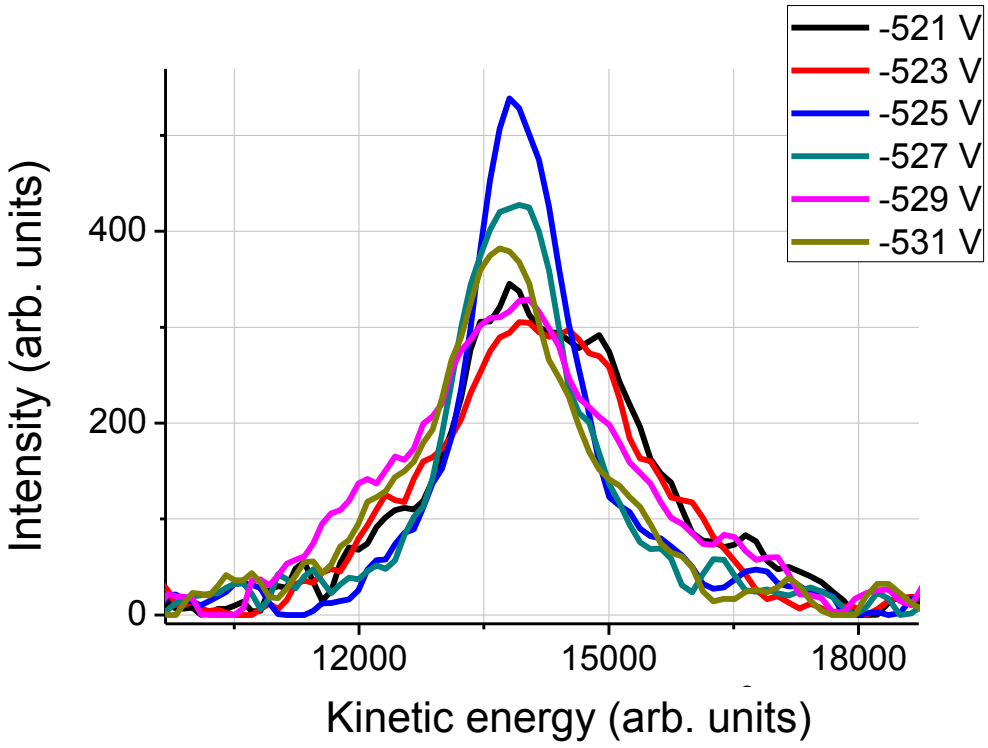

Figure 4.5: Photoelectron kinetic energy spectra for Xe, ionised with 400 nm, 4 ps laser pulses. HV_2 was kept at a constant value of -720 V whilst the voltage across the HV_1 electrode was varied (as shown in legend). The peak with the smallest Full Width Half Maximum (FWHM) value is the peak for HV_1 = -525 V and therefore the ratio of HV_2/HV_1 = 720/525 = 1.37, gives optimum focussing conditions and experimental resolution.

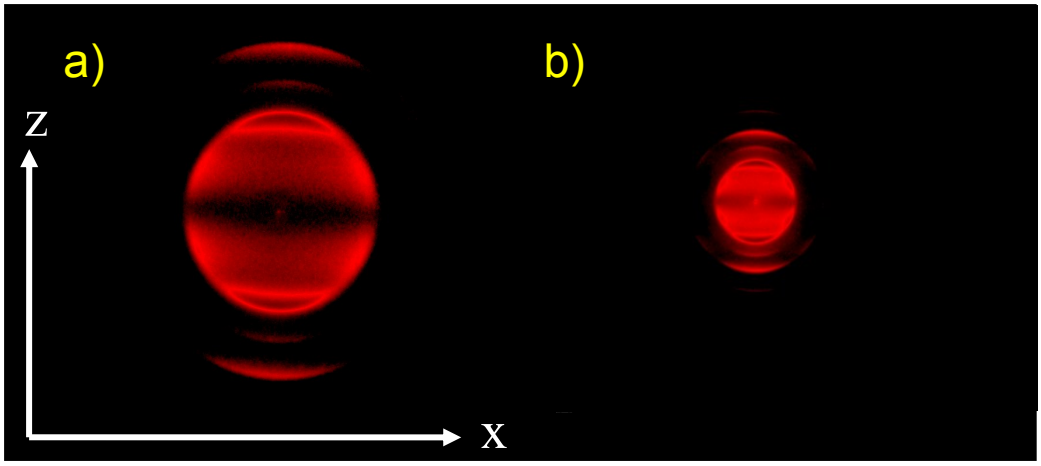

Figure 4.6: Raw VMI images of xenon taken with 550 nm, 20 μJ, 92 fs laser pulses at different absolute extraction voltage settings but with a similar HV_2/HV_1 ratio = 1.37. a) HV_2 = -800 V and HV_1 = -581 V. b) HV_2 = -3000 V and HV_1 = -2190 V. The detector dimensions are z = 1038 pixels and x = 1388 pixels.

The task of extracting the original 3-D photoelectron distribution from the detected 2-D image is simplified by the fact that, when using linearly polarised light, the outgoing electron distribution is rotationally symmetric around the polarisation direction, corresponding to the z axis [73]. This means that the angular distribution for a specific electron velocity can be simplified from *F(R, θ, φ) to F(R, θ)*. The 3-D distribution is retrieved using the inverse Abel transform [74]. The measured distribution at the detector can be described as

$$p(x,z) = \int_{-\infty}^{\infty} i(x,y,z)dy \,, \tag{4.2}$$

where $i(x,y,z)$ represents the 3-D photoelectron distribution. Considering one row of the image, taken along the x-axis at a certain z value, the distribution can be written as

$$f(x) = \int_{-\infty}^{\infty} i(x,y)dy = 2\int_{0}^{\infty} i(x,y)dy \,. \tag{4.3}$$

This step is valid as the cylindrical symmetry around the z-axis implies

$$\int_{-\infty}^{0} i(x,y)dy = \int_{0}^{\infty} i(x,y)dy \,. \tag{4.4}$$

The substitution, $r^2 = x^2 + y^2$ can be made, therefore

$$dy = \frac{dy}{dr}dr = \frac{r}{\sqrt{r^2 - x^2}}dr \,, \tag{4.5}$$

so that *f(x)* can be described by

$$f(x) = 2\int_{0}^{\infty} i(x,y)dy = 2\int_{0}^{\infty} \frac{ri(r)}{\sqrt{r^2 - x^2}}dr \,. \tag{4.6}$$

This is the Abel transform of *i(r)* and will give the 3-D distribution when applied to all values of z in the measured image.

All the relevant information in the 3-D distribution can be described by a 'slice' through the distribution, in the x/z plane, at y = 0 and this is described as an inverted image. An example of an inverted xenon image, as well as the raw image, measured at the detector, is shown in Figure 4.7. The polar angle, θ, is the photoelectron ejection angle with respect to the laser polarisation direction and the distance between a point on the detector and the origin is proportional to the magnitude of the initial velocity, v_0.

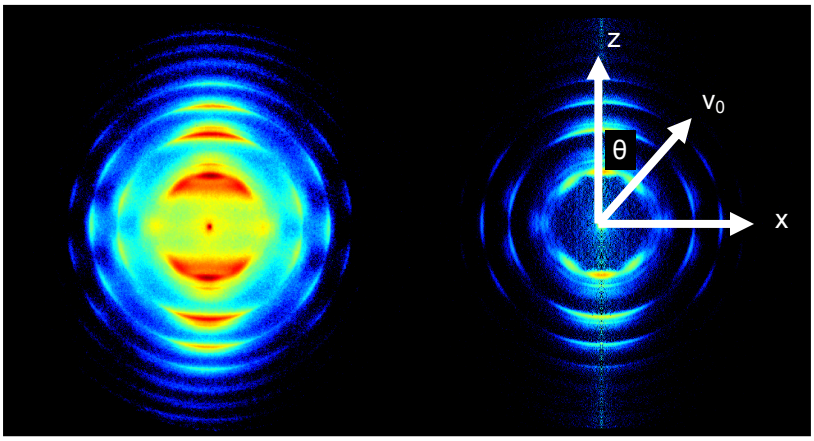

Figure 4.7: Left) Raw VMI image of xenon ionised with 800 nm, 130 fs, 42 μJ laser pulses. Right) inverted image giving a 'slice' through the x-z plane for y = 0. The radial distance from the origin is proportional to the magnitude of the initial velocity of the electron, v_0 and the angle of emission with respect to the laser polarisation is θ.

To produce a traditional photoelectron spectrum, the values measured at the detector, which are proportional to the number of electrons arriving at a certain point, must be expressed as a function of the kinetic energy of the electrons. By plotting the measured values as a function of the radius on the measured inverted image, and integrating over all angles, the radial velocity distribution is obtained. As $E_k \propto v_0^2$ the radial values are squared so that they are proportional to kinetic energy. An angle-integrated radial distribution and corresponding kinetic energy distribution for xenon are shown in Figure 4.8.

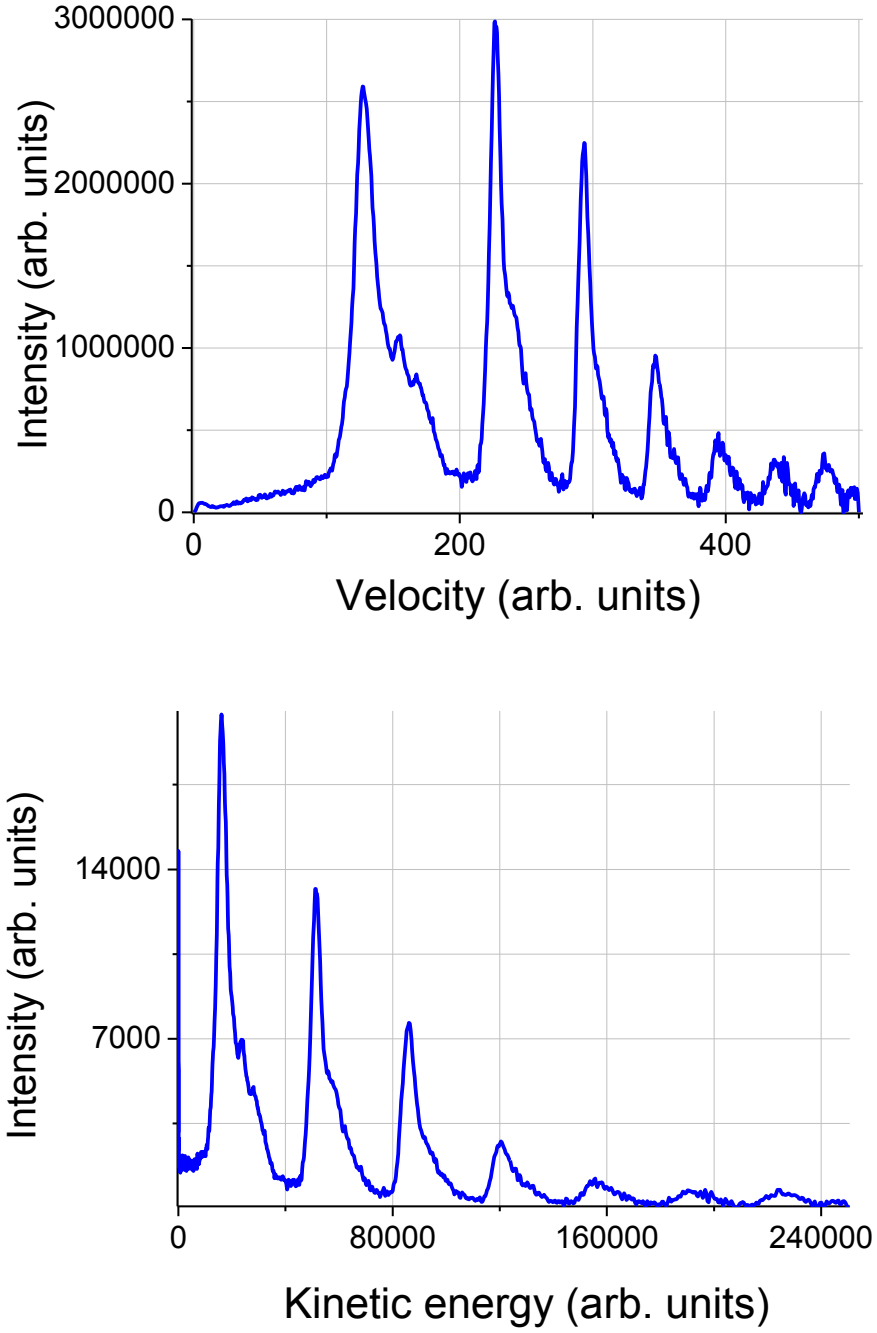

Figure 4.8: Top) Radial velocity distribution for inverted xenon image in Figure 4.7. Velocity is proportional to the radial distance, in pixels, from the origin. Bottom) Kinetic energy distribution from the same inverted image. Kinetic energy is proportional to the square of the radial distance from the origin.

4.2.2 Detector and accumulation software

The detector used in the VMI setup is a commercial detector (Photonis USA Inc., part no. 31376) consisting of a pair of chevron-style Microchannel plates (MCPs) and a phosphor screen. To ensure proper grounding of the field-free region in front of the detector, an additional electrode was placed before the MCPs. The detector is mounted on the vacuum side of the end flange of the interaction chamber and is coupled to the atmospheric side by fibre optics. Voltages are applied across the MCPs in the region of V_{MCP} = 1800 V and $V_{Phosphor}$ = 4800 V, with a voltage difference of 3000 V always maintained between V_{MCP} and $V_{phosphor}$. Electrons arriving at the detector create a cascade of electrons through the MCPs and the resulting cascade impinges on the phosphor screen whereby photons are produced. A diagram of the detector is depicted in Figure 4.9.

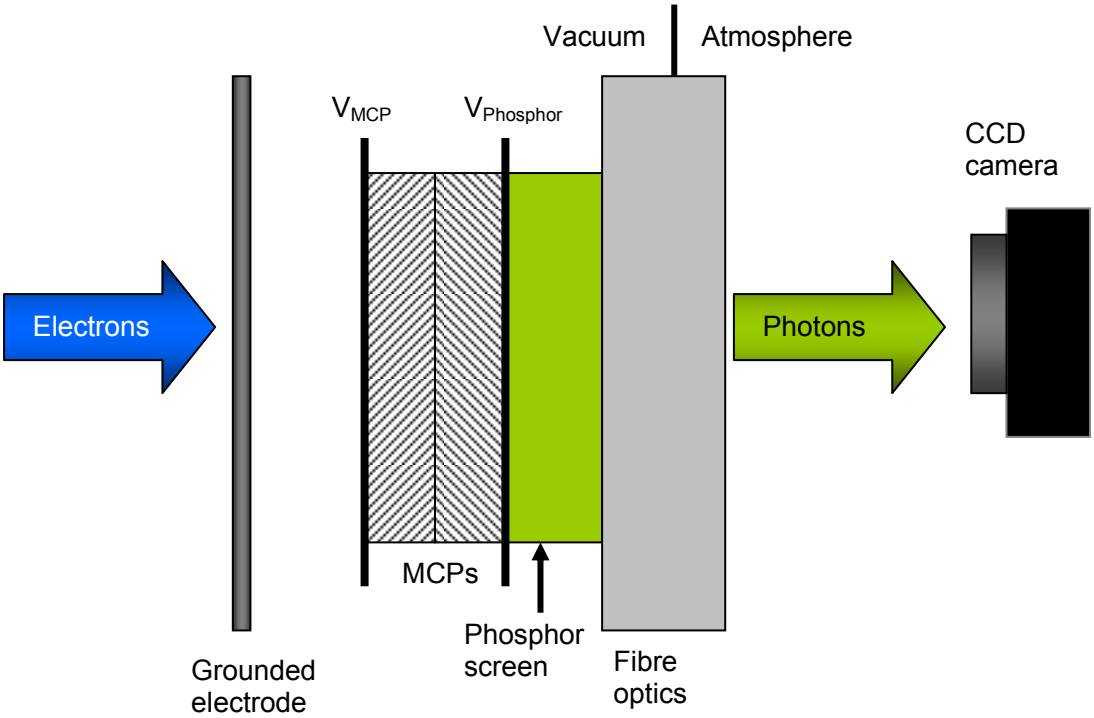

Figure 4.9: Diagram of the VMI electron detector.

The signal from the phosphor screen is recorded by a CCD camera (Allied Vision Technology, Stingray) which is connected to a computer. The camera resolution is 1388 x 1038 pixels. The cameras shutter speed is 82 ms so with the laser

repetition rate of 1 kHz, 82 shots are accumulated per image. Two different accumulation programs are used to record the images. Written in LabVIEW by Olof Johansson, these are *continuous_acquisition.vi* and *single_count_aquisition.vi* [67]. Continuous acquisition adds several images together over many laser shots. These images are added together for the duration of the experiment, with a corresponding number of background images taken, with the laser beam blocked from the chamber. The images are later added together, with the background subtracted. Single count acquisition applies a user-defined threshold to each image to ensure that only true counts are recorded, with all other pixels being set to zero. The threshold is determined by observing the maximum background count value. The program finds the centre of mass of each spot and adds one count to the corresponding coordinate in a new image. This is repeated over the course of the experiment, without the need to take background spectra. This technique is referred to as centroiding and provides better resolution than continuous acquisition although the images often need to be smoothed, radially.

4.2.3 Inversion Methods

Once the raw image is recorded, it needs to be inverted to provide the centre slice through the 3-D distribution which provides the angular and velocity distributions. There are several inversion methods available, including BASEX [75] and pBASEX [76]. These methods involve expanding the 2-D projection in a basis set of functions with analytically known Abel transforms. The 3-D distribution is then reconstructed as a linear combination of these functions with the same expansion coefficients used. BASEX does this in Cartesian coordinates which results in noise accumulating in a central line down the inverted image. pBASEX first converts the image to polar coordinates and fits Gaussian functions to the radial part of the raw image and Legendre polynomials are fitted to the angular part. This has the advantage of confining noise to the centre spot of the image. The basis set expansion methods avoid the need to use the inverse Abel integral directly. In this thesis, a modified version of the Polar Onion Peeling program (POP) [77] is used unless otherwise stated. The POP method borrows ideas from BASEX and pBASEX and is based on onion-peeling in polar coordinates [78], in which the raw 2-D projection is converted

from Cartesian to polar coordinates. The contribution to the 2-D projection from events outside the 'centre slice' through the 3-D distribution, in the x/z plane at y = 0, is subtracted at incrementally decreasing radii using the inverse Abel integral

The POP method essentially delivers the centre slice in the x/z plane at y = 0 by 'peeling away' the φ contribution, from events in the 3-D distribution, outside the centre slice, starting at the maximum radius and working towards the centre of the 2-D image. Every radius in the raw 2-D image has a φ contribution associated with it which must be removed to recover the inverted image. Each radius corresponds to electrons of a certain kinetic energy. Electrons with a given kinetic energy will produce a 3-D Newton sphere which is collapsed onto the 2-D detector. It is the contributions from the electrons in this 3-D distribution, but outside the centre slice, which must be removed to produce the inverted image. The raw Cartesian image, $G(x,z)$, is first converted to polar coordinates, giving $h(R, \theta)$. Starting at the maximum radius, $h(R_{max}, \theta)$, which represents the outermost ring of the measured 2-D distribution where there is no φ contribution, assuming there are no electrons with kinetic energy corresponding to radii larger than the detector, $h(R_{max}, \theta)$ is fitted to the angular distribution

$$I(\theta) = N(R)\sum_n \beta_n(R) P_n[\cos(\theta)], \tag{4.7}$$

where $P_n[\cos(\theta)]$ is the n^{th} order Legendre polynomial. The fit provides $N(R)$, an intensity factor, and $\beta_n(R)$, the anisotropy parameter. $\beta_n(R)$ describes the anisotropy in the photoelectron angular distribution at a given kinetic energy. $\beta = 0$ represents a completely isotropic distribution with positive values indicating a distribution peaked at 0 degrees and a negative value indicating a distribution peaked at 90 degrees. The basis functions used are idealised radial distribution functions produced by angular integration of perfectly isotropic images. In other words they are functions, representing the 2-D image, which would be produced by collapsing isotropic 3-D distributions onto a 2-D detector. The relevant basis function, for a certain radius, is then used to generate an idealised perfectly isotropic polar image, $h_{ideal}(R_{max}; R, \theta)$. The semicolon in this expression is used to signify that this is the image $h_{ideal}(R, \theta)$, associated with electrons of kinetic energy corresponding to R_{max}. This image is then

used, in conjunction with the experimentally observed intensity factor and anisotropy parameter, to create the idealised image

$$h_{\mathrm{f\,it}}(R_{\max};R,\theta) = h_{\mathrm{ideal}}(R_{\max};R,\theta)N(R)\sum_{\mathrm{n}}\beta_{\mathrm{n}}(R)P_{\mathrm{n}}[\frac{R}{R_{\max}}\cos(\theta)], \qquad (4.8)$$

where $R/R_{\max}$ is a factor accounting for the number of polar pixels at radius, R, compared to the number at $R_{\max}$, the maximum radius. $h_{\mathrm{fit}}(R_{\max};\ R,\ \theta)$ is then a representation of the φ-contribution of electrons of the same kinetic energy as those at radius, $R_{\max}$, and is removed from the raw image $h(R,\ \theta)$. This process is repeated for every radius, moving from the outer ring, into the centre, incrementally. Once the h_{fit} image, calculated for every radius, has been removed from $h(R,\ \theta)$, what will be left is the centre slice in the x/z plane at y = 0.

The original POP program only uses Legendre polynomials up to n = 4. The number used depends on the number of photons absorbed during the process and the authors were primarily concerned with one- or two-photon processes. Since more photons are absorbed in the processes concerning the results in this thesis, the original program was modified to include Legendre polynomials up to n = 10. The original program, *POP_8.5.vi*, was written in LabVIEW with most of the code written in C language syntax within a formula node interface. Since adding more Legendre polynomials was not a trivial exercise using the C language syntax of the original program, the whole program was re-written, in MATLAB, to include Legendre polynomials up to n = 10. The modified program is called *GPOP.m* and is presented in Appendix C. Figure 4.10 shows a comparison of inverted images, from the same experimental data, using the BASEX program, the original POP program and the modified POP program, *GPOP.m*. Figure 4.11 shows a comparison of the kinetic energy distributions and fitted anisotropy parameter, β_2, values obtained from each program. From Figure 4.10 it can clearly be seen that both POP programs bypass the problem of central line noise associated with the BASEX program. Central line noise can be a problem when looking at the 0-10 degrees angular segment of the VMI image. Where the GPOP program improves upon the POP program is in the angular fitting procedure. From the raw image in Figure 4.10, it can be seen that the first ring, closest to the centre of the image has two ‘nodes’ (areas of minimum intensity)

between 0 and 180 degrees. As each subsequent ring represents ATI peaks and sequential absorption of one extra photon, the number of nodes should increase by one, for each ring, as the change in angular momentum for an outgoing electron by absorption of one extra photon is $l = +1$. The second ring has three nodes, the third ring has four. This is replicated in the images inverted with BASEX and GPOP. It is not replicated for the image inverted with POP. Because POP only uses Legendre polynomials up to $n = 4$, it is unsuited to inverting images with features which are the result of processes involving more than two photon absorption. GPOP can invert images resulting from more than two photon absorption and eliminates central line noise. Figure 4.11 demonstrates how all three programs deliver almost identical radial spectra and that BASEX and GPOP deliver almost identical anisotropy parameters but that the POP program delivers slightly different anisotropy parameters.

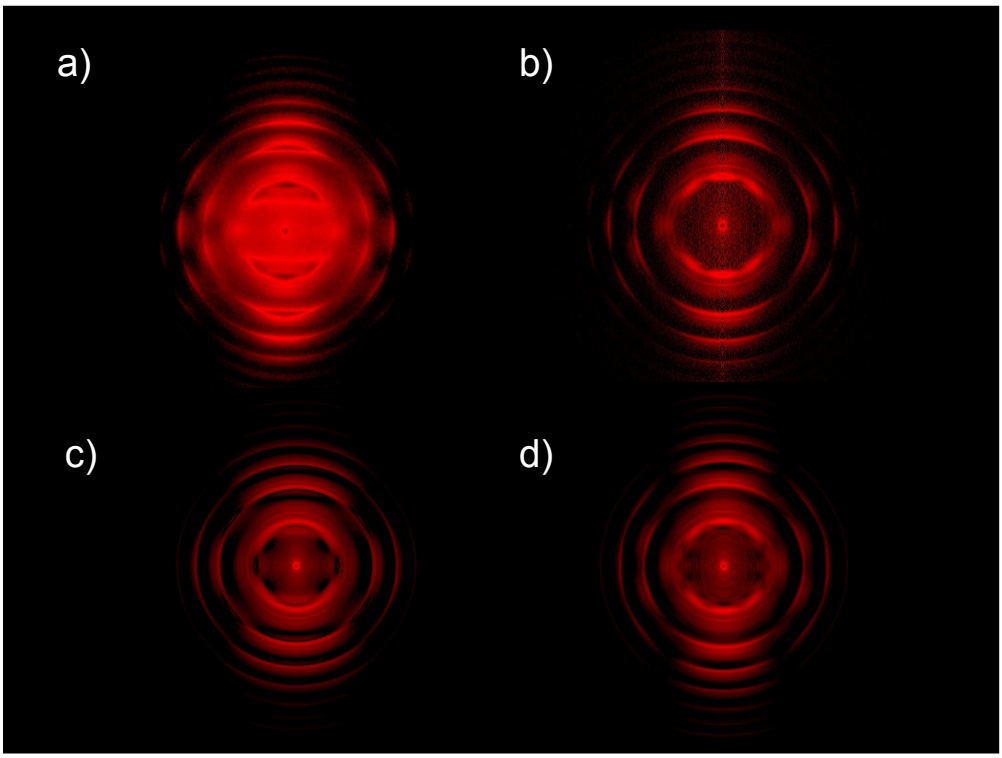

Figure 4.10: a) Raw VMI image of Xe taken with the continuous acquisition program ionised with 800 nm, 130 fs, 42 μJ pulses. b) Inverted image from raw image a) using the BASEX inversion program. c) Inverted image from raw image a) using the POP inversion program. d) Inverted image from raw image a) using the modified POP program, *GPOP.m*. All images are shown on a logarithmic intensity scale.

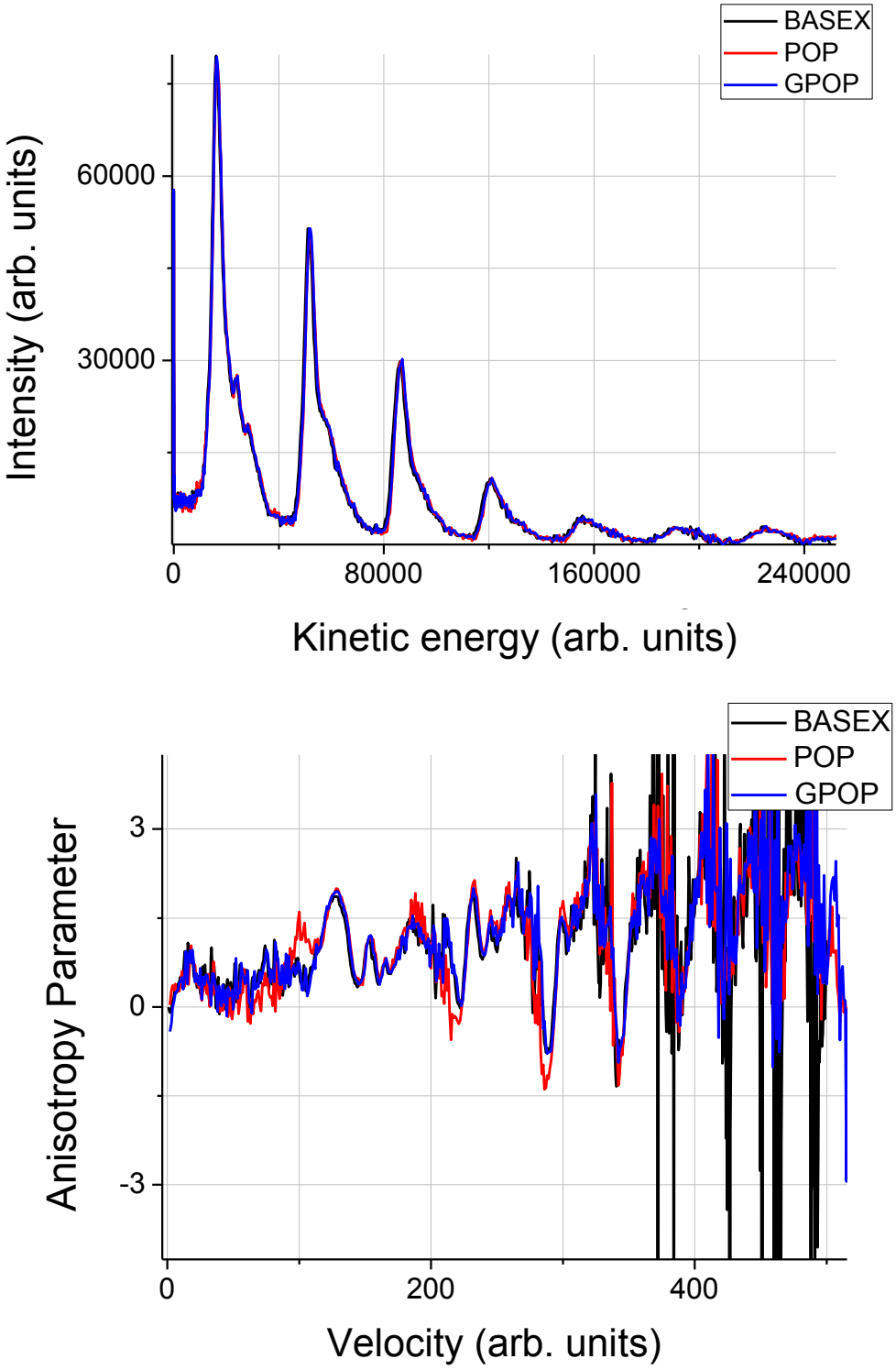

Figure 4.11: Top) Angle integrated kinetic energy distributions for the raw data presented in Figure 4.10, reconstructed with BASEX, POP and GPOP. Bottom) Fitted β_2 values as a function of velocity for the same data presented in Figure 4.10, reconstructed with BASEX, POP and GPOP.

4.2.4 Calibration of photoelectron kinetic energy distributions

The velocity distributions obtained after inverting the raw images are given in units of CCD camera pixels. When the velocity distributions are converted to kinetic energy distributions, they are therefore given in units of pixels^2. To calibrate the distributions, xenon images are recorded and inverted. Photoionisation of xenon has been studied extensively and its energy level structure is well known [79], making it a useful means of testing the experimental setup and calibrating the photoelectron spectra. The difference in position between peaks in any given Xe kinetic energy distribution is known which provides a calibration factor to be used with fullerene spectra. Depending on the wavelength and intensity of ionising light used, either the difference between the peaks corresponding to ionisation from the $P_{3/2}$ ground state and the first ATI peak can be used or the difference between the ground state peak and the peak corresponding to ionisation from the first excited $P_{1/2}$ spin-orbit state, 1.306 eV above the ground state. New Xe images are recorded for calibration every time the extraction voltages are changed, the laser is realigned into the chamber or the wavelength is changed and therefore the focussing lens position is optimised before the chamber. The example shown here describes a typical calibration process.

An inverted VMI image of Xe, taken with 800 nm, 130 fs, 42 μJ laser pulses, with the extraction voltages set at HV_2 = -2000 V and HV_1 = -1444 V is shown in Figure 4.12, along with the corresponding kinetic energy distribution. At this intensity, Xe undergoes direct multiphoton ionisation with Above Threshold Ionisation (ATI) peaks visible in both the inverted image and the kinetic energy distribution. ATI occurs when an atom or molecule coherently absorbs one or more photons than are needed to overcome the ionisation potential and so each ATI peak is separated by the energy of one photon. The ionisation potential of Xe is 12.13 eV [80]. The peak labelled ‘peak 1’ in the spectrum represents ionisation from the ground state via absorption of eight 800 nm photons of energy 1.55 eV, total energy 12.4 eV. Peak 2 represents ionisation from the ground state via absorption of nine photons, total energy, 13.95 eV and peak 3 represents ionisation from the ground state via

absorption of ten photons, total energy, 15.5 eV. So the peaks are separated by the kinetic energy of one photon, which at 800 nm is equal to 1.55 eV.

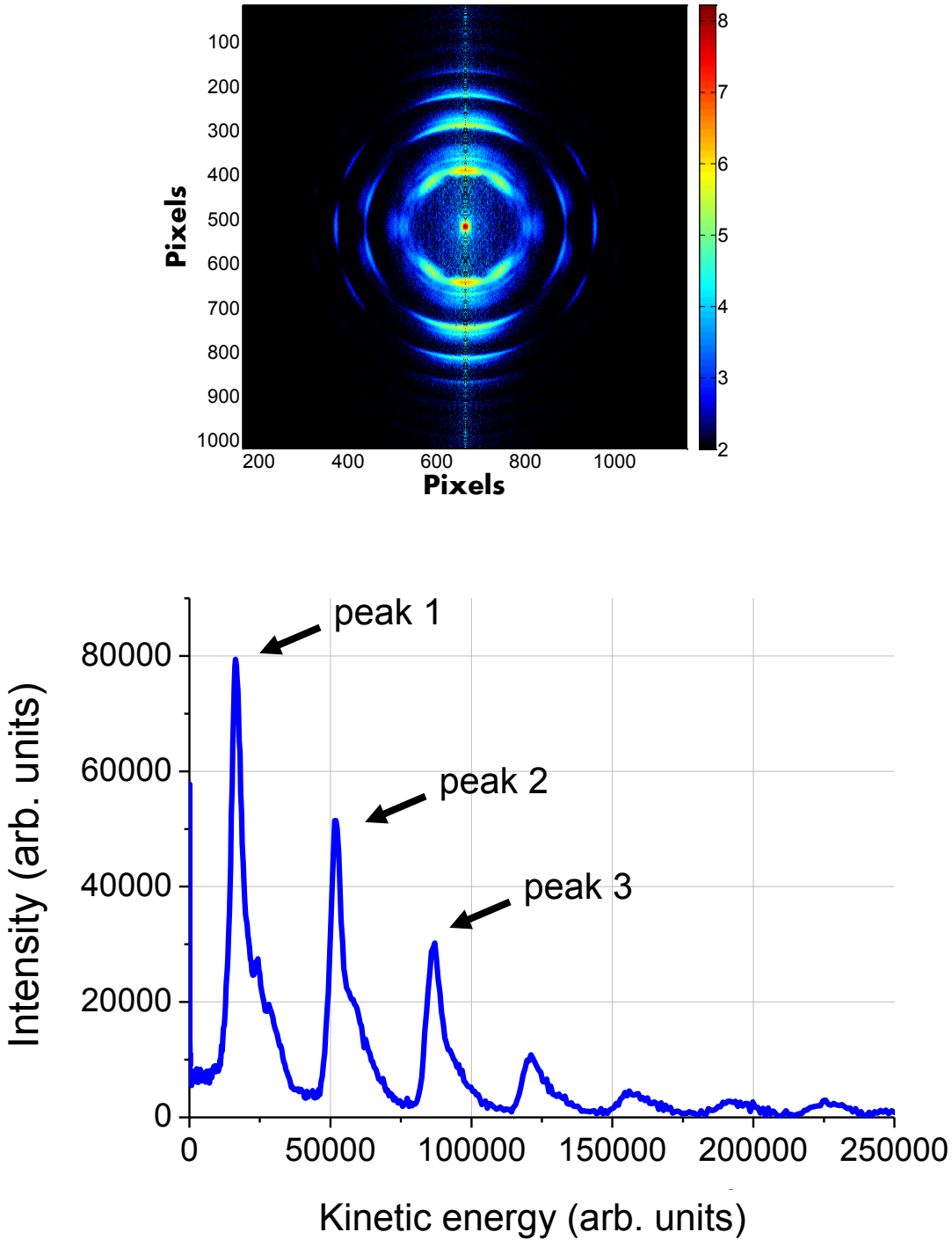

Figure 4.12: Top) VMI image of Xe, inverted with BASEX, ionised with 800 nm, 130 fs, 42 μJ laser pulses, shown in logarithmic intensity scale. Bottom) The corresponding, uncalibrated angle integrated kinetic energy distribution.

The peaks from the uncalibrated spectrum are then fitted to Gaussian peaks in *Origin* (Figure 4.13).

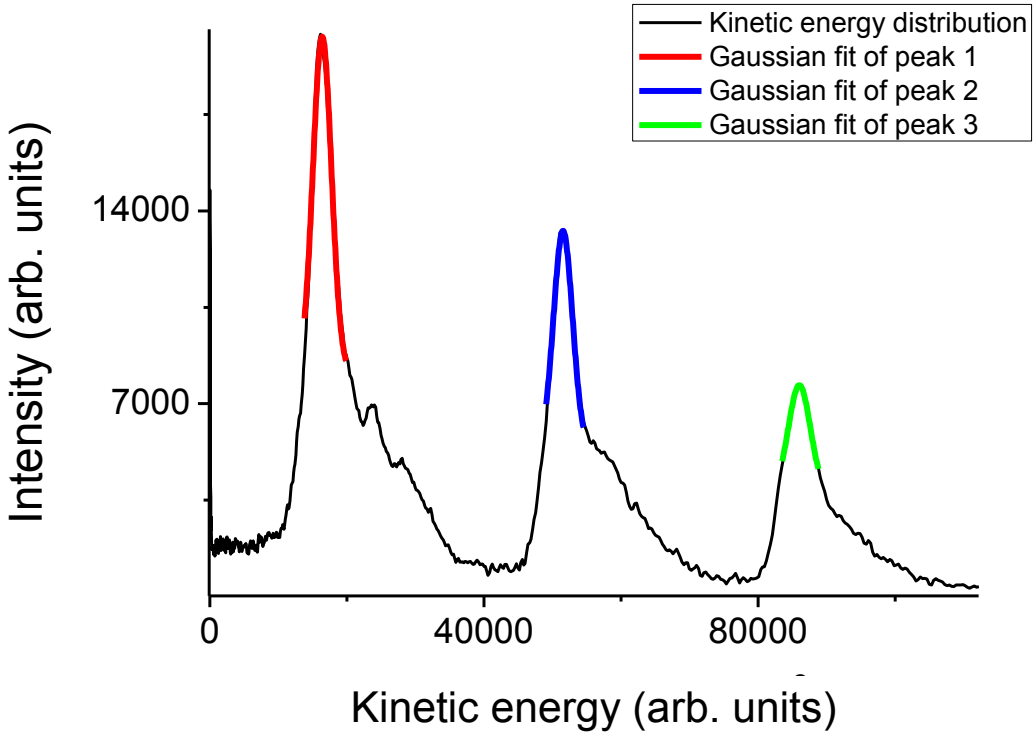

Figure 4.13: Kinetic energy distribution from Figure 4.12, with Gaussian curves fitted to the first three peaks.

Peak 1 has a position of 16387 ± 22 pixels^2, peak 2 has a position of 51533 ± 19 pixels^2 and peak 3 has a position of 86037 ± 16 pixels^2. By assuming that the kinetic energy difference between each peak is Δ_E = 1.55 eV, and the average difference between each peak is 34831 pixels^2, the calibration factor, k, then becomes

$$k = \Delta_E \div \Delta_p = 1.55 \div 34831 = (4.4501 \pm 0.002) \times 10^{-5} \text{ eV/pixels}^2.$$

The calibration factor, k, is then applied to the kinetic energy scale and a calibrated spectrum can be seen in Figure 4.14.

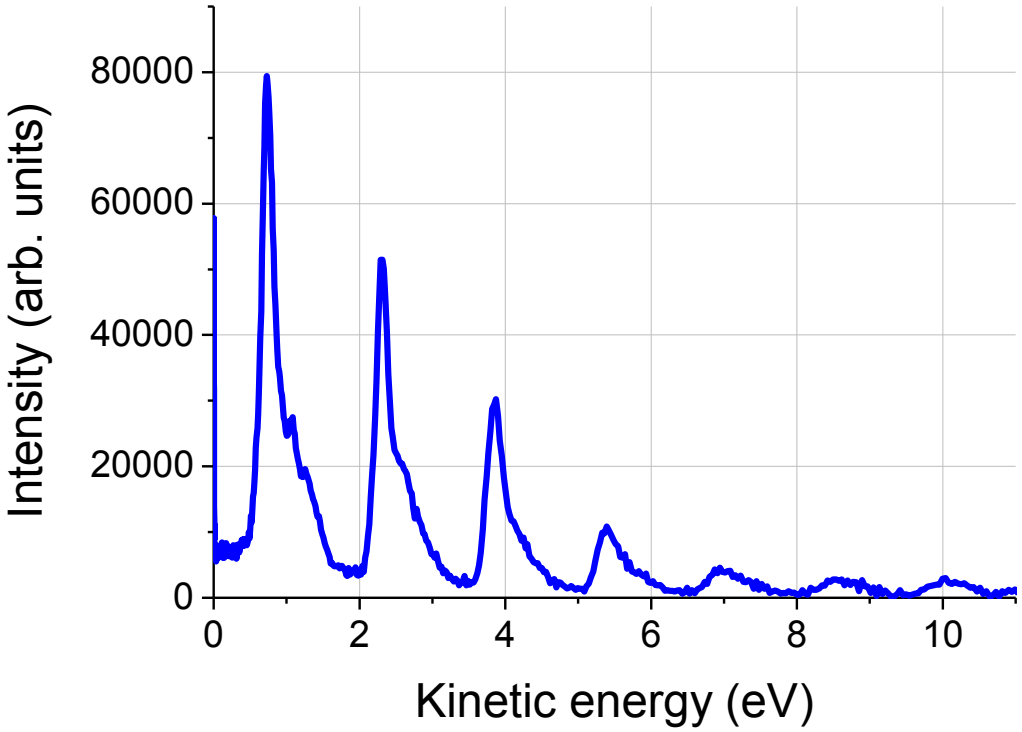

Figure 4.14: Calibrated Xe kinetic energy distribution in units of eV.

4.3 Mass Spectrometry

To detect the species of ions created in photoionisation experiments, a linear TOF mass spectrometer, with a Wiley-McLaren extraction zone [81], is used. Ions created in the interaction region are accelerated by an electric field, created by the electrodes of the ion optics, towards a field-free region of known length, where they do not undergo acceleration. Ions, created at the same point in space, with the same mass/charge (*m/z*) ratio will then arrive at the detector at the same time. The potential energy which the ion gains in the extraction region is equal to the applied potential multiplied by the charge on the ion

$$E_p = zU\,. \tag{4.9}$$

Immediately after their creation, the ions are accelerated towards the field-free region and the potential energy E_p will be converted to kinetic energy E_k. At the point the ion enters the field-free region, all of the initial potential energy will be converted to kinetic energy

$$zU = E_k = \frac{1}{2}mv^2 . \tag{4.10}$$

Since the kinetic energy is equal to the potential energy gained in the extraction region and the ions have zero acceleration in the field-free region, the time taken for the ions to traverse the time-of-flight tube is only dependent on the *m/z* ratio and by measuring the time of flight, the *m/z* ratio can be calculated.

The ions are not created at a point source, however, and some will be created closer to the field-free region than others. The Wiley-McLaren extraction zone compensates for this spread by making all ions pass through two electric fields of different strength. Ions created nearer the field-free region will possess a lower potential energy from the field than those further away, meaning they will have a lower kinetic energy and therefore velocity when entering the field-free region. If the extraction voltages are optimised, the point where the ions created further away from the field-free region 'catch up' with the ions created closer, will coincide with the detector. HV_1 acts as the repeller, HV_2 as the extractor, $HV_2/2$ as the extractor/2 and G_2 as the ground. Typical voltages used are HV_1 = 2000 V and HV_2 = 714 V. The $HV_2/2$ electrode provides a smoother potential drop between the extractor and the grounded electrode. The voltages are optimised by varying the value of HV_2 and optimising the resolution of the mass spectrum produced. A sketch of the TOF setup and electrodes can be seen in Figure 4.15. With the present set-up it is not possible to simultaneously detect ions and electrons. VMI images and mass spectra are recorded separately.

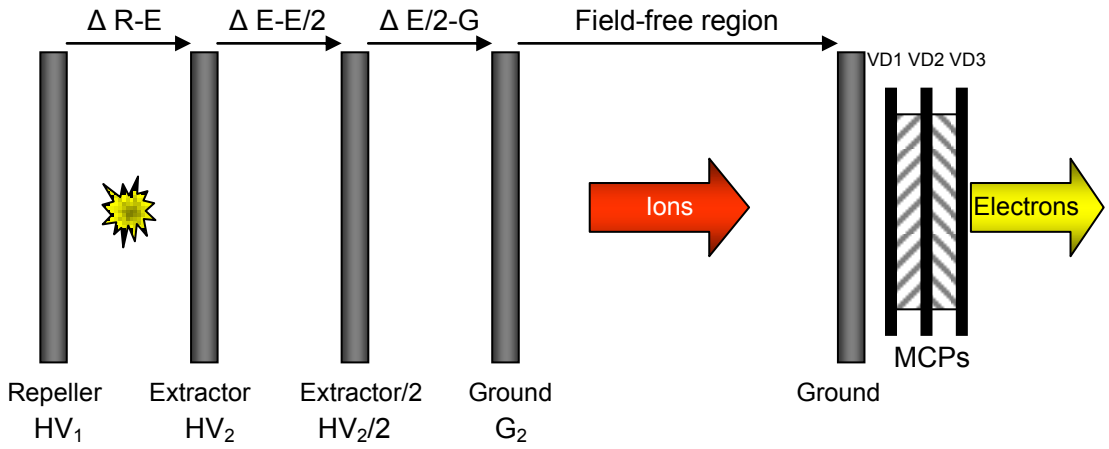

Figure 4.15: Sketch (not to scale) showing the setup of the linear time-of-flight mass spectrometer with Wiley-McLaren extraction zone and the MCPs with the electrodes VD1, VD2 and VD3 which are part of the ion detector. The arrows above the electrodes indicate the potential difference between each electrode.

The detector is a commercial MCP detector (Jordan TOF Products Inc., part no. C-0701) and consists of a pair of Chevron-style MCPs (Photonis USA, part no. MCP 18/12/5 D 40:1 (PS30220)). The voltage applied to the detector constituents is controlled by a voltage divider. This divides the applied voltage over the electrodes VD1, VD2 and VD3 which surround the two MCPs in the detector. When a typical voltage of -4.3 kV is applied over the detector, voltages of -1946, -1061 and -176 V are applied to VD1, VD2 and VD3, respectively. This ensures that the voltage across a single MCP is never greater than 1 kV and that the electron cascade produced by the ion's impact is accelerated through each MCP towards an anode. The anode, on the vacuum side of the chamber, measures the current due to the electron cascade and is connected to a preamplifier (TA1800, FAST ComTec) on the atmosphere side. The detector signal is amplified ten times in the preamplifier and then sent to a digital 500 MHz oscilloscope (MS06054A, Aglient Technologies). The oscilloscope is triggered by the signal from a fast photodiode inside the laser amplifier. The oscilloscope is connected to a computer and controlled by a LabVIEW program, *Mass_Spec.vi*. This collects the spectra accumulated in the oscilloscope and adds them together.

The spectra obtained are recorded as a function of the time-of-flight of the ions. These can be converted to *m/z* values by calibrating, using peaks in the spectrum of known *m/z*. An example spectrum is shown in Figure 4.16.

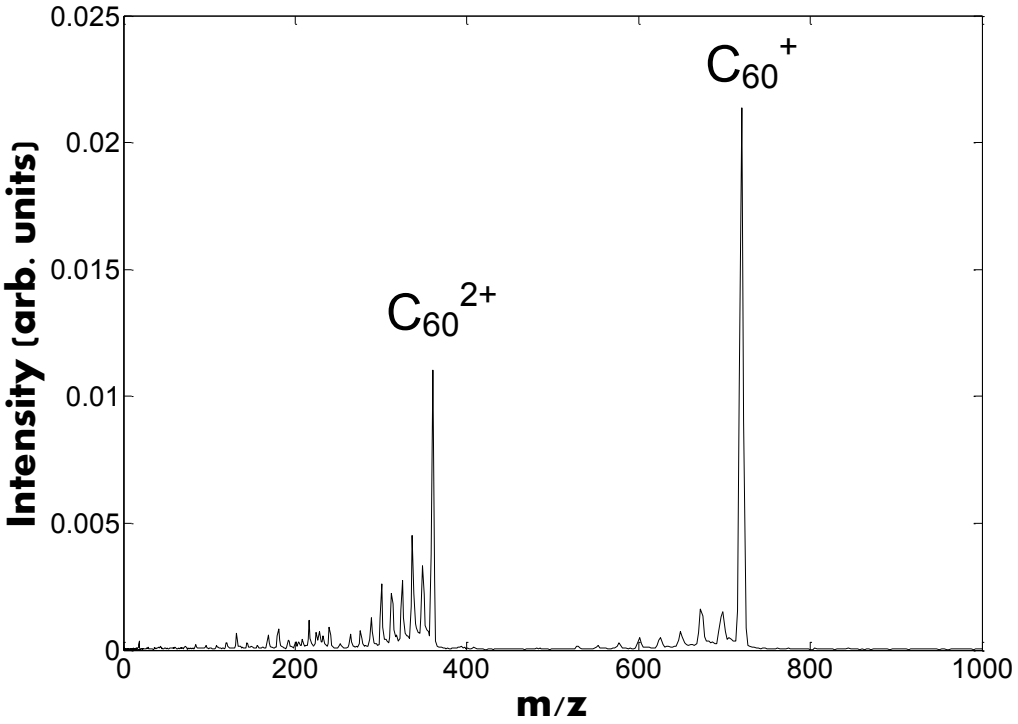

Figure 4.16: Mass spectrum for C_{60} ionised with 550 nm, 9.1 TW/cm^2, 92 fs pulses. The highest peak visible is the C_{60}^+ ion with *m/z* value 720. The C_{60}^{2+} peak appears at half that value: *m/z* = 360.

4.4 Lasers

4.4.1 Femtosecond Ti:sapphire oscillator

The laser oscillator is a Coherent Mantis, which produces sub-35 fs laser pulses with a central wavelength of around 800 nm and bandwidth of 80 nm at a repetition rate of 80 MHz, with typical power of around 500 mW when mode-locked. The gain medium in the oscillator is a titanium-doped sapphire crystal (Ti:sapph), the emission from which has the required bandwidth to produce femtosecond pulses according to the time-bandwidth product rule

$$\Delta t \times \Delta \nu = 0.441, \tag{4.11}$$

for bandwidth-limited Gaussian pulses, where Δt is the pulse width in time and $\Delta \nu$ is the spectral width, in frequency space [82]. The Ti:sapph crystal is pumped by a Coherent Optically Pumped Semiconductor (OPS) laser which emits at 532 nm. The normal operation of the Mantis is in continuous wave (CW) mode. Many wavelengths (longitudinal modes) are allowed to propagate in the cavity, constructively or destructively interfering with each other. To generate short, intense pulses, these modes need to be in phase. This is referred to as mode-locking. To initiate mode-locking, the Mantis employs a passive mode-locking technique, taking advantage of the optical Kerr effect. The Ti:sapph crystal changes its index of refraction as a function of the intensity of light passing through it, forming a Kerr lens. Therefore high intensity beams become self-focussed on passing through the gain medium. The instantaneous intensity of mode-locked light pulses is sufficient to form this lens but the weak intensity of the CW light is not. The Gaussian pump beam distribution means gain is higher in the centre of the lasing mode than at the edges. This gain distribution acts as a soft aperture, allowing the smaller mode-locked mode to see higher gain than the CW mode. This acts as a positive feedback, allowing the mode-locked mode to survive and the CW mode to cease. The starting mechanism involves changing the cavity length at the proper speed, inducing high-power fluctuations. Once the instantaneous power in one of these fluctuations is high enough, a Kerr lens

is formed, amplifying that fluctuation until it becomes the dominant pulse that will form the mode-locked output. A positive chirp (red wavelengths travelling faster than blue ones) is imparted by self-phase modulation in the crystal and, through positive material group velocity dispersion in the crystal and silicon wedges. To be sure of emitting transform-limited pulses at the output, the mirrors of the cavity have a coating which induces a negative chirp, to compensate. The output from the Mantis is relatively weak and must be passed through a regenerative amplifier before use.

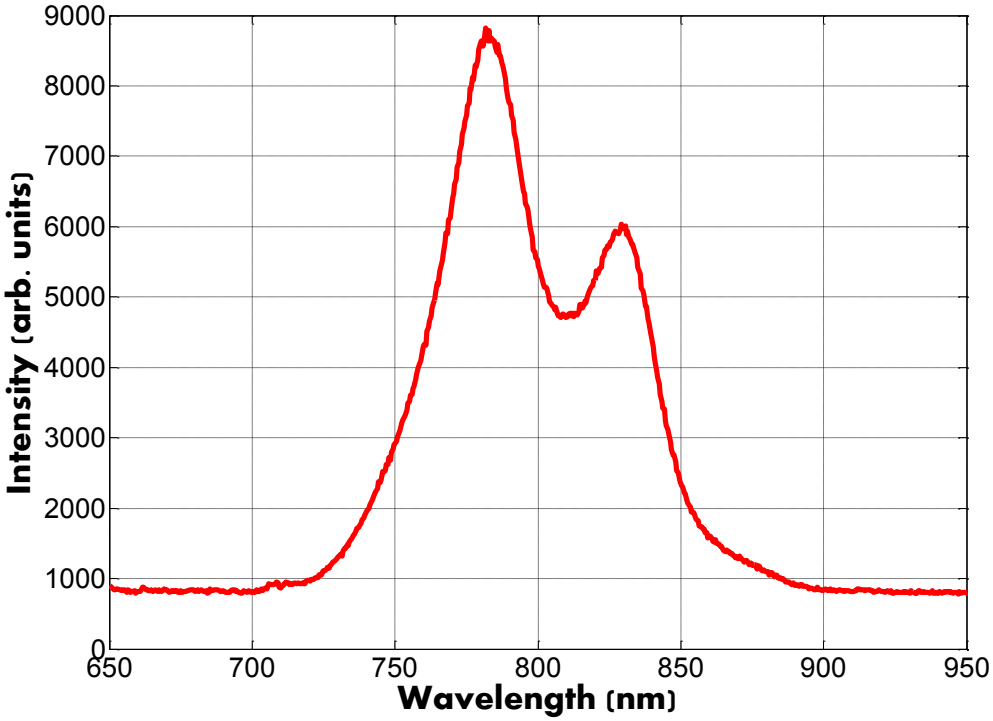

Figure 4.17: Wavelength spectrum recorded after Mantis output with an Ocean Optics HR2000 spectrometer. Central wavelength is around 800 nm and FWHM is around 80 nm. The 'dip' in the spectrum at around 810 nm is due to spectral hole burning in the gain medium. [83].

4.4.2 Femtosecond Ti:sapphire regenerative amplifier

The pulses from the oscillator are directed into and act as seed pulses for the regenerative amplifier (Coherent, Legend Elite). The output from the amplifier consists of pulses of central wavelength of 800 nm, bandwidth of 9 nm, pulse durations of between 120 fs and 3.8 ps, power of around 3.5 W and a repetition rate of 1 kHz. The seed pulses have a high peak intensity as they leave the oscillator and this must be reduced before they enter the amplifier to avoid damage to the crystal. The seed pulses first make a double-pass through a pulse stretcher assembly, consisting of a single diffraction grating, which introduces a positive chirp to the pulses, stretching them in time to a width of several hundred picoseconds, thus lowering the peak intensity and readying them to enter the amplifier. The amplifier cavity consists of a Ti:sapph crystal which is pumped by a Nd:YLF (Coherent, Evolution) laser. In front of the two end mirrors of the cavity are Pockel's cells which control the polarisation of the pulses and therefore can trap the pulse in the cavity to be amplified or allow it to leave the cavity. When the pump laser Q-switch is activated, pump pulses are supplied to the Ti:sapph crystal. When the gain in the crystal reaches a maximum, the amplification process begins. A seed pulse of vertical polarisation enters the cavity by reflection off the laser rod. It makes a pass through an inactivated Pockel's cell and $\lambda/4$ waveplate, reflects off the end mirror and double-passes the waveplate and Pockel's cell, now with horizontal polarisation. As soon as it leaves the Pockel's cell, a voltage is applied, negating the effect of the waveplate behind it. This means the pulse can be transmitted by the laser rod and is trapped in the cavity. After a number of round trips, usually 10-15, after which it has experienced a gain of over 10^6, a quarter-wave voltage is applied to the output Pockel's cell, changing the pulse's polarisation back to vertical and allowing it to leave the cavity by means of reflection off a polariser. The timing of the Pockel's cell electronics with respect to the pump laser is controlled by a signal delay generator (Coherent, SDG). After amplification the pulses are passed through a pulse compressor assembly which is similar to the stretcher but induces a negative chirp. A motorised translation stage is used to control the distance travelled by the pulse in the compressor. By optimising the translation stage for minimum pulse duration, the chirp of the pulse can be minimised. By the same method, the compressor can be de-tuned, producing pulses of up to 3.8 ps

duration. A diagram of the laser alignment and optics inside the Legend can be seen in Figure 4.18.

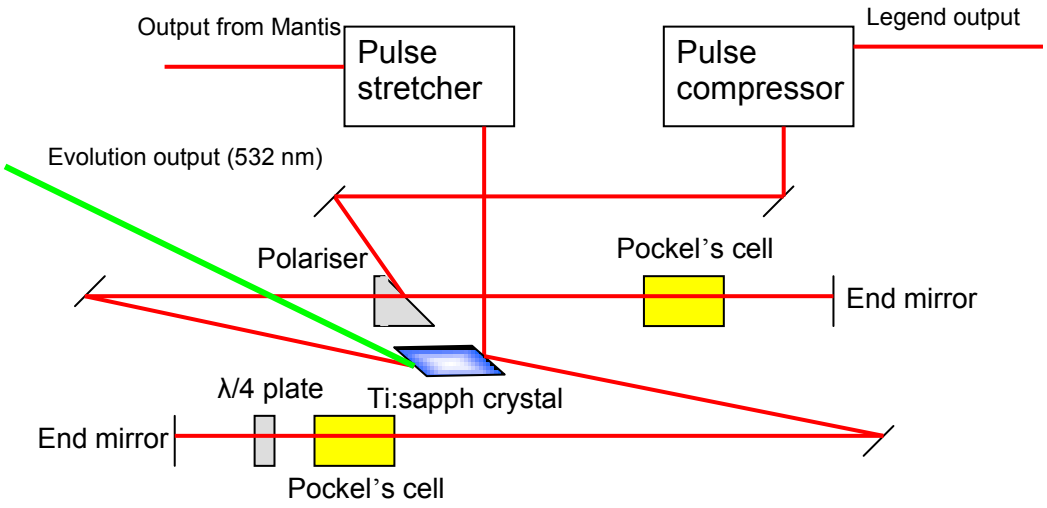

Figure 4.18: Diagram of the laser alignment and optics inside the Legend. The output from the Mantis is sent through the pulse stretcher, into the amplifier cavity and finally through the pulse compressor.

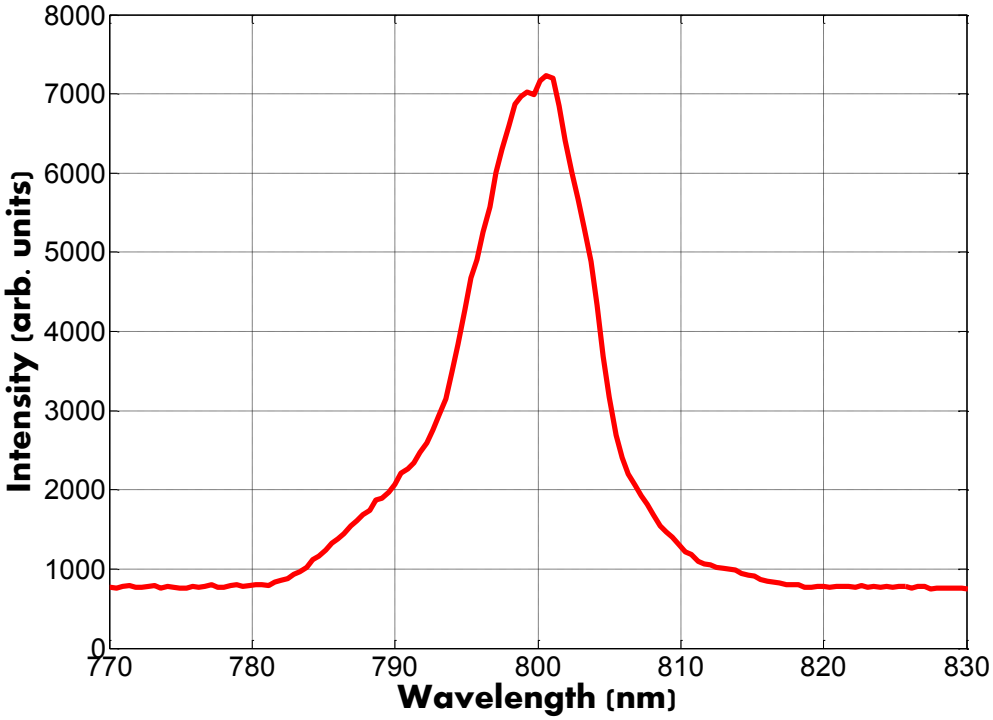

Figure 4.19: Wavelength spectrum recorded after Legend output. Central wavelength is around 800 nm and FWHM is around 9 nm.

4.4.3 Femtosecond non-collinear optical parametric amplifier

A commercial (Light Conversion, Topas-White) non-collinear optical parametric amplifier (NOPA) is used to produce sub-35 fs pulses of light of wavelength between 500-1000 nm and typical powers of 50 mW at a repetition rate of 1 kHz. 400 nm, 120 fs pulses can also be generated and used from within the Topas-White. The pump pulse into the Topas-White is a portion of the 800 nm output from the Legend. The seed pulse is a femtosecond white-light continuum (WLC) which is generated by directing around 2% of the pump pulse onto a sapphire plate. The WLC is then passed through a pulse shaper assembly, consisting of a double-pass negative dispersion pulse stretcher. The nonlinear negative chirp of the WLC pulse allows for output pulse compression to the transform limit and that the desired bandwidth fits under the pump pulse. This serves as a seeder for a two stage non-collinear parametric amplifier which employs a single BBO crystal (β-barium borate). The amplifier is

pumped by the 400 nm second harmonic of the pump, which is generated by passage through a separate BBO crystal. The second harmonic can be directed out of the Topas-White, at this stage, by inserting a high reflecting mirror, which transmits all the residual 800 nm light, after the BBO crystal, which provides the option of directing 400 nm, 120 fs pulses into the chamber. The pump beam is then split into two beams, which pump the first and second stage of the parametric amplifier. Both pulses are stretched using prisms. In the first stage, the seed pulse is overlapped with the first pump pulse in the BBO crystal, producing the signal pulse. In the second stage, the signal pump is overlapped with the second pump pulse in the BBO crystal, producing the amplified signal pulse. The wavelength of the signal pulse can be tuned by changing the delay of the first pump pulse with respect to the seed pulse and adjusting the crystal angle, with the delay of the second pump being tuned for power. All of these are controlled by motors which can be adjusted via a computer program. The amplified signal is then passed through a cylindrical telescope to form a nearly circular beam shape and finally, passed through a compressor, consisting of two wedged fused silica plates which introduce a positive group dispersion, compensating for the negative chirp of the signal pulse and producing transform limited output pulses. The position of the wedges is controlled by a motor which can be optimised to produce the shortest pulse duration.

4.4.4 Second harmonic bandwidth compressor

A commercial (Light Conversion, SHBC) second harmonic bandwidth compressor (SHBC) is used to generate 400 nm, 4 ps pulses with a bandwidth of around 3 nm and a typical power of around 1.1 W. The input to the SHBC is the 800 nm, 120 fs pulses from the Legend. Once the 800 nm pulses enter the SHBC, they are split by a 50/50 beamsplitter. Both arms are sent into a pulse stretcher, consisting of a diffraction grating and a cylindrical lens. The pulses in one arm acquire a positive chirp, whilst the pulses in the other acquire a negative chirp, due to the positioning of the respective cylindrical lenses. To achieve the narrowest second harmonic bandwidth, both arms must have chirps of equal magnitude and opposite signs. After the pulse stretcher, both arms pass through a beam reducing telescope and are overlapped, non-collinearly in a nonlinear BBO crystal, producing the output pulses.

4.4.5 Nd:YAG nanosecond laser

A commercial (Continuum. Minilite) solid state Nd:YAG laser is used to generate nanosecond pulses. The gain medium is pumped by a flashlamp and Q-switching is employed to produce short, high energy pulses of wavelength 1064 nm, the fundamental wavelength of Nd:YAG. These pulses are passed through a non-linear crystal in the laser head which results in second harmonic generation, producing an output pulse of wavelength 532 nm, pulse duration 5 ns, pulse energy of up to 50 mJ and a repetition rate of between 1 and 15 Hz.

4.4.6 Measuring laser pulse duration

To measure the pulse duration of the 800 nm output of the Legend, a commercial autocorrelator (APE Pulsecheck) is used. A small fraction of the 800 nm beam is directed through an identical vacuum viewport window as is on the vacuum chamber (to compensate for any chirp which may be imparted) and into the autocorrelator, where it is split in half, with each half travelling along different arms of a Michelson interferometer. The two beams are then overlapped in a nonlinear crystal, producing second harmonic generation. The second harmonic signal is sensitive to the combined intensity of the beams overlapped in the crystal, so by introducing a delay for one of the beams and recording the second harmonic signal as a function of the delay, a second order autocorrelation function is obtained. For beams with a Gaussian temporal profile, the FWHM of the autocorrelation function, $\Delta\tau$, is related to the FWHM of the input pulse, Δt, by the equation

$$\Delta\tau = 1.414\Delta t . \tag{4.12}$$

An autocorrelator measurement for 800 nm, 117 fs pulses is shown in Figure 4.20.

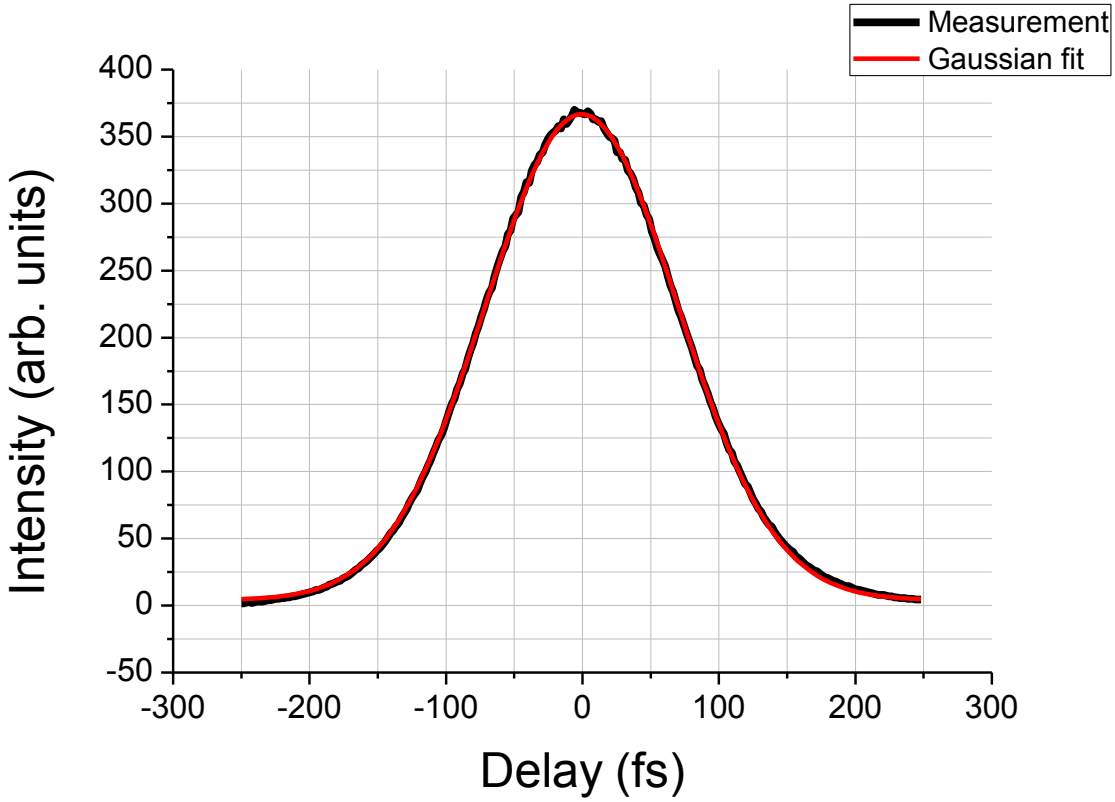

Figure 4.20: Pulse duration autocorrelation measurement taken with APE Pulsecheck. The autocorrelation has a FWHM of 166 fs. The pulse duration is therefore 117 fs.

The autocorrelator only works at wavelengths close to 800 nm as this is the wavelength the crystal is designed to produce a second harmonic signal at. Therefore, to measure the pulse duration of the Topas-white output at wavelengths outwith the range of the autocorrelator, an optical setup was built to mimic the function of the commercial autocorrelator [84]. The beam is split in half by a 50/50 beamsplitter, the two beams traverse a different arm of an interferometer, one stationary and one capable of delaying the pulse via a motorised translation stage. The two pulses are combined non-collinearly in a BBO crystal which produces second harmonic generation. The second harmonic signal is recorded, with a fast photodiode, as a function of delay and a second-order autocorrelation function is produced. By using equation 4.12, the FWHM of the laser pulses, Δt, can be determined from the FWHM of the autocorrelation function, $\Delta\tau$. A diagram of the experimental setup is shown in Figure 4.21.

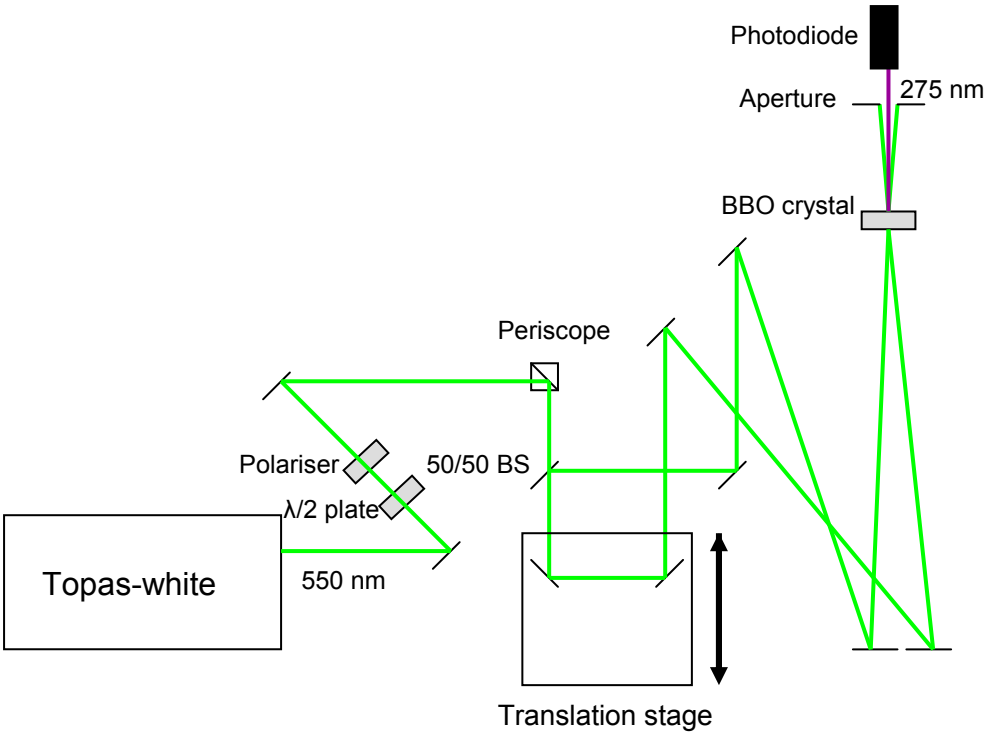

Figure 4.21: Diagram of the autocorrelation experimental setup to measure the pulse duration of 550 nm pulses from Topas-white.

An example of an autocorrelation function recorded in this way is shown in Figure 4.22. A Gaussian peak is fitted to the function and the FWHM of the autocorrelation function is 129.6 fs, therefore, by equation 4.12, the FWHM of the 550 nm, Topas-white output pulses is 92 fs. This is longer than expected and is likely to have been stretched as a result of passing through the λ/2 plate and polariser as well as the vacuum viewport, which all impart positive group dispersion to the pulse, thereby stretching it in time.

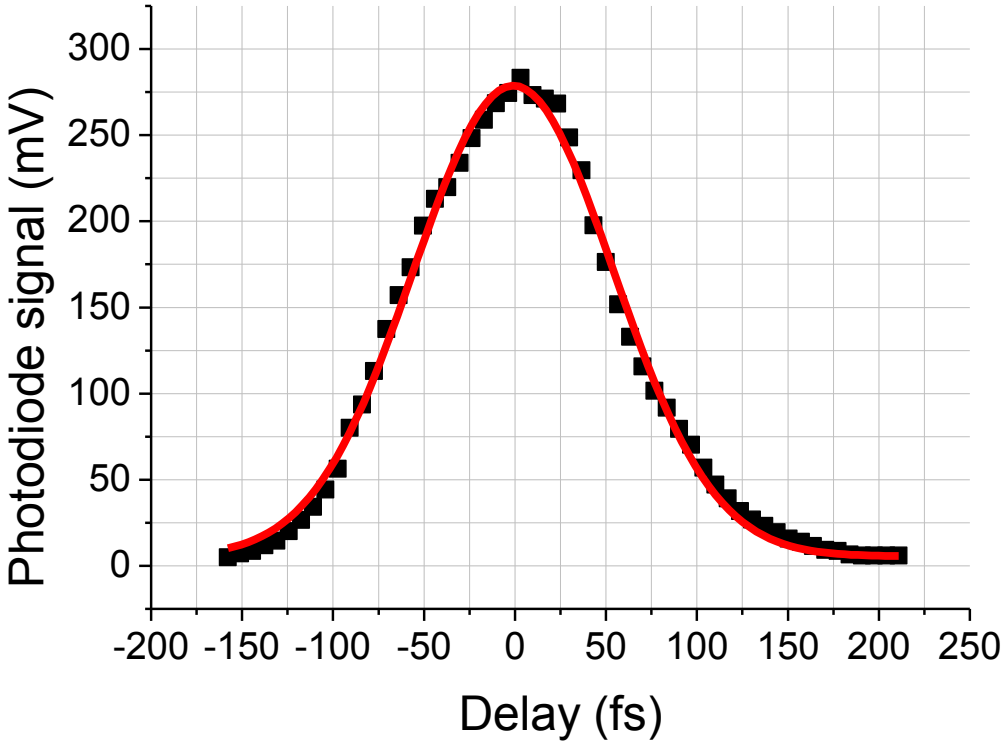

Figure 4.22: Second harmonic signal, for 550 nm pulses from the Topas-white, as a function of delay for the experimental setup in Figure 4.21.

4.4.7 Laser intensity

The peak intensity of the laser pulses, I_0, is given in units of W/cm^2 and may be calculated from the equation

$$I_0 = \sqrt{\frac{16\ln(2)}{\pi}} \times \frac{E_p}{\Delta t \times \pi w_0^{\,2}} = 1.8789 \times \frac{E_p}{\Delta t \times \pi w_0^{\,2}}, \qquad (4.13)$$

where E_p is the total pulse energy, measured in J, Δt is the FWHM of the laser pulse duration and w_0 is the beam waist (the radius when the intensity drops to $1/e^2$ of the peak intensity) [82]. The laser fluence, F, is the time-integrated intensity, given in units of J/cm^2, and may be calculated from the equation

$$F = \sqrt{\frac{\pi}{4\ln(2)}} \times \Delta t \times I_0 = 0.94 \times \Delta t \times I_0 . \tag{4.14}$$

The pulse energy is measured in the lab using a thermopile sensor connected to a Coherent FieldMaxII-TO power meter. The pulse duration can be measured using the methods described in 4.4.6. The laser beam is focussed, using a lens, so that the beam waist at the point the laser pulse interacts with the fullerenes is on the order of tens of microns which makes it difficult to measure explicitly. By measuring the unfocussed beam waist, the experimental beam waist can be calculated using the equation

$$w_0 = \frac{2\lambda}{\pi} \times \frac{F}{D}, \tag{4.15}$$

where λ is the wavelength, F is the focal length of the lens and $D/2$ is the unfocussed beam waist [82].

The unfocussed beam waist can be measured, experimentally, by placing an aperture on a translation stage, with an opening of around 1 mm, in front of the beam, with a power meter behind the aperture. By scanning the aperture across the beam, horizontally, the power can be measured as a function of the horizontal distance travelled by the aperture, giving a horizontal cross section of the beam. A Gaussian fit is then made, from which the beam waist can be extracted. In Figure 4.23, below, the measurement is carried out for the 800 nm, Legend output and a beam waist of 2.85 ± 0.04 mm is measured. With a 30 cm focal length lens, this gives a focussed beam waist of 26.8 ± 0.4 μm. This gives the area of the focal spot as

$$A = \pi w_0^{\,2} = (2.26 \pm 0.06) \times 10^{-5}\,\mathrm{cm}^2 .$$

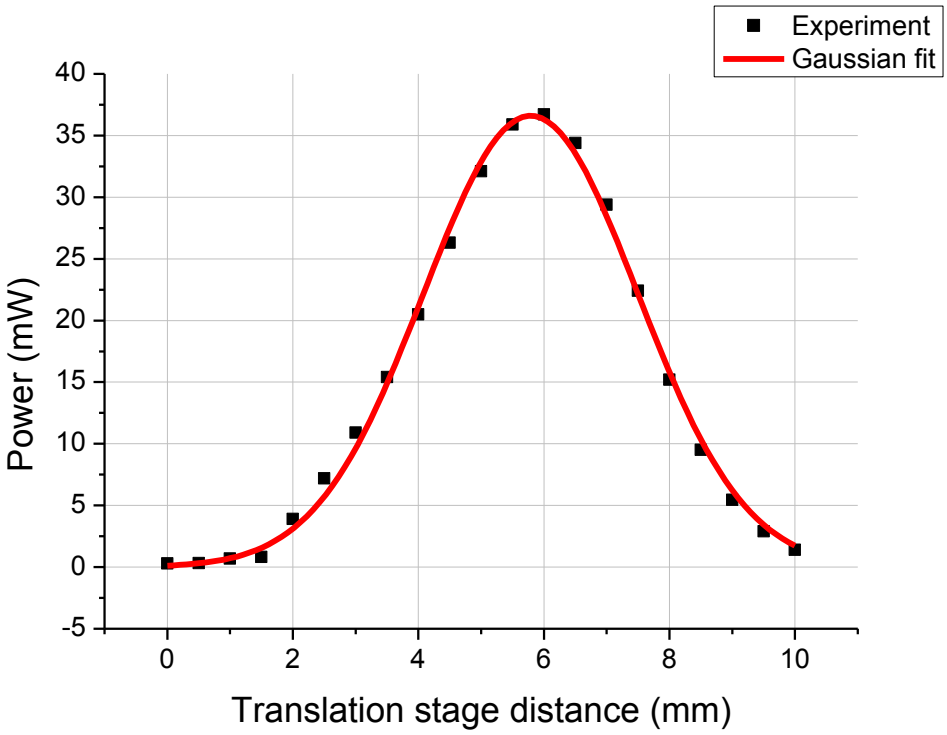

Figure 4.23: Average power measured after the beam from the Legend was passed through an aperture of opening 1 mm, which was scanned in the horizontal direction.

The focussed beam waist was also measured by a laser ablation technique described in ref. [85]. This gave the area of the focal spot as $A = (3.4 \pm 0.4) \times 10^{-5}\,\mathrm{cm}^2$ [67]. The value calculated from the unfocused beam waist is determined assuming a 'perfect' lens is being used and is therefore effectively the smallest possible focussed beam size. In reality, the experimental beam size is likely to be larger.

It is possible to calibrate the laser intensity at the focal spot by using xenon VMI spectra, recorded at a range of laser powers. The AC Stark shift can be approximated as the ponderomotive shift, U_p, and therefore increases with laser intensity. As the Stark shift increases, different states can be shifted into resonance and peaks resulting from (n + 1) resonance-enhanced multiphoton ionisation (REMPI) will, 'appear' in the spectra as the power is increased [86]. By identifying at what laser power a peak corresponding to a certain state appears, a calibration factor linking laser power to laser intensity can be determined. This principle is illustrated in Figure 4.24.

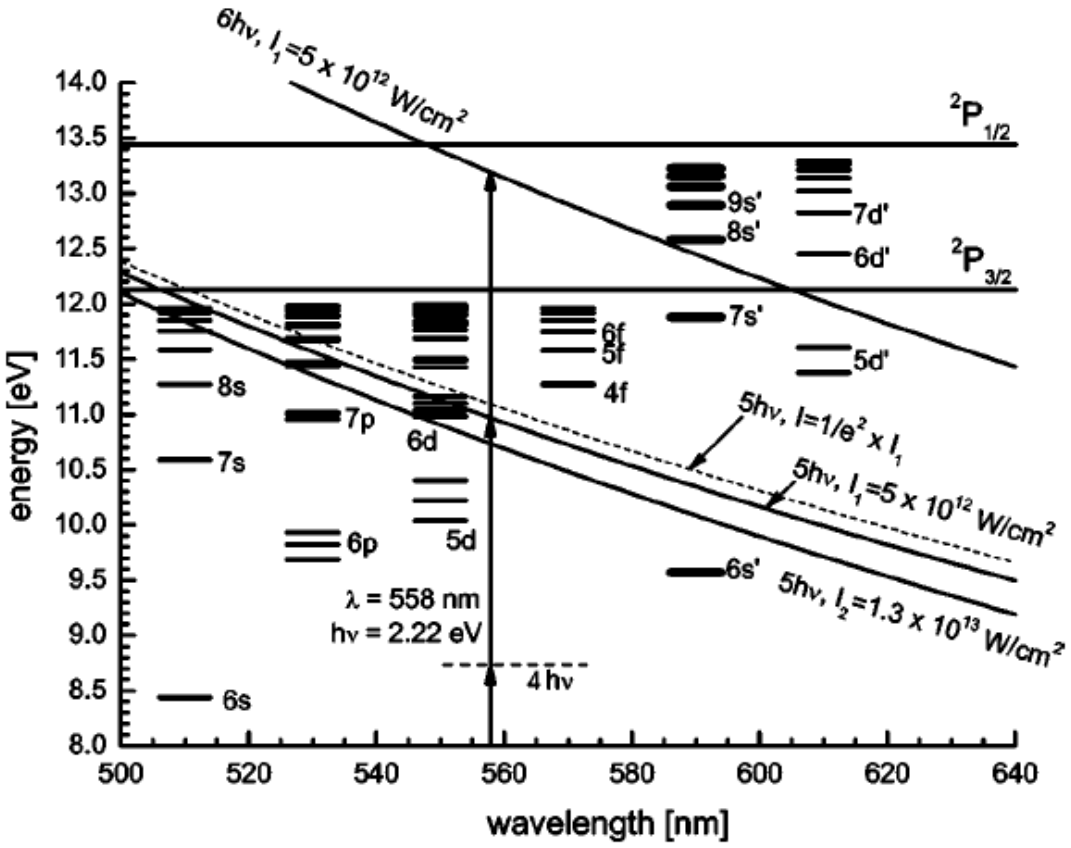

Figure 4.24: Energy level diagram for both fine structure states of the $^2P_{3/2}$ ground state and $^2P_{1/2}$ excited spin-orbit state of Xe^+. The solid curves represent the energy of 5 and 6 photons, relative to various electronic states in the atom, for the laser intensities 5 x 10^{12} W/cm^2 and 1.3 x 10 ^{13} W/cm^2. By increasing the laser intensity, the ponderomotive shift is increased and electronic states are shifted into resonance. Peaks corresponding to certain states will appear in the PES at specific laser intensities. Figure from ref. [86].

At 800 nm, the 4f state of xenon is shifted into resonance at an intensity of 1.8 x 10^{13} W/cm^2 [87]. Using the experimental setup, the 4f state appears at a laser power of 32 ± 1.1 μJ, when using 130 fs, 800 nm pulses using a lens with a 30 cm focal length. By using the focussed beam area determined by ablation experiments, the intensity at a laser power of 32 μJ would be

$$I = \left(\frac{32 \times 10^{-6}}{130 \times^{-15} \times 3.4 \times 10^{-5}}\right) \times 1.8789 = (1.36 \pm 0.21) \times 10^{13} \text{ W/cm}^2.$$

The Xe calibration method was judged to be the most accurate as it is related directly to the focussed laser beam at the exact point in space where the laser-fullerene interactions take place, therefore all intensity values presented in this thesis are calculated via this method. Therefore the calibration factor for 800 nm, 130 fs pulses, using a lens with 30 cm focal length, is

$$S = \frac{1.8\times10^{13}}{32} = (5.63\pm0.18)\times10^{11}\left(\frac{W/cm^2}{\mu J}\right).$$

The calibration factors obtained using the three methods described are summarised in Table 4.1.

Table 4.1: A comparison of the calibration factors obtained from the three calibration methods described above for 800 nm, 130 fs laser pulses.

Calibration method	**Calibration factor** $\left(\frac{W/cm^2}{\mu J}\right)$
Xe calibration	$(5.63\pm0.18)\times10^{11}$
Laser ablation	$(4.25\pm0.66)\times10^{11}$
Perfect lens calculation	$(6.41\pm0.19)\times10^{11}$

Similar calibrations are undertaken when using different pulse durations and different wavelengths. Pulse duration measurements and a focussed beam area calculation, using the measured unfocused beam area, are used to compare and are in reasonable agreement with the xenon calibrations.

The powers available when using the 400 nm, frequency doubled output from the Topas-white are not sufficient to shift any intermediate states into resonance when ionising xenon and so the ponderomotive shift at this wavelength was calculated by measuring how much the peak, due to the non-resonant ionisation from the ground state, is shifted by over a range of laser powers. If no ponderomotive shift is present,

the peak due to non-resonant 4-photon ionisation of xenon should appear at a kinetic energy of 0.27 eV. The ponderomotive shift means that the position of this peak is shifted down in energy by the ponderomotive energy, U_p. This shift was measured over a range of laser powers and an intensity calibration was calculated in the same way as described above. A table of the calibration factors used for different wavelengths can be found in Appendix B.

4.4.8 Optics

This section describes the optics used to direct the laser beams into the chamber and control their properties. When using the 800 nm, Legend output, the beam is first raised, using a periscope. This is to ensure that the beam height matches that of the chamber and also that the polarisation is rotated to vertical. This is necessary for carrying out VMI experiments. The pulse energy is controlled with a λ/2 plate (AHWP05M-980, Thorlabs) and a Glan-Laser calcite polarizer (GL15, Thorlabs). The polarizer is set to transmit vertically polarized light and the angle of the λ/2 plate can be adjusted so that more or less light is transmitted by the polarizer. The polarizer is sensitive to high laser powers and so neutral density filters and a 50/50 beamsplitter are used to reduce the power before the λ/2 plate and polarizer. The beam is focussed by a lens placed before the interaction chamber. A 5/95 beamsplitter can be employed to direct part of the beam into the autocorrelator to measure pulse duration. The output from the Topas-white is passed directly through a λ/2 plate and polarizer, to control the power and then raised by a periscope before being passed through a lens and into the interaction chamber. For the 400 nm pulses, generated in either the Topas-white or the SHBC, a periscope is used to adjust the height and polarization and a combination of neutral density filters and adjusting an aperture for the pump beam, before the doubling crystal, is used to control the laser power. Diagrams depicting the optical setup for each set of experiments can be seen in Figure 4.25.

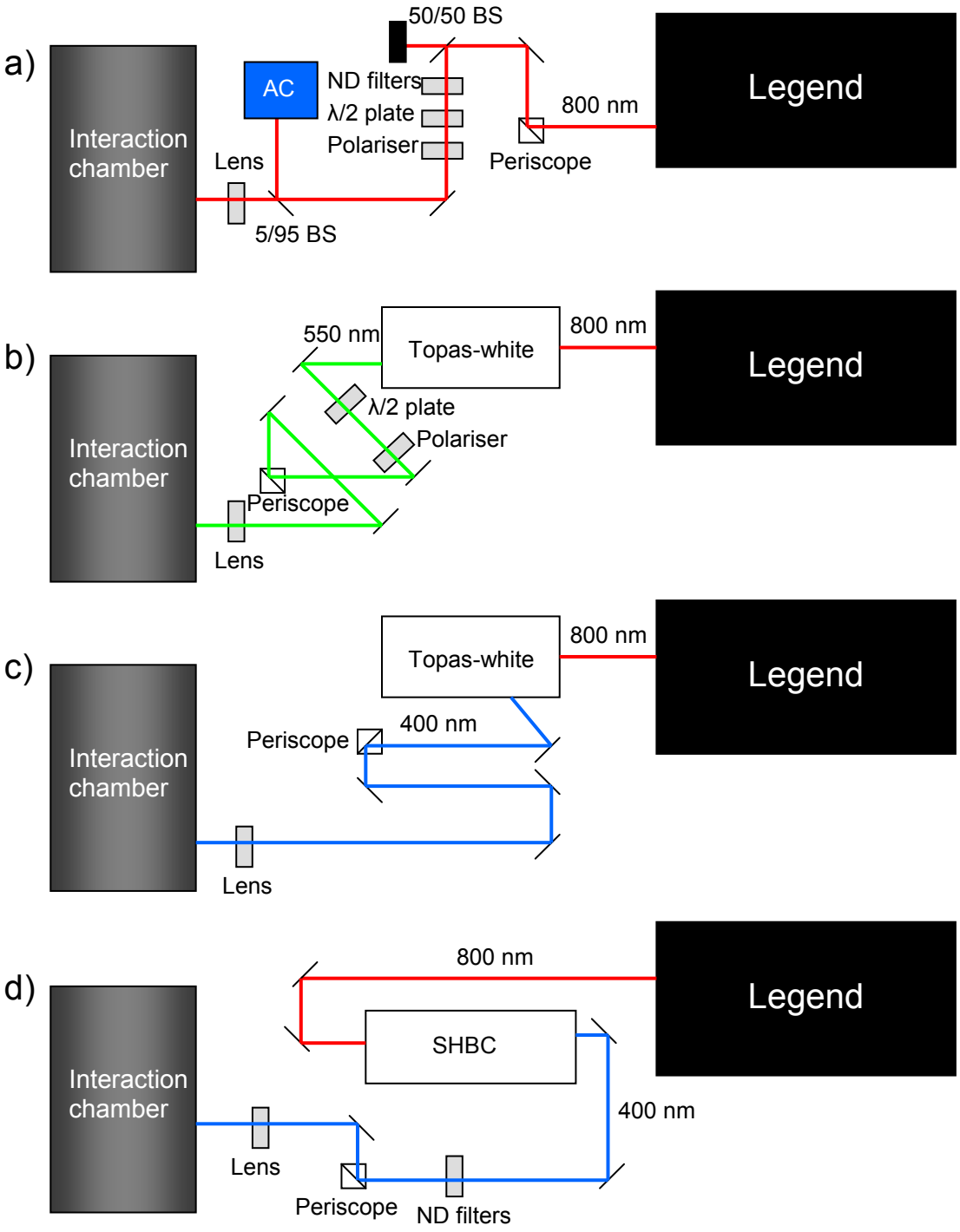
a)
Interaction chamber
AC
50/50 BS
ND filters
λ/2 plate
Polariser
Lens
5/95 BS
800 nm
Periscope
Legend
b)
Interaction chamber
550 nm
Topas-white
800 nm
λ/2 plate
Polariser
Periscope
Lens
Legend
c)
Interaction chamber
Topas-white
800 nm
Periscope
400 nm
Lens
Legend
d)
Interaction chamber
800 nm
SHBC
400 nm
Lens
Periscope
ND filters
Legend

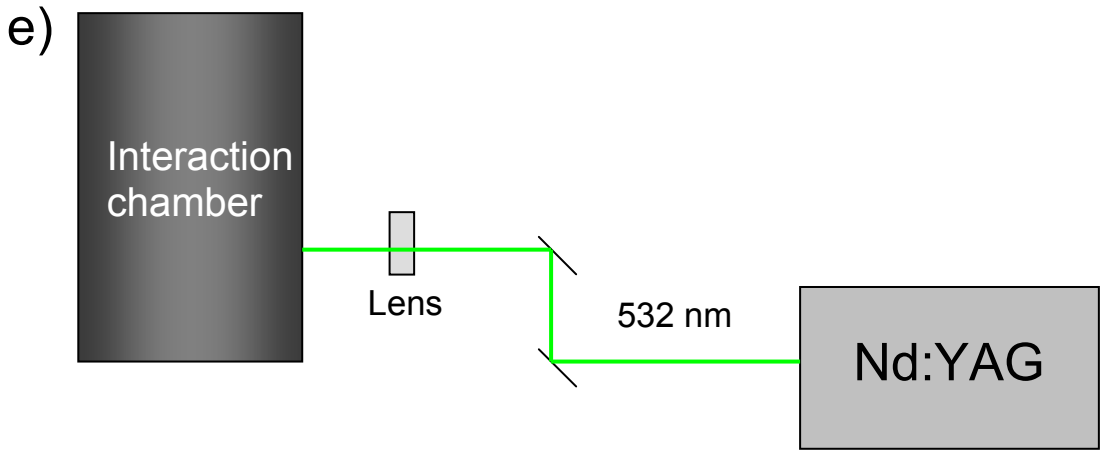

Figure 4.25: Optical setup for a) 800 nm, 120 fs, b) 550 nm, 92 fs, c) 400nm, 120 fs, d) 400 nm, 4 ps, e) 532 nm, ns.

4.4.9 Pump-probe setup

Pump-probe experiments with 400 nm pump pulses and 900 nm probe pulses were carried out. The 400 nm pulses were the frequency-doubled output from the Legend, passed through a BBO doubling crystal. The 900 nm pulses were the output from the Topas-white. The 800 nm output from the Legend is reduced in size, using curved mirrors and passed through a BBO doubling crystal to produce 400 nm pulses. The 400 nm beam is directed onto mirrors situated on a motorised translation stage, which can be moved to lengthen or shorten the beam path. A $\lambda/2$ plate can be inserted after the translation stage to make the beam vertically or horizontally polarised. The beam is then directed onto a dichroic mirror which directs it into the vacuum chamber. The 900 nm beam is passed through the dichroic mirror, after which it overlaps with the 400 nm beam, in space, and passes into the vacuum chamber. Both beams pass through the vacuum chamber and are directed back into the chamber and focussed, using a curved mirror with a 30 cm focus length. The optical setup is illustrated in Figure 4.26.

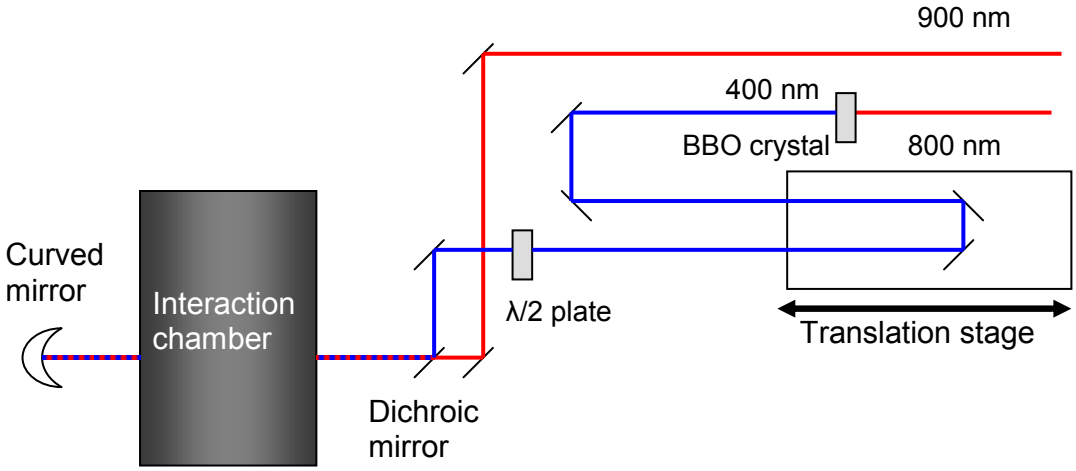

Figure 4.26: Optical setup for pump-probe experiments with 400 nm and 900 nm pulses.

Spatial overlap is achieved by directing the beams, after focussing with the curved mirror, through a 50 μm aperture at the focal point and moving the beams until both pass through. Temporal overlap, outside the chamber, is achieved by passing the beams through a nonlinear BBO crystal and moving the translation stage until the maximum sum-frequency signal is detected with a photodiode. The temporal overlap inside the chamber is determined by analysing xenon ion yields as a function of translation stage distance. The ion yield is highest when the 400 and 900 nm beams are fully overlapped.

Chapter 5 – Experimental setup and techniques: Fusion of carbon nanotubes with ultrashort laser pulses

This chapter describes the experimental setup, equipment and techniques used to obtain the results presented in Chapter 8 of this thesis. Section 5.1 describes the experimental setup and techniques for resistance measurements of buckypaper and section 5.2 describes the experimental setup and techniques for the Raman analysis of thin carbon nanotube films.

5.1 Buckypaper resistance measurements

5.1.1 Buckypaper sample

The buckypaper samples were provided by the National High Magnetic Field Laboratory at Florida State University. Buckypaper was first synthesised in 1998 [88] by creating a stable liquid suspension of nanotubes using non-ionic surfactants which can then be membrane-filtered leaving a thin film of paper-like material which produces a good dispersion of well-aligned carbon nanotubes. Buckypaper can be made with multi-walled nanotubes (MWNTs) or single-walled nanotubes (SWNTs) but the sample used was made from SWNTs. Buckypaper retains much of the properties of the individual molecules and can be considered to be a reasonably effective transfer of individual nanotube qualities into a composite material [89]. Figure 5.1 highlights the structural difference between raw single-walled nanotubes and buckypaper. The raw sample displays a highly tangled ‘rope’ and ‘bundle’ structure whereas the buckypaper sample shows a much greater degree of dispersion and alignment of the individual nanotubes. For measurements, a rectangular sample was cut from the main sample with dimensions of around 12 mm in the experimental y-axis and 15 mm in the x-axis.

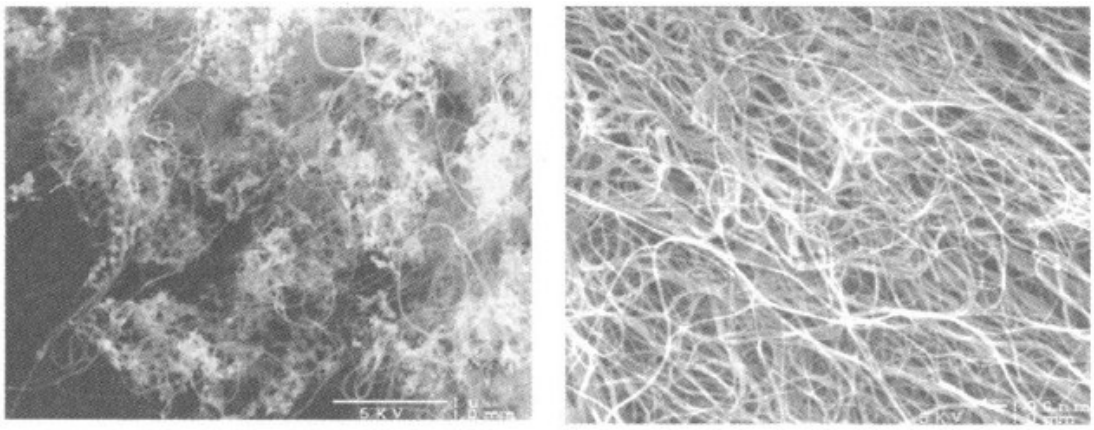

Figure 5.1: Scanning electron microscopy (SEM) images of (left) raw single-walled carbon nanotubes and (right) purified buckypaper. Figure from ref. [88].

5.1.2 Experimental setup

The buckypaper sample was fixed in a quartz sample holder (situated in a vacuum chamber with typical pressures of 10^{-6} mbar) allowing it to be irradiated by the laser beam and for electrical contacts to be maintained at the corners of the sample. The vacuum chamber was pumped by a 210 l/s turbomolecular pump (Pfeiffer, TMV 261) and backed by a 2-stage roughing pump (Edwards, EZM-12). A sketch of the experimental setup can be seen in Figure 5.2.

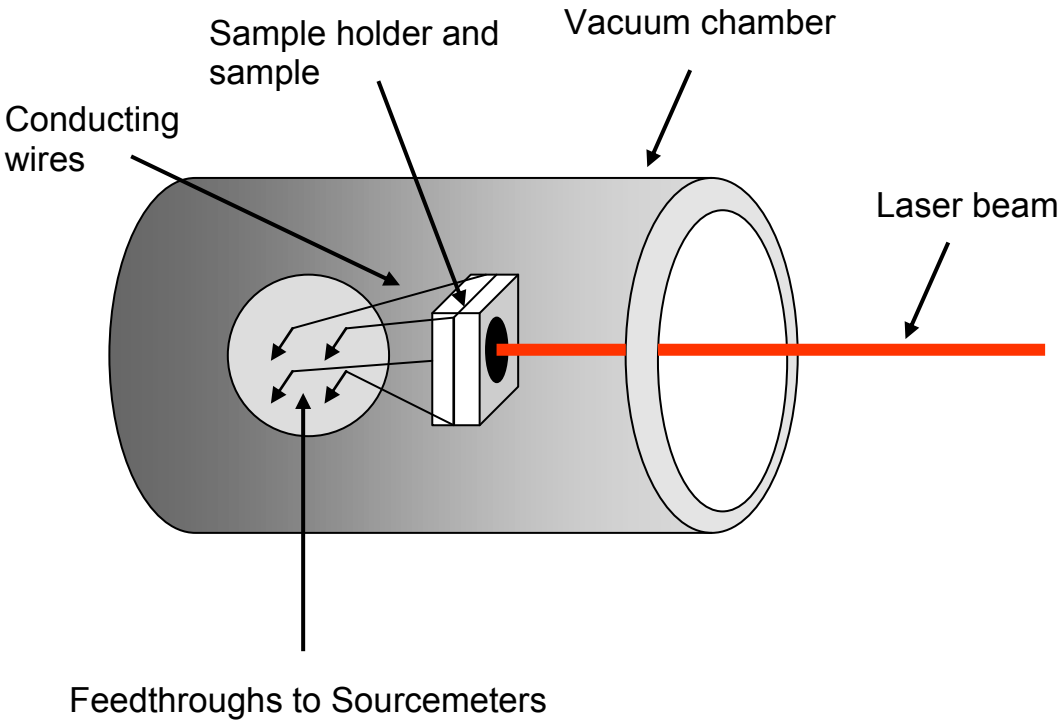

Figure 5.2: Sketch of experimental setup for buckypaper resistance measurements.

The laser used was the 800 nm, 120 fs output from the Legend and the beam was passed through a cylindrical lens which produced a beam which was elliptical and elongated in the vertical direction. Where the beam hit the sample, the dimensions were around 15 mm in the vertical direction and 6 mm in the horizontal direction. The beam was made elliptical so that it could be moved across the sample, in the horizontal direction, over the course of the irradiation; to ensure that as much of the sample as possible was exposed to irradiation whilst ensuring reasonably high laser intensity. Using a larger, circular, beam to irradiate a similar sample area would have resulted in a very low intensity. The laser power was controlled by adjusting the Evolution pump laser power in the Legend and with neutral density filters.

The resistance of the sample was measured prior to each irradiation. Each irradiation period lasted for 30 minutes. During this time, the laser beam would be moved, using a directing mirror, in the horizontal direction, so that three areas of the sample would experience irradiation. The three areas were the centre of the sample (in the horizontal direction), slightly left of centre and slightly right of centre. Each of

these areas was irradiated for 10 minutes. A resistance measurement was carried out while the sample was being irradiated and, after irradiation, the sample was then left to sit, unirradiated, for 10 minutes and a resistance measurement was taken again.

The sample holder was made of two, 25 mm x 25 mm, quartz plates which the sample was placed in-between. The back plate was screwed onto a base and the front plate could be screwed onto the back plate. The front plate contained a 10 mm circular hole at its centre which allowed the laser beam to irradiate the sample surface. A sketch of the buckypaper sample holder can be seen in Figure 5.3.

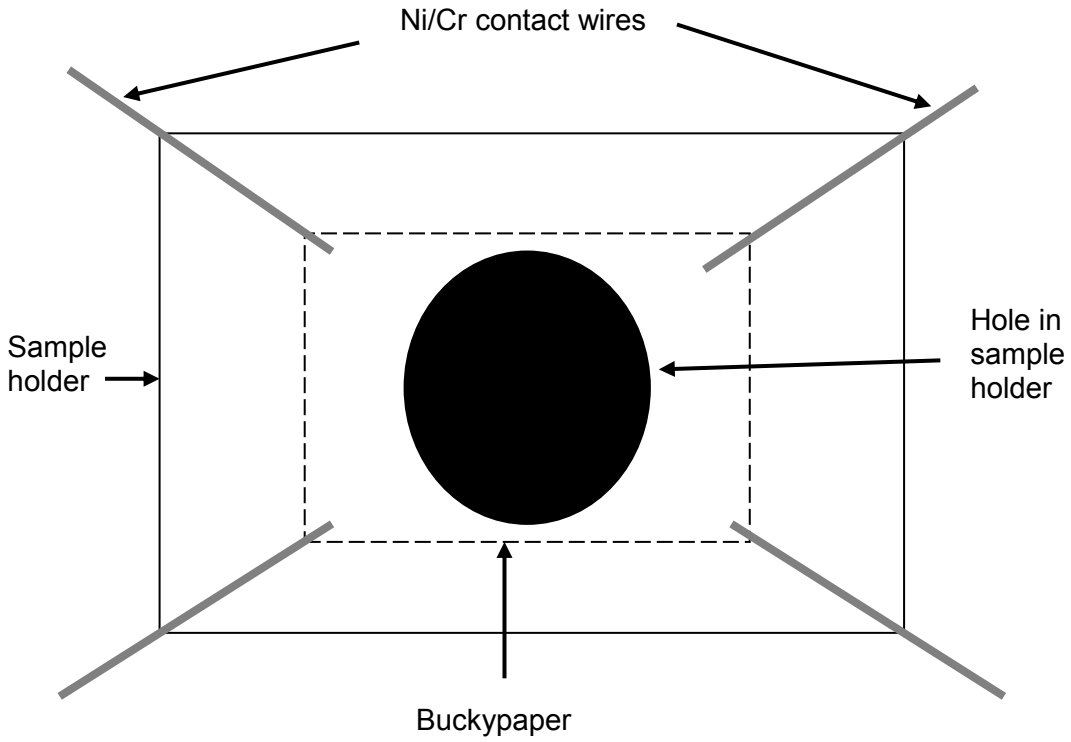

Figure 5.3: Sketch of buckypaper sample holder.

Electrical contacts were placed at each corner of the sample in order to carry out a 4-probe resistance measurement. The contacts consisted of nickel/chromium wires and were held in place on the sample surface by conducting silver paint. The Ni/Cr wires were soldered to copper wires which were connected to feedthroughs on a flange of the vacuum chamber. On the atmosphere side of the flange the feedthroughs were connected to a pair of sourcemeters (Keithley, 2410 and Keithley 2611).

5.1.3 Resistance measurements

Sheet resistance measurements were carried out using the 4-probe Van der Pauw method [90]. In this method, electrical contacts are placed at each corner of the sample, as seen in Figure 5.4, and numbered 1, 2, 3 and 4.

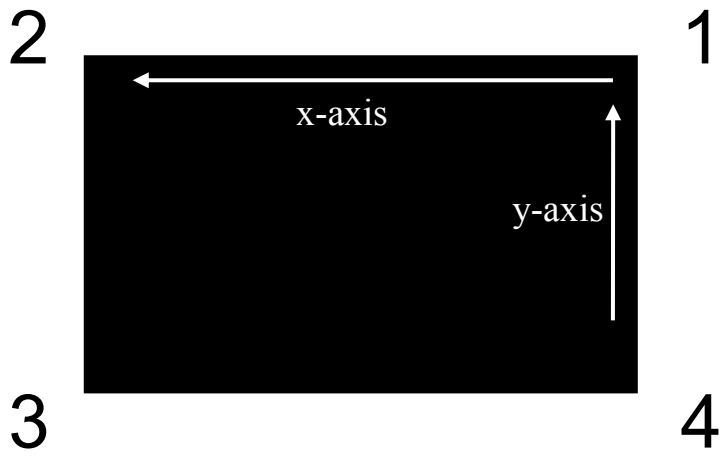

Figure 5.4: Diagram of the numbering system used to label the four electrical contacts in the van der Pauw method for measuring sheet resistance. The notation in the above diagram will be used throughout this thesis. The experimental frame, and therefore the assignment of a number to each corner of the sample, is defined by the laser beam. The orientation seen above is effectively the orientation the laser beam 'sees' as it travels towards the sample.

A small current (in this case 10 mA) is then passed through two electrodes so that it passes across one edge of the sample, 1 and 2 for example. The voltage is then measured across the other two electrodes, in this case 3 and 4. The resistance, $R_{12,34}$, is then calculated using Ohm's law

$$R_{12,34} = \frac{V_{34}}{I_{12}}, \tag{5.1}$$

where V_{34} is the voltage measured across electrodes 3 and 4 and I_{12} is the current passed through electrodes 1 and 2. To measure the sheet resistance, four measurements are taken; $R_{12,34}$, $R_{23,41}$, $R_{34,12}$ and $R_{41,23}$. The resistance across the x-axis ($R_{horizontal}$) can be calculated by taking the average of $R_{23,41}$ and $R_{41,23}$ whilst the resistance across the y-axis ($R_{vertical}$) can be calculated by taking the average of $R_{12,34}$ and $R_{34,12}$. The sheet resistance, R_S, can then be calculated from the van der Pauw formula [90],

$$\exp(-\frac{\pi R_{\text{horizontal}}}{R_S}) + \exp(-\frac{\pi R_{\text{vertical}}}{R_S}) = 1. \qquad (5.2)$$

Two sourcemeters were used to measure the resistance. One was used to supply the current and the other was used to measure the voltage. A LabVIEW program was written to control the two sourcemeters during measurements, which is presented in Appendix D.

5.2 Carbon nanotube Raman measurements

As well as buckypaper, fusion experiments were carried out on samples made from nanotube solutions deposited on quartz slides. This part of the project was carried out together with Devin Dunseith as part of his Masters project. Devin, together with Andrei Gromov, prepared and characterised the samples and also carried out initial Raman measurements.

5.2.1 Sample preparation

Samples consisting of films of single-walled carbon nanotubes (SWNT) were prepared on quartz slides. (The nanotubes were HiPco produced tubes from Carbon Nanotechnologies Inc., USA). The film was prepared in such a way that two layers of tubes were deposited, one on top of the other, with the 'directions' of deposition of each layer being orthogonal to each other. Dry nanotubes were added to a 10 $mgml^{-1}$

solution of sodium dodecyl sulphate (SDS) in water at 1 mg per 10 ml. The SDS acts as a surfactant, producing homogeneous dispersions of SWNTs. The mixture was sonicated with an ultrasonic processor tip for 20 minutes and then centrifuged for 30 minutes. The supernatant liquid was decanted off and the solution was centrifuged again. To deposit the sample on the slide, the 'casting' method was used [91]. This involves placing the slide at an angle of 5^{o} with respect to a horizontal surface and pipetting 40 μL of the SWNT solution dropwise onto the slide. This is left to dry in ambient conditions for 24 hours, rinsed with deionised water for 30 seconds and then left to dry for another 24 hours. To deposit the second layer of SWNTs, the slide is then turned 90 degrees and the process repeated.

5.2.2 Sample characterisation

The samples were analysed using Raman Spectroscopy, Atomic Force Microscopy (AFM) and Scanning Electron Microscopy (SEM) to make sure that nanotubes were deposited in sufficient density and that the alignment of the tubes was satisfactory during the deposition. Figure 5.5 shows the full Raman spectrum, taken with a 785 nm laser, prior to irradiation of the sample. The characteristic features of Raman spectroscopy of carbon nanotubes are present [92].

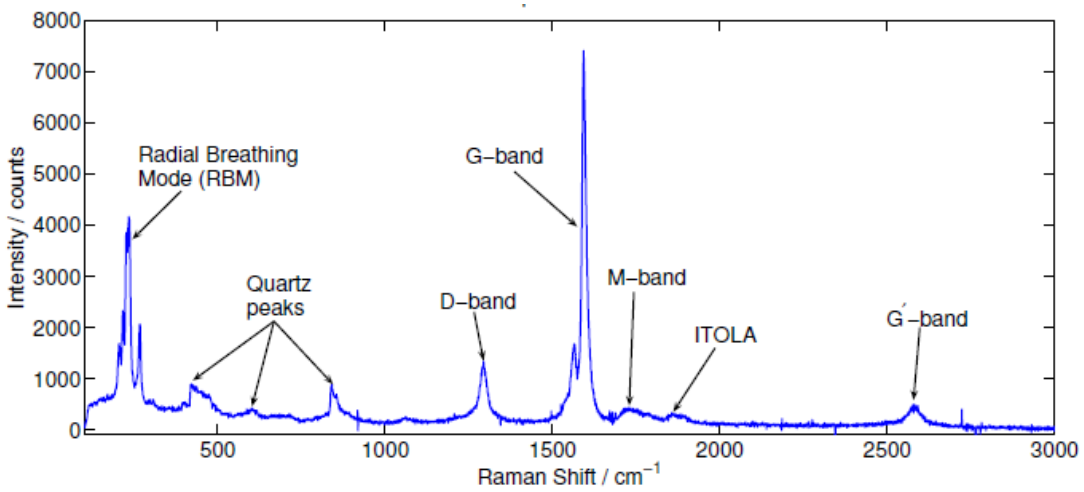

Figure 5.5: Raman spectrum, prior to irradiation of the sample, with 785 nm laser. Figure from ref [93].

Figure 5.6 shows an AFM image taken of the sample after the first deposition, with tubes deposited in only one direction (the x-direction in relation to the AFM translation stage) and an AFM image taken after the second deposition step, with tubes deposited in directions orthogonal to one another (the x-direction and the y-direction in relation to the AFM translation stage). It can be seen from the image after the first deposition that tubes are reasonably well aligned in the x-direction and that there is a reasonable distribution of tubes on the surface. The image after the second deposition shows that the two layers of tubes are reasonably well aligned orthogonal to each other and that there is a reasonable degree of overlap between the two layers which is likely to aid fusion between tubes.

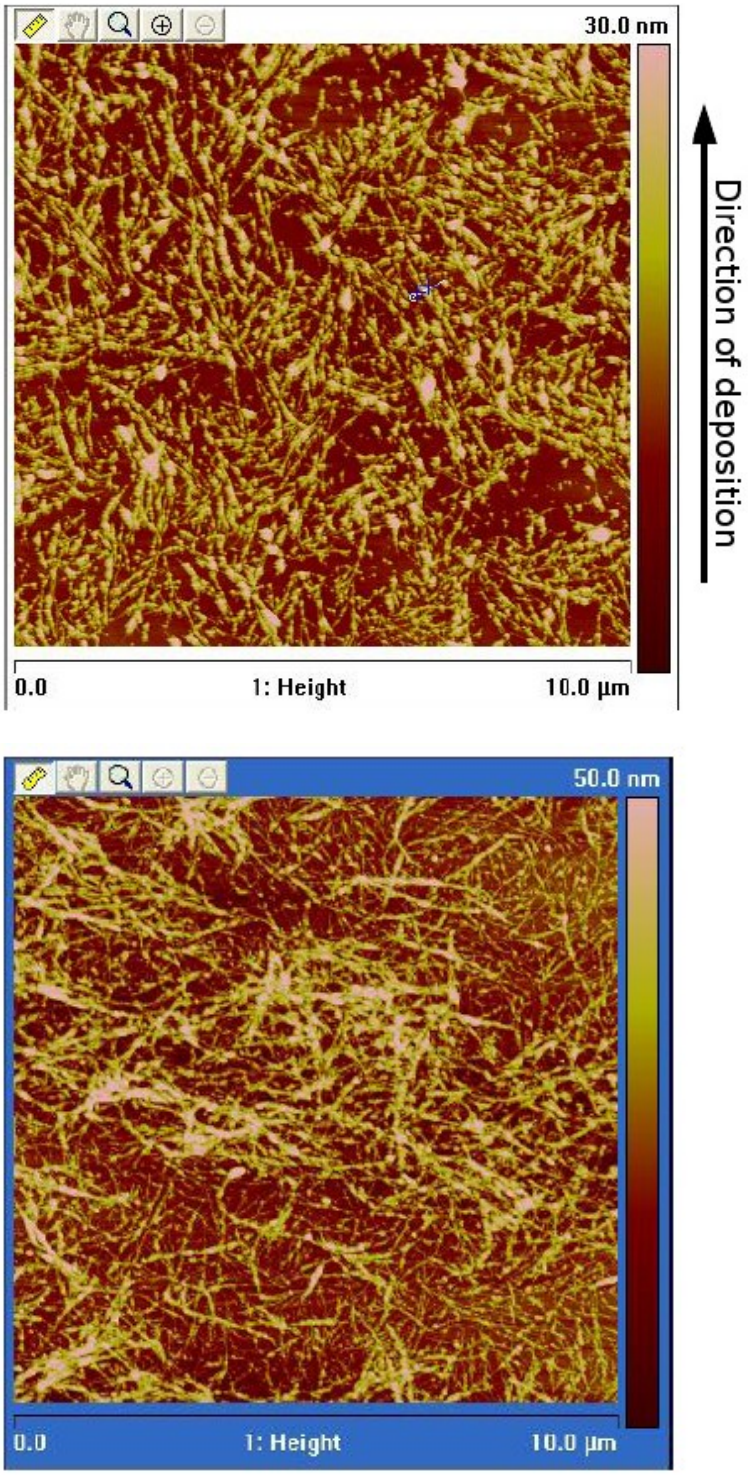

Figure 5.6: AFM images taken of the nanotube sample top) after the first deposition step and bottom) after the second deposition step. Figure adapted from ref [93].

Figure 5.7 shows an SEM image taken of the sample after the second deposition step. Similar to the AFM images, it shows a reasonable nanotube distribution with a reasonable degree of overlap between the two layers.

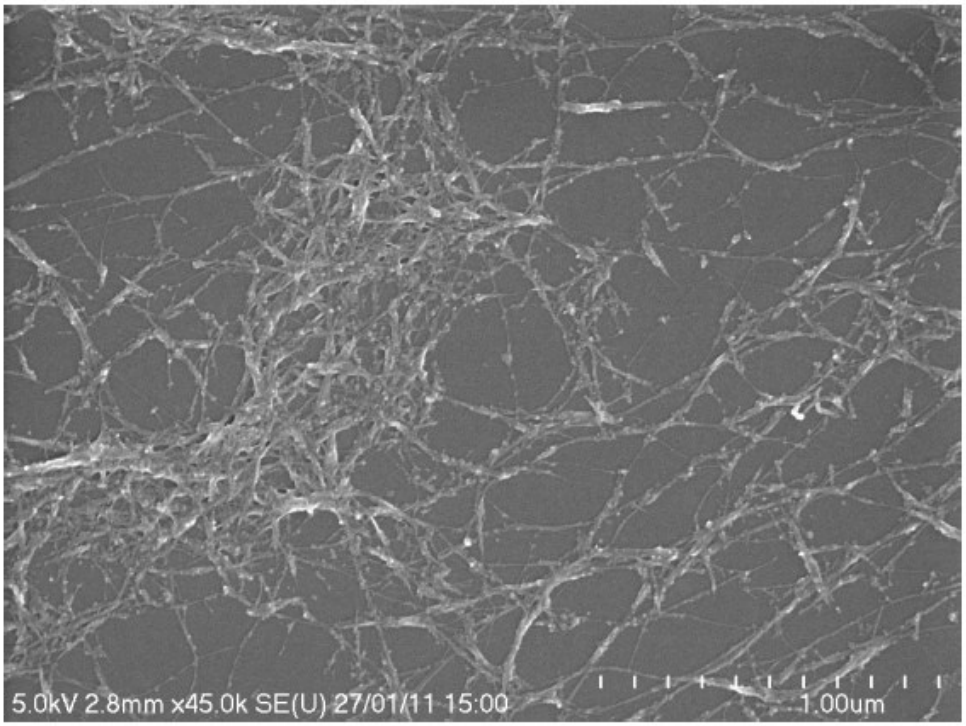

Figure 5.7: SEM image taken at x 45,000 magnification of the nanotube sample after the second deposition step. Figure from ref [93].

5.2.3 Experimental setup

The sample was mounted on a quartz sample holder (described in section 5.1.2) in a vacuum chamber. The vacuum chamber was pumped by a turbomolecular pump (Leybold) and backed by a 2-stage roughing pump (Edwards, EZM-12) and achieved typical pressures of 10^{-6} mbar. The laser was aimed at a spot on the sample and the sample was shot with the 800 nm, 120 fs output from the Legend in single shot mode, once. Light sensitive paper was placed behind the sample so that the spot could be found, by eye, when analysing with the Raman spectrometer. After each shot, the vacuum chamber was brought back to atmospheric pressure and the sample

was moved so that a different area of the sample would be shot and the process was repeated.

The laser was focussed using a 50 cm focussing lens although the sample was placed around 40 cm from the lens as the intensity at the focal spot would likely have damaged the sample and a larger irradiation area was preferable in terms of irradiating as many nanotubes as possible and facilitating finding the irradiation spots to perform analysis. This made calculating the spot size and therefore laser intensity difficult and so the laser spot size was estimated by placing light sensitive paper in the beam path and irradiating for a period of time. The diameter of the circular damaged area was then assumed to be the beam diameter. By this method, the diameter of the damaged area was measured at 0.5 ± 0.05 mm, giving a beam area of $(2.0 \pm 0.4) \times 10^{-3}$ cm^2.

5.2.4 Raman spectroscopy of carbon nanotubes

In Raman Spectroscopy [94], light is shone on a sample and the electric field of the radiation acts to polarise the electron cloud around the nuclei in the irradiated molecule and create a short-lived excited 'virtual energy state'. A photon is emitted, relaxing the molecule to either the ground state (known as elastic, Rayleigh, scattering) or a vibrationally excited state (known as inelastic scattering). It is the inelastic scattering process which is of interest in Raman spectroscopy. If the emitted photon carries away less energy than the absorbed photon, this is known as Stokes scattering and the molecule is left vibrationally "hotter" than before the photon absorption. If the emitted photon carries away more energy than the absorbed photon, this is known as anti-Stokes scattering and the molecule is left in a vibrationally "colder" state than before absorption. For anti-Stokes scattering to take place, the molecule must, initially, be in an excited vibrational state. The various scattering processes are depicted in Figure 5.8. If the virtual energy state is resonant with a real excited state, the Raman signal is greatly increased as this is known as resonant Raman spectroscopy.

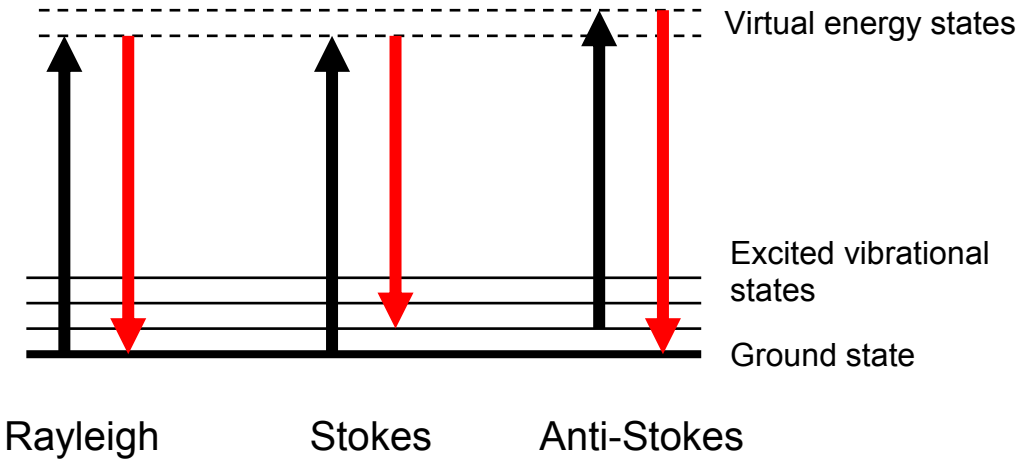

Figure 5.8: Diagram of the various scattering processes in Raman spectroscopy. The length of the black arrows represent the energy of the absorbed photon. The length of the red arrows represent the energy of the emitted photon.

The density of states for carbon nanotubes consists of a series of sharp peaks known as van Hove singularities [92]. When the photon energy of the incoming light is equal to the energy difference between two of these peaks, the Raman signal is greatly increased. The energy spacing between the peaks depends on the chirality of the tubes and consequently, for a given photon energy, only scattering from some of the tubes in the sample may be detected. This is represented by a Kataura plot, shown in Figure 5.9

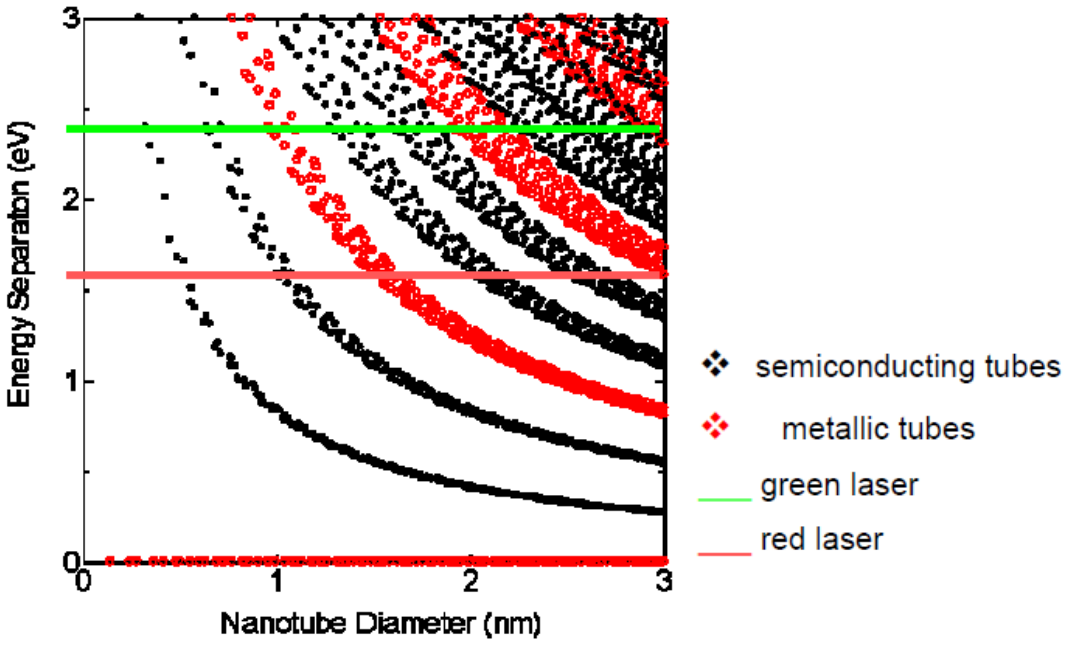

Figure 5.9: Kataura plot showing different resonance excitations as a function of photon energy and tube diameter for semiconducting and metallic nanotubes. Figure from ref [95].

Various features are present in the Raman spectra of carbon nanotubes but the one of most interest in this thesis is the radial breathing mode (RBM) peak. The RBM is the radial expansion and contraction of the carbon nanotube in relation to the tube axis. The frequency shift of the RBM, ω_{RBM} is typically between 100 and 400 cm^{-1} and is inversely proportional to the diameter of the nanotube, d, according to the relationship

$$\omega_{RBM} = \frac{A}{d} + B, \tag{5.2}$$

where A and B are parameters which vary, depending on the substrate used. The values when using a quartz substrate are reported to be A = 248 nm cm^{-1} and B = 0 cm^{-1} [96]. Although the exact relationship between the RBM frequency shift and tube diameter is complicated and may depend on the substrate used and the dispersion of the tubes in the sample, the general relationship is that higher frequency shifts signify tubes with smaller diameters.

The Raman spectrometer used was a Renishaw In-Via micro-Raman system. All Raman spectra presented in Chapter 8 were taken with 514 nm laser excitation. At this wavelength, a large signal was present around the area of interest for the RBM peaks (from 100 to 600 cm^{-1}). This is due to the substrate as it is observed even when no nanotubes are present. This signal was removed by subtracting the signal for an area of the substrate with no nanotubes present, from all Raman spectra. Figure 5.10 shows a Raman spectrum for an area of the sample where no tubes are present beside a Raman spectrum for an area of the sample where tubes are present. Figure 5.11 shows the nanotube spectrum from Figure 10 with the 'background' signal subtracted.

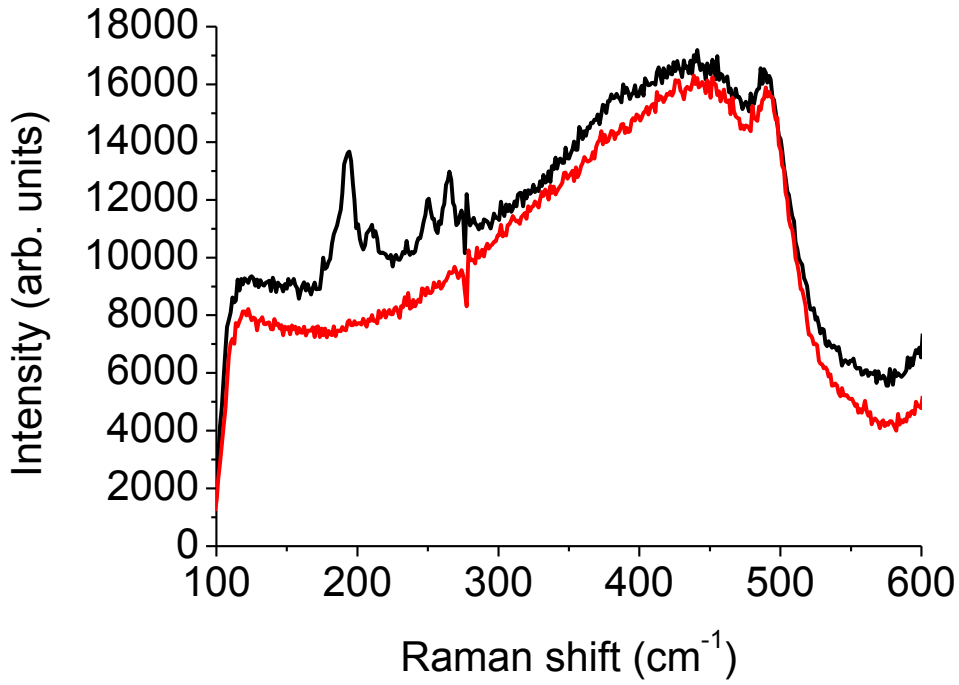

Figure 5.10: Raman spectra taken with 514 nm laser where black) carbon nanotubes are present and red) no carbon nanotubes are present. In the spectrum where the tubes are present, RBM peaks can be observed from around 180 to 300 cm^{-1}. In the spectrum where no tubes are present, no RBM peaks are observed but a large structure due to the substrate is observed from 100 to 600 cm^{-1}.

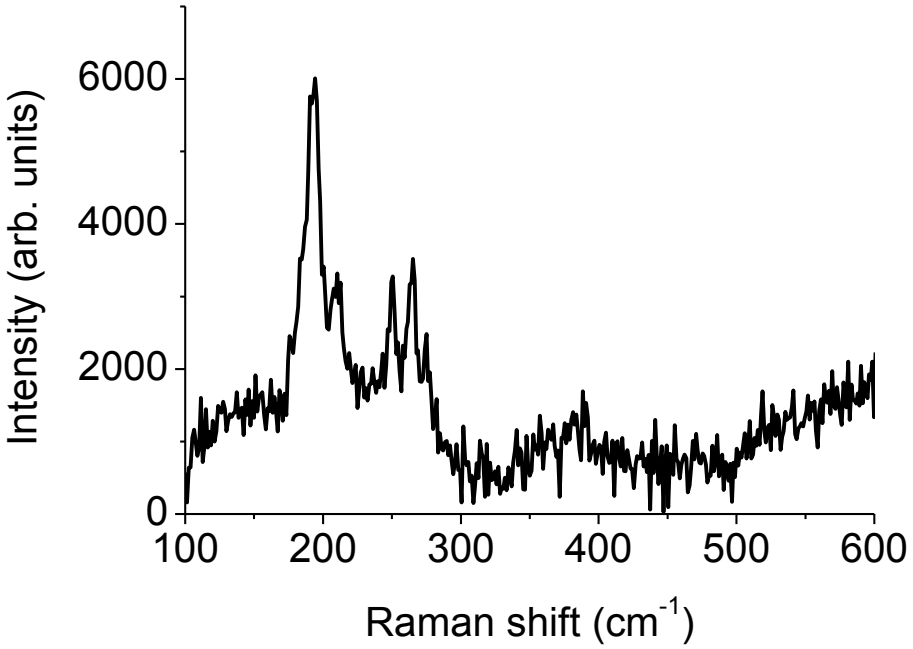

Figure 5.11: Raman spectrum of nanotubes from Figure 5.10 with Raman spectrum of substrate, from Figure 5.10, subtracted. A range of peaks are observed in the unirradiated spectra between around 190 to 260 cm^{-1}. This corresponds to a nanotube diameter range (according to equation 5.2) of around 0.95 to 1.31 nm.

Chapter 6 – Thermal electron emission from fullerenes in strong laser fields

In this chapter, the excitation, energy redistribution and emission of electrons in fullerene molecules subjected to ultrashort, intense laser pulses is discussed. Previous studies have suggested that with laser pulses of duration 50 fs up to a few hundred fs, the ionisation mechanism for C_{60} is largely thermal in nature [3, 4, 5]. Early investigations in this area used linear time-of-flight mass spectrometry and photoelectron spectroscopy to probe the fragment distributions and photoelectron distributions [3,4]. Evidence for the 'two-temperature' [18] nature of the ionisation mechanism was seen in the heavy fragmentation and low electron apparent temperatures using longer laser pulses and the lighter fragmentation and higher electron apparent temperatures with shorter laser pulses. The interpretation was that, with pulses of duration 50 fs up to a few hundred fs, the electronic system is left highly excited and thermally equilibrated but energy does not have time to leak into vibrational modes before ionisation. This results in statistical, non-direct ionisation. With pulses shorter than 50 fs, very little fragmentation is observed and clear ATI peaks are seen in the PES, suggesting more direct mechanisms at play. In later studies [5] the temperatures fitted to angle-integrated photoelectron spectra, obtained using a linear time-of-flight spectrometer, were compared to theoretical models, based on a thermal ionisation mechanism, with the results supporting the thermal electron emission hypothesis. However, initial angle-resolved photoelectron spectroscopy studies, carried out with a VMI setup, by the Campbell group, showed that the kinetic energy distribution of photoelectrons emitted after excitation on this timescale is peaked along the laser polarisation direction [6]. This anisotropy in the photoelectron distributions is evident in the initial angle-resolved results although was not the focus of the first paper published using the VMI setup. If electron excitation and ionisation are purely statistical processes, the emitted electrons should have no 'memory' of the laser pulse and would be expected to be emitted in an isotropic distribution. These results challeneged the initial hypothesis that electron emission on this time scale was a purely thermal, statistical process. The aim of my project was then to investigate ionisation on these time scales using a VMI setup to determine to what extent the

ionisation mechanism could be described by a thermal, statistical process, if direct mechanisms played a significant role in ionisation and what causes the anisotropy in the photoelectron distributions.

No detectable delay (on the μs timescale of the TOF mass spectrometer) in electron emission after this "thermal" ionisation is observed although the emission is not expected to be direct with respect to the laser pulse as thermal emission is a non-direct, statistical process. In this chapter, angle-resolved PES will be presented for C_{60} and C_{70} ionisation by laser pulses of varying wavelength, intensity and pulse duration, as well as results from pump-probe experiments on C_{60}, in an attempt to explain the excitation and ionisation processes at play on these timescales. An introduction to the transient thermal electron model is given, followed by experimental results and a discussion on the thermal nature of the ionisation process and the anisotropy present in the photoelectron distributions will be presented.

6.1 Transient thermal electron emission

When C_{60} is excited by laser pulses on the ns timescale, structureless PES are obtained with a Boltzmann-like energy distribution described by

$$S(\varepsilon)d\varepsilon \propto \exp(-\varepsilon / k_{\mathrm{B}}T_{\mathrm{a}})d\varepsilon\,, \tag{6.1}$$

where ε is the electron kinetic energy, k_{B} is the Boltzmann constant and T_{a} is the electron apparent temperature [4]. The temperatures are microcanonical temperatures as the molecules can be considered as isolated systems in the high vacuum conditions used in the experiments. Electron temperatures of 3000-4000 K (0.26-0.34 eV) are observed and the mass spectra reveal heavy fragmentation. When the pulse duration is decreased to between 50 fs and a few hundred fs, similar structureless, Boltzmann-like energy distributions are observed in the PES but with significantly higher apparent temperatures and much less fragmentation is observed in the mass spectra. This has been interpreted as a statistical excitation, energy redistribution and ionisation process whereby energy is initially deposited in the electronic subsystem

where rapid thermal equilibration takes place via electron-electron interactions. If the pulse duration is long enough, energy is allowed to leak into the vibrational degrees of freedom and the excitation energy is equilibrated over all degrees of freedom within the molecule. Under these circumstances, thermionic emission occurs. For shorter pulse durations, enough energy builds up in the electronic subsystem for ionisation to occur before energy is leaked into the vibrational degrees of freedom. When ionisation occurs from a molecule with a hot electronic subsystem and cold vibrational degrees of freedom, this is known as transient thermal electron emission [5]. The heat capacity of the electronic subsystem is much lower than that of the electronic and vibrational subsystems combined and so electron apparent temperatures are much higher. Energy from the hot electrons is assumed to couple to the vibrational modes in an exponential decay with a fitted time constant of 240 fs, determined from the energy dependence of Penning ionisation yields [5, 97]. The time taken for energy equilibration in the electronic subsystem has been estimated to be less than 50 fs [22], although no such parameter is included in the thermal ionisation model as it is presumed only to describe the lower limit of excitation timescale for which the thermal model holds.

The model used for the excitation and emission process is described in detail in Ref. 5, where it was used successfully to describe the fluence dependence of photoelectron apparent temperatures obtained from ionising C_{60} with pulse durations 180 fs to 750 fs. It has also been used to describe thermionic emission from C_{60} [38]. The model is based on the principle of detailed balance and the statistical method was originally used by Weisskopf, to describe the emission of neutrons from highly excited nuclei [98]. The principle of detailed balance states that particle emission from a body (nucleus or cluster) in statistical equilibrium is related to the reverse process, particle absorption, by the expression,

$$\frac{k_{\text{decay}}}{k_{\text{formation}}} = \frac{\rho_{\text{products}}}{\rho_{\text{parent}}}, \tag{6.2}$$

where k_{decay} and $k_{\text{formation}}$ are the rate constants for the emission and absorption of a particle, respectively, and ρ_{products} and ρ_{parent} are the level densities of the product

(cluster ion and free electron) and parent (neutral cluster), respectively. This implies that the rate of electron emission from an excited C_{60} molecule can be equated with the rate of electron capture by a C_{60}^{+} ion, which can be estimated. This gives the rate constant for emission of electrons with kinetic energy ε from a cluster with an internal energy E_{int}, described by the Weisskopf formula,

$$k(\varepsilon, E_{\text{int}}) = \frac{2m_{\text{e}}}{\pi^2\hbar^3}\sigma(\varepsilon)\varepsilon\frac{\rho_{\text{d}}(E_{\text{int}} - \Phi - \varepsilon)}{\rho_{\text{p}}(E_{\text{int}})}d\varepsilon, \tag{6.3}$$

where $\sigma(\varepsilon)$ is the electron capture cross section, m_{e} is the electron mass, ρ_{d} and ρ_{p} are the level densities of the ionised and neutral molecule respectively and Φ is the ionisation energy. Expansion of the daughter level density gives the expression,

$$k(\varepsilon, E_{\text{int}}) = \frac{2m_{\text{e}}}{\pi^2\hbar^3}\sigma(\varepsilon)\varepsilon\frac{\rho_{\text{d}}(E_{int})}{\rho_{\text{p}}(E_{\text{int}})}\exp(-\frac{\Phi}{k_B T_d})\exp(-\frac{\varepsilon}{k_{\text{B}} T_d})d\varepsilon, \tag{6.4}$$

where T_{d} is the microcanonical temperature of the daughter at energy $E_{int} - \Phi$. Equation 6.4 can be approximated with the simple Arrhenius-type formula,

$$k_{\text{emission}} = A\exp(-\frac{\Phi}{k_{\text{B}} T_{\text{a}}}) \tag{6.5}$$

where T_{a} is the apparent electron emission temperature and the pre-exponential factor, A is approximated as 2.7×10^{15} s^{-1} [5].

The original model used in these studies was written in MATLAB by Olof Johansson and is based on the model written by Juraj Fedor which, in turn, is based on the earlier work by Klavs Hansen [5]. The intensity of the laser pulse, $I(t)$, is modelled, as a function of time and the internal energy in the electronic subsystem is described by

$$E\,\text{int}(t + dt) = E\,\text{int}(t)\sigma_{\text{ph}} I(t)\exp(-\frac{t + dt}{\tau}), \tag{6.6}$$

where σ_{ph} is the average photon absorption cross section and τ is the exponential decay constant set at 240 fs [5], accounting for energy leakage into vibrational modes. The electronic subsystem is treated as a Fermi gas and the average electron temperature as a function of time is given by

$$T(t) = \sqrt{\frac{4E_{\text{int}}(t)E_F}{\pi^2 N}}\,, \tag{6.7}$$

where E_F is the Fermi energy, and assumed to be 30 eV [99], and N is the number of valence electrons (240 for C_{60}). The rate constant for electron emission can then be obtained from equation 6.5 and the time-dependent electron yield is given by

$$Y(t) = k(t)\exp\left(-\int_{-\infty}^{t}(k(t')dt')\right). \tag{6.8}$$

The emission temperature of a photoelectron, $T_a(t)$, is related to the average electron temperature before emission, $T(t)$, by the expression [38],

$$T_a(t) = T(t) - \left(\frac{\Phi}{2C_V}\times k_B\right), \tag{6.9}$$

where C_V is the Fermi gas heat capacity.

One significant difference has been made to the original thermal emission model. A term accounting for the more efficient transfer of energy from the electrons to the vibrations at higher electronic energy has been included in the model. Electronic excitation energy has been shown to affect the electron-phonon coupling strength in metals and carbon nanotubes [100, 101]. The electron-phonon coupling strength, represented by the constant, τ, in the above equations, should therefore be dependent on internal energy, rather than constant as in the original model. When using the model, the average photon absorption cross section is fitted to obtain temperatures similar to the experimental data. It was found that higher photon absorption cross sections had to be fitted to spectra taken at higher intensities and that

this represented an exponential increase. This can be accounted for by introducing an exponential decay in internal energy, justified by the higher electron-phonon coupling strength at higher electronic energy. The term,

$$E_{\text{int}}(t) = E_{\text{int}}(t) \times \exp(-\frac{E_{int}(t)}{E_{\text{const}}}) \tag{6.10}$$

where E_{const} is the decay constant and taken to be 2.5 x 10^{-17} J (156 eV), is therefore included in the model. This provides consistent fits across all measurement series and allows a constant photon absorption cross section to be used in all fits. Using this equation, the change in τ as a function of internal energy can be estimated, according to the expression,

$$\tau(t) = t \log\left(\frac{E_{total}(t)}{E_{\text{int}}(t)}\right) \tag{6.11}$$

where E_{total}(t) represents the total energy absorbed by the molecule at time, *t*. This is, effectively, what the internal electronic energy would be if no coupling to vibrational modes were to take place. Figure 6.1 shows how E_{total}, E_{int} and τ change as a function of time, according to the model, for C_{60} excitation with 800 nm, 180 fs, 3.5 TW/cm^2 laser pulses.

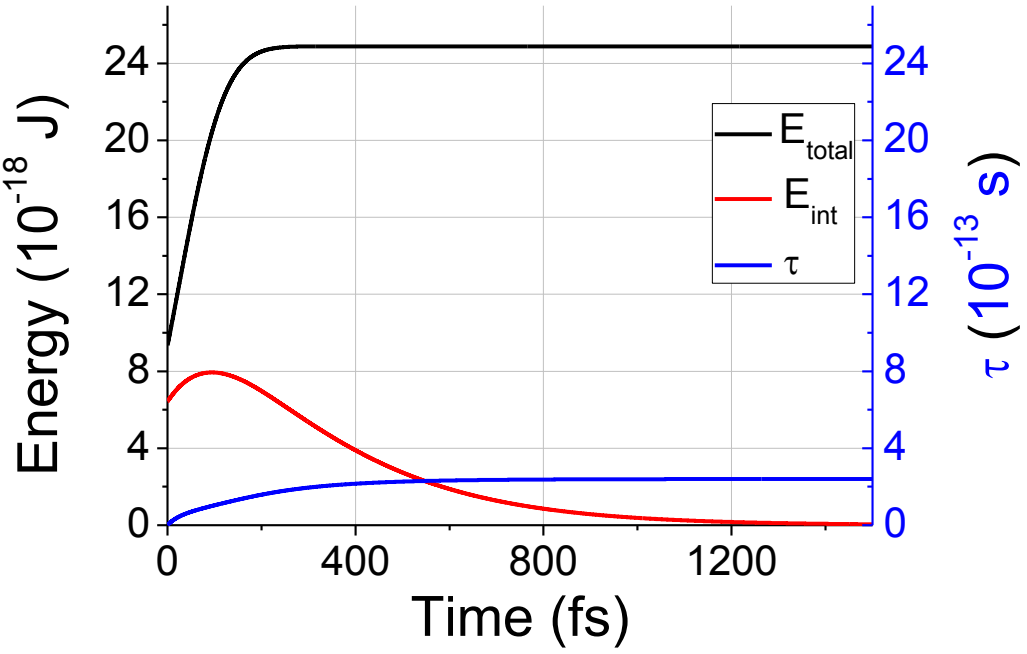

Figure 6.1: E_{total}, E_{int} and τ as a function of time, according to the model, for C_{60} excitation with an 800 nm, 180 fs, 3.5 TW/cm^2 laser pulses.

6.2 Results and discussion

The following section will present the results on thermal electron emission from fullerenes in strong electric fields, collected together with Olof Johansson. First, the method of fitting electron apparent temperatures to angle-resolved photoelectron kinetic energy distributions will be explained. Then VMI images, angle-resolved PES and mass spectra will be presented for C_{60} and C_{70} ionisation with lasers of wavelength 800, 625, 550 and 400 nm and various pulse durations and intensities as well as pump-probe experiments with 400 nm and 900 nm pulses. These results will be discussed in terms of the thermal ionisation model and the anisotropy present in the VMI images.

6.2.1 Angle-resolved photoelectron spectroscopy

Symmetrized quadrants of the inverted VMI images obtained were divided into angular segments of 10 degrees, from 0 to 90 degrees. Traditional PES can then be obtained for each segment and information, such as electron apparent temperature and the relative number of electrons emitted over a given angular range, can be extracted as a function of angle, with respect to the laser polarisation direction.

Apparent temperatures are fitted by plotting the PES on a log-lin scale and fitting a straight line to the distribution by eye. The inverse of the slope yields the apparent temperature according to the equation

$$\log\big(S(\varepsilon)\big) \propto -\frac{\varepsilon}{k_B T_a}. \tag{6.12}$$

For many of the PES recorded, features resulting from direct ionisation are also present (excited state peaks at kinetic energies below the photon energy and ATI peaks extending to higher kinetic energies) which makes fitting using an automated least-squares fitting procedure difficult since any peaks resulting from direct ionisation should be subtracted before fitting. Fits are made so as to try and ignore the distribution below the energy of one photon and disregard ATI peaks. Errors in the fit are also estimated by eye. The upper limit is estimated by taking ATI peaks into account and fitting accordingly. The lower limit is estimated by simply fitting the lowest temperature which looks reasonable beside the distribution. An example of a fitted temperature and the errors is shown in Figure 6.2. Some of the errors are relatively large using this method but that reflects the difficulties in choosing a fit, especially where large ATI peaks are present or there was a relatively low signal during the experiment.

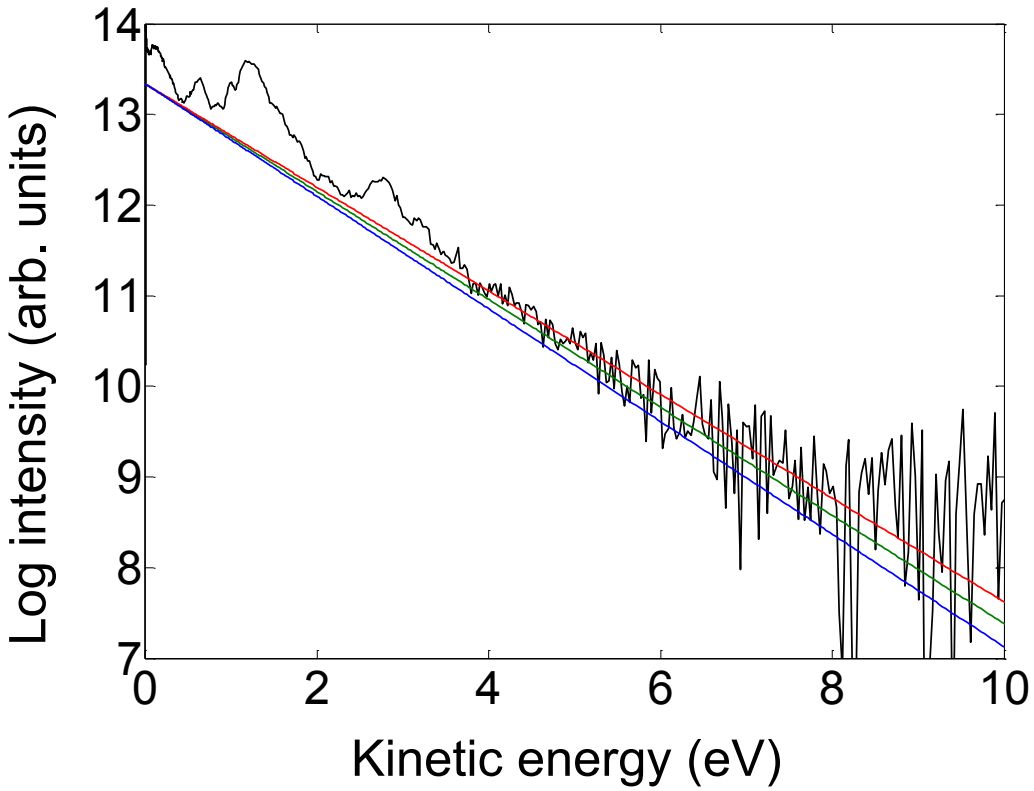

Figure 6.2: Electron apparent temperature fitted to the 0-10^0 angular segment of the PES obtained from ionisation of C_{60} with 800 nm, 180 fs, 5.2 TW/cm^2 laser pulses. The fitted temperature is 1.68 ± 0.07 eV ($19{,}490 \pm 810$ K). The green line represents the fit with the red and blue lines representing the upper and lower errors, respectively.

6.2.2 C_{60} ionisation

800 nm excitation

Series of experiments were carried out, ionising C_{60} with laser pulses of wavelength 800 nm and pulse durations from 130 fs to 3.8 ps. Measurements, in which VMI images and mass spectra were collected, were carried out at different laser intensities and for pulse durations of 130 fs, 180 fs and 1 ps. A series of measurements at constant laser fluence with pulse durations in the ps range was also

carried out. Inverted VMI images, angle-resolved PES for the 0-10° and 80-90° segments and mass spectra for experiments carried out with 180 fs pulses and intensities ranging from 4.3 to 13.2 TW/cm^2 are presented in Figures 6.3, 6.4 and 6.5 respectively.

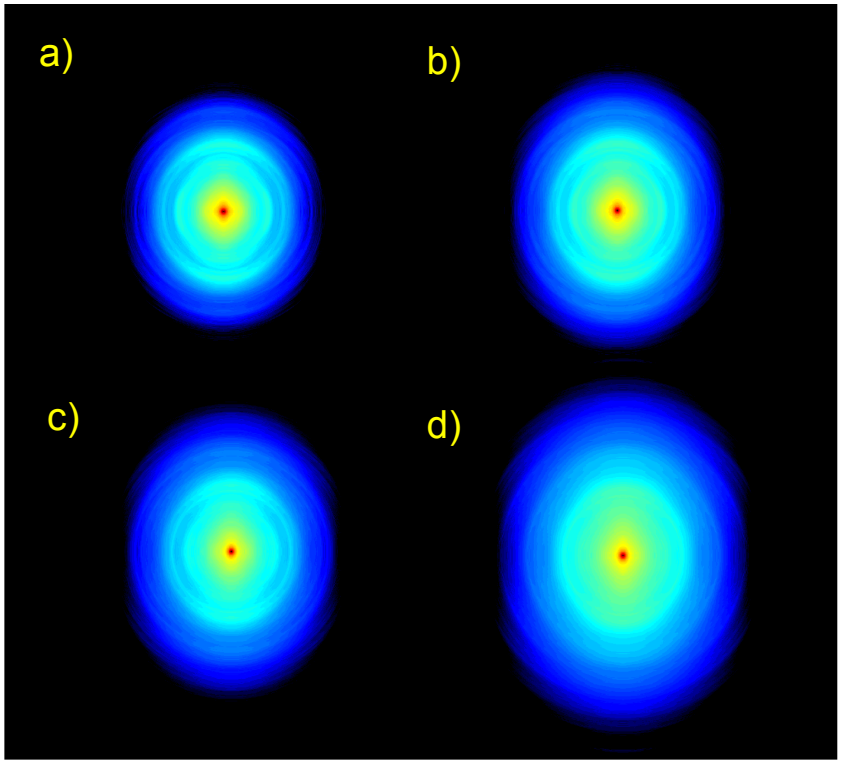

Figure 6.3: Inverted VMI images of C_{60} ionised with 800 nm, 180 fs laser pulses. The laser intensities (fluences) are a) 4.3 ± 0.1 TW/cm^2 (0.73 ± 0.02 J/cm^2) b) 6.7 ± 0.2 TW/cm^2 (1.1 ± 0.1 J/cm^2) c) 10.3 ± 0.2 TW/cm^2 (1.7 ± 0.1 J/cm^2) d) 13.2 ± 0.3 TW/cm^2 (2.2 ± 0.1 J/cm^2).

From the inverted VMI images (Figure 6.3), it is clear that the photoelectron distribution is anisotropic; with the distributions extending to higher electron kinetic energies at 0° than at 90°, that is to say, higher apparent temperatures parallel to the direction of laser polarisation than perpendicular to it, and that the degree of anisotropy increases with increasing laser intensity. The PES can be described as largely structureless, exponential distributions with a number of peaks superimposed

on a thermal background. These peaks represent direct ionisation from excited states of the molecule and ATI peaks. Fits were made for each angular segment to extract apparent temperatures. Only the PES representing the 0-10^{o} and the 80-90^{o} segments are shown in Figure 6.4, for clarity, and the anisotropy, clear from the inverted images, can be seen in the significantly larger apparent temperatures and the larger areas of the distribution for the 0-10^{o} segments, indicating that more electrons are emitted parallel to the laser polarisation and with higher average energy. The apparent temperatures show a smooth, gradual increase for each angular increment from 90^{o} to 0^{o} (highlighted in Figure 6.7). The temperatures also show a steady increase with intensity (and hence fluence). ATI peaks become more prevalent with increasing intensity and at smaller angles relative to the laser polarisation axis. The mass spectra show singly, doubly and, at higher intensities, triply charged parent ions and their fragments, created by the loss of C_2 units. At the highest intensities, we also see heavy fragmentation resulting in small mass carbon rings and chains.

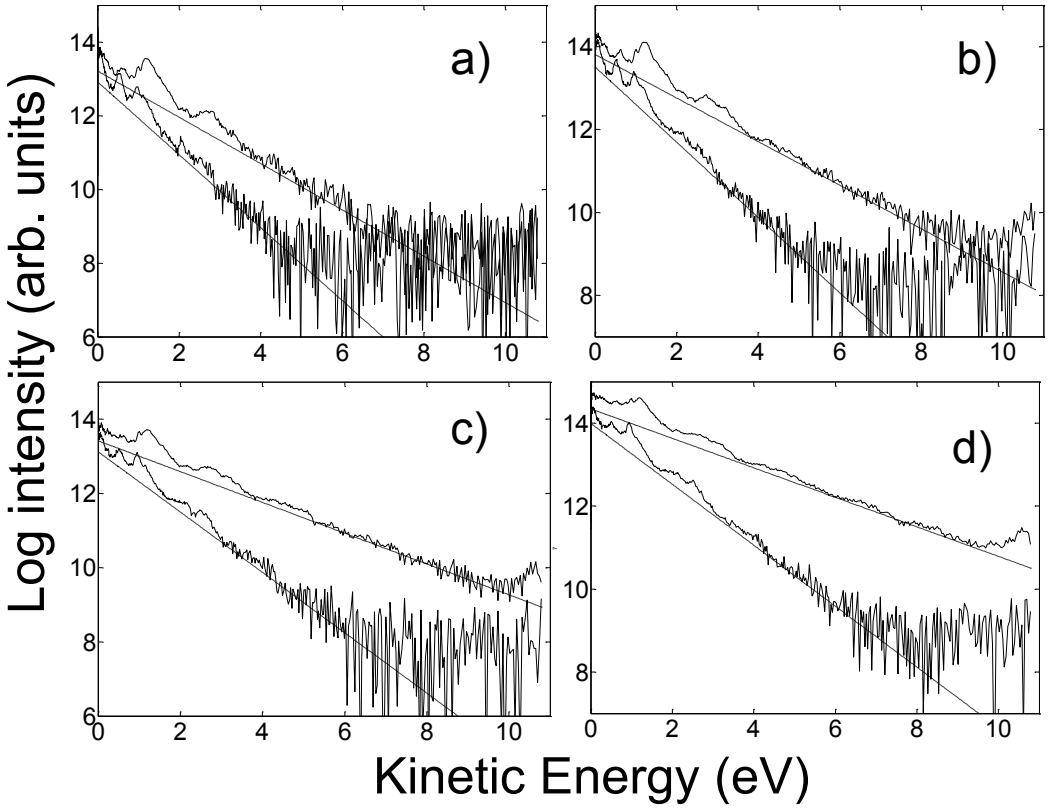

Figure 6.4: Angle-resolved PES, showing 0-10^{o} and 80-90^{o} segments for C_{60} ionised with 800 nm, 180 fs laser pulses. The intensities (fluences) are the same as shown in Figure 6.3. The apparent temperatures extracted from the 80-90^{o} and 0-10^{o} segments, respectively, are a) 1.01 and 1.59 eV (11,720 and 18,440 K) b) 1.10 and 1.90 eV (12,760 and 22,040 K), c) 1.23 and 2.41 eV (14,270 and 27,950 K) d) 1.36 and 2.81 eV (15,780 and 32,600 K).

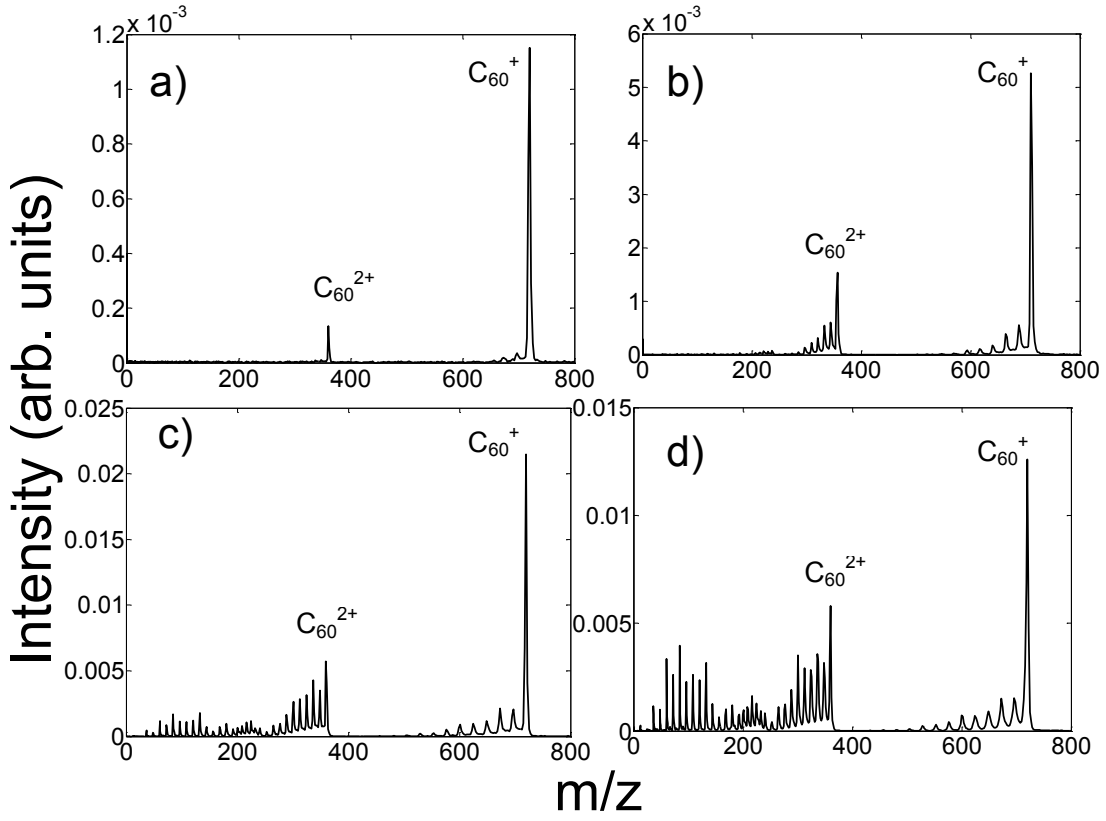

Figure 6.5: Mass spectra taken for C_{60} ionised with 800 nm, 180 fs laser pulses. The intensities (fluences) are the same shown in Figure 6.3.

The 800 nm, 180 fs data and the data taken from experiments with 800 nm, 130 fs laser pulses are very similar. Measurements taken at the two different pulse durations and similar fluences show similar apparent temperatures perpendicular to the laser polarisation and, with the 130 fs pulses having a higher intensity, a slightly higher temperature parallel to laser polarisation is observed. ATI peaks are also more prevalent in the 130 fs spectra.

A series of measurements at different intensities was made with pulse duration 1 ps and measurements were taken at pulse durations of 2, 3 and 3.8 ps, at a constant fluence of 2 J/cm^2. Thermionic ionisation is known to become the dominant mechanism on the timescale of a few picoseconds [4]. Figure 6.6 shows the inverted VMI images, angle-resolved PES and mass spectra for C_{60} ionised with 1 ps and 3.8 ps pulses.

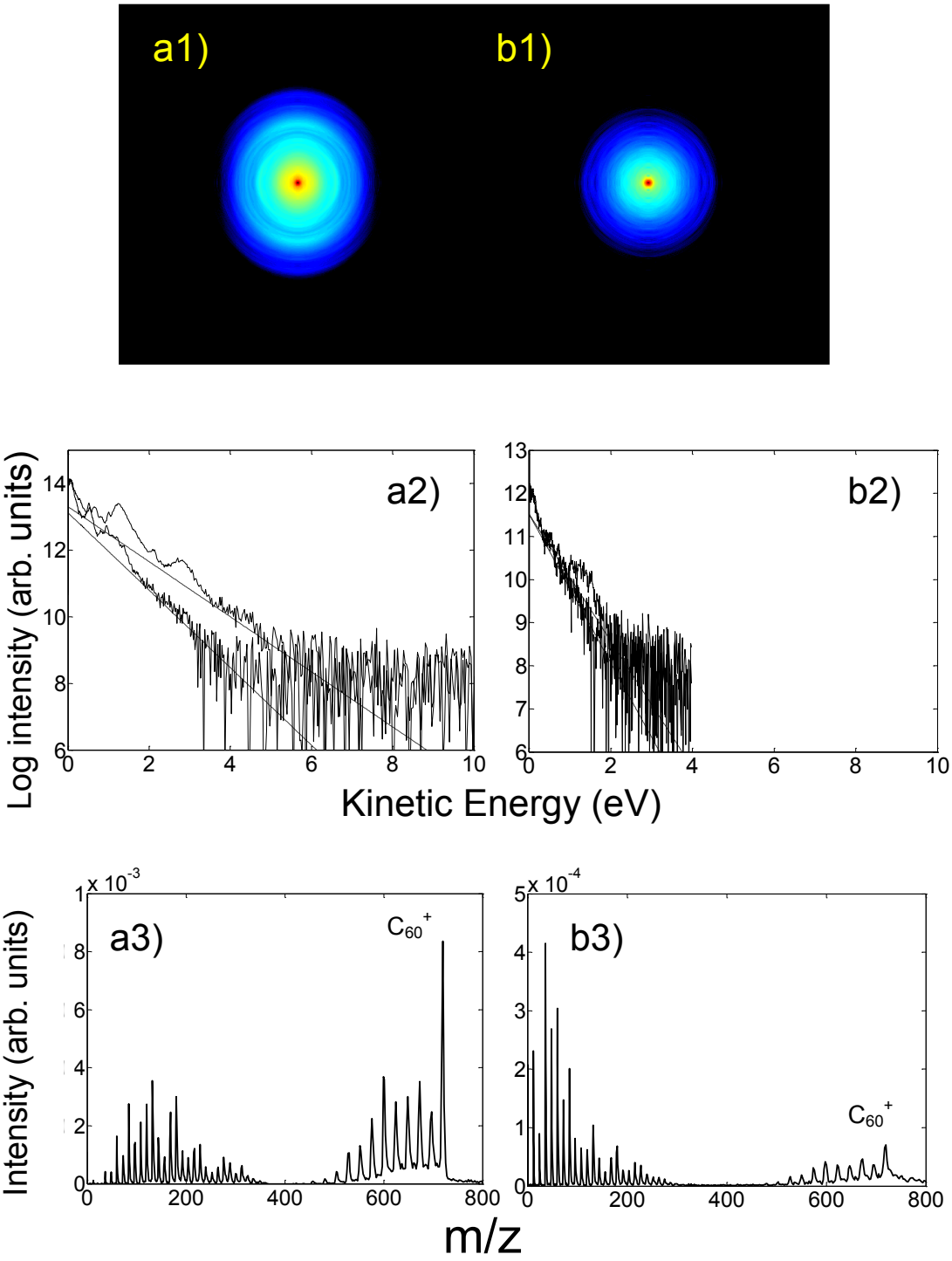

Figure 6.6: 1) Inverted VMI images, 2) angle-resolved PES and 3) mass spectra for C_{60} ionised with a) 800 nm, 1 ps, 2.0 ± 0.1 TW/cm^2 (1.9 ± 0.1 J/cm^2) and b) 800 nm, 3.8 ps, 0.51 ± 0.02 TW/cm^2 (2.0 ± 0.1 J/cm^2).

As the pulse duration is increased we see lower apparent temperatures, less asymmetry in the VMI images and the emergence of the heavily fragmented bimodal mass spectra. This is a clear indication that, for longer pulse durations, more energy is transferred to vibrations and less energy is carried away by the photoelectrons.

Plots of apparent temperature as a function of emission angle, relative to the laser polarisation, are shown for laser pulses of different intensity and pulse duration in Figure 6.7.

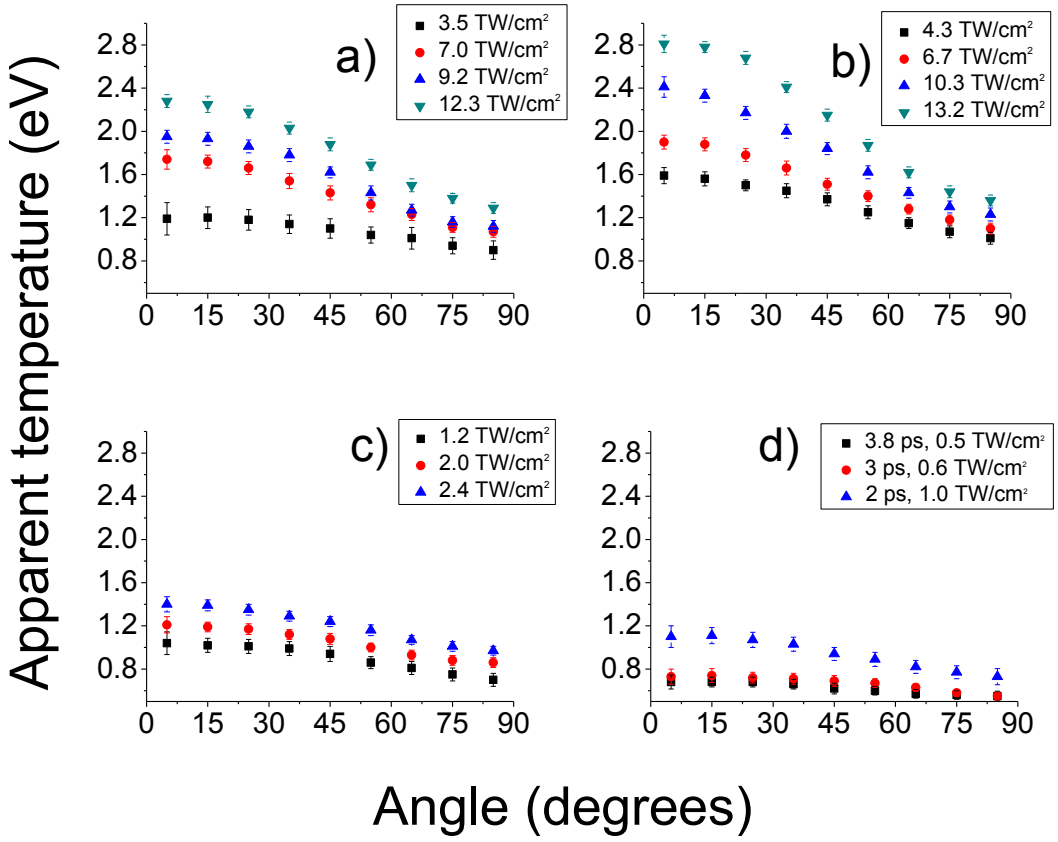

Figure 6.7: Apparent temperature as a function of angle of emission, relative to the laser polarisation axis, for different laser pulse durations and intensities. Pulse durations are a) 130 fs, b) 180 fs, c) 1 ps and d) 2 - 3.8 ps.

625 nm excitation

A series of experiments was carried out, ionising C_{60} with laser pulses of wavelength 625 nm and pulse duration 50 fs over a range of intensities. Inverted VMI images, angle-resolved PES for the 0-10^{o} and 80-90^{o} segments and mass spectra for experiments carried out with intensities 5.5 and 14.3 TW/cm^2 are presented in Figure 6.8. As with the 800 nm measurements, the VMI images for 625 nm, 50 fs excitation show a clear anisotropy; with the electron distribution stretching to higher kinetic energy parallel to the direction of laser polarisation than perpendicular to it. The apparent temperatures, at all angles of emission, increase with increasing laser intensity although it should be noted that the apparent temperatures obtained along the laser polarisation axis do not increase as much, relative to the perpendicular temperatures, with increasing intensity, as with the 800 nm measurements. Plots of apparent temperature as a function of emission angle, relative to the laser polarisation, are shown for different intensities in Figure 6.9.

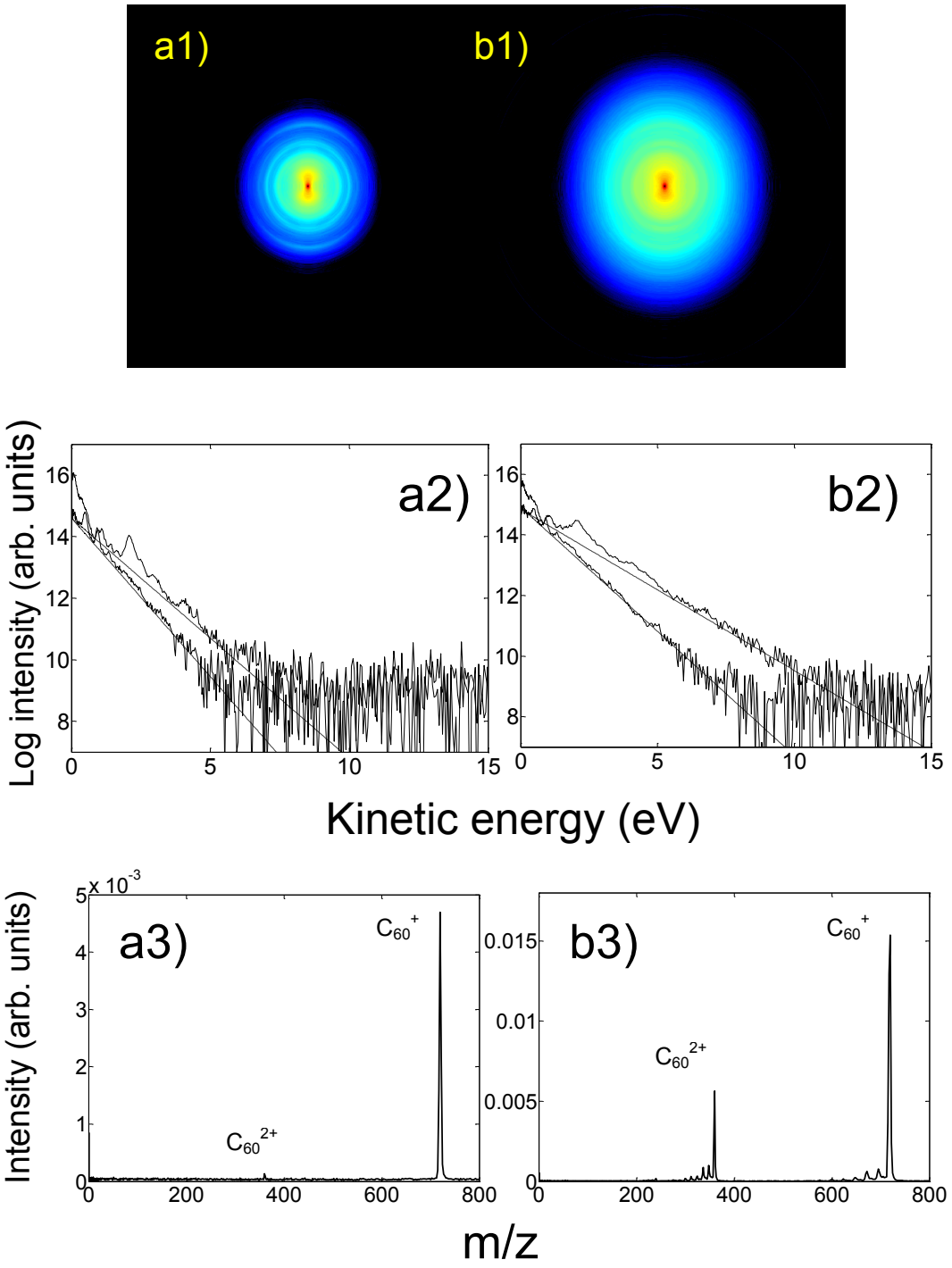

Figure 6.8: 1) Inverted VMI images, 2) angle-resolved PES and 3) mass spectra for C_{60} ionised with 625 nm, 50 fs laser pulses of intensity (fluence) a) 5.5 ± 0.4 TW/cm^2 (0.26 ± 0.02 J/cm^2) b) 14.3 ± 1.0 TW/cm^2 (0.67 ± 0.05 J/cm^2). The apparent temperatures extracted from the 80-90^o and 0-10^o segments, respectively, are a) 0.97 and 1.28 eV (11,250 and 14,850 K) and b) 1.22 and 1.88 eV (14,150 and 21,810 K).

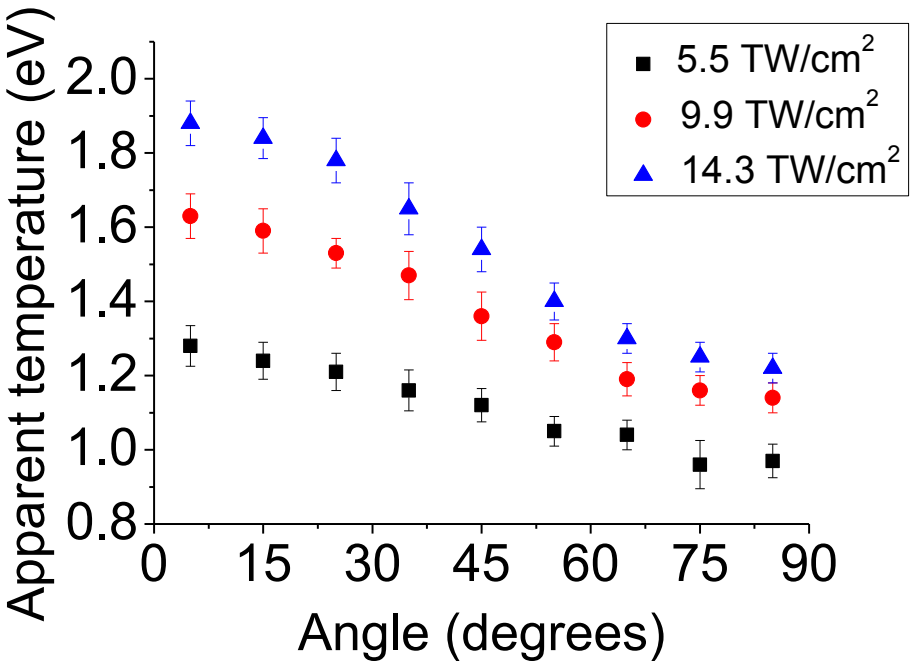

Figure 6.9: Apparent temperature as a function of angle of emission, relative to the laser polarisation, for C_{60} ionised by 625 nm, 50 fs laser pulses of intensities 5.5 TW/cm^2, 9.9 TW/cm^2 and 14.3 TW/cm^2.

550 nm excitation

A series of experiments was carried out, ionising C_{60} with laser pulses of wavelength 550 nm and pulse duration 92 fs over a range of intensities. Inverted VMI images, angle-resolved PES for the 0-10^o and 80-90^o segments and mass spectra for experiments carried out with intensities 4.4 and 16.5 TW/cm^2 are presented in Figure 6.10. Plots of apparent temperature as a function of emission angle, relative to the laser polarisation, are shown for different intensities in Figure 6.11.

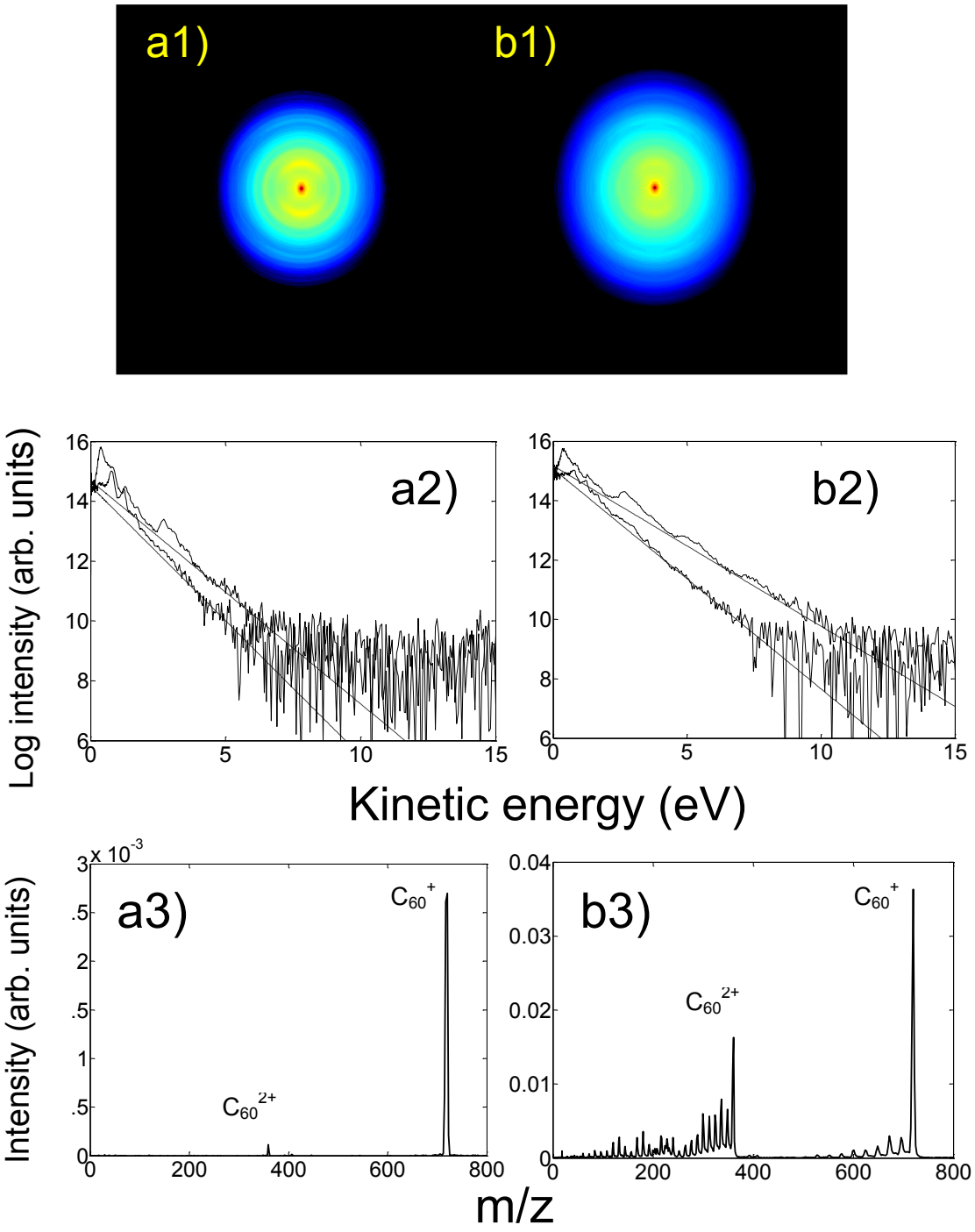

Figure 6.10: 1) Inverted VMI images, 2) angle-resolved PES and 3) mass spectra for C_{60} ionised with 550 nm, 92 fs laser pulses of intensity (fluence) a) 4.4 ± 0.2 TW/cm2 (0.38 ± 0.02 J/cm2) b) 16.5 ± 1.3 TW/cm2 (1.4 ± 0.1 J/cm2). The apparent temperatures extracted from the 80-90^{o} and 0-10^{o} segments, respectively, are a) 1.11 and 1.34 eV (12,880 and 15,540 K) and b) 1.35 and 1.85 eV (15,670 and 21,460 K).

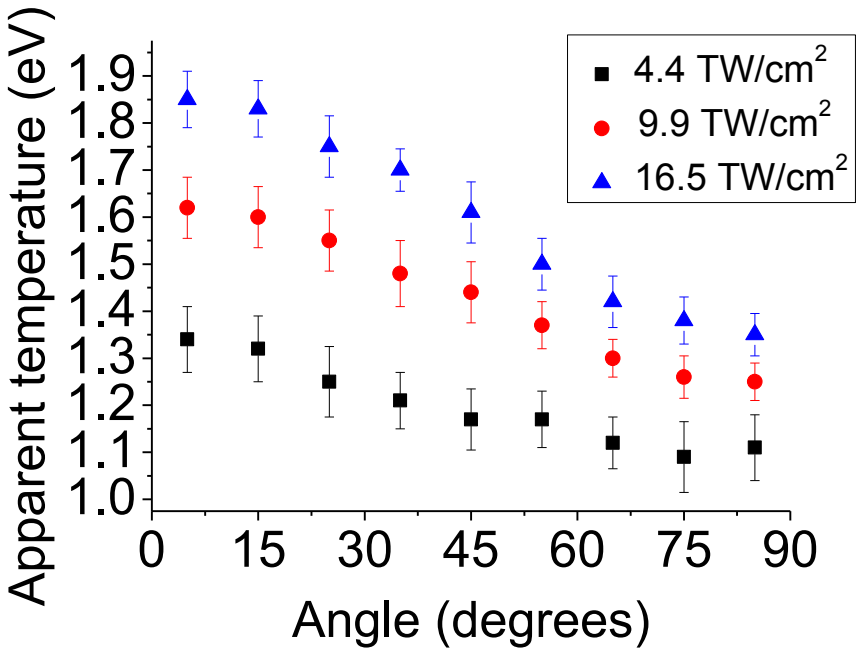

Figure 6.11: Apparent temperature as a function of angle of emission, relative to the laser polarisation, for C_{60} ionised by 550 nm, 92 fs laser pulses of intensities 4.4 TW/cm^2, 9.9 TW/cm^2 and 16.5 TW/cm^2.

400 nm excitation

A series of experiments was carried out, ionising C_{60} with laser pulses of wavelength 400 nm and pulse duration 120 fs over a range of intensities. Inverted VMI images, angle-resolved PES for the 0-10^o and 80-90^o segments and mass spectra for experiments carried out with intensities 1.4 and 4.2 TW/cm^2 are presented in Figure 6.12. Plots of apparent temperature as a function of emission angle, relative to the laser polarisation, are shown for different intensities in Figure 6.13. The first optically allowed transition, from the HOMO to the LUMO+1 can be made by one 400 nm photon. For this reason there is a much higher photoabsorption cross section at 400 nm and the molecule absorbs much more energy. Therefore at similar fluences, we see much higher apparent temperatures for the 80-90^o angles and much heavier fragmentation with 400 nm pulses than at longer wavelengths.

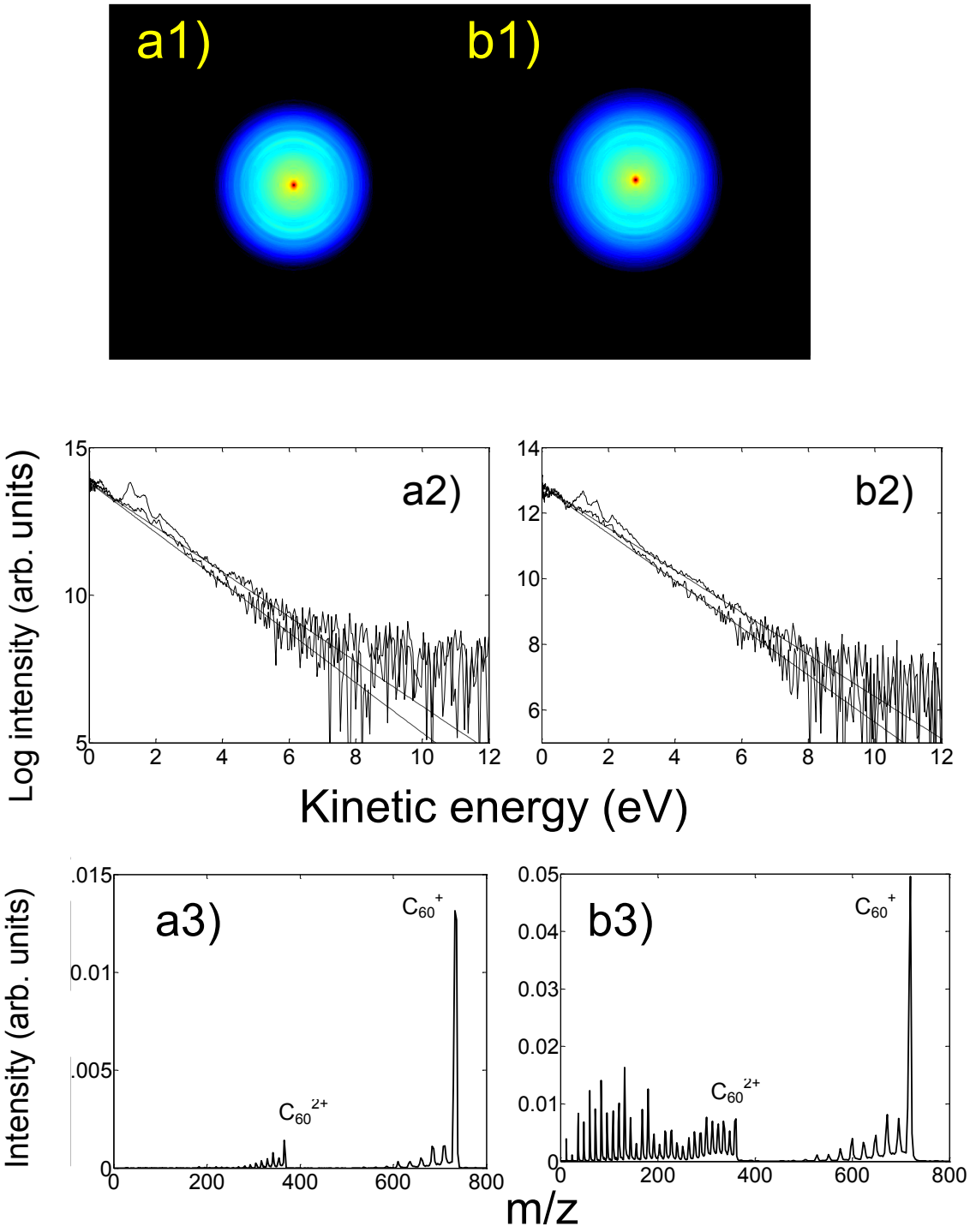

Figure 6.12: 1) Inverted VMI images, 2) angle-resolved PES and 3) mass spectra for C_{60} ionised with 400 nm, 120 fs laser pulses of intensity (fluence) a) 1.4 ± 0.2 TW/cm^2 (0.15 ± 0.02 J/cm^2) b) 4.2 ± 0.7 TW/cm^2 (0.47 ± 0.08 J/cm^2). The apparent temperatures extracted from the 80-90^o and 0-10^o segments, respectively, are a)

1.18 and 1.32 eV (13,690 and 15,310 K) and b) 1.39 and 1.56 eV (16,120 and 18,100 K)

.

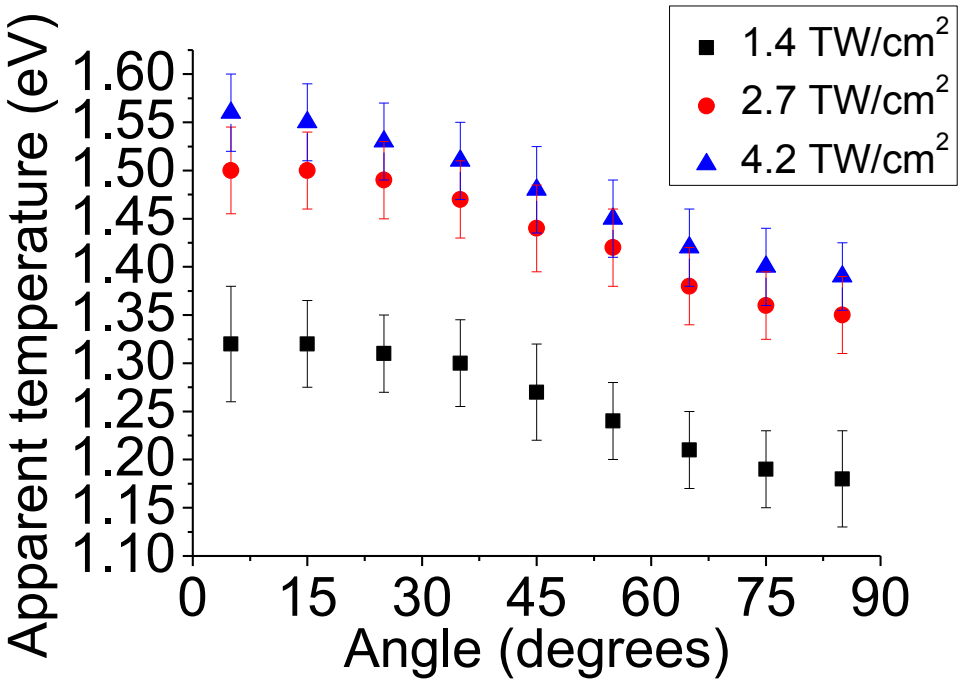

Figure 6.13: Apparent temperature as a function of angle of emission, relative to the laser polarisation, for C_{60} ionised by 400 nm, 120 fs laser pulses of intensities 1.4 TW/cm^2, 2.7 TW/cm^2 and 4.2 TW/cm^2.

6.2.3 Thermal ionisation

One interpretation of the results, based on earlier work [5], presented in section 6.2.2 is that the ionisation mechanism for C_{60}, ionised by laser pulses of duration ranging from 50 fs up to 1 ps, is thermal in nature. However, in this case isotropic photoelectron angular distributions would be expected, similar to those observed for experiments with ns pulses where thermionic emission is known to dominate (Figure 6.14). Here we propose that for fs-ps excitation, anisotropy is introduced via an angle-dependent momentum 'kick' imparted by the laser electric field. Although electron emission is not direct with respect to the ionising laser pulse for thermal emission, calculations predict that a significant proportion of the emitted electrons are emitted during the pulse. This results in higher kinetic energies for electrons emitted along the laser polarisation axis and has a dependency which decreases as the angle of emission is increased towards 90^{o}. For that reason, when discussing the thermal nature of the ionisation, it is the electrons emitted perpendicular to the laser polarisation axis which should be analysed and compared to the thermal ionisation model. In terms of the angle-resolved PES presented in section 6.2.2, these are the electrons emitted between 80 and 90 degrees. Electrons emitted at this angle are negligibly affected by the laser electric field.

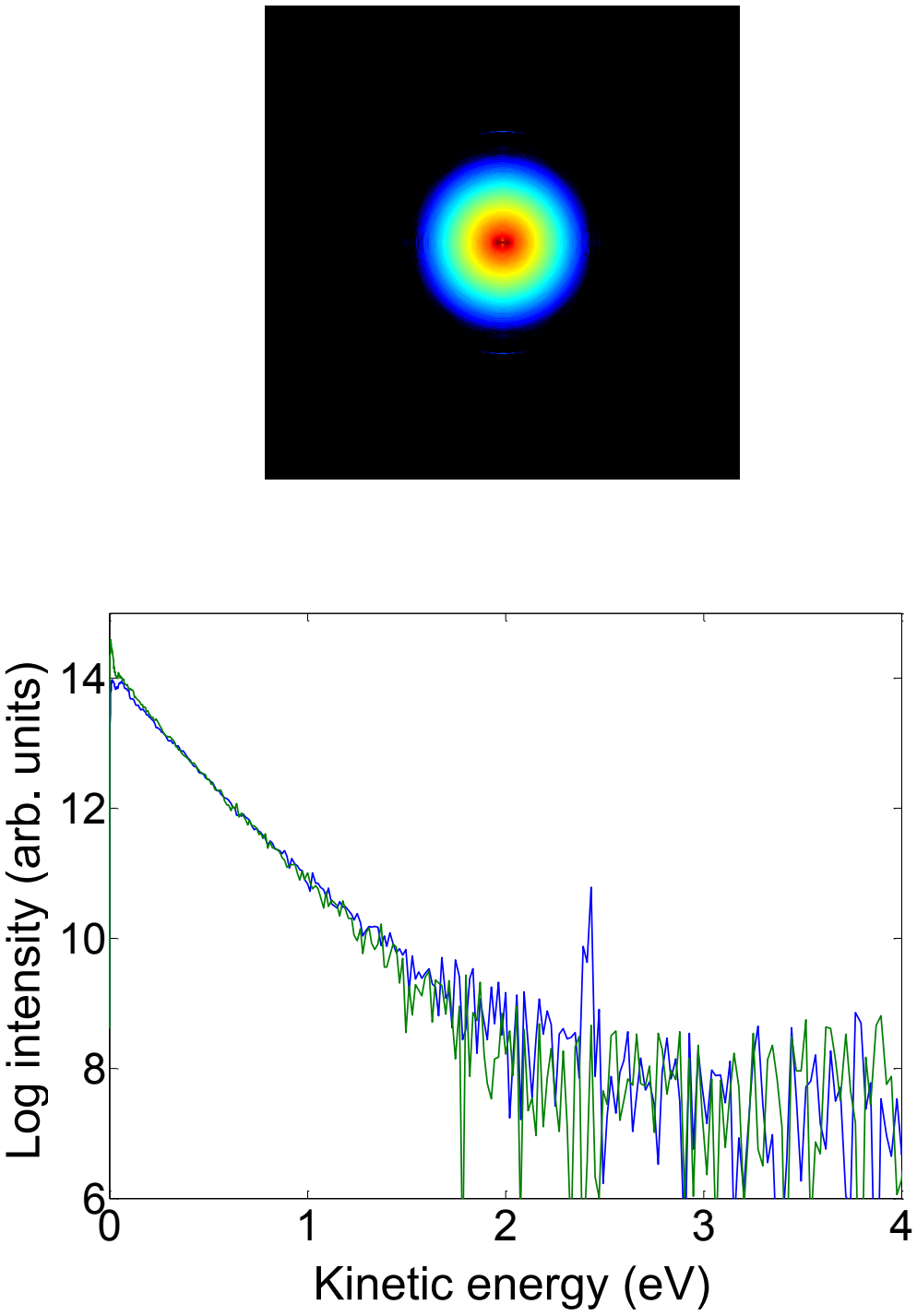

Figure 6.14: Top) inverted VMI image of C_{60} ionised with 532 nm, 5 ns, 7 mJ laser pulses. Bottom) angle-resolved PES, showing 0-10^{o} (blue) and 80-90^{o} segments (green). The VMI image shows an isotropic image and the temperature fitted to each angular segment is 0.31 eV (3,600 K).

To compare the transient thermal ionisation model to the experimental results, the perpendicular apparent temperatures are compared to apparent temperatures obtained using a Monte Carlo simulation, written by Olof Johansson. The simulation models the laser pulse used in the experiment and then calculates the internal energy of the molecule, $E_{int}(t)$, as a function of time. From this a time-dependent thermal electron distribution is calculated and a PES is obtained by plotting the electron yield versus electron kinetic energy

Figure 6.15 shows an example of the calculated electron yield plotted beside the laser pulse, as a function of time, for an 800 nm, 180 fs, 6.7 TW/cm^2 pulse.

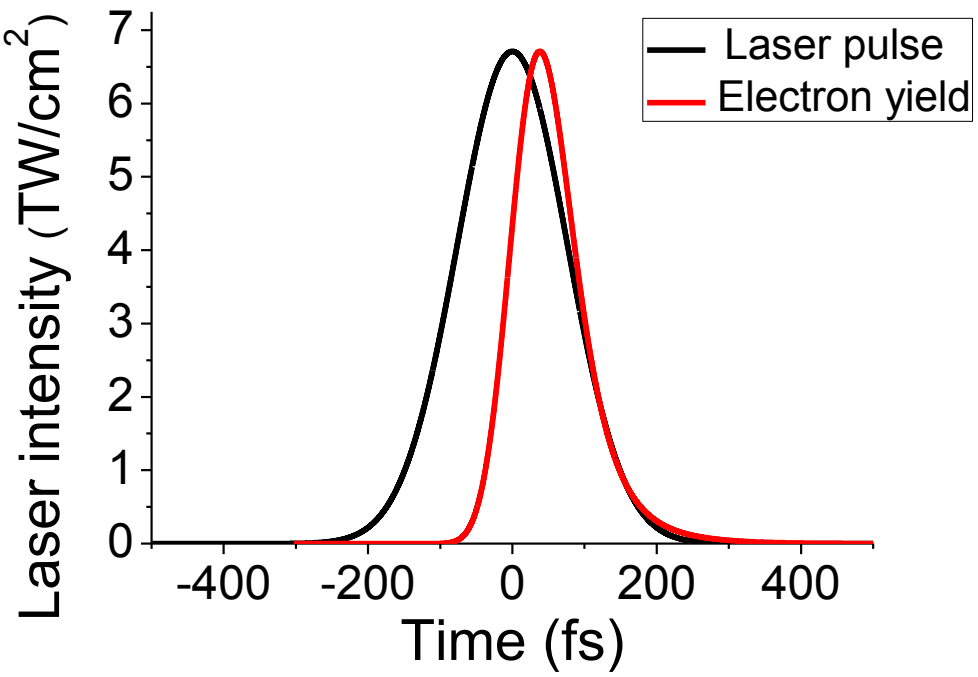

Figure 6.15: Calculated electron yield plotted beside laser pulse intensity envelope as a function of time for 800 nm, 180 fs, 6.71 TW/cm^2 pulse. The yield magnitude has been normalised so that its maximum is the same as the laser pulse. A photoabsorption cross section of 0.12 Å^2 was used.

The Monte Carlo simulation constructs a photoelectron kinetic energy distribution from the distribution of thermally emitted electron energies as a function

of time (equation 6.9), weighted with the calculated electron yield as a function of time (equation 6.8). An apparent temperature can be fitted from a log-lin plot of the electron yield versus the electron energy. Since no direct ionisation is included in the model, temperatures are fitted automatically with a least-squares fitting procedure. The only parameter which is fitted to the experimental data is the apparent averaged photoabsorption cross section. The cross sections used are 0.12 $Å^2$ for 800 nm, 0.165 $Å^2$ for 625 nm, 0.14 $Å^2$ for 550 nm and 0.62 $Å^2$ for 400 nm. The trend in the cross sections, as a function of wavelength corresponds to measurements of the absorbance of C_{60} in solution as a function of wavelength [102]. The temperature obtained is independent of angle of emission. In a purely statistical ionisation process, the angular distribution should be isotropic. Figure 6.16 shows the PES calculated from the laser pulse and yield shown in Figure 6.15.

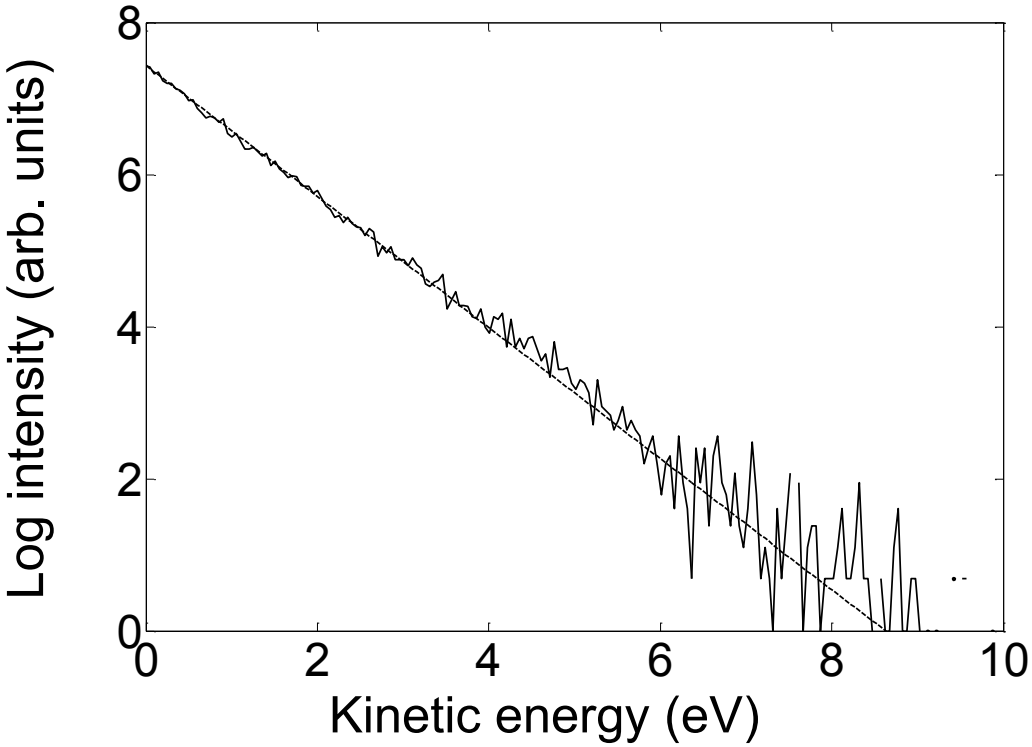

Figure 6.16: Calculated kinetic energy distribution, using the same laser parameters as those described in Figure 615. The apparent temperature fitted to the distribution is equal to 1.17 eV (13,570 K).

Figure 6.17 shows the measured apparent temperature for electrons emitted perpendicular to the laser polarisation as a function of fluence for various series of

measurements. Also shown on the graph are the temperatures obtained using the Monte Carlo calculation.

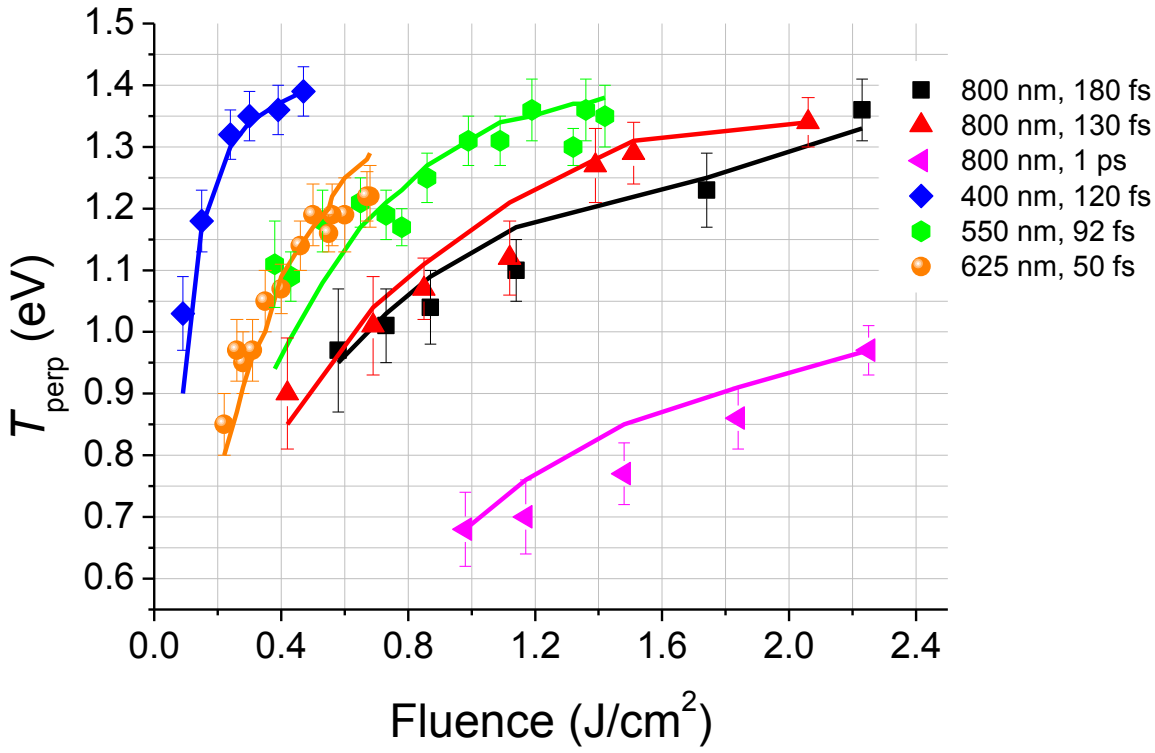

Figure 6.17: Experimental values for apparent temperature, perpendicular to the laser polarisation axis (symbols), and calculated values of apparent temperature using the Monte Carlo simulation (lines).

The calculated temperatures give a very satisfactory fit with the experimental perpendicular temperatures for all wavelengths and pulse durations and so it seems a reasonable conclusion that the underlying ionisation mechanism is thermal in nature.

6.2.4 Electric field-induced anisotropy

Figure 6.18 shows the difference between the apparent temperatures measured parallel and perpendicular to the laser polarisation axis, ΔT, as a function of laser intensity for various wavelengths. A clear trend (seemingly linear) of increasing ΔT with increasing intensity can be observed in each series although it can also be seen

that ΔT seems to be larger for longer wavelengths. Therefore it seems ΔT not only has an intensity dependence but a wavelength dependence.

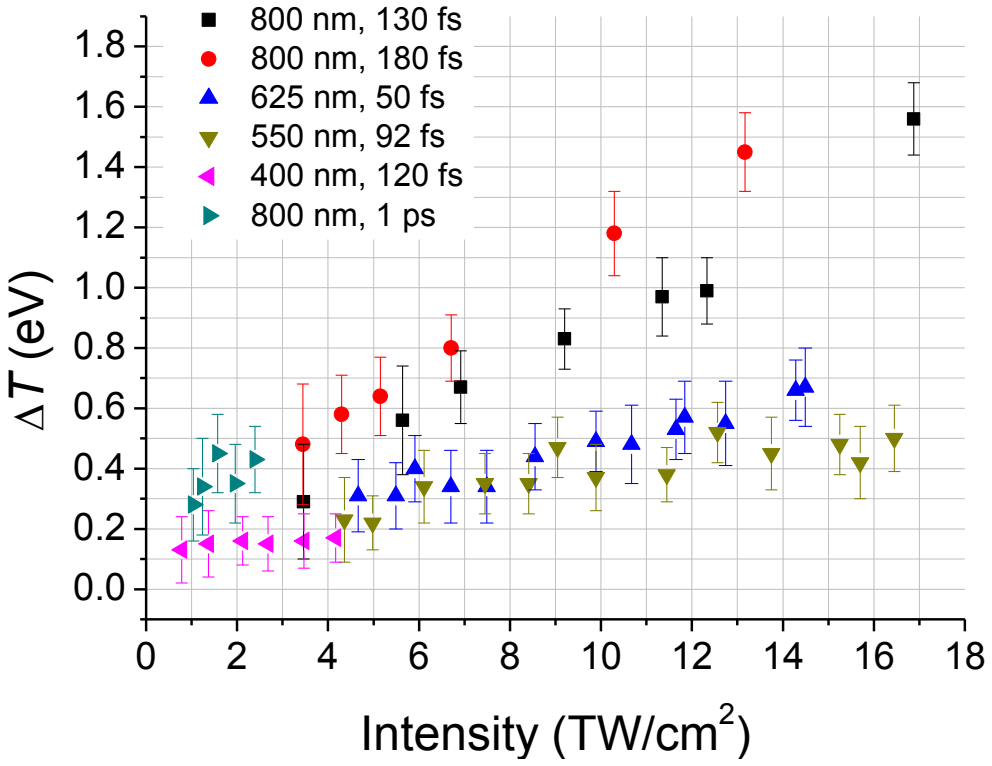

Figure 6.18: The difference between apparent temperatures measured parallel and perpendicular to the laser polarisation direction, ΔT, as a function of laser intensity for various laser wavelengths.

The ponderomotive energy, U_p, is the energy gained by a free electron by oscillating in an electric field [13] and can be expressed as

$$U_p[\mathrm{eV}] = \frac{e_0^{\,2} I}{2 m_e \varepsilon_0 c \omega^2} = 9.34 \times 10^{-20} \times \lambda(\mathrm{nm})^2 \times I, \qquad (6.13)$$

where e_0 is the elementary charge, I is the laser intensity, m_e is the electron mass, ε_0 is the vacuum permittivity, c is the speed of light, ω is the angular frequency of the laser field and λ is the laser wavelength. Figure 6.19 shows ΔT plotted versus U_p for each series of measurements. There is a much closer correlation between each series than when plotted against intensity. This suggests that ΔT and hence the anisotropy

observed in the VMI images and angle-resolved PES is dependent on the ponderomotive energy.

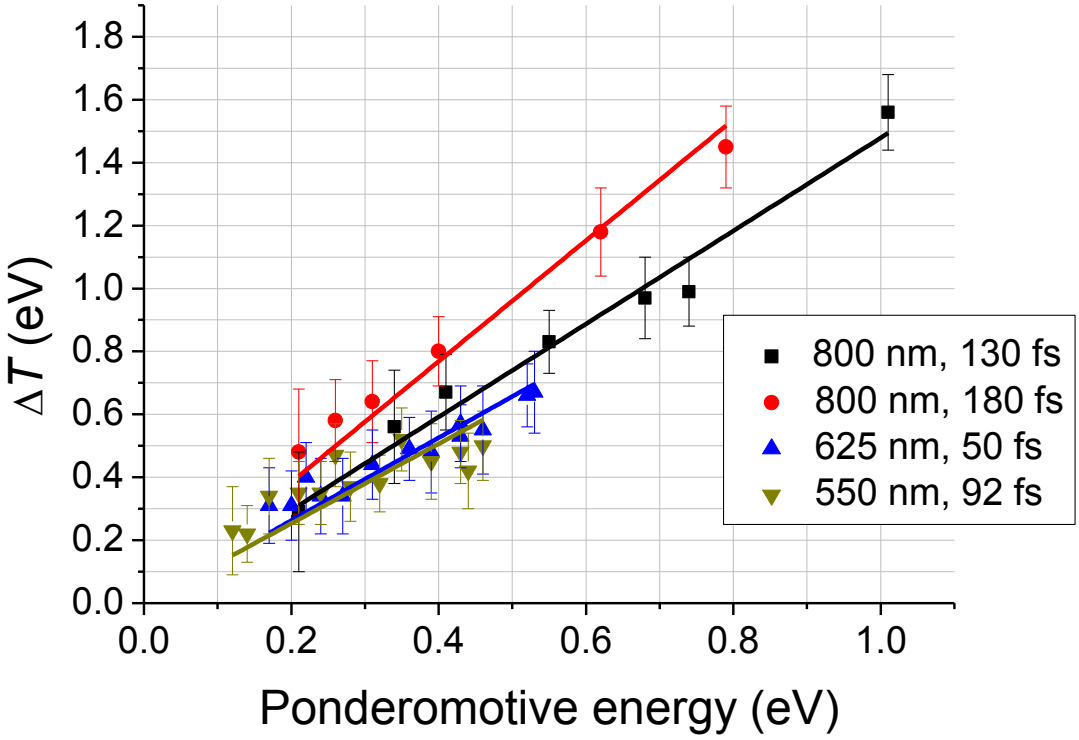

Figure 6.19: The difference between apparent temperatures measured parallel and perpendicular to the laser polarisation direction, ΔT, as a function of the ponderomotive energy for various laser wavelengths. Linear fits have been made to each data series (lines).

Linear fits have been made to each data series in Figure 6.19, with the y-intercept kept at zero. The gradients give an indication of the average measured kinetic energy increase for electrons emitted parallel to the laser polarisation in units of U_p. The fitted gradients are; 800 nm, 180 fs = 1.92 ± 0.05 U_p, 800 nm, 130 fs = 1.44 ± 0.05 U_p, 625 nm, 50 fs = 1.31 ± 0.04 U_p and 550, 92 fs = 1.25 ± 0.08 U_p. All series show an average temperature difference of between U_p and $2U_p$.

The mechanism proposed is one in which the thermal electrons emitted during the laser pulse can gain a momentum kick from the vector potential of the laser electric field. Previous work on field ionisation of Xe [103] has shown that when

photoelectrons are born in the presence of an electric field, they can receive an increase in momentum of

$$-e_0\mathbf{A} = \mathbf{e_z}\frac{E_0}{\omega}\sin(\omega t_0), \tag{6.14}$$

where e_0 is the electron charge, **A** is the vector potential of the electric field, e_z is the unit vector along the polarisation direction, E_0 is the electric field amplitude and ω is the laser angular frequency. The maximum increase in kinetic energy which can be gained in this way is $2U_p$. The maximum momentum kick will occur at the minima of the laser electric field when the vector potential is at a maximum, whilst the vector potential is zero at the maximum of the laser electric field. For direct ionization processes, such as multiphoton ionisation of Xe and the one-photon ionisation of excited-state electrons and their ATI peaks, shown elsewhere in this thesis, the photoelectrons are likely to be born at or very close to the electric field maximum and so will not experience any increase in momentum. As the thermal ionisation is not dependent on the electric field strength, there is no correlation between the time of electron emission and the phase of the electric field, so photoelectrons may experience momentum kicks corresponding to kinetic energy increases of between 0 and $2U_p$.

Monte Carlo calculations were carried out, similar to those described in section 6.2.3, but an additional momentum kick is added, depending on the time of emission with respect to the laser electric field. Kinetic energy distributions are calculated, with the momentum kick incorporated, and apparent temperatures can be obtained. The apparent temperatures obtained with the momentum kick included can be compared to the experimental temperatures measured parallel to the laser polarisation and the temperatures obtained with no momentum kick included can be compared to the experimental temperatures measured perpendicular to the laser polarisation. In this way, the anisotropy, ΔT, can be calculated using the model and compared with experimental anisotropies.

Figure 6.20 shows the experimental temperature differences plotted against the calculated temperature differences for the 800 nm laser pulses at pulse durations 130

fs, 180 fs and 1 ps. The experiments and calculations show a close agreement, with the calculations mirroring the observation that the anisotropy is greater at 180 fs than 130 fs and both series showing a linear-like increase. The relationship between U_p and ΔT is not necessarily a strict linear one as the apparent temperature parallel to the laser pulse not only depends on the magnitude of the momentum kick but how many photoelectrons are born during the laser pulse and at what stage of the pulse the photoelectrons are born. The intensity profile of the pulse changes over time, imparting different momentum kicks to electrons born at different stages and those electrons born after the laser pulse has passed will gain no momentum kick. Figure 6.21 shows the calculated electron distribution over time, with respect to the laser pulse for 800 nm, 130 fs pulses at 3.5 TW/cm^2 and 16.9 TW/cm^2. It can clearly be seen that the two distributions differ significantly in terms of their overlap with the laser pulse.

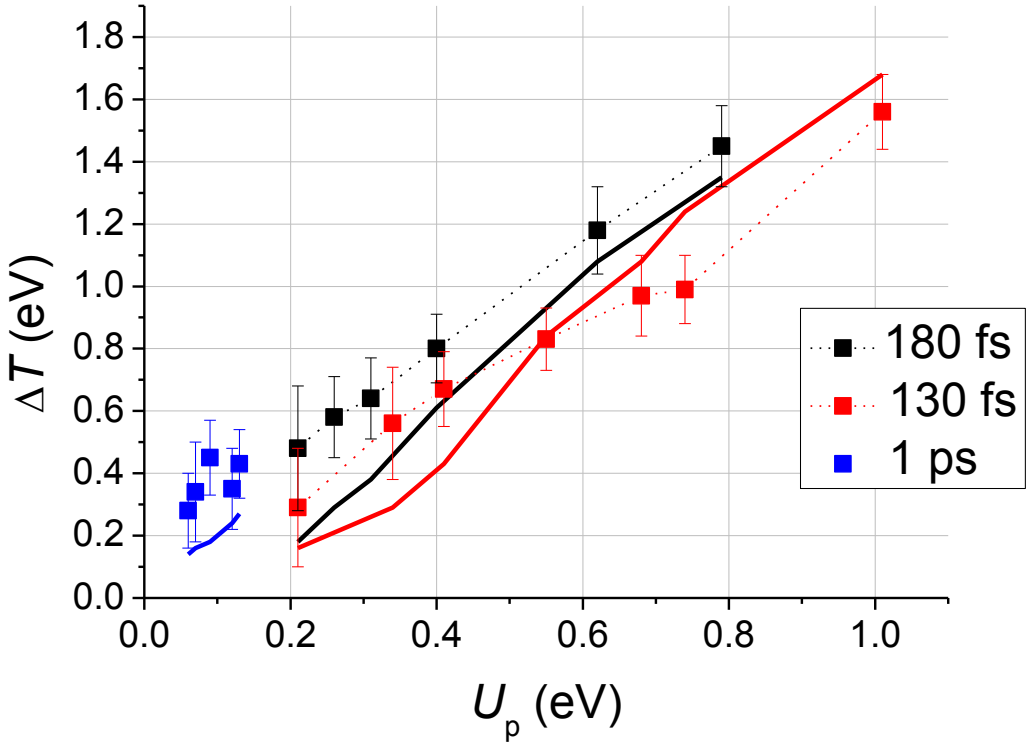

Figure 6.20: Experimental (symbols) and calculated (solid lines) temperature differences, ΔT, for 800 nm pulses of pulse duration 130 fs, 180 fs and 1 ps.

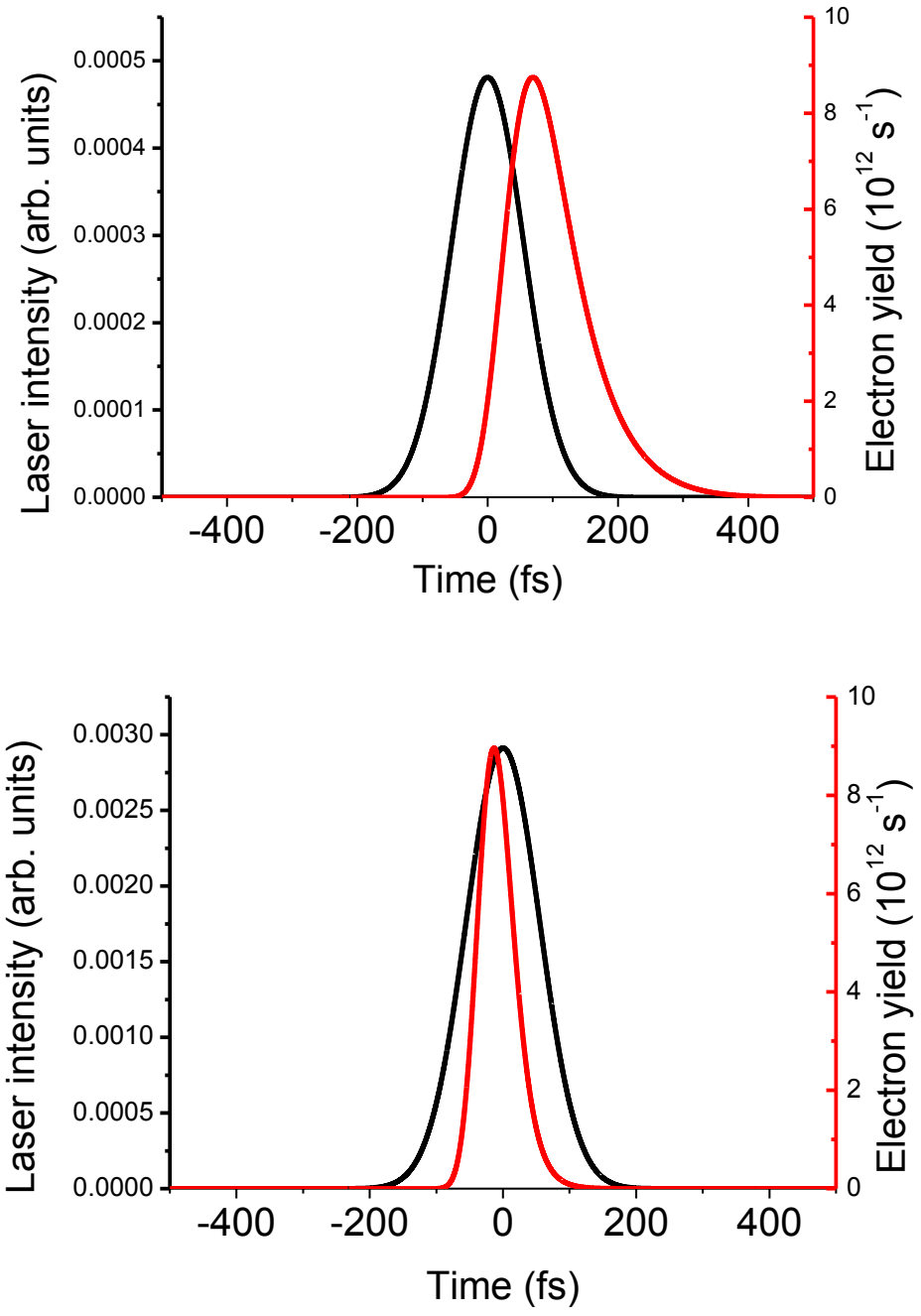

Figure 6.21: Laser intensity vs electron yield plots for 800 nm, 130 fs pulses of intensity top) 3.5 TW/cm^2 and bottom) 16.9 TW/cm^2.

Figure 6.22 shows the experimental temperature differences plotted against the calculated temperature differences for 625 nm, 50 fs pulses, 550 nm, 92 fs pulses and 400 nm, 120 fs pulses of varying intensity. The calculated values for the 550 nm pulses show a good agreement with the experimental values although the anisotropy

increases more sharply with increasing ponderomotive energy than the experimental values. The 625 nm experimental anisotropy values are significantly higher than the calculated values although the trend with increasing ponderomotive energy seems to match well. It may be that with such a short pulse (50 fs) the calculations underestimate how many photoelectrons are emitted during the pulse. For such a short pulse even a small misjudgement in the electron yield distribution over time will likely result in a large discrepancy with experimental values. The calculated values for the 400 nm pulses are slightly lower than the experimental values although, in absolute terms, the difference is very small.

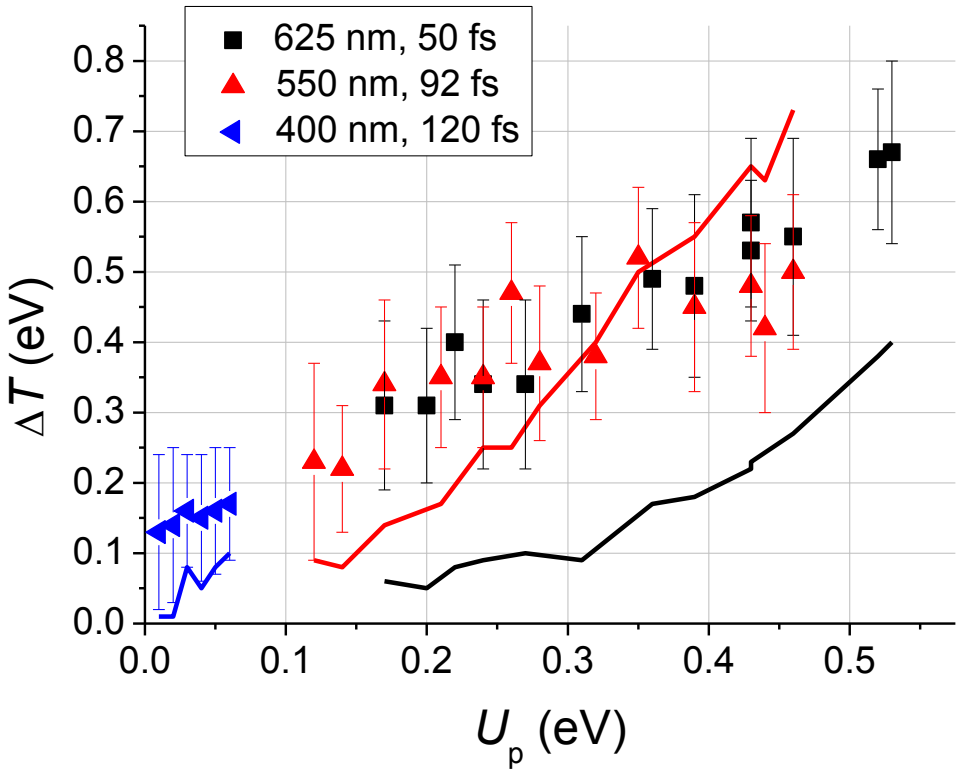

Figure 6.22: Experimental (symbols) and calculated (lines) temperature differences, ΔT, for 625 nm, 50 fs pulses, 550 nm, 92 fs pulses and 400 nm, 120 fs pulses.

Linear fits were made to the calculated ΔT data series to compare to the gradients obtained for the experimental data. All gradients are summarised in Table 6.1.

Table 6.1: Fitted gradients for experimental and calculated temperature anisotropies.

Laser pulse	Experimental Gradient	Calculated Gradient
800 nm, 180 fs	$1.92 \pm 0.05\ U_p$	$1.61 \pm 0.1\ U_p$
800 nm, 130 fs	$1.44 \pm 0.05\ U_p$	$1.55 \pm 0.1\ U_p$
625 nm, 50 fs	$1.31 \pm 0.04\ U_p$	$0.55 \pm 0.04\ U_p$
550 nm, 92 fs	$1.25 \pm 0.08\ U_p$	$1.33 \pm 0.07\ U_p$
400 nm, 120 fs	$3.64 \pm 0.64\ U_p$	$1.62 \pm 0.2\ U_p$
800 nm, 1 ps	$3.74 \pm 0.43\ U_p$	$2.08 \pm 0.06\ U_p$

Overall, the gradients for the experimental data and the calculated values are in good agreement, showing ΔT values of between U_p and $2U_p$. The exceptions are the experimental 400 nm and 800 nm, 1 ps data and the calculated 625 nm data. This may be explained, in the 400 and 800 nm cases, by the difficulty in fitting accurate temperatures, by eye, when there is such a small temperature difference and being even 0.1 eV out will result in a dramatic, relative, over-estimation of ΔT. The model for calculating the momentum kick is relatively simple and does not take into account the focal volume of the laser pulse, therefore it may be that for pulses as short as 50 fs, a small error in the calculation of the time-dependent electron yield will result in a large error in the calculated apparent temperature, in the case of the 625 nm data.

6.2.5 Electric field-induced barrier suppression

As can be seen in the angle resolved PES in section 6.2.2, not only is the apparent temperature higher along the laser polarisation direction but more electrons are emitted parallel to the laser polarisation than perpendicular to it. The area under the distributions at 0-10 degrees is significantly larger than that for 80-90 degrees. Figure 6.23 shows the fitted kinetic energy distributions for the $0\text{-}10^o$ and $80\text{-}90^o$ segments for C_{60} ionised with laser pulses of wavelength 800 nm and 550 nm and similar intensity.

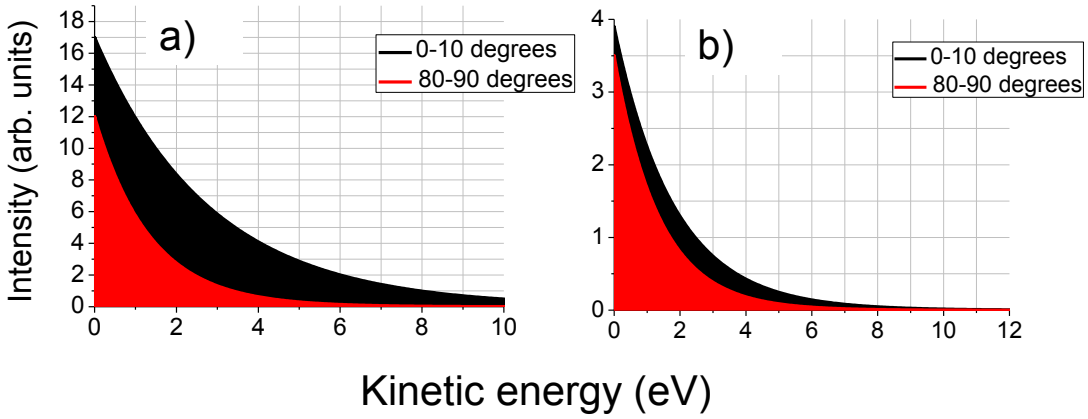

Figure 6.23: Fitted kinetic energy distributions for the 0-10 and 80-90 degree angular segments for C_{60} ionised with laser pulses a) 800 nm, 180 fs, 13.2 TW/cm^2 and b) 550 nm, 92 fs, 13.8 TW/cm^2. The area underneath the distribution is related to the number of electrons emitted. The ratio between the number of electrons emitted at 0-10^o and 80-90^o is significantly higher for the 800nm pulses.

Figure 6.24 shows the ratio between the number of counts over the angles 0-10 degrees and the number of counts over the angles 80-90 degrees, plotted against intensity for various wavelengths. The number of counts at each angular segment was determined by calculating the area under the fitted exponential distributions. For the 800 nm measurements, there is a clear intensity dependence with the count ratio increasing at higher intensities. For the shorter wavelengths, the plots show flat lines and much lower ratios.

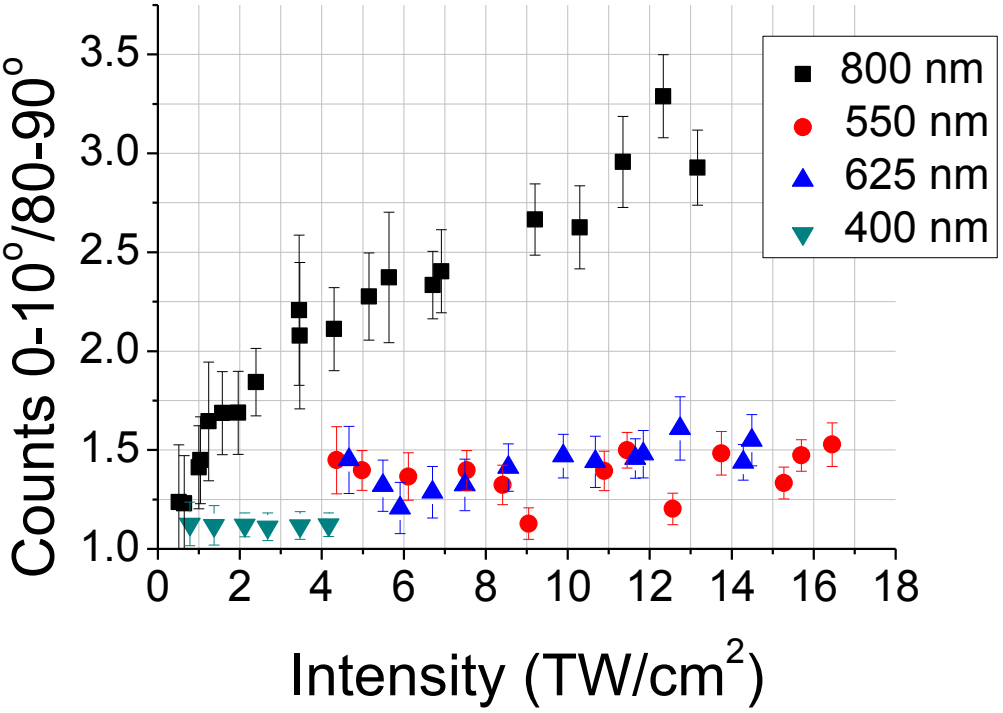

Figure 6.24: The ratios between the number of counts at 0-10° and the number of counts at 80-90° angular segments, as a function of laser intensity for various wavelengths.

The increased number of counts parallel to the laser polarisation axis and the resulting intensity dependence at 800 nm is interpreted as a suppression of the confining ionisation barrier by the electric field. Similar to the field ionisation described in chapter 2, the ionisation potential will oscillate in time with the electric field and suppression of the barrier will be directional, with the greatest suppression parallel to the polarisation axis. The oscillation of the ionisation potential in the electric field can be described by

$$\Phi(t) = \Phi_0 + e_0 E_0 R \sin(\omega t)\cos(\theta), \qquad (6.15)$$

where Φ_0 is the ionisation potential under field-free conditions, e_0 is the electron charge, E_0 is the electric field strength, R is the Debye length and taken to be half the length of the C_{60} potential well, ω is the laser angular frequency and θ is the angle of emission.

Since a molecule which has undergone statistical energy equilibration will have a distribution of highly excited electrons, the ionization potential does not need to be lowered as much as would be the case under 'normal' field ionisation conditions. Even at the highest experimental intensities used, the Keldysh parameter is much higher than 1, according to the expression

$$\gamma = \sqrt{\frac{\Phi}{2Up}}, \tag{6.16}$$

indicating that we are well below the intensity threshold to observe field ionisation. However, if electrons were excited enough so that their binding energy was greatly reduced, the ionisation potential would effectively decrease, allowing field ionisation to take place. Field ionisation is also dependent on wavelength in that the electrons need time to tunnel through the suppressed barrier. If the frequency of the electric field is too high, they may not be able to escape before the field changes sign and the barrier is at a maximum again. This may explain why this effect is seen with 800 nm measurements and is not so apparent for shorter wavelengths.

When the ionisation potential varies with the electric field according to equation 6.15, the rate constant (equation 6.5) becomes dependent on the emission time which can be averaged over the period of the laser pulse, T_p [104]. Averaging the Weisskopf expression over one laser period gives the expression.

$$k(\varepsilon) = \frac{1}{T_p}\int_0^T k(\varepsilon,t)dt \frac{1}{T_p}\int_0^T \exp(e_0 E_0 R \sin(\omega t)\cos(\theta)/T_a)dt \tag{6.17}$$

where T_a is the emission temperature of the photoelectron. The last integral can be expressed as,

$$I_0\left(\frac{e_0 E_0 R\cos(\theta)}{T_a}\right) \tag{6.18}$$

where I_0 is the modified Bessel function of the first kind. Therefore the number of electrons emitted at angle θ is proportional to the function in equation 6.18. From this, the count ratio between electrons emitted at 0^o and 90^o can be calculated as a function of intensity. To calculate the average electric field strength of the laser pulse, the average intensity of the laser pulse is used, which is equal to the peak intensity, multiplied by a factor of 0.53. Figure 6.25 shows the calculated count ratios alongside the experimental count ratios for 800 nm laser pulses.

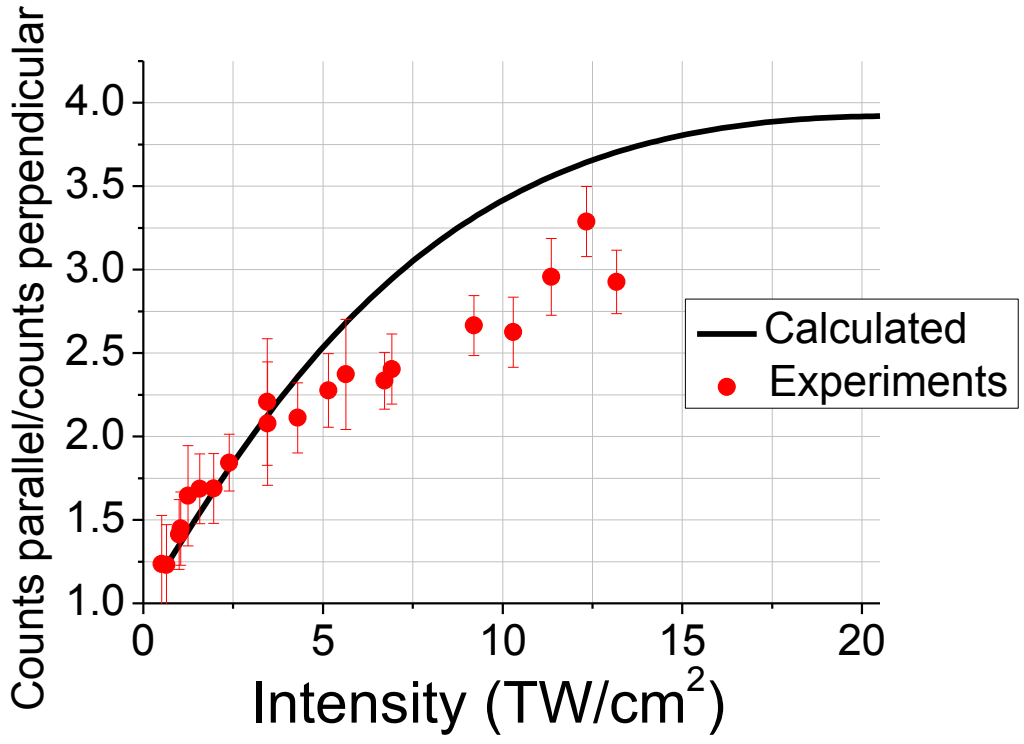

Figure 6.25: The calculated ratio of the number of electrons emitted parallel to laser polarisation over the number of electrons emitted perpendicular, as a function of intensity, according to the Bessel function, $I_0(qE_0r_0\cos(\theta)/T_a)$, alongside the experimental count ratios for 800 nm laser pulses.

The calculations match the experimental count ratios reasonably well. The lowest intensities in Figure 6.25 correspond to the ps pulses which match the calculated function very well. The count ratios for the higher intensity pulses are slightly lower than the calculated values although seem follow the shape of the curve reasonably well. These intensities correspond to shorter pulses of 130 and 180 fs and

it may be that the electrons are emitted in the latter part of the laser pulse where the intensity is lower than average, which would explain why the experimental count ratios are lower than the calculated values.

Experimental count ratios, as a function of angle for 180 fs, 13.2 TW/cm^2 pulses and 1 ps, 2.4 TW/cm^2 pulses are shown in Figure 6.26, alongside the calculated count ratios.

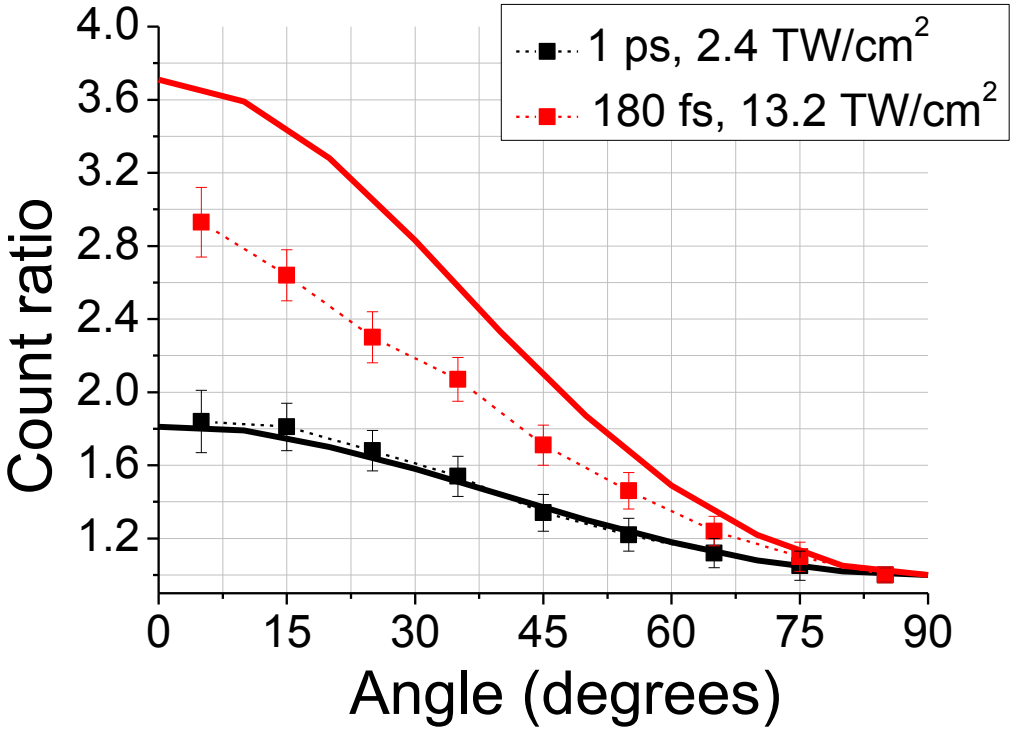

Figure 6.26: Experimental count ratios (squares and dotted lines) as a function of angle for 800 nm pulses with pulse duration and intensity of red) 180 fs, 13.2 TW/cm^2 and black) 1 ps, 2.4 TW/cm^2. 180 fs with corresponding calculated values (sold lines).

6.2.6 Ponderomotive streaking

If the anisotropy in the photoelectron apparent temperatures is caused by the electric field of the laser pulse used to ionise the molecule, it should be possible to induce anisotropy in an otherwise isotropic distribution with a second, non-ionising

laser pulse. Pump-probe experiments were carried out with 140 fs, 400 nm pump pulses and 900 nm probe pulses, estimated to have a pulse duration of around 60 fs. 400 nm pulses cause only a very slight anisotropy, due to the relatively small ponderomotive energy at this wavelength, and the polarisation was rotated to horizontal so that the polarisation direction was facing the detector, which should ensure an isotropic electron distribution at the detector. The C_{60} molecule is ionised by the 400 nm pulse but with no significant anisotropy in the apparent temperatures. The 900 nm probe pulse is not strong enough to ionise the molecule on its own but relatively high intensities can be used, meaning a large ponderomotive energy as the photon absorption cross section is very small at 900 nm. Therefore, photoelectrons born during or after the 400 nm pulse should receive a momentum kick from the vertically polarised 900 nm pulse when the pulse overlaps with the electron distribution in time. A similar technique has been used previously to measure laser pulse durations and was termed 'ponderomotive streaking' [105].

The temporal overlap between the pulses is found by recording the C_{60} ion yield as a function of the delay between the pulses. When the two pulses are overlapped, a maximum in the ion yield signal should appear and delay time 'zero' can be defined. Although the 900 nm pulse is too weak to ionise C_{60} on its own, it can produce enhanced ionisation from molecules pre-excited by the 400 nm pulse. VMI images were recorded over a range of delays and the temperature difference between the photoelectrons emitted parallel to the 900 nm polarisation direction and perpendicular to it were obtained. It was found that there was a very small degree of anisotropy even when the 900 nm beam was blocked, possibly due to the 400 nm beam not being completely horizontally polarised.

Figure 6.27 shows the ion yield signal as a function of delay as well as the measured anisotropy in the VMI images as a function of delay for pump pulses of intensity 3 TW/cm^2. Figure 6.28 shows the same graph but for 2 TW/cm^2 pump pulses. Gaussian peaks are fitted to the ion yield data and exponentially modified Gaussian functions are fitted to the anisotropy data. A clear increase in anisotropy is measured when the 900 nm pulse overlaps with the 400 nm pulse and at positive time delays, when the 900 nm pulse follows the 400 nm pulse. This suggests the peak of electron emission occurs during the 400 pulse and continues, decreasing, afterwards.

The exponential decays fitted to the two functions are 144 ± 77 fs at 3 TW/cm^2 and 333 ± 137 fs at 2 TW/cm^2.

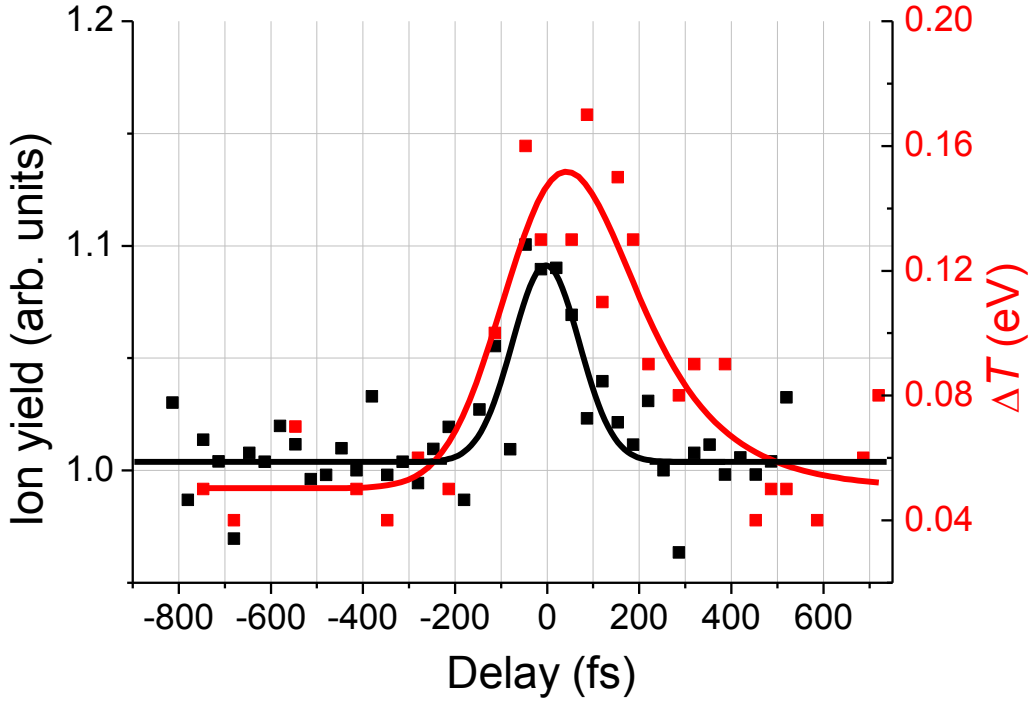

Figure 6.27: Ion yields and ΔT values as a function of time delay in a 'ponderomotive streaking' pump-probe experiment with 140 fs, 3 TW/cm^2, 400 nm pump pulses and 60 fs, 5 TW/cm^2, 900 nm probe pulses.

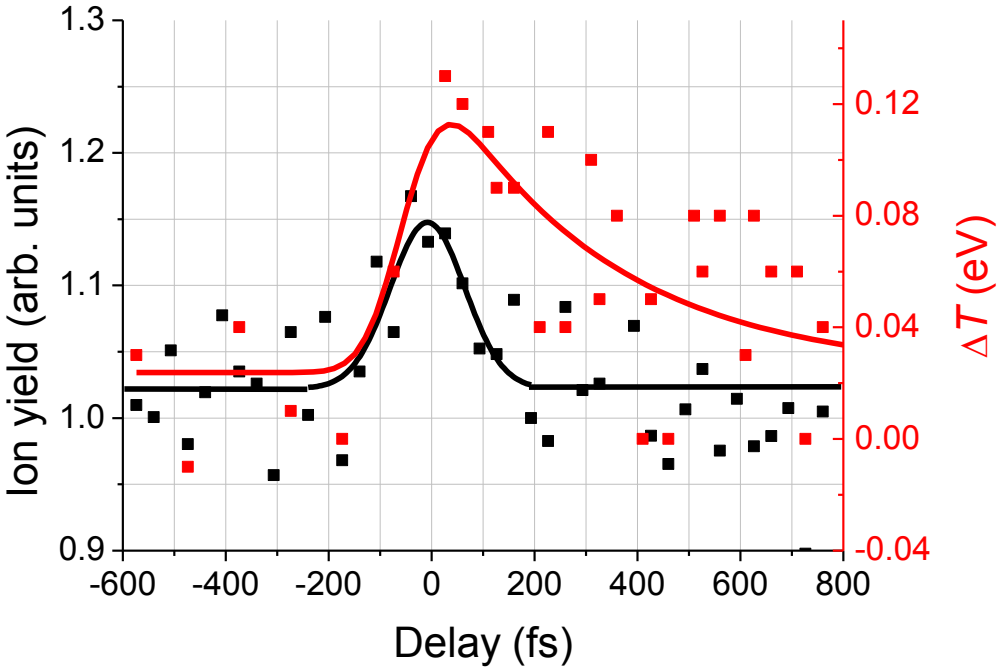

Figure 6.28: Ion yields and ΔT values as a function of time delay in a 'ponderomotive streaking' pump-probe experiment with 140 fs, 2 TW/cm^2, 400 nm pump pulses and 60 fs, 5 TW/cm^2, 900 nm probe pulses.

Figure 6.29 shows the electron yield as a function of time, with respect to the laser pulse for 400 nm, 140 fs pulses of 3 and 2 TW/cm^2, as predicted by the thermal ionisation model. It is clear that the calculated electron yields do not extend to times as long as those suggested from the streaking experiments. Similar exponentially modified Gaussian functions fitted to the calculated yields produce decay constants of 39 fs and 52 fs for the 3 and 2 TW/cm^2 pulses, respectively.

These results clearly demonstrate the effect of the laser electric field on the emitted electron distribution and its ability to cause anisotropy in the kinetic energy distribution. The delayed nature of the thermal emission is also demonstrated. This provides strong evidence that the underlying ionisation mechanism is thermal and statistical and that the anisotropy observed in the photoelectron kinetic energy distribution is due to the effect of the laser electric field.

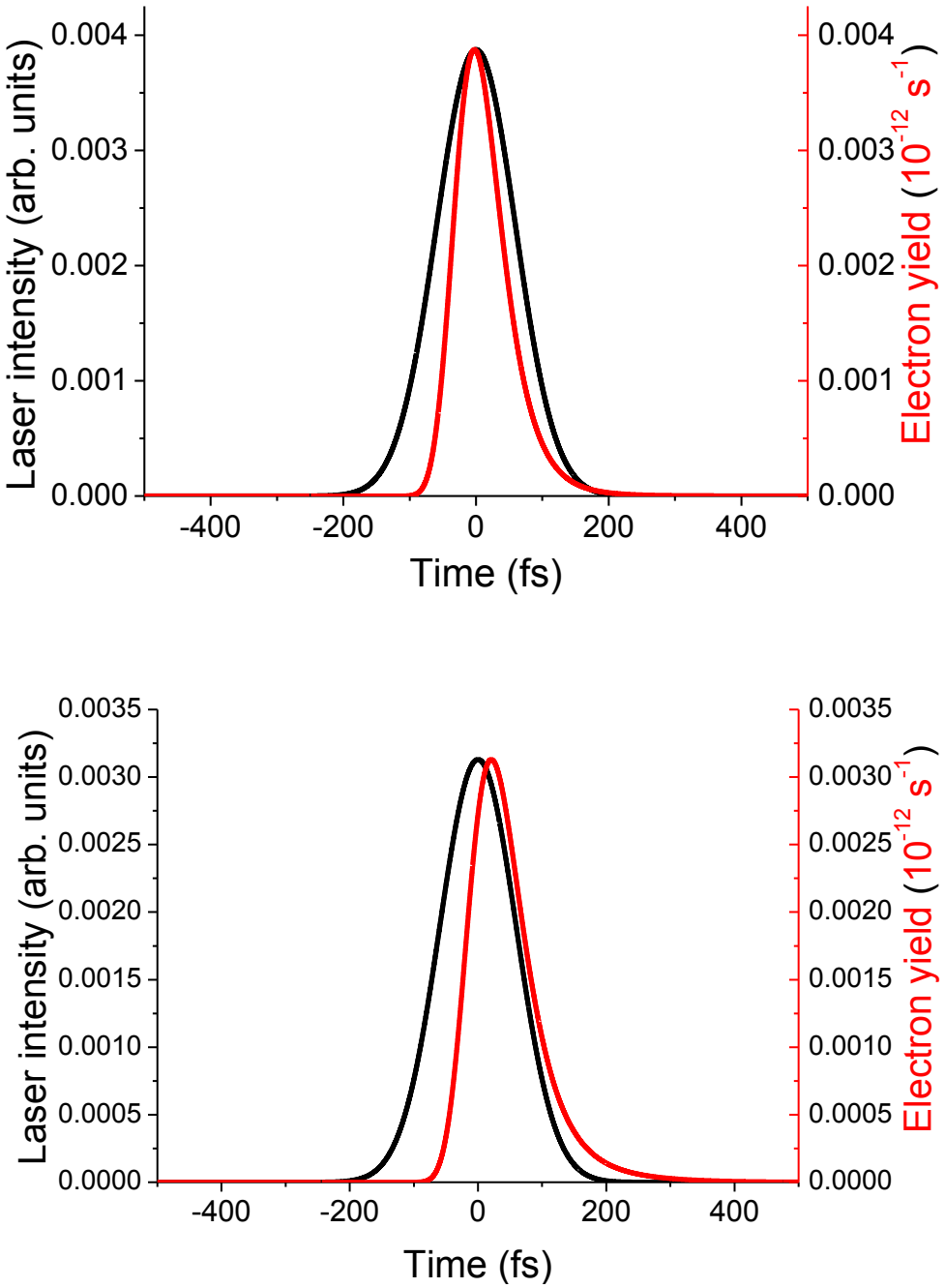

Figure 6.29: Calculated electron yield plotted beside laser pulse intensity envelope as a function of time for 400 nm, 140 fs pulses of intensity top) 3 TW/cm^2 and bottom) 2 TW/cm^2.

6.2.7 C_{70} ionisation

VMI measurements were carried out, ionising C_{70} (Φ = 7.3 eV) with 800 nm laser pulses at pulse durations 120 fs and 180 fs at varying intensities. The spectra obtained appear similar to those obtained with C_{60}, with peaks superimposed on a thermal background. This section will provide a brief summary of the C_{70} results, compared to the C_{60} results also obtained at 800 nm. Figure 6.30 shows a plot of laser fluence versus the apparent temperature measured perpendicular to the laser polarisation direction. The C_{70} results show a fairly similar pattern to the C_{60} results.

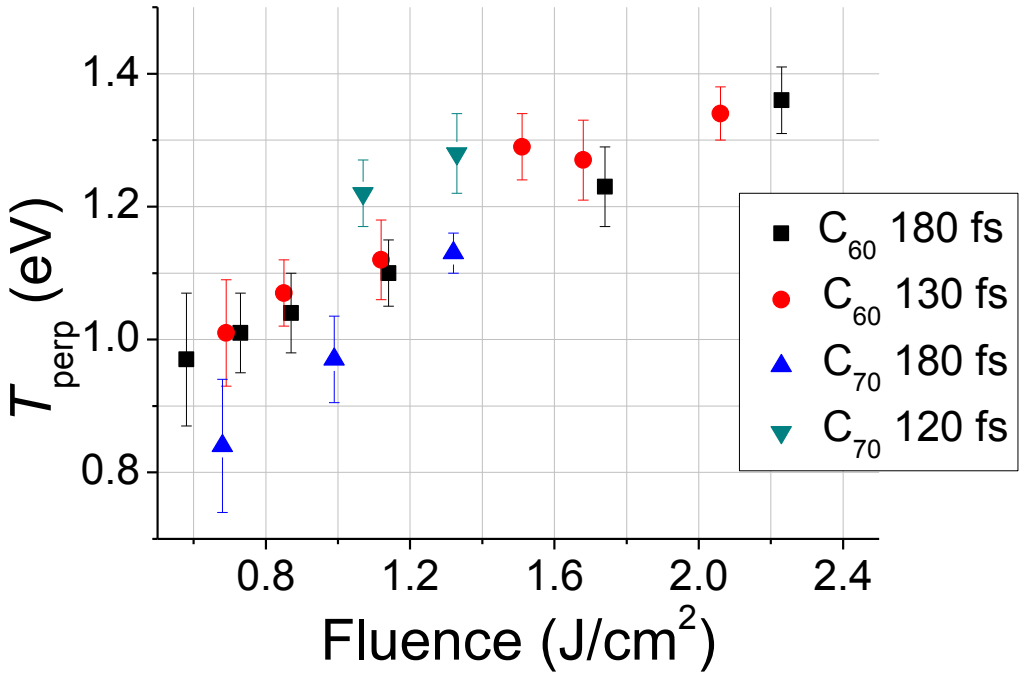

Figure 6.30: Experimental values for apparent temperature, perpendicular to the laser polarisation axis versus fluence for C_{70} and C_{60} ionised with 800 nm pulses.

Figure 6.31 shows the measured apparent temperature difference, ΔT, between electrons emitted perpendicular to and parallel to the laser polarisation axis for C_{70} and C_{60} ionised with 800 nm laser pulses. Again, very similar results are observed. The gradients obtained for C_{70} are; for 180 fs = 1.73 ± 0.19 U_p, and for 120 fs =

1.41 ± 0.14 U_p. These compare to C_{60} gradients for 180 fs = 1.92 ± 0.05 U_p and for 130 fs = 1.44 ± 0.05 U_p.

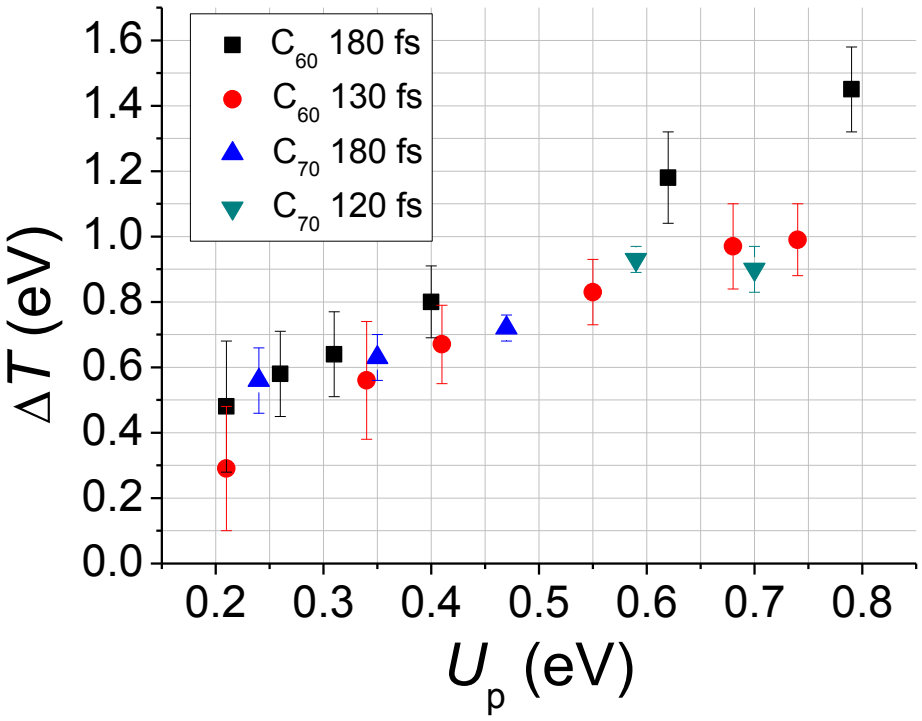

Figure 6.31: The difference between apparent temperatures measured parallel and perpendicular to the laser polarisation direction, ΔT, as a function of the ponderomotive energy for C_{60} and C_{70} at 800 nm.

Figure 6.32 shows the count ratio between the number of electrons emitted parallel to and perpendicular to the laser polarisation direction for C_{70} and C_{60} at 800 nm. Like the C_{60} data, the C_{70} count ratio shows a steady increase with intensity although the overall count ratios are slightly smaller than those obtained for C_{60}.

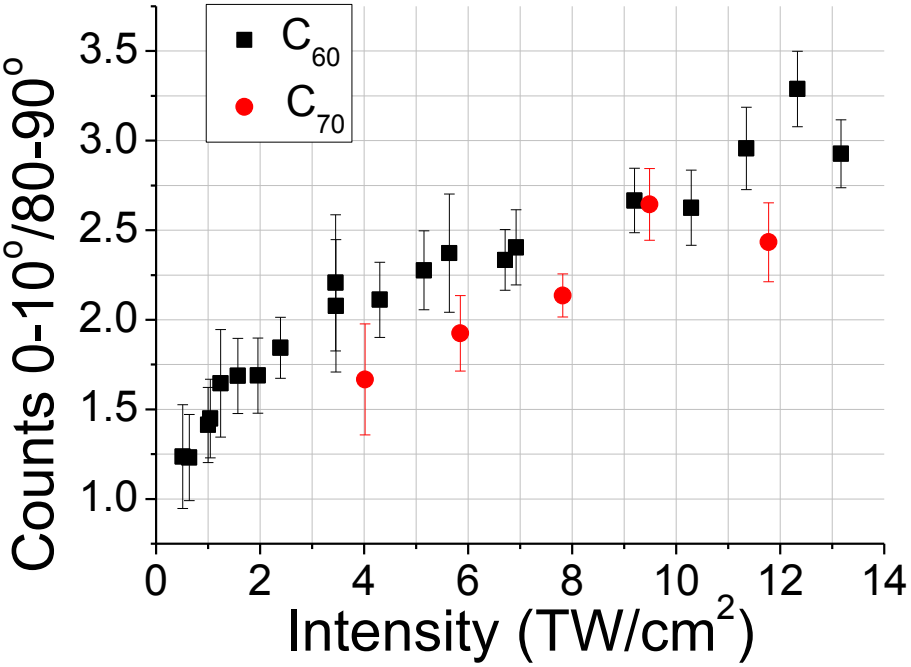

Figure 6.32: The ratios between the number of counts at 0-10° and the number of counts at 80-90° angular segments, as a function of laser intensity for C_{60} and C_{70} at 800 nm.

6.3 Conclusion

Results concerning thermal electron emission in strong laser fields for the fullerenes C_{60} and C_{70} have been presented. All results presented are consistent with the hypothesis that, for laser pulses of duration between 50 fs up to a few hundred fs, the absorbed energy is, to a large extent, equilibrated amongst the electronic subsystem and that thermal emission occurs before the vibrations can be significantly excited. Anisotropy in the photoelectron angular distribution is accounted for by electrons emitted parallel to the laser polarisation acquiring a momentum kick from the laser field which results in higher, measured, apparent temperatures. The temperature difference is therefore dependent on the laser ponderomotive energy.

Apparent temperatures measured perpendicular to the laser polarisation for a variety of wavelengths, pulse durations and intensities were compared to results from a thermal electron emission model and the results proved to be in close agreement. The effect of the laser field-induced momentum kick on apparent temperatures was modelled with a Monte Carlo simulation and, generally, the results were in very close agreement. The results suggest that electron emission is delayed with respect to the laser pulse but that a significant number of electrons are typically emitted during the pulse. The observation that more electrons are emitted parallel to the laser polarisation direction is explained by field-induced barrier-suppression. Experimental results were compared to calculations and the trend of increasing count ratios with increasing laser intensity was successfully reproduced. The results from ponderomotive streaking experiments suggest that anisotropy can be introduced with a second, 'probe' pulse and that a significant number of electrons are emitted during the 'pump' pulse, supporting the conclusion that the temperature anisotropy is due to an electric-field induced momentum kick.

The results presented in this thesis re-affirm the thermal model for C_{60} ionisation with laser pulses of intermediate duration after the initial use of VMI introduced some doubt surrounding the anisotropy of the photoelectron images produced. The model presented here, including the laser-induced momentum kick, is likely to apply to all large molecules and clusters and constitutes a step forward in the

ability to understand and interpret the ionisation dynamics of these molecules. The ionisation mechanisms at shorter time scales is still unknown and future studies might use similar techniques with shorter laser pulses to attempt to describe to what extent the thermal model holds and how important direct mechanisms become with decreasing pulse duration. In light of the results presented in this thesis, some of the previous work concerning field ionisation in large molecules may be re-interpreted as simply the thermal ionisation mechanism coming into effect although it has been shown in this thesis that field ionisation does become important in the ionisation of C_{60}. The excitation energy stored in the electronic system can produce field ionisation at lower laser intensities than would be expected by simply calculating the Keldysh parameter This has implications for previous work which hypothesises that molecular structure has a direct influence on the Keldysh parameter and therefore the likelihood of field ionisation occurring.

Chapter 7 – Superatom molecular orbitals of fullerenes

In this chapter, the peaks which appear in photoelectron spectra of fullerenes ionised by laser pulses of duration from less than 100 fs, up to a few ps, will be discussed. Similar peaks have been seen in previous ultrashort pulse PES of fullerenes and were assigned as Rydberg peaks [8]. The discovery of superatom molecular orbitals (SAMOs) in STM studies of C_{60} on a solid surface [7] raises the possibility that these peaks may arise from population of and ionisation from SAMOs. A brief introduction to the previous work on Rydberg peaks and SAMOs will be presented. Experimental results obtained by ionising C_{60} and C_{70} with laser pulses of varying wavelength, collected together with Olof Johansson, will be presented along with an analysis of the photoelectron angular distributions (PADs) of the peaks in the spectra, which will provide insight as to what states are responsible for these peaks and how they are ionised.

7.1 Introduction

7.1.1 Excited states in fullerenes

When fullerenes are ionised by laser pulses of duration from below 100 fs to a few ps, the photoelectron spectra can be described as a series of peaks at kinetic energies below the photon energy, superimposed on the exponential, thermal background, discussed in the previous chapter. At high intensities, ATI peaks appear in the spectra and at longer pulse durations, on the ns timescale, these peaks disappear as the thermal distribution develops towards thermionic emission. These peaks were identified as being due to single photon ionisation from highly excited Rydberg states by Boyle *et al*. [8]. The peak structure was seen to be reproducible over a range of wavelengths [45], with peaks corresponding to the same binding energies appearing in spectra taken with pulses of different wavelengths and pulse duration. It is thought

that the excited states responsible for these peaks are populated in the early stages of the laser pulse and one-photon ionised in the latter stages. The technique of Rydberg fingerprint spectroscopy [52] has recently shown that such peak structure can be used as a structure-sensitive spectral fingerprint for aromatic molecules.

Experimental and theoretical results were published concerning the discovery of SAMOs in C_{60} molecules adsorbed on copper surfaces using scanning tunnelling microscopy [7]. These are large, diffuse orbitals which appear like those found in atoms, with significant electron density inside the fullerene cage. They are thought to be a property of hollow-shell molecules. From the density of states calculations carried out by the same group, the binding energies of the SAMOs identified correspond to the binding energies of some of the peaks previously assigned as Rydberg peaks. The s SAMO is predicted to have a binding energy of around 2 eV. The p SAMO is predicted to have a binding energy of around 1.5 eV and the s' and d SAMOs, which are very close in energy are predicted to have a binding energy of around 1 eV.

7.1.2 Photoelectron angular distributions

The photoelectron angular distribution for electrons of a specific kinetic energy resulting from single-photon ionisation of a randomly orientated sample can be described as

$$I(\theta) = \frac{\sigma}{4\pi}(1 + \beta_2 P_2(\cos\theta)), \tag{7.1}$$

where σ is the angle-integrated photoionisation cross section, β_2 is the anisotropy parameter and P_2 is the second order Legendre polynomial [106]. The intensity cannot be negative and so this limits the β_2 value to between -1 and 2.

The angular part of an outgoing electron's wavefunction can be described as a superposition of spherical harmonic functions, Y_{LM}, known as partial waves. Optical selection rules state that outgoing electron waves are made up of only two partial

waves corresponding to $l_i \pm 1$, where l_i is the angular momentum quantum number of the initial state. Partial waves will interfere due to their relative phase difference, which is caused by the electron's interaction with the ion core as it leaves the molecule and so is related to the quantum defect [68]. In the case where the initial state is an s-state, the outgoing wave will be comprised entirely of one partial wave, that of a pure p-wave and so the β_2 value for one-photon ionisation would be 2, in the absence of significant electron correlation effects. For higher l, where interference occurs, the β parameter is expected to change as the kinetic energy of the emitted electron changes.

In a coherent multi-photon process where the state being ionised (the initial state) has no time to depolarise after being excited by direct photon absorption, anisotropy is introduced into the system and higher order partial waves will contribute to the PAD. For linearly polarised light, an N-photon process will result in a PAD described by [107]

$$I(\theta) = \sum_{k=0}^{N} A_{2k} P_{2k}(\cos\theta), \tag{7.2}$$

where A is a coefficient that describes the dynamics of photoionisation, the experimental geometry, the orbital from which the electron is ejected, the spatial distribution of the sample and the ionisation energy [108].

Simple PADs which can be described by equation 7.1 are therefore indicative of a simple one-photon ionisation process where the initial state has no direct 'memory' of how it was populated or that it was not populated directly by multi-photon excitation.

7.2 Results and Discussion

The following section will present results on the identification of the peaks present in photoelectron spectra of C_{60} and C_{70}. Photoelectron spectra of C_{60} and C_{70}

ionised by fs laser pulses of varying wavelength will be presented as well as an analysis of the PADs extracted from the observed peaks in the spectra. Analysis of the anisotropy parameters obtained will then be used to identify certain peaks.

The peak structure is superimposed on the thermal background discussed in Chapter 6. To analyse the peaks, apparent temperatures are fitted to the thermal background which is then subtracted. Figure 7.1 shows the photoelectron kinetic energy spectrum for ionisation of C_{60} with 500 nm, 7.3 μJ laser pulses with both the thermal component and the peak structure. In the same figure is a PES showing the peak structure with the thermal background subtracted.

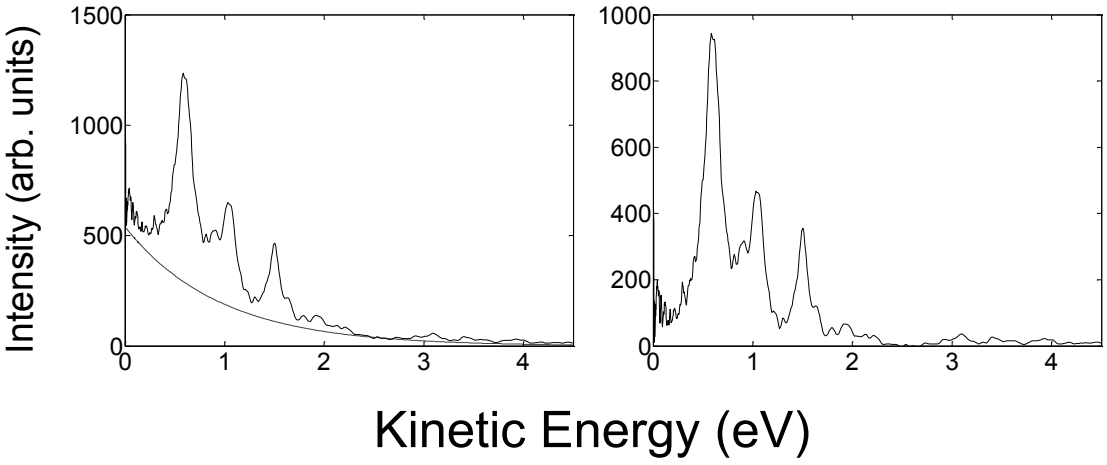

Figure 7.1: Left) 0-10^{o} segment of PES from C_{60} ionised with 500 nm, 7.3 μJ laser pulses. Right) The same PES with the thermal background, represented by the dashed line on the left-hand PES, subtracted. Both spectra are plotted in lin-lin scale.

7.2.1 Ionisation of C_{60}

A series of measurements were carried out, ionising C_{60} with fs laser pulses of wavelength between 400 and 800 nm in order to study the peak structure observed, superimposed on the thermal background present at these pulse durations. The 800 nm pulses are the fundamental output from the Legend and are around 120 fs. The 400 nm pulses were generated by passing the Legend output through a BBO doubling

crystal and are assumed to be the same pulse duration, around 120 fs. All other wavelengths were generated in the Topas-white and their pulse durations are estimated to be between 50 and 100 fs. All experiments were carried out at relatively low laser powers in order to suppress the thermal ionisation and resolve the peak structure better. The centroiding accumulation method (section 4.2.2) was used as this provides better resolution, especially at low powers. In some cases, the VMI images were smoothed before inversion in order to better identify the peaks present. The VMI images were split into angular segments of 10 degrees between 0 and 90 degrees and photoelectron spectra for each angle were produced. Lorentzian peaks were then fitted to each spectrum. The peak areas were obtained and anisotropy parameters were fitted, according to equation 7.1. The VMI images and photoelectron spectra for the 400, 500, 600 and 800 nm pulses are presented below, along with the fitted anisotropy parameters for each relevant peak in the spectra obtained for every wavelength.

Photoelectron spectra obtained by ionisation of C_{60} with fs laser pulses of varying wavelength show a similar peak structure which corresponds closely to the peak structure predicted by Feng *et al*. due to the population and ionisation of SAMOs [7]. Angle-integrated photoelectron spectra, plotted versus the electron binding energy, for wavelengths 400, 500, 600 and 800 nm are presented in Figure 7.2.

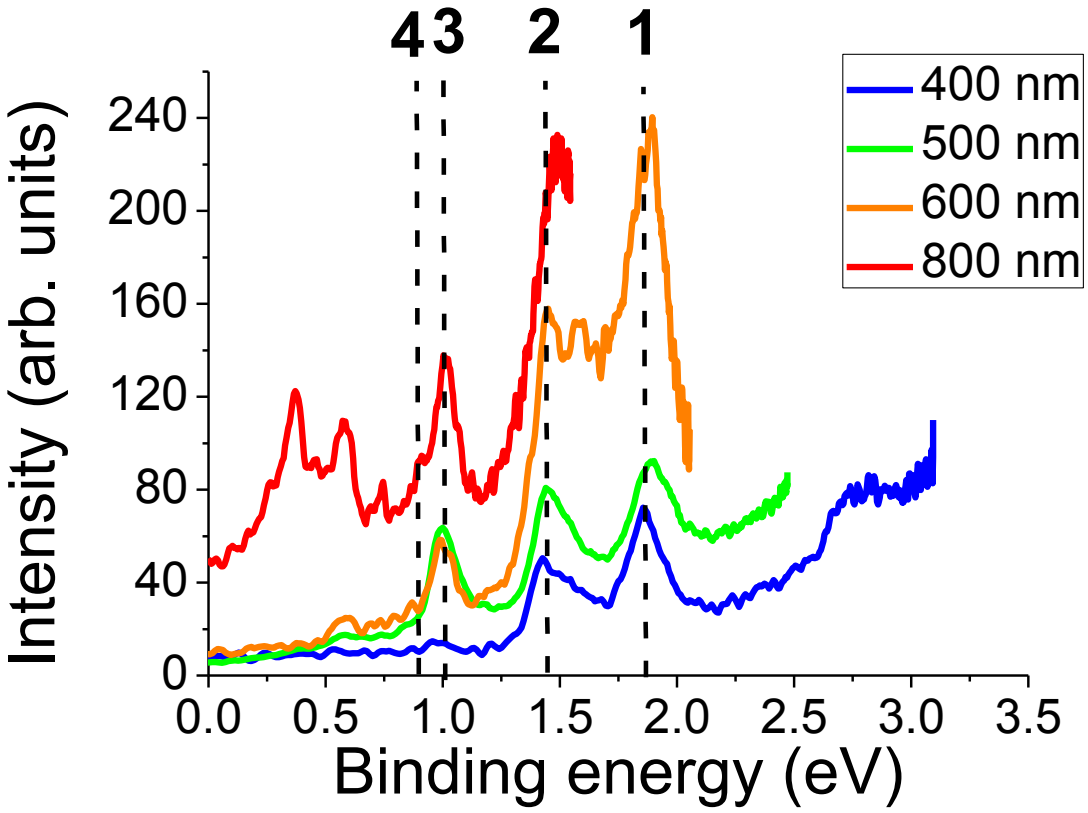

Figure 7.2: Angle-integrated photoelectron spectra of C_{60} plotted versus the electron binding energy obtained for different laser wavelengths.

From Figure 7.2, it can be seen that peaks with almost identical binding energies appear in the photoelectron spectra, regardless of wavelength. The most prominent peaks, and those of interest in this chapter, have been labelled 1, 2, 3 and 4, as can be seen in Figure 7.2. Peak 1 has a binding energy just below 2 eV, peak 2 has a binding energy just below 1.5 eV, peak 3 has a binding energy around 1 eV and peak 4 follows peak 3 closely, with a binding energy of just below 1 eV. Peak 4 is much smaller than the other three and is difficult to resolve in many of the spectra. If one were to compare the peaks, at first glance, to those identified as SAMO peaks based on their binding energies, peak 1 might be assigned as the s-SAMO, peak 2 might be assigned as the p-SAMO and peaks 3 and 4 might be assigned as the s'- and d-SAMOs discussed in Ref. 7.

Figures 7.3 and 7.4 show the inverted VMI image and the angle-resolved photoelectron spectra (at angles 0-10^{o}, 40-50^{o} and 80-90^{o}), for ionisation with 400 nm pulses, with Lorentzian peaks fitted to the structure at the relevant kinetic energies. Figure 7.5 shows the fitted anisotropy parameters for each peak.

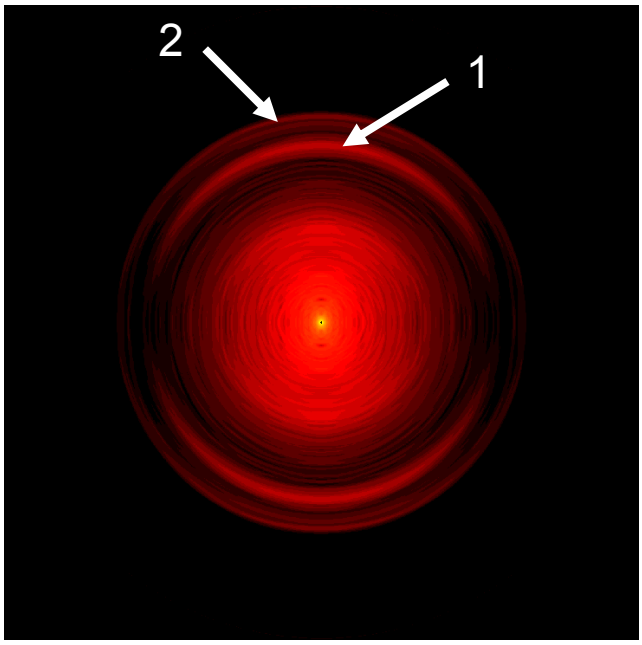

Figure 7.3: Inverted VMI image of C_{60} ionised with 400 nm, fs laser pulses. Peaks 1 and 2 are identified in the image.

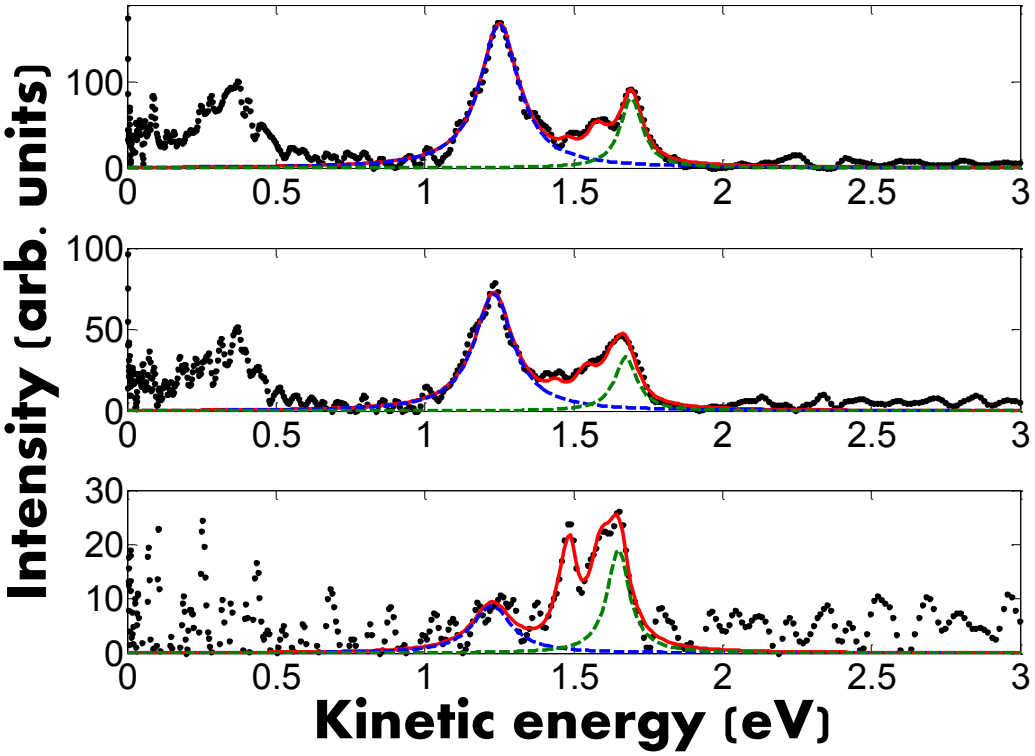

Figure 7.4: Angle-resolved photoelectron spectra obtained by ionising C_{60} with 400 nm, fs laser pulses. Top) 0-10 degrees, middle) 40-50 degrees, bottom) 80-90 degrees. Lorentzian peaks have been fitted to peaks 1 (blue) and 2 (green) for all angles.

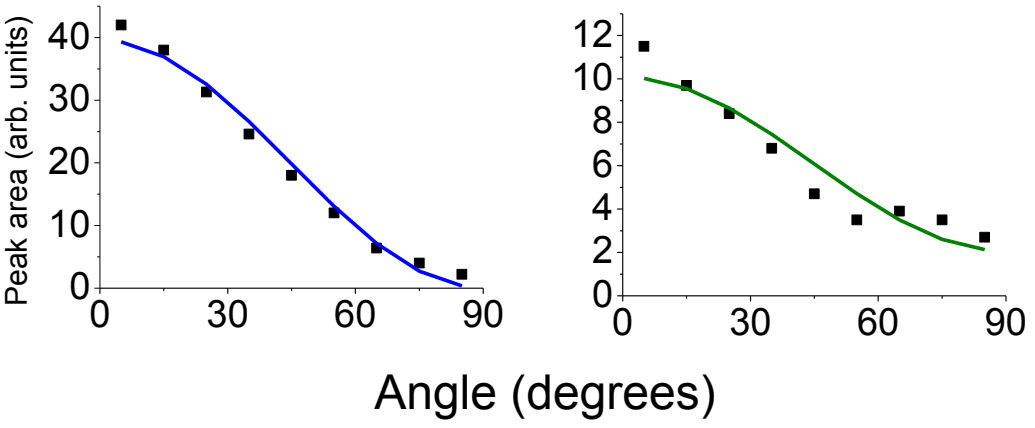

Figure 7.5: Fitted peak areas for peaks 1 (blue) and 2 (green) from Figure 7.4, as a function of angle. The fits provided β_2 values of 2.00 for peak 1 and 1.12 for peak 2.

As can be seen in Figure 7.4, peak 2 is not well resolved and has other peaks close by. This makes choosing a fit somewhat difficult. Extra peaks are fitted although not shown in the figure and the combined fit is shown in red. This introduces an error in the fit for β_2 (although this is difficult to quantify) and it is clear that the peak area as a function of angle graphs 'look better' for peaks which are more resolved, such as peak 1 in Figures 7.4 and 7.5.

Figures 7.6 and 7.7 show the inverted VMI image and the angle-resolved photoelectron spectra (at angles 0-10^o, 40-50^o and 80-90^o), for ionisation with 500 nm pulses, with Lorentzian peaks fitted to the structure at the relevant kinetic energies, respectively. Figure 7.8 shows the fitted anisotropy parameters for each peak.

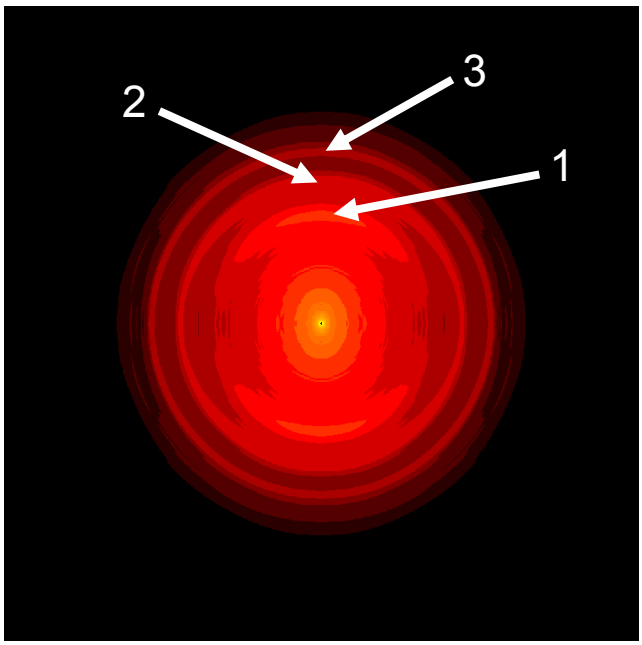

Figure 7.6: Inverted VMI image of C_{60} ionised with 500 nm, fs laser pulses. Peaks 1, 2 and 3 are identified in the image.

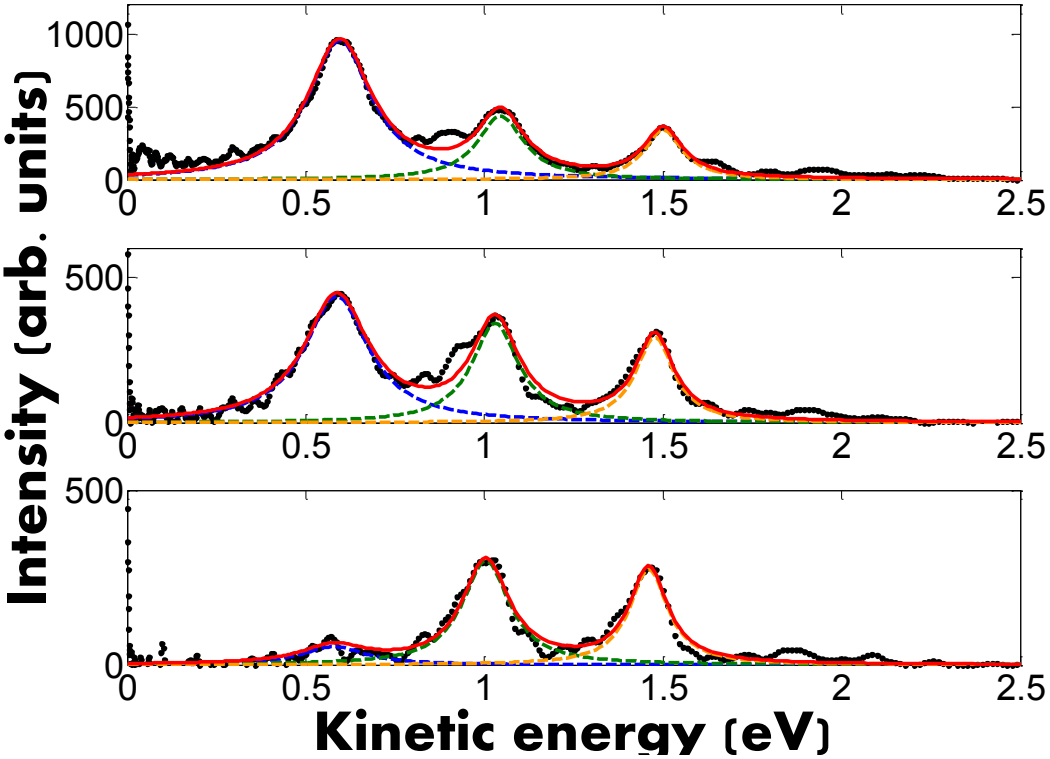

Figure 7.7: Angle-resolved photoelectron spectra obtained by ionising C_{60} with 500 nm, fs laser pulses. Top) 0-10 degrees, middle) 40-50 degrees, bottom) 80-90 degrees. Lorentzian peaks have been fitted to peaks 1 (blue), 2 (green) and 3 (orange) for all angles.

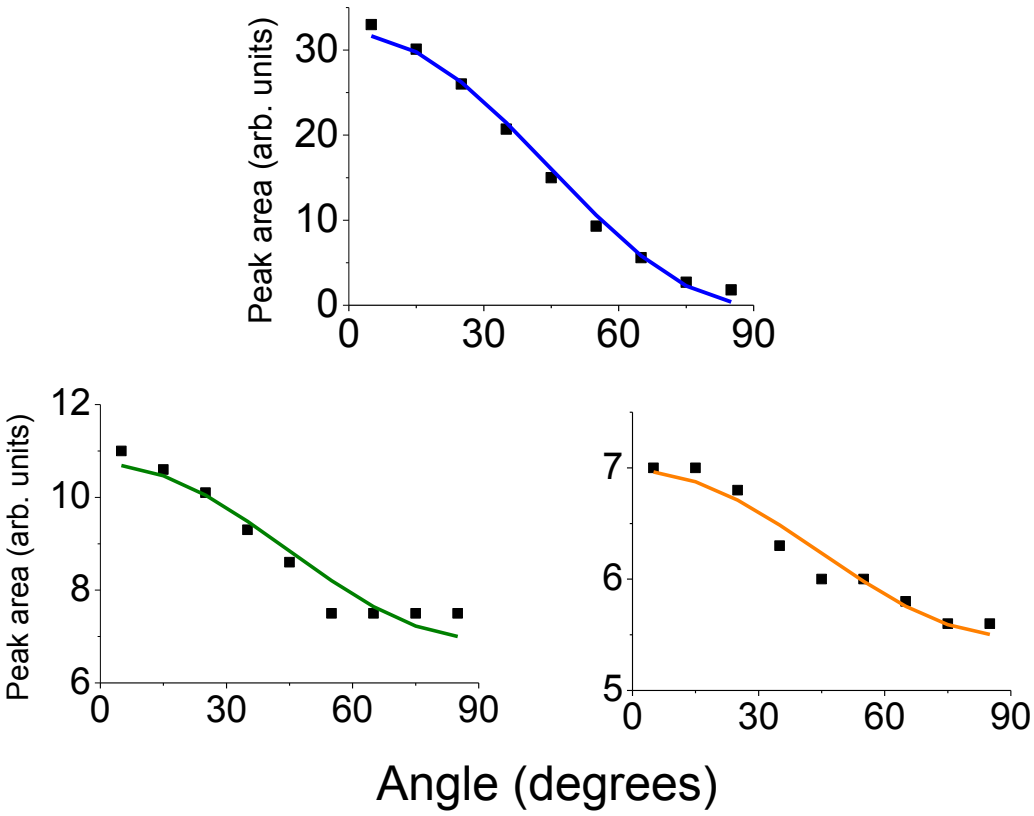

Figure 7.8: Fitted peak areas for peaks 1 (blue), 2 (green) and 3 (orange) from Figure 7.7, as a function of angle. The fits provided β_2 values of 1.97 for peak 1, 0.30 for peak 2 and 0.17 for peak 3.

Figures 7.9 and 7.10 show the inverted VMI image and the angle-resolved photoelectron spectra (at angles 0-10^{o}, 40-50^{o} and 80-90^{o}), for ionisation with 600 nm pulses, with Lorentzian peaks fitted to the structure at the relevant kinetic energies, respectively. Figure 7.11 shows the fitted anisotropy parameters for each peak.

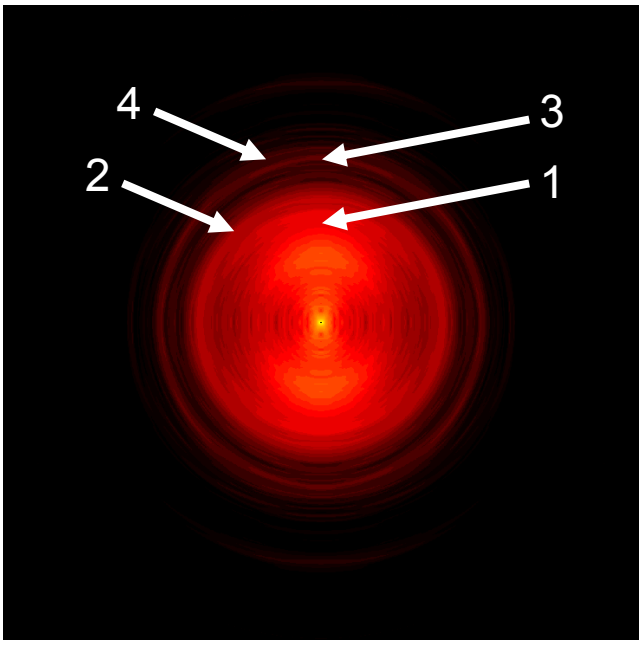

Figure 7.9: Inverted VMI image of C_{60} ionised with 600 nm, fs laser pulses. Peaks 1, 2, 3 and 4 are identified in the image.

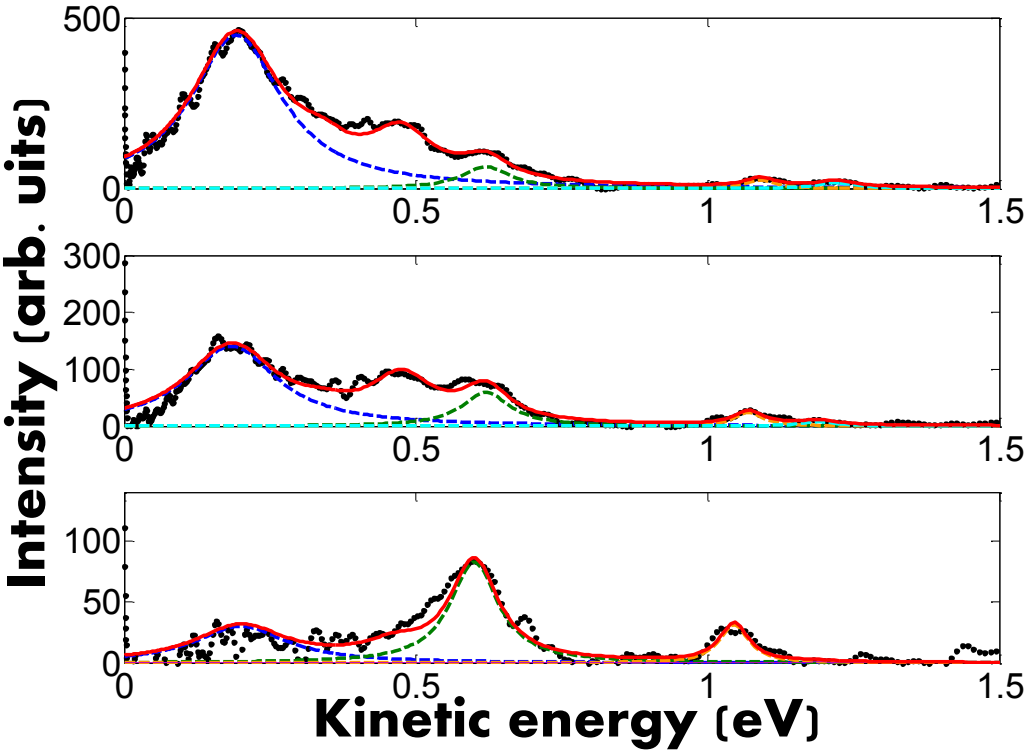

Figure 7.10: Angle-resolved photoelectron spectra obtained by ionising C_{60} with 600 nm, fs laser pulses. Top) 0-10 degrees, middle) 40-50 degrees, bottom) 80-90 degrees. Lorentzian peaks have been fitted to peaks 1 (blue), 2 (green), 3 (orange) and 4 (light blue) for all angles.

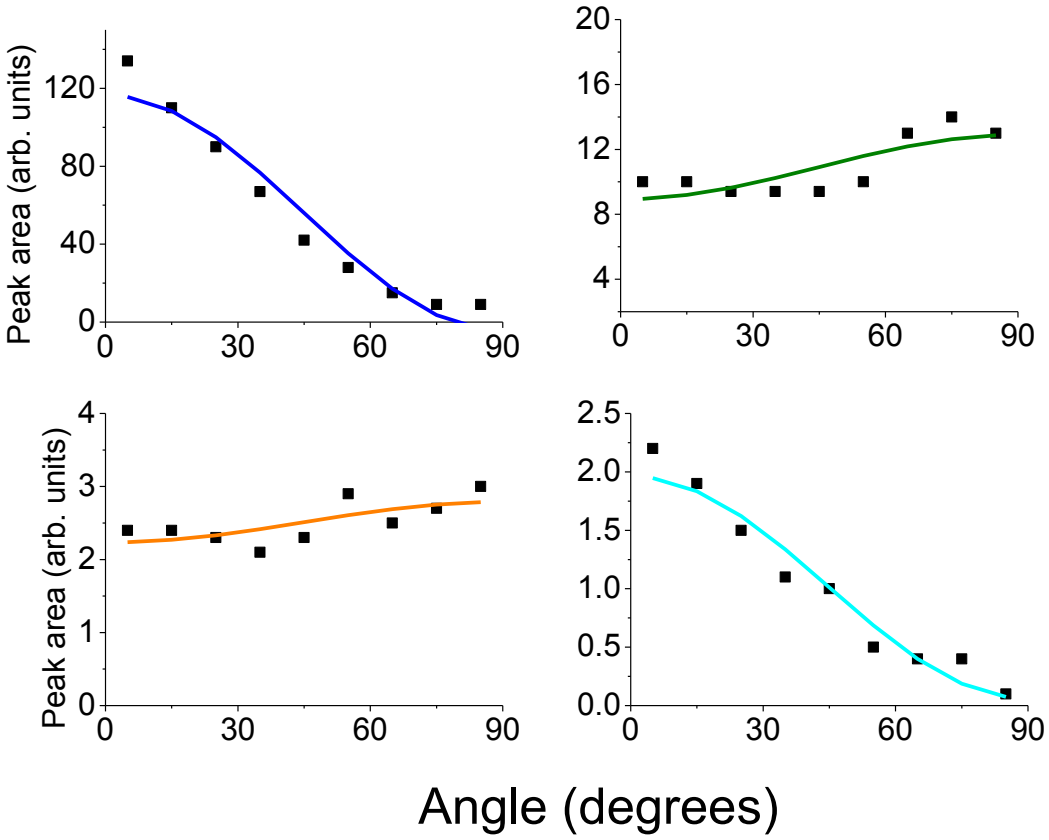

Figure 7.11: Fitted peak areas for peaks 1 (blue), 2 (green), 3 (orange) and 4 (light blue) from Figure 7.10, as a function of angle. The fits provided β_2 values of 2.25 for peak 1, -0.23 for peak 2, -0.14 for peak 3 and 1.83 for peak 4.

Figures 7.12 and 7.13 show the inverted VMI image and the angle-resolved photoelectron spectra (at angles 0-10^{o}, 40-50^{o} and 80-90^{o}), for ionisation with 800 nm pulses, with Lorentzian peaks fitted to the structure at the relevant kinetic energies, respectively. Figure 7.14 shows the fitted anisotropy parameters for each peak.

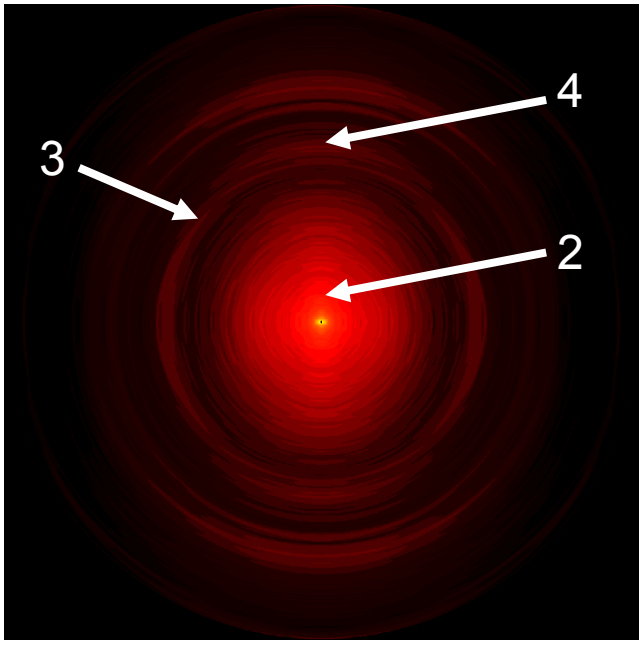

Figure 7.12 Inverted VMI image of C_{60} ionised with 800 nm, fs laser pulses. Peaks 2, 3 and 4 are identified in the image.

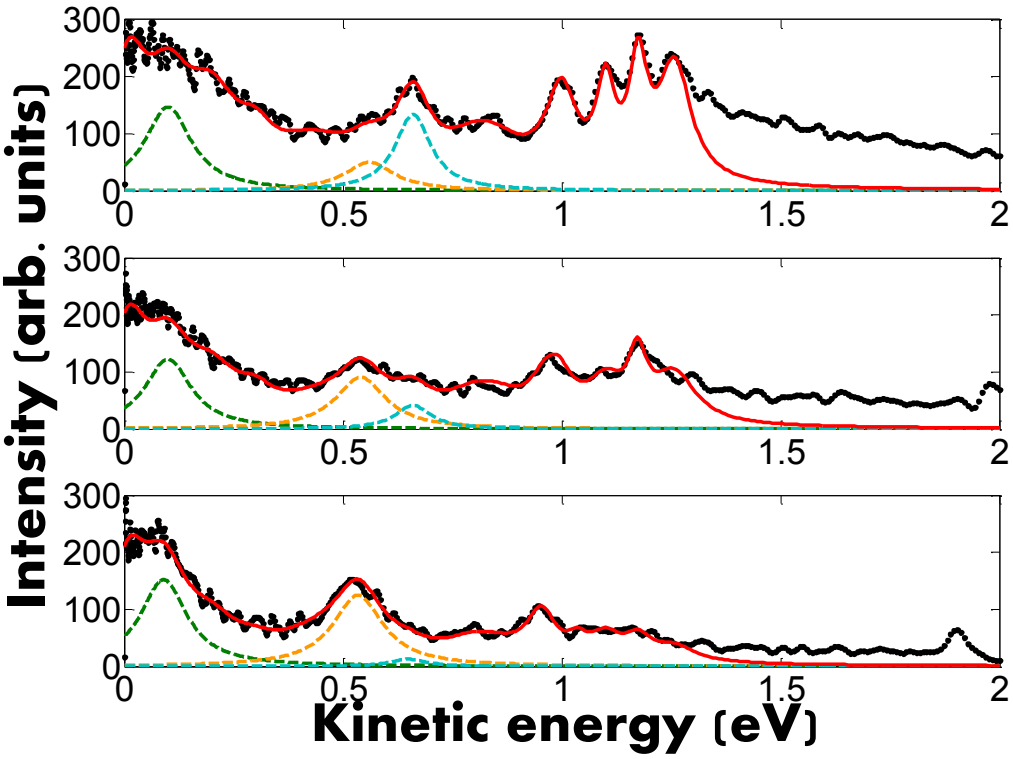

Figure 7.13: Angle-resolved photoelectron spectra obtained by ionising C_{60} with 800 nm, fs laser pulses. Top) 0-10 degrees, middle) 40-50 degrees, bottom) 80-90 degrees. Lorentzian peaks have been fitted to peaks 2 (green), 3 (orange) and 4 (light blue) for all angles.

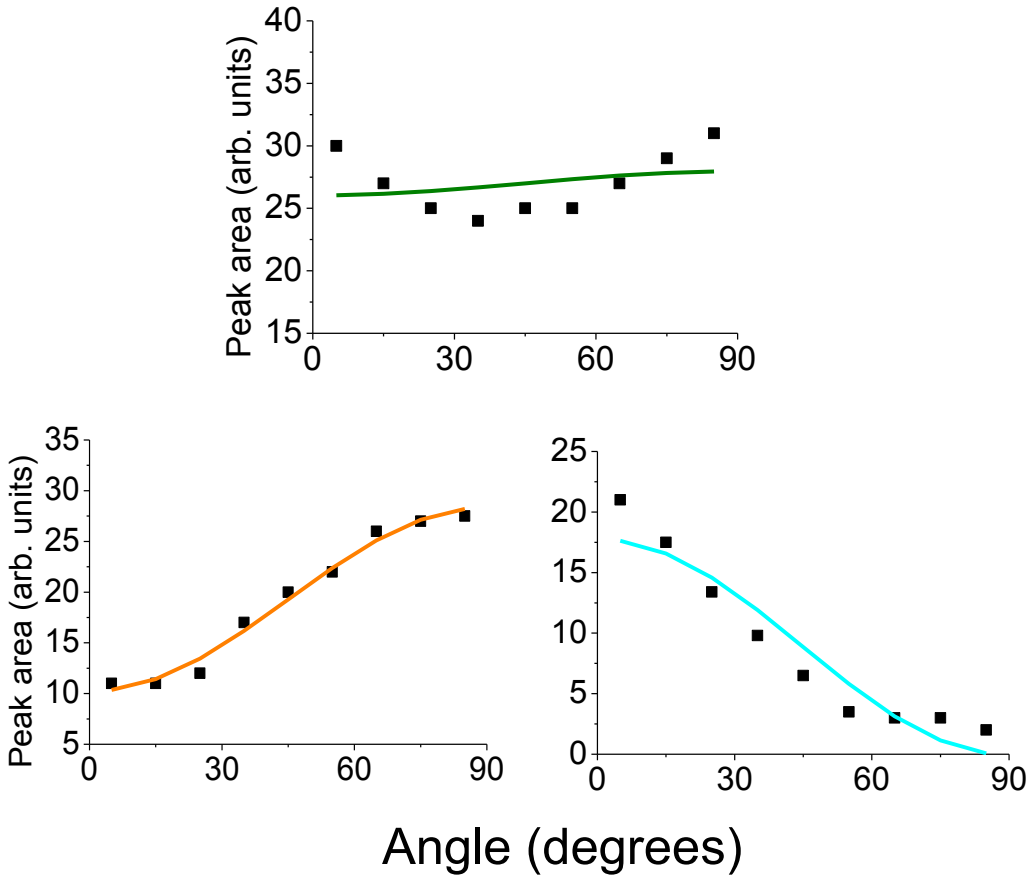

Figure 7.14: Fitted peak areas for peaks 2 (green), 3 (orange) and 4 (light blue) from Figure 7.13, as a function of angle. The fits provided β_2 values of -0.05 for peak 2, -0.54 for peak 3 and 2.02 for peak 4. Peak 2 does not give a particularly good fit. This is most likely due to the unresolved structure around the peak area making fitting difficult.

Table 7.1 shows the binding energies and β_2, anisotropy parameter, values for peak 1 at each wavelength for which the peak was visible and resolvable. Tables 7.2, 7.3 and 7.4 show the corresponding information for peak 2, 3 and 4, respectively.

Table 7.1: Binding energies associated with the fitted peak positions and fitted anisotropy parameters for the peak assigned as 'peak 1' in the ionisation of C_{60} with fs laser pulses of varying wavelength.

Wavelength (nm)	Binding energy (eV)	Anisotropy parameter
400	1.87	2.00 ± 0.12
490	1.92	1.89 ± 0.07
500	1.89	1.97 ± 0.06
514	1.85	1.88 ± 0.10
530	1.87	2.18 ± 0.07
545	1.90	1.71 ± 0.09
600	1.87	2.25 ± 0.20

Time-dependent density functional theory (TD-DFT) calculations were carried out by Francoise Remacle, at the Universite de Liège, to determine the binding energies of the SAMO sates. The calculations showed an excited state comprised entirely of the s-SAMO with a binding energy of 2.15 eV and a higher lying s-SAMO with binding energy 0.78 eV. A pure p-state was identified with a binding energy of 1.26 eV.

Peak 1 has an experimentally derived binding energy of 1.88 ± 0.02 eV, which is in reasonably close agreement with the s-SAMO peak predicted to have a binding energy of 2.15 eV by the TD-DFT calculations. Furthermore, the experimental β_2 values for peak 1 show no dependence on excitation wavelength and have a constant value close to 2. This is the behaviour which would be expected from one-photon ionisation from an s-orbital as the outgoing electron partial wave will be comprised entirely of a pure p-wave. It therefore seems reasonable to attribute peak 1 to the population of and subsequent one-photon ionisation of the s-SAMO.

Table 7.2: Binding energies associated with the fitted peak positions and fitted anisotropy parameters for the peak assigned as 'peak 2' in the ionisation of C_{60} with fs laser pulses of varying wavelength.

Wavelength (nm)	Binding energy (eV)	Anisotropy parameter
400	1.42	1.16 ± 0.14
490	1.45	0.59 ± 0.07
500	1.45	0.30 ± 0.04
514	1.38	0.57 ± 0.06
530	1.43	0.13 ± 0.04
545	1.45	0.05 ± 0.01
600	1.45	-0.24 ± 0.07
625	1.46	-0.29 ± 0.02
700	1.39	-0.46 ± 0.03
800	1.45	-0.05 ± 0.06

Peak 2 has an experimental binding energy of 1.43 ± 0.02 eV, which is in close agreement with the p-SAMO peak predicted to have a binding energy of 1.26 eV by the calculations. Some of the fits for peak 2 are relatively poor which may suggest a small peak overlapping with the larger peak. Nevertheless the experimental β_2 values change as the wavelength is varied, which is consistent with the behaviour of an outgoing electron wave which is comprised of two, interfering partial waves.

Table 7.3: Binding energies associated with the fitted peak positions and fitted anisotropy parameters for the peak assigned as 'peak 3' in the ionisation of C_{60} with fs laser pulses of varying wavelength.

Wavelength (nm)	Binding energy (eV)	Anisotropy parameter
490	1.02	0.13 ± 0.02
500	1.00	0.17 ± 0.01
530	0.97	0.04 ± 0.03
545	1.02	-0.06 ± 0.01
600	0.99	-0.14 ± 0.05
625	1.01	-0.32 ± 0.05
800	1.00	-0.54 ± 0.02

Table 7.4: Binding energies associated with the fitted peak positions and fitted anisotropy parameters for the peak assigned as 'peak 4' in the ionisation of C_{60} with fs laser pulses of varying wavelength.

Wavelength (nm)	Binding energy (eV)	Anisotropy parameter
600	0.86	1.84 ± 0.16
625	0.87	1.16 ± 0.01
800	0.90	2.02 ± 0.24

Peaks 3 and 4 have experimental binding energies of 1.00 ± 0.01 eV and 0.88 ± 0.02 eV, respectively. The experimental binding energy for peak 4 is in reasonable agreement with the predicted binding energy of the s'-SAMO state, 0.78 eV, from the calculations. Ref. 7 predicts the d-SAMO to be very close in energy to the s'-SAMO, around 1 eV, which agrees with the experimental binding energy of peak 3. The β_2 value of peak 3 shows a wavelength dependence as would be expected of any orbital which was not an s-state and the β_2 value for peak 4 is relatively close to 2, as would be expected of an s-state at wavelengths 600 and 800 nm, although it is slightly

smaller for 625 nm. It should be noted however that peak 4 is the smallest of the four peaks analysed in the spectra obtained and therefore the least resolved, which makes fitting peak areas to it more difficult than with the first three peaks.

Figure 7.15 shows the fitted anisotropy parameters for each peak as a function of photoelectron kinetic energy. Also shown are the calculated anisotropy parameters for the peaks identified in the Liège calculations as the s-SAMO (peak 1) and p-SAMO (peak 2) as a function of kinetic energy. The anisotropy parameter calculations assume an electron is ionised from an initial state, ψ_i, to a final state as an unbound plane wave. The distribution of emitted photoelectrons as a function of momentum, k, can then be described as,

$$I(k,\theta,\varphi) \propto \left| \int \psi_i \mu \exp(-2\pi i k \cdot r) dr \right|^2, \tag{7.3}$$

where μ is the dipole operator. The calculations show that the s-SAMO has an anisotropy parameter of 1.88 which does not change with kinetic energy. This is in good agreement with the experimentally obtained β_2 value for peak 1. The calculated β_2 value is smaller than 2 because the s-SAMO is not a true s-orbital where l is a good quantum number. The electrons of the fullerene cage affect the wavefunction, as can be seen in Figure 2.7 in Chapter 2. The calculated β_2 for the p-SAMO varies with photoelectron kinetic energy and bears close resemblance to the experimental change in β_2 with kinetic energy.

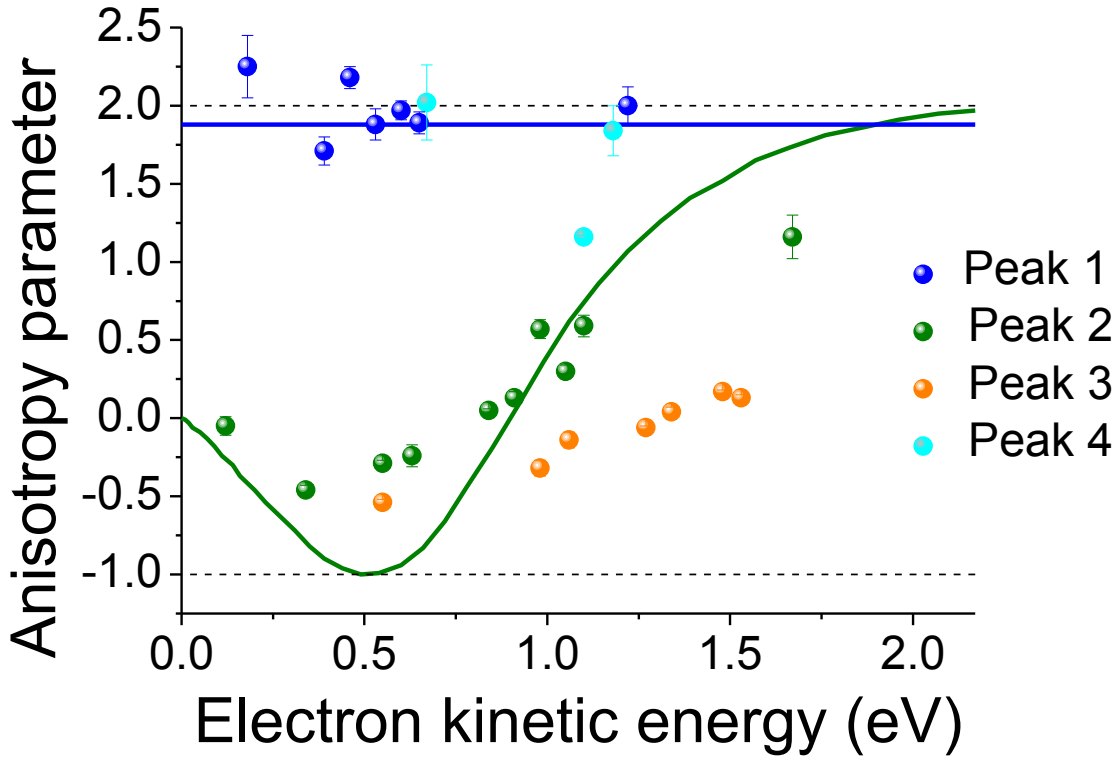

Figure 7.15: Anisotropy parameter, β_2, as a function of photoelectron kinetic energy. The dots represent experimental data and the corresponding lines represent the calculated values. The dashed lines represent the maximum and minimum values β_2 can take.

7.2.2 Ionisation of C_{70}

A measurement was carried out, ionising C_{70} with 400 nm, 120 fs laser pulses to compare to the results obtained by ionising C_{60}. Figure 7.16 shows the angle-resolved photoelectron spectra (at angles 0-10^o and 40-50^o) with Lorentzian peaks fitted to the structure at the relevant kinetic energies. Figure 7.17 shows the fitted anisotropy parameters for each peak.

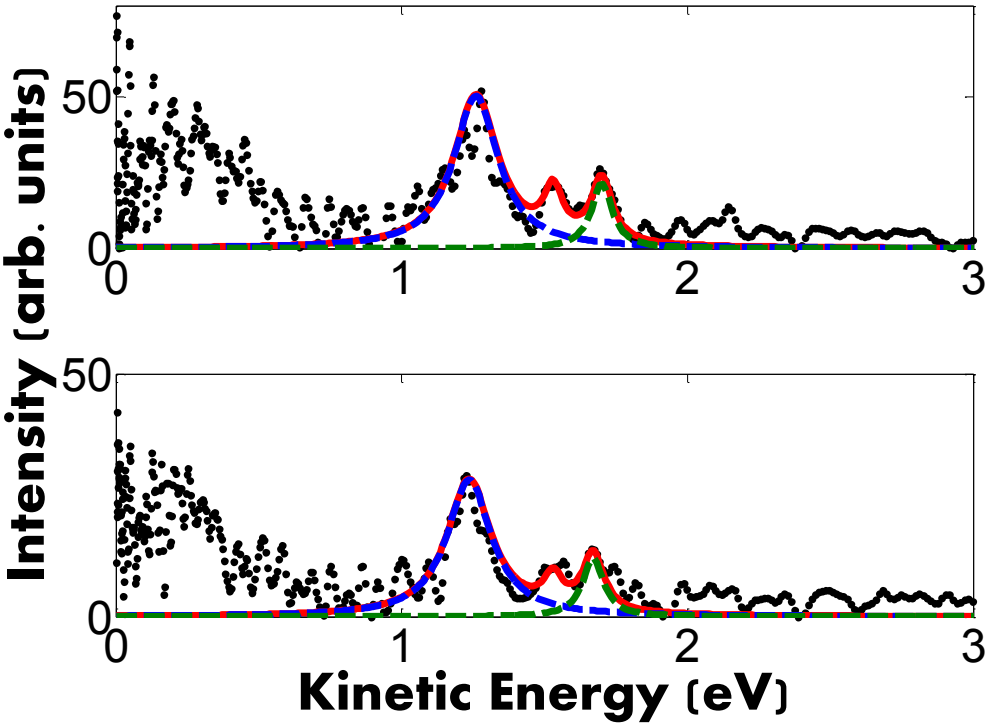

Figure 7.16: Angle-resolved photoelectron spectra obtained by ionising C_{70} with 400 nm, 120 fs laser pulses. Top) 0-10 degrees, bottom) 40-50 degrees. Lorentzian peaks have been fitted to peaks 1 (blue) and 2 (green) for all angles except 80-90°, where no peak structure was observed.

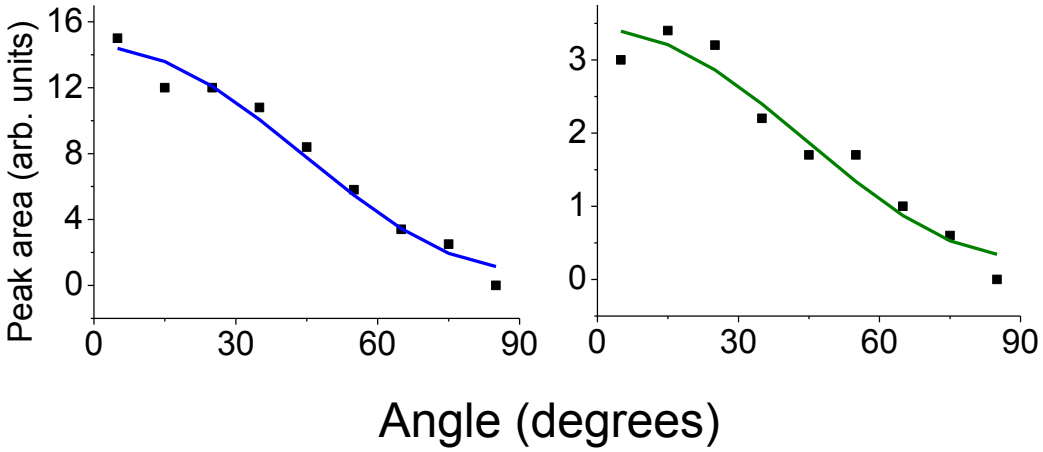

Figure 7.17: Fitted peak areas for peaks 1 (blue) and 2 (green) from Figure 7.16, as a function of angle. The fits provided β_2 values of 1.62 for peak 1 and 1.53 for peak 2.

The binding energy for peak 1 is 1.87 eV, which is very similar to the binding energy of the corresponding peak in the C_{60} spectra and the β_2 value is 1.62 compared to a value of 1.99 for the corresponding C_{60} spectrum. The binding energy for peak 2 is 1.42 eV which is also very similar to the binding energy of the corresponding peak in the C_{60} spectra and the β_2 value is 1.53 compared to a value of 1.12 for the corresponding C_{60} spectrum. It seems a reasonable conclusion that very similar SAMO peaks can be seen in C_{70} photoelectron spectra as for the C_{60} photoelectron spectra. Similar calculations to those undertaken for C_{60} are currently underway in Liège on C_{70} SAMOs.

7.3 Conclusions

Angle-resolved photoelectron spectra have been presented for C_{60} and C_{70} ionisation over a range of laser wavelengths and the PADs have been analysed. A peak structure is observed in every spectrum which is consistent with previous gas phase studies. Four peaks have been analysed and by looking at experimental binding energies and anisotropy parameters, β_2, and comparing with theoretical calculations, these peaks are assigned as SAMOs.

Peak 1 has an experimental binding energy of 1.88 eV and an average β_2 value of 1.98, which does not vary with wavelength. This is assigned as the s-SAMO. Peak 2 has an experimental binding energy of 1.43 eV and the β_2 value varies with wavelength in a similar way to the calculated values for the p-SAMO, therefore, peak 2 is assigned as the p-SAMO. Peak 3 has an experimental binding energy of 1.00 eV and its β_2 value changes with wavelength. This may be tentatively assigned as the d-SAMO but more detailed studies are being carried out together with Francois Remacle. Peak 4 has an experimental binding energy of 0.88 eV and a β_2 value which does not seem to change with wavelength and has an average value of 1.68. This peak is assigned as the s'-SAMO.

That the PADs of the SAMO peaks can be described by equation 1 suggests that they are the result of single-photon ionisation. This speaks against the SAMO

peaks arising from direct resonance enhance multiphoton ionisation (REMPI). Calculations on the rate of ionisation suggest that the SAMO states have a very high ionisation rate, ca. three orders of magnitude higher than any other excited states with approximately the same energies, and effectively ionise 'spontaneously'. This may explain why the SAMO peaks are so prominent in the PES, compared to other highly excited populated states.

The interpretation that the peaks observed are due to the population and ionisation of SAMO states, as opposed to Rydberg states is convincing due to the close agreement with experimental studies of SAMOs in the solid state and with theoretical calculations. Further evidence of SAMOs in fullerene molecules might be gained through similar experiemnts and comparison with calculations for a range of larger fullerene molecules and endohedral fullerenes. This would also provide the opportunity to discover how molecular properties affect the SAMO states in terms of their shape and energy, which will be important for future applications.

Chapter 8 – Fusion of carbon nanotubes with ultrashort laser pulses

This chapter describes experiments undertaken in an attempt to induce fusion between carbon nanotubes using ultrashort laser pulses. A brief introduction to fusion of carbon nanotubes is given. Section 8.2.1 describes experiments measuring the resistance of buckypaper samples irradiated with laser pulses. Section 8.2.2 describes experiments where thin carbon nanotube films were irradiated and analysed with Raman spectroscopy.

8.1 Introduction

The fusion and welding of carbon nanotubes has been observed when nanotube samples have been exposed to high energy electron beams and high electric fields [10, 61, 62, 63]. In these studies, it was suggested that the effect of the electron beam is to introduce defects in the tube structure which become vulnerable to bond breakage. Dangling bonds from nearby tubes may then join, linking the tubes together. C_{60} clusters have also displayed fusion between individual molecules when irradiated with ultrashort laser pulses [65]. Fusion of carbon nanotubes may provide a method to harness the extraordinary properties of these molecules. It has been suggested that 2-D and 3-D networks of covalently bonded nanotubes could be highly effective as nanoelectronic circuits [64] and transferring the individual tubes properties to large-scale composites could provide very interesting and useful new materials.

8.2 Results and Discussion

8.2.1 Fusion of carbon nanotubes in buckypaper

Resistance measurements were carried out on buckypaper samples which were irradiated by 800 nm, 120 fs laser pulses of varying intensity. Measurements were carried out before and after each period of irradiation and during each irradiation. The idea was that if significant fusion were to occur within the sample, a permanent drop in resistance should be observed.

The resistance was measured using a 4-probe, Van der Pauw method. During irradiation, a small current (10 mA) was passed along one edge of the sample and the voltage was measured across the opposite edge. The resistance was then obtained using Ohm's Law, as described in section 5.1.3. Figure 8.1 shows the resistance measurements during each period of irradiation at different intensities. The resistance measurement was started a few seconds before irradiation began. One area of the sample was irradiated for 10 minutes and then the laser beam was moved, manually, with a directing mirror, to a different area of the sample. Three areas of the sample were irradiated for 10 minutes each before the laser was blocked and the measurement was continued for another 10 minutes. Figure 8.1 i) shows when irradiation began, when the laser was moved and when irradiation stopped. The process was identical for each measurement.

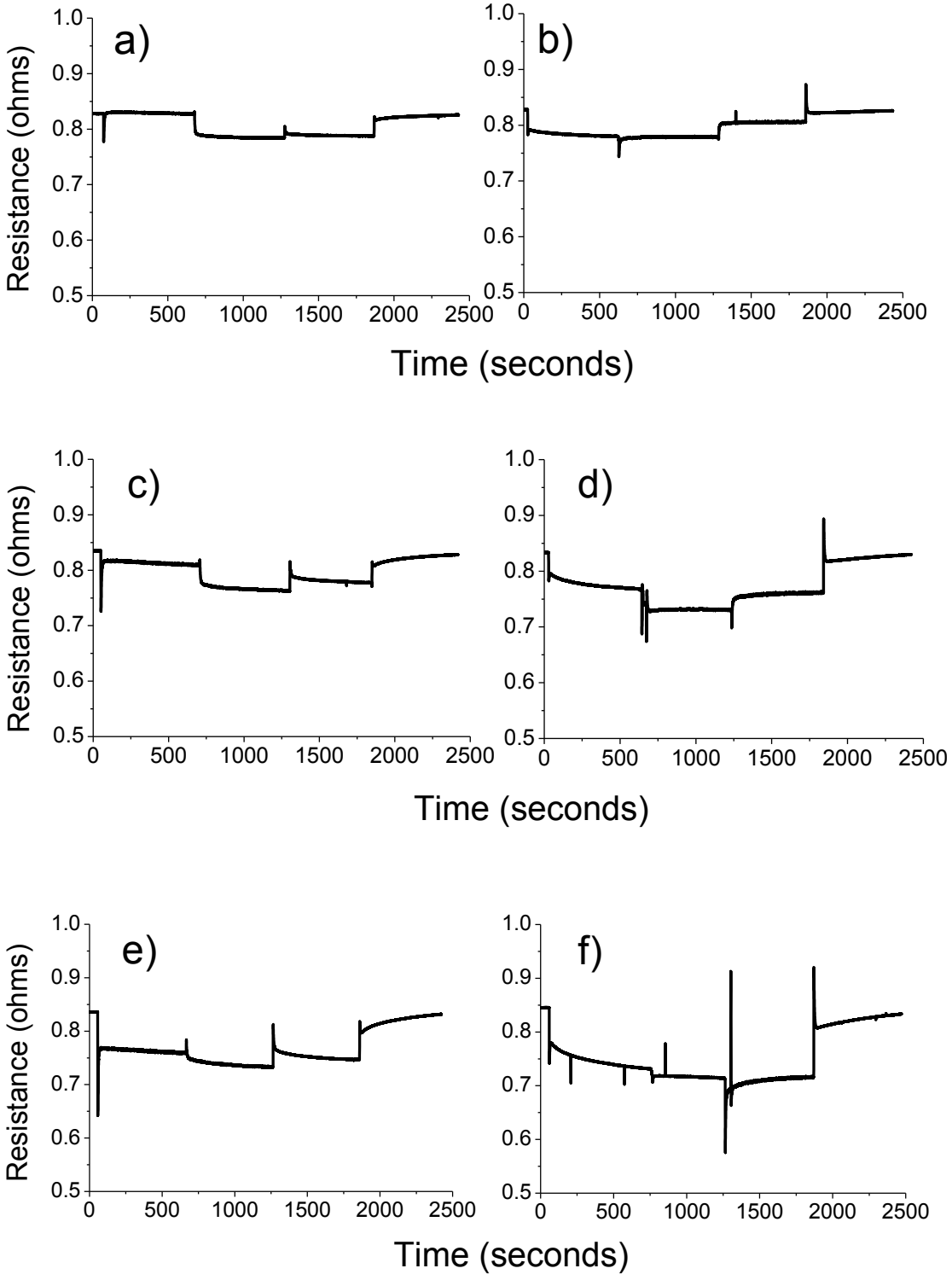
a)
b)
c)
d)
e)
f)
Resistance (ohms)
Time (seconds)
1.0
0.9
0.8
0.7
0.6
0.5
0
500
1000
1500
2000
2500

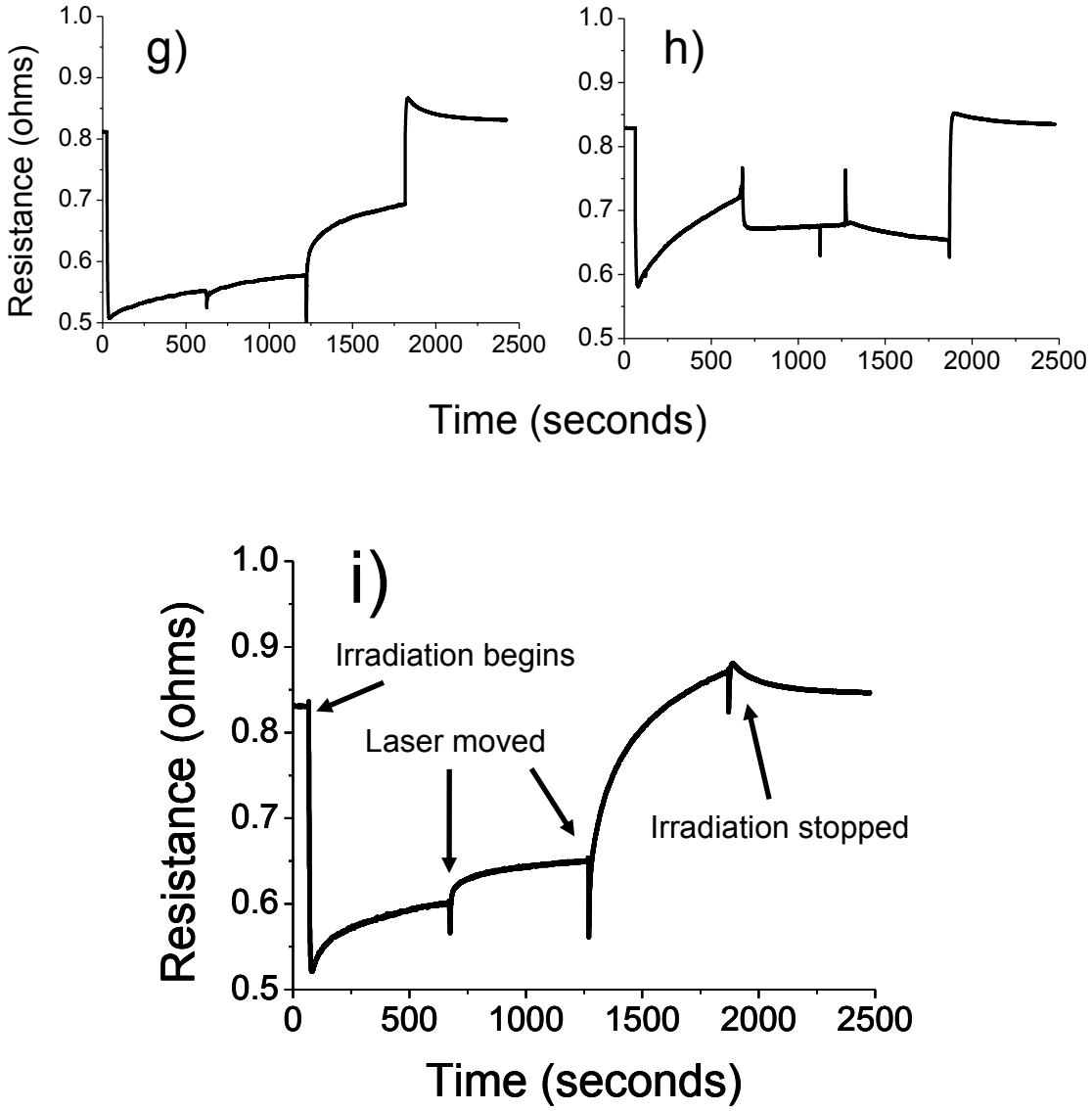

Figure 8.1: Resistance measurements carried out during laser irradiation of buckypaper samples by 800 nm, 120 fs pulses of intensity a) 2.05 GW/cm^2, b) 2.84 GW/cm^2, c) 4.68 GW/cm^2, d) 6.57 GW/cm^2, e) 9.81 GW/cm^2, f) 13.38 GW/cm^2, g) 22.49 GW/cm^2, h) 34.84 GW/cm^2 and i) 43.44 GW/cm^2.

There is generally a drop in resistance while the sample is being irradiated at each intensity and a quick increase when the laser is blocked. It is not clear what effects contribute to the observed behaviour although there does not seem to be any permanent change in the resistence of the sample, after the irradiation has stopped. This would suggest that fusion has not taken place. It is interesting to note the

difference in behaviour with increasing intensity. At lower intensities, the resistance seems to drop over the 10 minute periods of irradiation on a single area and then rise steadily once the laser is blocked. At higher intensities, the opposite happens. The resistance, after an initial drop when the laser is unblocked, increases over the 10 minute irradiation period and then, after the sharp increase when the laser is blocked, steadily decreases. This may be due to ablation of the sample by the laser beam. At high intensities, if tubes are damaged and ablated from the surface, the resistance should increase.

Sheet resistance measurements were carried out prior to and after each irradiation, as described in section 5.1.3. Figure 8.2 shows the change in sheet resistance before and after each irradiation.

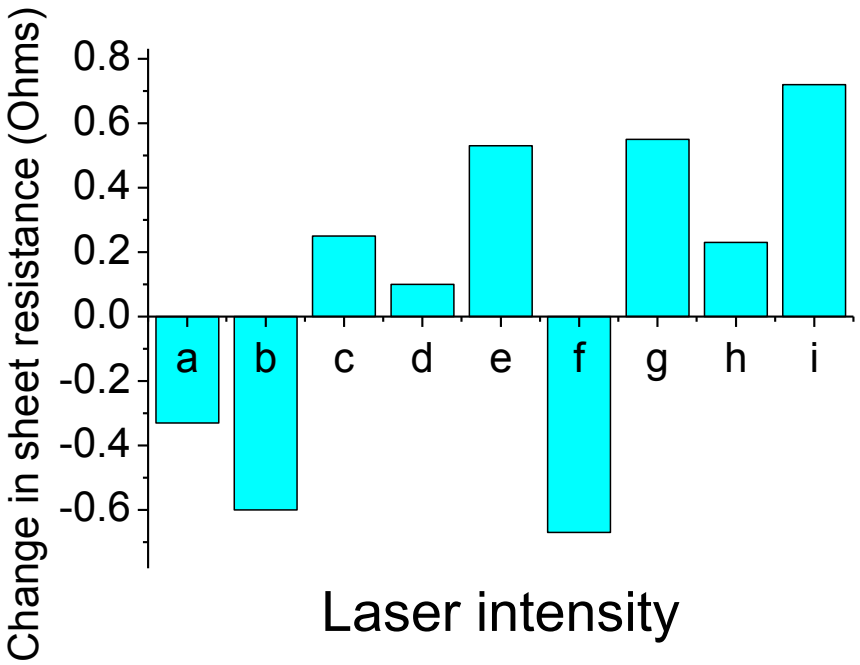

Figure 8.2: Sheet resistance measurements carried out before and after laser irradiation of buckypaper samples by 800 nm, 120 fs pulses of intensity a) 2.05 GW/cm^2, b) 2.84 GW/cm^2, c) 4.68 GW/cm^2, d) 6.57 GW/cm^2, e) 9.81 GW/cm^2, f) 13.38 GW/cm^2, g) 22.49 GW/cm^2, h) 34.84 GW/cm^2 and i) 43.44 GW/cm^2.

No clear pattern emerges from the sheet resistance measurements or the resistance measurements during the laser irradiation to suggest that a permanent structural change in the sample has taken place, caused by nanotube fusion. Although a decrease in sheet resistance was measured after irradiation by 2.05, 2.48 and 13.38 GW/cm^2 pulses, most of the intensities used resulted in an increase in sheet resistance. There is no apparent trend, related to laser intensity, and the changes in sheet resistance were relatively small, with the largest absolute change (+0.72 Ω at 43.44 GW/cm^2), only representing an increase of around 1%. It was concluded that either nanotube fusion in buckypaper was not achieved by this method or that the effect was too small to be detected or that the signs of fusion were swamped by other effects.

8.2.2 Fusion of thin film carbon nanotube samples

Samples consisting of thin carbon nanotube films were prepared with two depositions of a nanotube solution being deposited on a quartz substrate, in directions orthogonal to each other. This resulted in a sample with two nanotube 'layers' lying in orthogonal directions to each other. This should result in a sample with multiple instances of tubes lying across each other which should be conducive to fusion of the nanotubes. This arrangement should also facilitate resitance measurements. The sample was irradiated with single 800 nm, 120 fs laser pulses of varying intensity. The sites at which the sample was irradiated were investigated with Raman spectroscopy. The radial breathing mode (RBM) peaks were of particular interest as their position in the Raman spectrum is dependent on the diameter of the carbon nanotubes in the sample. RBM peaks at smaller Raman shifts indicate tubes with larger diameters. If fusion occurs between nanotubes, originally present within bundles, this may result in tubes with a larger diameter and therefore RBM peaks at lower Raman shifts.

The areas which had been shot with the laser were visible under the microscope of the Raman spectrometer, as the pattern left by the evaporation of the surfactant was removed at these spots. This left circular areas on the sample, indicating where the laser pulse had hit. From this, the centre of the laser spot could be estimated by measuring the diameter of the circle. Raman spectra were taken at

increasing radii from the centre of the circle at 0^o, 90^o, 180^o and 270^o. Since these represent the points of a compass, they will be labelled north, east, south and west, respectively.

Figure 8.3 shows Raman spectra taken at increasing radii from the centre of the spot heading north of the 0.41 ± 0.07 TW/cm^2 pulse. RBM peaks, similar to those observed in unirradiated areas of the sample can be seen at shifts of 193, 212, 252 and 264 cm^{-1} which correspond to tube diameters of around 1.29, 1.17, 0.98 and 0.94 nm respectively. This is consistent with the range of nanotube diameters expected for the commercial nanotubes used in the experiment of 0.7-1.4 nm [109]. Generally, these peaks decrease in intensity closer to the centre of the laser spot as the local intensity increases and tubes are most likely destroyed or ablated from the substrate. The spectrum taken 112 μm from the centre shows a relatively broad peak centred at around 156 cm^{-1} which is not observed at other distances. This corresponds to a nanotube diameter of around 1.59 nm, significantly larger than any measured in unirradiated areas. The position of the peaks appearing in the Raman spectra can be rationalised by comparing with the Kataura plot (Figure 5.9) in section 5.2.4. Not all tubes will be resonant with the 514 nm laser light used and so only tubes of certain diameters will produce peaks in the spectra.

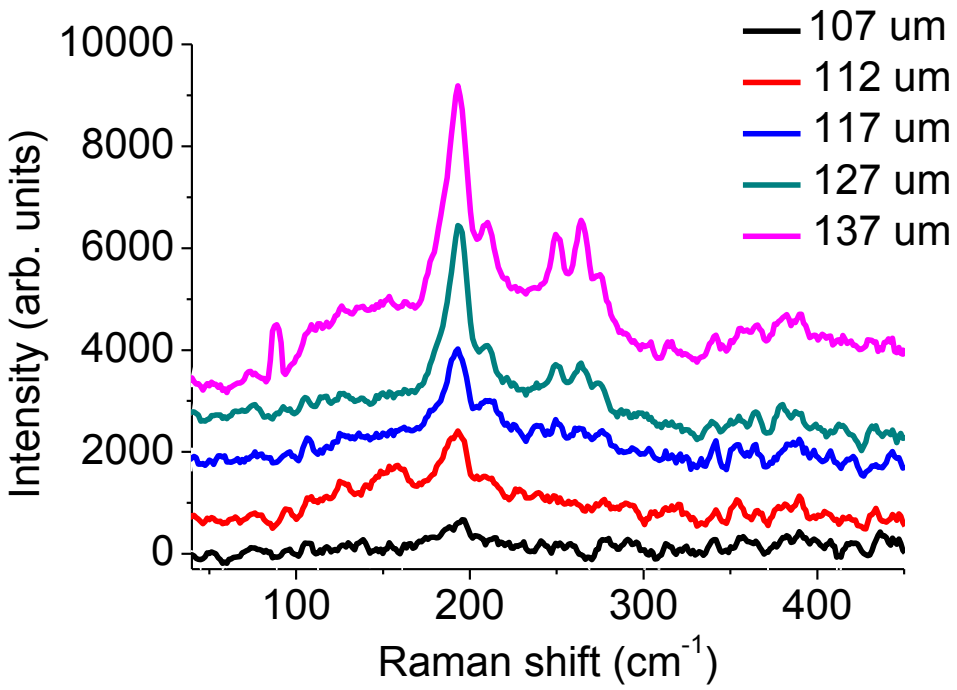

Figure 8.3: Raman spectra taken at increasing distances from the centre of the 0.41 TW/cm^{-1} spot in the north direction.

Figure 8.4 shows a similar set of Raman spectra but taken at increasing distances from the centre in the south direction. The same, ubiquitous RBM peaks are observed as well as a large, prominent peak at around 131 cm^{-1} (giving a tube diameter of 1.89 nm), at 112 μm from the centre, the same distance as the peak observed in the north spectra.

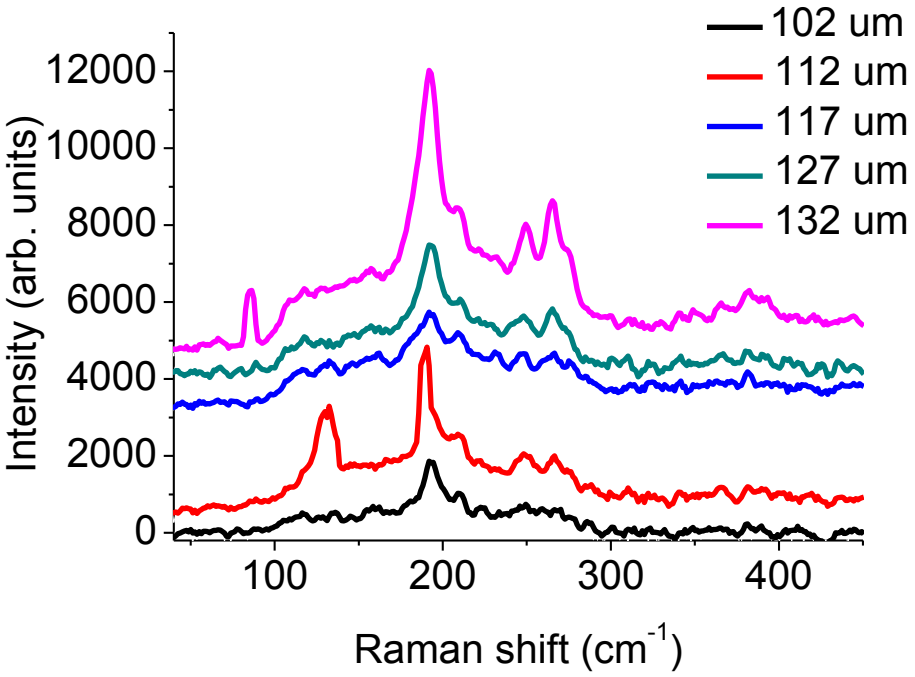

Figure 8.4: Raman spectra taken at increasing distances from the centre of the 0.41 TW/cm^{-1} spot in the south direction.

Figures 8.5 and 8.6 show Raman spectra taken at increasing distances in the east and west directions respectively. There are no smaller frequency RBM peaks as obvious as in the north and south spectra although small peaks appear at smaller shifts than the main peaks at 113 μm in the east spectra and 108 μm in the west spectra at Raman shifts of 156 and 161 cm^{-1} respectively (giving tube diameters of 1.59 and 1.54 nm).

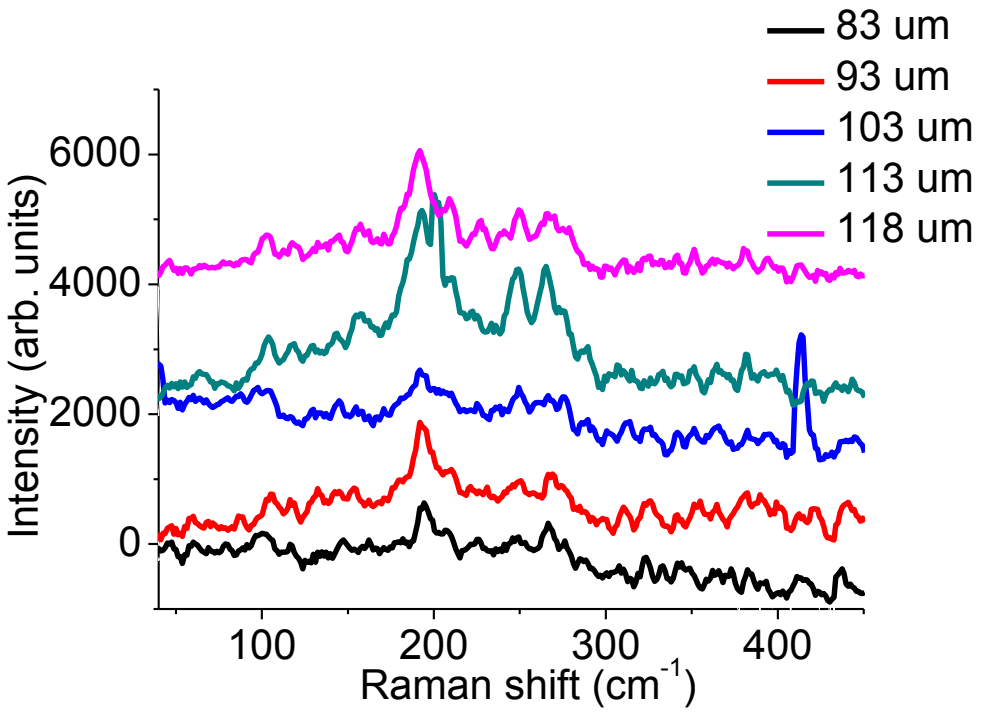

Figure 8.5: Raman spectra taken at increasing distances from the centre of the 0.41 TW/cm^{-1} spot in the east direction.

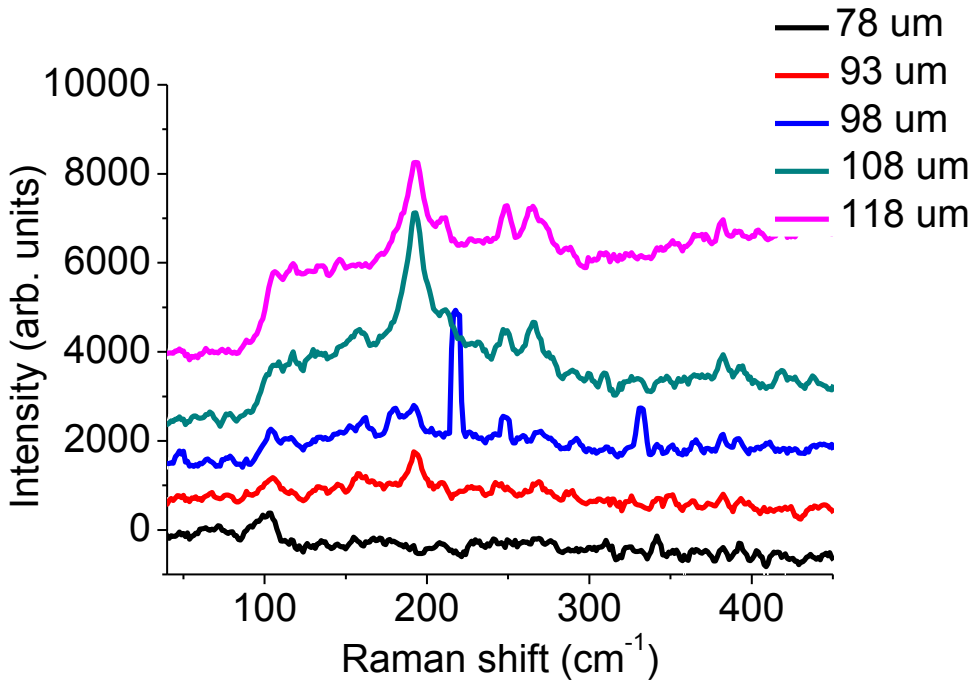

Figure 8.6: Raman spectra taken at increasing distances from the centre of the 0.41 TW/cm^{-1} spot in the west direction.

Figures 8.7 and 8.8 show Raman spectra taken at increasing distances in the west and east directions from the 0.67 ± 0.12 TW/cm^2 spot, respectively. The west spectra show a small, broad peak at 161 cm^{-1} (1.54 nm), 121 μm from the spot centre. A similar peak can be seen in the Raman spectrum 121 μm to the east of the spot centre at around 155 cm^{-1} (1.60 nm) although this does not seem to be as prominent and could be due to noise.

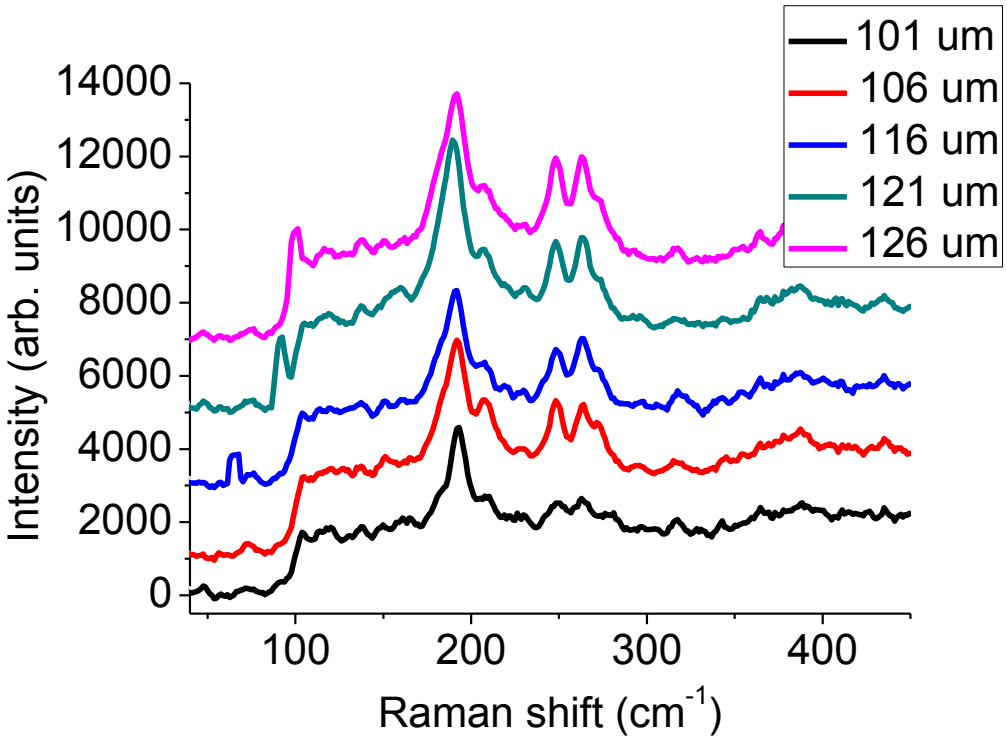

Figure 8.7: Raman spectra taken at increasing distances from the centre of the 0.67 TW/cm^{-1} spot in the west direction.

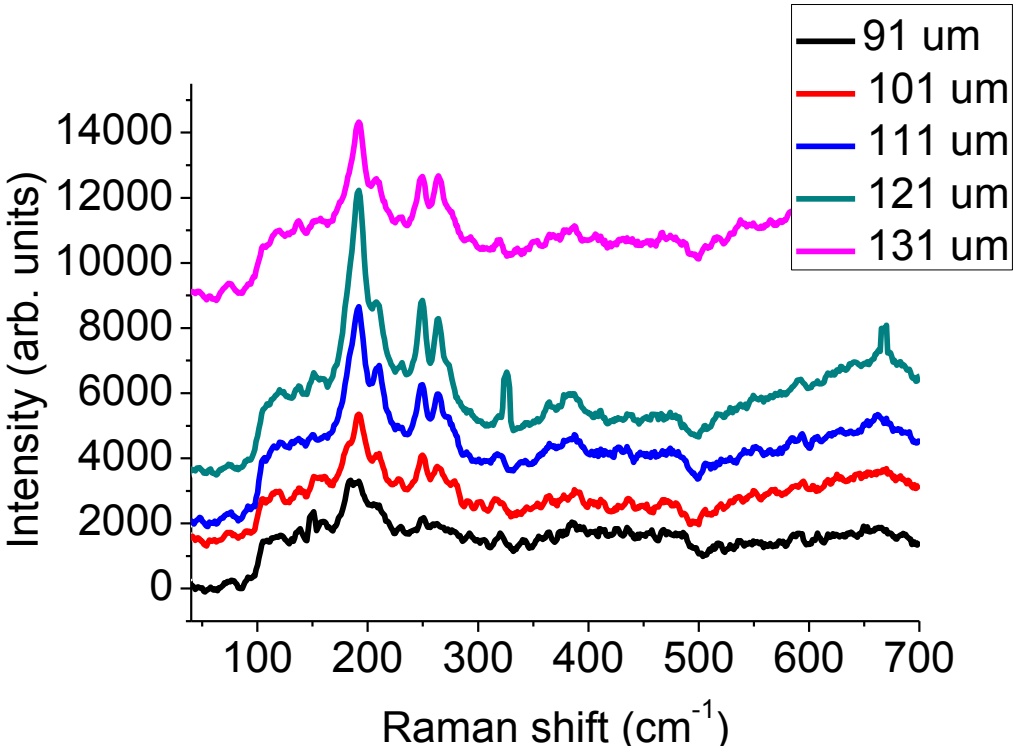

Figure 8.8: Raman spectra taken at increasing distances from the centre of the 0.67 TW/cm^{-1} spot in the east direction.

Figure 8.9 shows the corresponding spectra from the 0.67 TW/cm^2 spot from the north direction. No small shift RBM peaks can be identified in any of the spectra. The spectra to the south of the centre spot do not show any obvious small shift RBM peaks either.

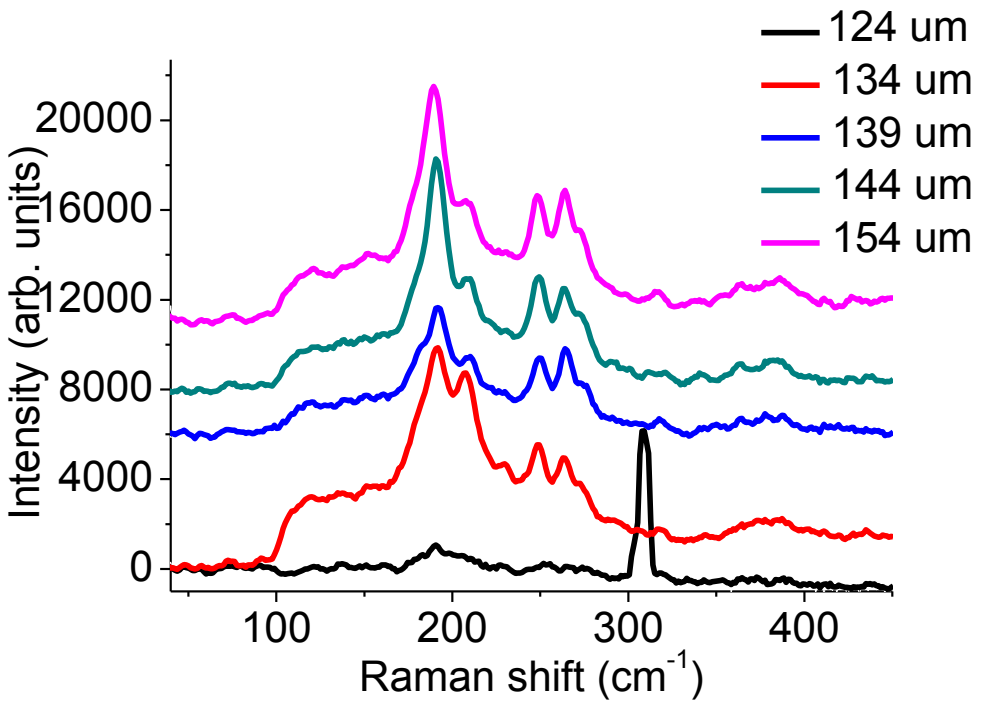

Figure 8.9: Raman spectra taken at increasing distances from the centre of the 0.67 TW/cm^{-1} spot in the north direction.

Figure 8.10 shows the spectra from the 1.44 ± 0.24 TW/cm^2 spot from the north direction in increasing radii. A small, broad peak at 155 cm^{-1} (1.60 nm) can be observed at 180 μm from the centre. No peak is observed south of the centre.

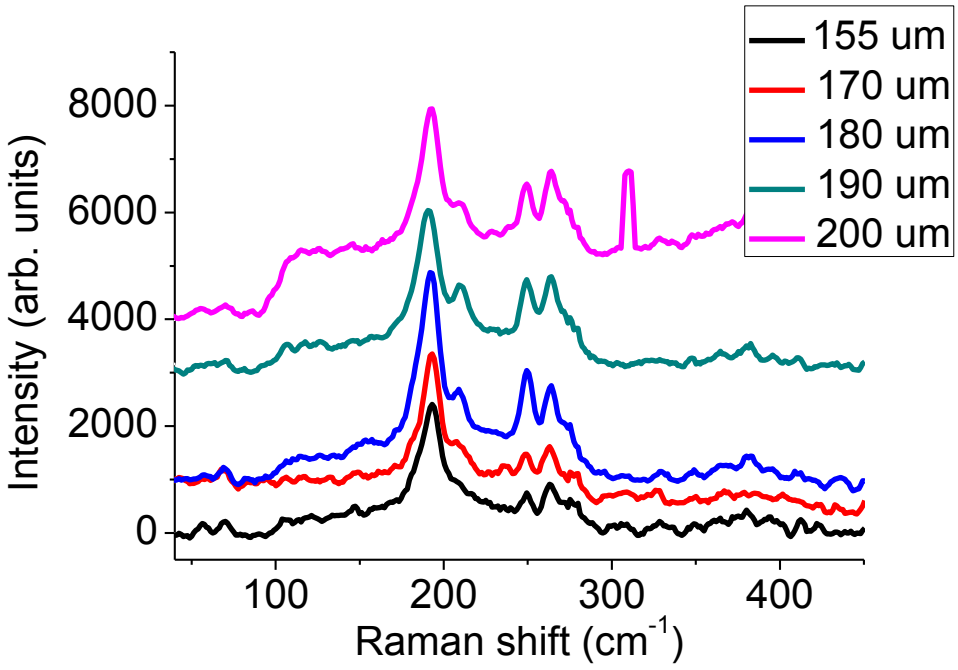

Figure 8.10: Raman spectra taken at increasing distances from the centre of the 1.44 TW/cm^{-1} spot in the north direction.

Figure 8.11 shows the spectra from the 1.44 TW/cm^2 spot from the east direction in increasing radii. A small, broad peak at 156 cm^{-1} (1.59 nm) can be observed at 170 μm from the centre. The spectra have not had a background subtracted but this should not affect the peak structure observed. No peaks are observed west of the centre.

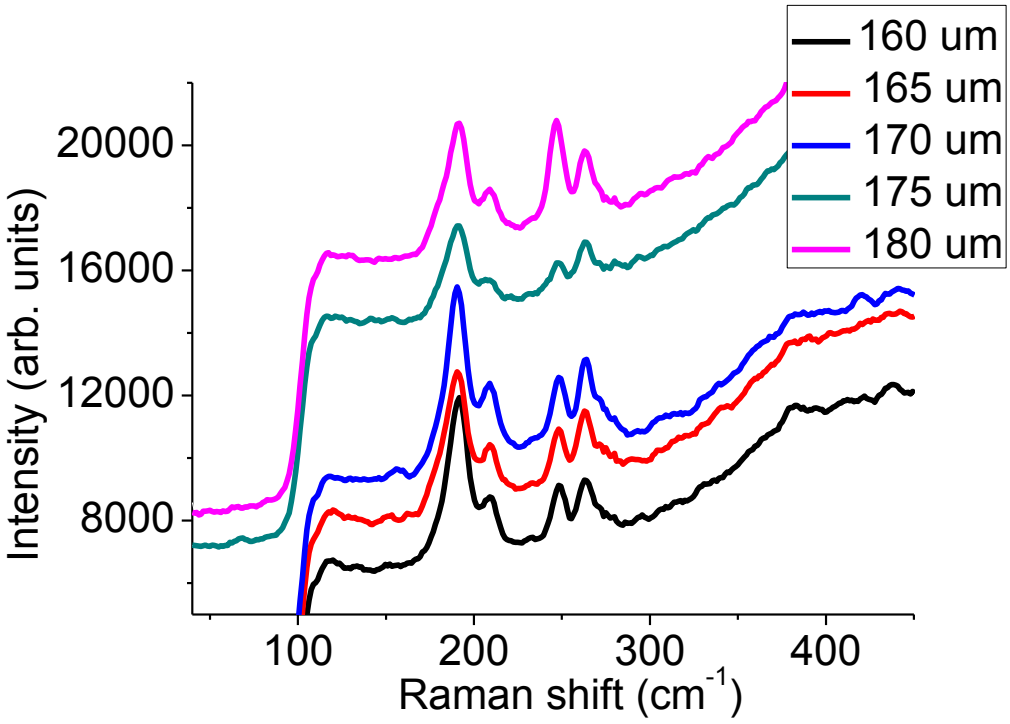

Figure 8.11: Raman spectra taken at increasing distances from the centre of the 1.44 TW/cm^{-1} spot in the east direction.

At first glance, the evidence for and pattern of low shift RBM peaks in areas irradiated by the laser spot is not overly convincing. However there is consistency in where the peaks are observed in relation to distance from the laser spot centre. For the 0.41 TW/cm^2 laser pulse, low shift RBM peaks are observed in all four directions at between 108 and 113 μm from the spot centre. With increasing laser intensity, the distance from the centre at which possible 'fusion' peaks emerge increases, as would be expected if fusion were to occur only around a narrow band of local laser intensities. With the 0.67 TW/cm^2 laser pulse, low shift RBM peaks are observed 121 μm to the east and west of the centre spot. With the 1.44 TW/cm^2 laser pulse, low shift RBM peaks are observed between 170 and 180 μm to the north and east of the centre spot. In all laser irradiation spots, the low frequency RBM peaks are observed immediately outside the visble 'damaged' area of the sample. Since the damaged areas appear as circles it is a reasonable assumption that the damage threshold is realtively uniform across the sample, we can say with some confidence that the low frequency peaks appear at areas which are subjected to the same local laser intensity. This supports the conclusion that these peaks are due to the fusion of carbon

nanotubes. The laser intensity at which fusion occurs is the highest available intensity which does not cause complete destruction of the nanotubes in the sample.

The majority of the low frequency RBM peaks appear at around 156 cm^{-1}, corresponding to a nanotube diameter of around 1.59 nm. Whilst clear peaks are not observed in every series recorded, it should be noted that the likelihood of observing peaks should be very dependent on the particular area of the sample irradiated. Factors such as the density of tubes and the degree of overlap between the two layers as well as Raman resonance conditions will play a significant part in determining whether fusion takes place and how easy to detect it is.

Across the area of the sample irradiated by the laser pulse, there is a Gaussian spatial intensity profile. The interpretation of the results presented is that the fusion of carbon nanotubes only occurs in a narrow region of the spatial intensity profile. If the intensity is too high, tubes are likely to be destroyed or ablated from the substrate surface. If the intensity is too low, the bond breakage required to facilitate fusion between tubes is unlikely to take place. This is the reason why possible fusion RBM peaks appear at roughly the same distance from the centre of the laser spot at the same overall laser pulse intensity and why the distance at which these peaks appear increases with increasing laser intensity. In an attempt to compare the intensities at the distances of interest, the Gaussian profiles of the laser pulses were calculated and the intensities at the distances corresponding to the emergence of low shift RBM peaks were determined.

Assuming a Gaussian pulse with a beam waist of 250 μm, the average intensity at the distances from the centre of the pulse corresponding to the distances at which low frequency RBM peaks were observed were calculated. Table 8.1 shows the average intensities calculated for each laser pulse.

Table 8.1: Average laser intensities calculated at the distances from the beam centre corresponding to the position of low frequency RBM peaks for each laser pulse.

Peak intensity of laser pulse (TW/cm^2)	Distance from beam centre at which low frequency RBM peaks were observed (μm)	Average intensity at distance which low frequency RBM peaks were observed at (TW/cm^2)
0.41 ± 0.07	111 ± 5	0.24 ± 0.04
0.67 ± 0.12	121 ± 5	0.34 ± 0.06
1.44 ± 0.24	175 ± 5	0.44 ± 0.08

The average intensities calculated are in reasonably close agreement but show an increase with increasing peak laser intensity. This may be due to the laser beam waist being overestimated. The initial beam waist measurement was carried out in a fairly unprecise manner due to the difficulties associated with carrying out a precise measurement and may have resulted in an overestimation of the beam waist. The measured beam waist was 250 ± 50 μm, if we were to assume the smallest beam waist within the errors of the initial measurement, a beam waist of 200 μm, this would result in average intensities at the distance at which low frequency RBM peaks appear of 0.28 ± 0.05 TW/cm^2, 0.41 ± 0.07 TW/cm^2 and 0.39 ± 0.07 TW/cm^2 for 0.63 TW/cm^2, 1.03 TW/cm^2 and 2.22 TW/cm^2 pulses respectively.

8.3 Conclusions

The resistance of buckypaper samples irradiated with ultrashort laser pulses was measured in an attempt to observe signs of fusion between carbon nanotubes. No evidence of fusion was observed in the resistance measurements. It is not clear whether this is because no fusion took place or that any drop in resistance brought about by fusion is too small to detect or whether other effects make any drop in resistance due to fusion too difficult to observe.

Samples consisting of orthogonally deposited nanotube layers were shot with single laser pulses and analysed with Raman spectroscopy in an attempt to observe fusion between nanotubes. The samples were prepared with the intention to carry out resistance measurements as well as Raman measurements but such large areas of the tube structure were destroyed by the laser pulse that this would have proved fruitless. A number of low frequency RBM peaks were observed at consistent distances from the beam centre for each laser spot which suggests tubes with larger diameters are present in these areas. Unirradiated areas of the sample show tube diameters in the range 0.94-1.29 nm (consistent with the size distribution of the commercial nanotube sample used) whereas tube diameters suggested by the lower frequency RBM peaks are typically around 1.59 nm (outwith the size range of the sample used). With increasing laser intensity, the distance from the beam centre at which these peaks appear increases but the peaks always appear just outside the visibly damaged area where no, or very few, tubes are present. This suggests that fusion is taking place at a specific, narrow, local intensity range. The laser beam area used in these experiments was not as accurately measured as it could have been, making an accurate estimate of the critical intensity value difficult. Repeat experiments with a more accurately measured beam area should help to determine whether the low frequency RBM peaks appear at a consistent laser intensity and what that intensity is.

Raman spectroscopy may not be the ideal method for detecting fusion in carbon nanotubes. Fusion may occur which does not result in a significant increase in tube diameter and it is not possible to determine the exact nature of the fusion taking place with this method. An imaging technique such as STM should provide a greater ability to determine wheather fusion has occurred and what the nature of that fusion is. Future experiments would benefit from a setup which allows laser irradiation and imaging of specific areas of the sample.

Chapter 9 – Conclusions & outlook

The ionisation mechanism of C_{60} and C_{70} with laser pulse durations from 50 fs up to a ps was investigated. Previous work has identified the mechanism on this timescale to be thermal in nature although initial VMI experiments carried out within the group identified an anisotropy in the electron distributions which speaks against a statistical ionisation mechanism. The primary focus of this work was to use VMI spectroscopy to determine of the mechanism was thermal or direct and what the root of the observed anisotropy is. Experimental apparent temperatures for a range of laser wavelengths, pulse durations and fluences were compared to those obtained from a thermal ionisation model and a close agreement was found between experiments and calculations. Therefore the results support a thermal ionisation mechanism on this timescale. The electron distributions observed display an anisotropy in the apparent temapertaure and in the number of electrons emitted, with more electrons and higher apparent temperatures measured along the laser polarisation axis. The anisotropy in the apparent temperatures was found to be almost linearly dependent on the ponderomotive energy, U_p, of the laser pulses used to ionise the molecule. This has been interpreted as being due to an angle-dependent momentum 'kick' imparted to the electrons emitted during the laser pulse. The electrons can receive this kick because they are not emitted in phase with the laser electric field. The increase in electron energy, due to the momentum kick, correpesonds to an energy between 0 and $2U_p$ depending on when the electron is emitted with respect to the maximum of the laser electric field and the increase in the measured apparent temperature was typically between U_p and $2U_p$. Pump-probe experiments were carried out with a 400 nm pump pulse, which causes only a small anisotropy, and a 900 nm probe pulse, which should cause a large anisotropy were it able to ionise C_{60} on its own. It was observed that the probe pulse causes significant anisotropy in the electron apparent temperature distributions when it overlaps or arrives shortly after the pump pulse, giving an indication of the timescale for electron emission and providing a convincing experimental demonstration of the statistical, delayed nature of the electron emission. The anisotropy in the number of electrons emitted was found to be due to a suppression of the ionisation barrier by the electric field of the laser pulse. This

anisotropy is only observed for 800 nm pulses, which have a longer period than those of shorter wavelengths. Experimental count ratios were compared to calculations based on an electric-field induced ionisation barrier suppression and a close agreement was found.

The thermal ionisation model used is a relatively simple one and it would be desirable to make improvements to it in order to make further comparisons to experimental results. The current model does not take the focal volume of the laser pulse into account or the Gaussian spatial intensity profile and so incorporating this into the model would be good. Also, the mechanism by which energy is transferred from the electronic system to the vibrational system is based on a simple exponential time dependency. This has been modified somewhat for the results presented in this thesis to include a dependency on electronic internal energy. Further work to accurately model the mechanism by which energy is transferred from the electronic system to the vibrational system would be beneficial.

The results presented confirm the initial interpretation that the underlying mechanism is thermal but that the laser field affects the photoelectron distribution. For the first time, experimental evidence for the timescale of thermal electron emission has also been presented in the form of ponderomotive streaking pump-probe results. A new understanding of how significant exciation of the electronic system allows field ionisation to be observed in large molecules below laser intensites predicted by the Keldysh parameter is also presented. These results provide a valuable insight into the ionisation dynamics of all large molecules and clusters and will help in the interpretation of experiments where such molecules are ionised. They also constitute a significant step forward in the understanding of the circumstances in which large molecules and clusters can be used in practical applications and future studies utilising techniques such as coherent control and high harmonic generation. Future work might focus on even shorter laser pulse durations than covered in this thesis and use similar techniques to determine what mechanisms are relevant on shorter timescales and if direct mechanisms can be used to control the ionisation of large molecules.

The peaks in the PES, superimposed on the thermal background, for C_{60} and C_{70} ionised with fs laser pulses over a range of wavelengths were investigated. The PADs for series of peaks were determined for wavelengths between 400 and 800 nm. The experimental results were compared to calculations carried out at the Universite de Liège and the anisotropy parameters and binding energies of the peaks observed were found to correspond well with those expected for ionisation from SAMO orbitals within the C_{60} molecule. Peaks corresponding to the s-SAMO, p-SAMO and s'-SAMO were indentified with another peak tentatively assigned as the d-SAMO. The fact that simple PADs can be attributed to these peaks suggests that the ionisation mechanism is not direct and may be due to a non-direct multiphoton ionisation mechanism. The SAMO peaks are so prominent in the spectra because their ionisation rates are predicted to be orders of magnitude higher than those of other excited states of similar energy.

The close agreenment with previous experimental studies of SAMOs in the sold state and with theoretical calculations gives significant weight to the interpretation that SAMOs have been identified for this first time in the gas pahse. Future work will focus on comparing the peaks observed for a range of larger fullerenes and endohedral fullernes. Comparison with theoretical calulcations will help determine if similar SAMO orbitals are observed in all fullerene molecules and what effect the molecular structure has on their energies and anisotropy parameters. Endohedral fullerenes, in particular, are predicted to have stabilised SAMO orbitals with higher binding energies. This may be important in developing applications based on SAMO oribitals within e.g. molecular electronics.

Experiments were carried out in an attempt to fuse carbon nanotubes together with ultrashort laser pulses. The resistance of buckypaper samples was measured whilst and after irradiation with laser pulses. Any fusion of nanotubes should increase conductivity through the sample and lower resistance. Although the resistance of the sample dropped during irradiation, no permanent change in resistance was measured. Either fusion was not achieved by this method of other effects made detecting the effects of fusion too difficult. Samples consiting of orthogonally deposited layers of carbon nanotubes were irradiated with single laser pulses and analysed with Raman spectroscopy to determine if signs of fusion could be observed. A number of low

frequency RBM peaks were observed at specific areas of the samples. This may indicate that, at a certain laser intensity (one low enough not to ablate the sample and high enough to cause bond breakage) fusion has occurred and tubes with a larger diameter are produced as a result. The measurements taken suggest that fusion may have taken place at areas of the sample where the local average intensity was somewhere in the region of between 0.24 and 0.44 TW/cm^2.

The laser beam area was not measured as accurately as possible during these experiments and so accurately determining the laser intensity used and therefore the laser intensity at the point at which low frequency RBM peaks were observed was difficult. It would be desirable to repeat the experiment whilst making a more accurate beam area measurement so that the intensity at which the peaks appear can be determined with more confidence. Once a reasonable determination of the laser intensity is made, carrying out similar experiments with a laser with a uniform intensity profile would be interesting to see if signs of fusion can be observed across large areas of a sample, rather than at a narrow distance range from the centre of the beam.

The results presented in this thesis represent an initial study into the fusion of carbon nanotubes with ultrafast laser pulses. Whilst the results are encouraging, future studies should incorporate imaging techniques into the experimental design in order to better gauge the extent and exact nature of any fusion taking place. Translation stages which give the opportunity to accurately control the focal size at the sample and the exact position of irradiation on the sample would also aid in this respect.

References

1. Dantus, M., Rosker, M.J., and Zewail, A.H., *Real-time Femtosecond probing of "transition states" in chemical reactions*. Journal of Chemical Physics, 1987. **87**(4): p.2395-2397.
2. Campbell, E.E.B., G. Ulmer, and I.V. Hertel, *Delayed ionization of C_{60} and C_{70}*. Physical Review Letters, 1991. **67**(15): p. 1986-1988.
3. Campbell, E.E.B., Hansen, K., Heden, M., Kjellberg, M., and Bulgakov, A.V., *Ionisation of fullerenes and fullerene clusters using ultrashort laser pulses*. Photochemical & Photobiological Sciences, 2006. **5**(12): p. 1183-1189.
4. Campbell, E.E.B., Hansen, K., Hoffman, K., Korn, G., Tchaplyguine, M., Wittman, M., and Hertel, I.V., *From Above Threshold Ionization to Statistical Electron Emission: The Laser Pulse-Duration Dependence of C_{60} Photoelectron Spectra*. Physical Review Letters, 2000. **84**(10): p. 2128-2131.
5. Hansen, K., K. Hoffman, and E.E.B. Campbell, *Thermal electron emission from the hot electronic subsystem of vibrationally cold C_{60}*. Journal of Chemical Physics, 2003. **119**(5): p. 2513-2522.
6. Kjellberg, M., Johnasson, O., Jonnson, F., Bulgakov, A.V., Bordas, C., Campbell, E.E.B., and Hansen, K., *Momentum-map-imaging photoelectron spectroscopy of fullerenes with femtosecond laser pulses*. Physical Review A, 2010. **81**(2): p. 023202.
7. Feng, M., Zhao, J., and Petek, H., *Atomlike, Hollow-Core-Bound Molecular Orbitals of C_{60}*. Science, 2008. **320**(5874):p. 359-362.
8. Boyle, M., Hoffman, K., Schulz, C.P., Hertel, I.V., Levine, R.D., and Campbell, E.E.B., *Excitation of Rydberg Series in C_{60}*. Physical Review Letters, 2001. **87**(27): p. 273401.
9. Bellucci, S., *Carbon nanotubes: physics and applications*. Physica Status Solidi (C), 2005. **2**(1): p 34-47.
10. Zou, H., Yang, Y., Li, Q., Zhang, J., Liu, Z., Guo, X., and Du, Z., *Electron beam-induced structure transformation of single-walled carbon nanotubes*. Carbon, 2002. **40**(12): p. 2282-2284.
11. Kroto, H.W., Heath, J.R., O'Brien, S.C., Curl, R.F., and Smalley, R.E., *C_{60}: Buckminsterfullerene*. Nature, 1985. **318**(6042): p. 162-163.
12. You, J.Q., Nori, F., Lin, Y.L., *Electronic structure of C_{60} and C_{70} molecules: Generating function approach*. Solid State Communications, 1994, **91**(2): p. 117-120.
13. Bucksbaum, P. H., Freeman, R.R., Bashkansky, M., and McIlrath, T.J., *Role of the ponderomotive potential in above-threshold ionization*. J. Opt. Soc. Am. B, 1987. **4**(5): p. 760-764.

14. Postumus, J.H., *The dynamics of small molecules in intense laser fields*. Reports on Progress in Physics, 2004. **67**(5): p. 623-665.

15. Keldysh, L.V., *Ionization in the field of a strong electromagnetic wave*. Soviet Physics JETP, 1965. **20**(5): p. 1307-1314.

16. Agostini, P., Fabre, F., Mainfray, G., and Petite, G., *Free-Free Transitions Following Six-Photon Ionization of Xenon Atoms*. Physical Review Letters, 1979. **42**(17): p. 1127-1130.

17. Hansen, K., and Campbell, E.E.B., *Radiative cooling of fullerenes*. Journal of Chemical Physics, 1996. **104**(14): p. 5012.

18. Anisimov, S.I., Kapeliovitch, B.L. and Perel'man, T.L., *Electron emission from metal surfaces exposed to ultrashort laser pulses*. Soviet Physics JETP, 1974. **39**(2): p. 375-377.

19. Campbell, E.E.B., T. Raz, and R.D. Levine, *Internal energy dependence of the fragmentation patterns of C_{60} and C_{60}^+*. Chemical Physics letters, 1996. **253**: p. 261-267.

20. Weidele, H., Kreisle, D., Recknagel, E., Schulze Icking-Konert, G., Handschuh, H, Gantefor, G., and Eberhardt, W., *Thermionic emission from small clusters: direct observation of the kinetic energy distribution of the electrons*. Chemical Physics Letters, 1995. **237**(5-6): p. 425-431.

21. Boyle, M., *Energy Adsorption and Redistribution Dynamics in Isolated C_{60} Molecules*. 2005. PhD Thesis, Freie Universitat Berlin.

22. Shchatsinin, I., Laarman, T., Stibenz, G., Steinmeyer, G., Stalmashonak, A., Zhavorankov, N., Schulz, C.P., and Hertel, I.V., *C_{60} in intense short laser fileds down to 9 fs: Excitation on time scales below e-e and e-phonon coupling*. The Journal of Chemical Physics. 2006. **125**(19): p 194320.

23. Verlet, J.R.R., *Femtosecond spectroscopy of cluster anions: insights into condensed-phase phenomena from the gas-phase.* Chemical Society Reviews, 2008. **37**(3): p. 505-517.

24. Bhardwaj, V.R., Corkum, P.B., and Rayner, D.M., *Recollision during the High Laser Intensity Ionization of C_{60}*. Physical Review Letters. 2004. **93**(4): p. 043001.

25. Tchaplyguine, M., Hoffmann, K., Duhr, O., Hohmann, H., Korn, G., Rottke, H., Wittmann, M., Hertel, I.V., and Campbell, E.E.B., *Ionization and fragmentation of C_{60} with sub-50 fs laser pulses*. Journal of Chemical Physics, 2000. **112**(6): p. 2781-2789.

26. Hoffman, K., *Femtosekunden-Laserspektrosopie an Fullerenen, in Fachbereich Physik*. 2000 PhD Thesis. Freie Universitat Berlin: Berlin.

27. Bauer, D. Ceccherini, F., Macchi, A., and Cornolti, F., *C_{60} in intense femtosecond laser pulses: Nonlinear dipole response and ionization*. Physical Review A, 2001. **64**(6): p. 063203.

28. Bhardwaj, V.R., Corkum, P.B., and Rayner, D.M., *Internal Laser-Induced Dipole Force at Work in C_{60} Molecule*. Physical Review Letters. 2003. **91**(20): p. 203004.

29. Jaron-Becker, A., Becker, A., Faisal, F.H.M., *Single-active-electron ionization of C_{60} in intense laser pulses to high charge states*. The Journal of Chemical Physics. 2007. **126**: p. 124310.

30. Zhang, G.P., *Hartree-Fock Dynamical Electron-Correlation Effects in C_{60} after Laser Excitation*. Physical Review Letters. 2003. **91**(17): p. 176801.

31. Zhang, G.P., and George, T.F., *Manifestation of electron-electron interactions in time-resolved ultrasfast pump-probe spectroscopy in C_{60}: Theory*. Physical Review B. 2007. **76**: p. 085410.

32. Lezius, M., Blanchet, V., Rayner, D.M., Villeneuve, D.M., Stolow, A., and Ivanov, M.Y., *Nonadiabatic Multielectron Dynamics in Stong Field Molecular Ionization*. Physical Review Letters, 2001. **86**(1): p. 51-54.

33. Lezius, M., Blanchet, V., Ivanov, M.Y., and Stolow, A., *Polyatomic molecules in strong laser fields: Nonadiabatic multielectron dynamics*. Journal of Chemical Physics, 2002. **117**(4): p. 1575-1588.

34. Markevich, A.N., Romanov, D.A., Smith, S.M., Schlegel, H.B., Ivanov, M.Y., and Levis, R.J., *Sequential nonadiabatic excitation of large molecules and ions driven by strong laser fields*. Physical Review A. 2004. **69**(1): p. 0131401.

35. Hertel, I., V., Shchtsinin, I., Laarman, T., Zhavoronkov, N., Ritze, H.H., and Schulz, C.P., *Fragmentation and Ionization Dynamics of C_{60} in Elliptically Polarized Femtosecond Laser Fields*. Physical Review Letters. 2009. **102**(2): p. 203003.

36. Shchatsinin, I., Laarman, T., Zhavoronkov, N., Schulz, C.P., and Hertel, I.V., *Ultrafast energy redistribution in C_{60} fullerenes: A real time study by two-color femtosecond spectroscopy*. The Journal of Chemical Physics. 2008. **129**(20): p. 204308.

37. Laarmann, T., Shchatsinin, I., Stalmashonak, A., Boyle, M., Zhavoronkov, N., Handt, J., Schmidt, R., Schulz, C.P., and Hertel, I.V., *Control of Giant Breathing Motion in C_{60} with Temporally Shaped Pulses*. Physical Review Letters. 2007. **98**(5): p – 058302.

38. Anderson, J.U., Bonderup, E. and Hansen, K. *Thermionic emission from clusters.* Journal of Physics B: At. Mol. Opt. Phys., 2002. **35**: p. R1-30.

39. Schlipper, R., Kusche, R., von Issendorff, B., and Haberland, H., *Thermal emission of electrons from highly excited sodium clusters*. Applied Physics A, 2001. **72**(3): p. 255-259.

40. Maier, M., Hoffmann, M.A., and von Issendorf, B., *Thermal emission of electrons from highly excited Na_{16}^{+} to Na_{250}^{+}*. New Journal of Physics, 2003. **5**: p. 3.1-3.7.

41. Pontius, N., Luttgens, G., Bechthold, P.S., Neeb, M., and Eberhardt, W., *Size-dependent hot-electron dynamics in small Pd_n^- clusters*. Journal of Chemical Physics, 2001. **115**(22): p 10479-10483.

42. DeWitt, M.J. and Levis, R.J., *Observing the Transition from a Multiphoton-Dominated to a Field–mediated Ionization Process for Polyatomic Molecules in Intense Laser Fields*. Physical Review Letters, 1998. **81**(23): p.5101.

43. Kjellberg, M., Bulgakov, A.V., Goto, M., Johansson, O., and Hansen, K., *Femtosecond electron spectroscopy of coronene, benzo[GHI]perylene, and anthracene*. The Journal of Chemical Physics, 2010. **133**(7): p. 074308.

44. Goto, M., and Hansen, K., *Competitive ionization processes of anthracene with a Femtosecond pulse in the multi-photon ionization regime*. Journal of Chemical Physics, 2011. **135**(21): p. 214310.

45. Boyle, M., Laarmann, K., Hoffmann, M., Heden, M., Campbell, E.E.B., Schulz, C.P., and Hertel, I.V., *Excitation dynamics of Rydberg states in C_{60}*. The European Physical Journal D. 2005. **36**(3): p. 339-351.

46. Boyle, M., Heden, M., Schulz, C.P., Campbell, E.E.B., and Hertel, I.V., *Two-colour pump-probe study and internal-energy dependence of Rydberg-state excitation in C_{60}*. Physical Review A, 2004. **70**(5): p. 051201.

47. Freeman, R.R., Bucksbaum, H., Milchberg, H., Darack, S., Schumacher, D., and Geusic, M.E., *Above-threshold ionization with subpicosecond laser pulses*. Physical Review Letters, 1987. **599**10): p. 1092.

48. Wesdorp, C., Robicheaux, F., Noordam, L.D., *Rydberg carbon clusters prepared by pulsed field recombination*. Chemical Physics Letters. 2000. **323**: p. 192-197.

49. Schick, C.P., and Weber, P.M., *Ultrafast Dynamics in the Three-Photon, Double-Resonance Ionization of Phenol via the S2 Electronic State*. Journal of Physical Chemistry A, 2001. **105**(15): p. 3735-3740.

50. Remacle, F., and Levine, R.D., *On the Inverse Born-Oppenheimer Separation for High Rydberg States of Molecules*. Journal of Quantum Chemistry, 1998. **67**(2): p. 85-100.

51. Lassesson, A., Hansen, K., Jonsson, M., Gromov, A., Campbell, E.E.B., Boyle, M., Pop, D., Schulz, C.P., Hertel, I.V., Taninaka, A., and Shinohara, H., *A Femtosecond laser study of the endohedral fullerenes $Li@C_{60}$ and $Li@C_{82}$*. European Physical Journal D: At. Mol. Opt. Phys., 2005. **34**(1-3): p. 205-209.

52. Gosselin, J.L., and Weber, P.M., *Rydberg Fingerprint Spectroscopy: A New Spectroscopic Tool with Local and Global Structural Sensitivity*. Journal of Physical Chemistry, 2005. **109**(22): p. 4899-4904.

53. Silkin, V.M., Zhao, J., Giunea, F., Chulkov, E.V., Echenique, P.M., and Petek, H., *Image potential states in graphene*. Physical Review B, 2009. **80**(12): p. 121408.

54. Zhao, J., Feng, M., Yang, J., and Petek, H., *The Superatom States of Fullerenes and Their Hybridization into the Nearly Free Electron Bands of Fullerites*. ACS Nano, 2009. **3**(4): p. 854-864.

55. Feng, M., Huang, T., Zhu, X., and Petek, H., *The Electronic Properties of Superatom States of Hollow Molecules*. Accounts of Chemical Research, 2010. **44**(5): p. 360-368.

56. Iijima, S., *Helical microtubes of graphitic carbon*. Nature, 1991. **354**(6348): p. 56- 568.

57. Salvetat, J.P., Kulik, A.J., Bonard, J., Briggs, A., Stockli, T., Meterier, K., Bonnamy, S., Beguin, F., Burnham, N.A., and Forro, L., *Elastic Modulus of Ordered and Disordered Multiwalled Carbon Nanotubes*. Advanced Materials, 1999. **11**(2): p. 161-165.

58. Mann, D., Javey, A., Kong, J., Wang, Q., and Dai. H., *Ballistic Transport in Metallic Nanotubes with Reliable Pd Ohmic Contacts*. Nano Letters, 2003. **3**(11): p. 1541-1544.

59. Wei, B.Q., Vajtai, R. and Ajayan, P.M., *Relaibility and current carrying capacity of carbon nanotubes*. Applied Physics Letters, 2001. **79**(8): p. 1172-1174.

60. Globus, A., Bailey, D., Han, J., Jaffe. R., Levit, C., Merkle, R., and Srivaslava, D., *NASA applications of molecular technology*. The Journal of the British Interplanetary Society, 1998. **51**: p. 145-152.

61. Chen, K.H., Wu, C.T., Hwang, J.S., Wen, C.Y., Chen, L.C., Wang, C.T., and Ma, K.J., *Electron beam induced formation of carbon nanorods*. Journal of Physics and Chemistry of Solids, 2001. **62**(9-10): p. 1561-1565.

62. Ho, G.W., Wee, A.T.S. and Lin, J. *Electric field-induced carbon nanotube junction formation*. Applied Physics Letters, 2001.**79**(2): p. 260-262.

63. Terrones, M., Banhart, F., Grobert, N., Charlier, J.C., Terrone, H., and Ajayan, P.M., *Molecular Junctions by Joining Single-Walled Carbon Nanotubes*. Physical Review Letters, 2002. **89**(7): p. 075505.

64. Romo-Herrera, J.M., Terrones, M., Terrones, H., Dag, S., and Meunier, V., *Covalent 2D and 3D Networks from 1D Nanostructures: Designing New Materials*. Nano Letters, 2007. **7**(3): p. 570-576.

65. Heden, M., Hansen, K., and Campbell, E.E.B., *Molecular fusion of (C_{60})N clusters in the gas phase after femtosecond laser irradiation*. Physical Review A, 2005. **71**(5): p. 055201.

66. Kjellberg, M., *Ionization of large molecules with ultrashort laser pulses*. PhD Thesis. 2010, University of Gothenburg.

67. Johansson, O., *Angle-resolved femtosecond photoelectron spectroscopy of fullerenes*. 2010. PhD thesis, University of Edinburgh.

68. Kruit, P. and Read, F.H., *Magnetic field parallerliser for 2π electron-spectrometer and electron-image magnifier*. Journal of Physics E: Scientific Instruments, 1983. **16**(4): p. 313.

69. Reid, K.L., *Photoelectron Angular Distributions*. Annual Review of Physical Chemistry, 2003. **54**: p. 397-424.

70. Horke, D.A., Chatterly, A.S., and Verlet, J.R.R., *Femtosecond Photoelectron Imaging of Aligned Polyanions: Probing Molecular Dynamics through the Electron-Anion Coulomb Repulsion*. J. Phys. Chem. Lett., 2012. **3**(7): p. 834-838.

71. Helm, H., Bjerre, N., Dyer, M.J., Huestis, D.L., and Saeed., M., *Images of Photoelectrons Formed in Intense Laser Fields*. Physical Review Letters, 1993. **70**(21): p. 3221-3224.

72. Eppink, A.T.J.B. and Parker, D.H., *Velocity map imaging of ions and electrons using electrostatic lenses: Application in photoelectron and photofragment ion imaging of molecular oxygen*. Review of Scientific Instruments, 1997. **68**(9): p. 3477-3484.

73. Whitaker, B., ed. *Imaging in Molecular Dynamics, Technology and Applications (A User's Guide)*. 2003, Cambridge University Press: New York.

74. Bracewell, R.N., *The Fourier Transform and its Applications*. Third ed. 2000: McGraw-Hill.

75. Dribinski, V., Ossadtchi, A., Mandelshtam, V.A., and Reisler, H., *Reconstruction of Abel-transformable images: The Gaussian basis-set expansion Abel transform method*. Review of Scientific Instruments, 2002. **73**(7): p. 2643-2642.

76. Garcia, A.G., Laurent, N. and Powis, I., *Two-dimensional charged particle image inversion using a polar basis function expansion*. Review of Scientific Instruments, 2004. **75**(11): p. 4989-4996.

77. Roberts, G.M., Nixon, J.L., Lecointre, J., Wrede, E., and Verlet, J.R.R., *Toward real-time charged-particle image reconstruction using polar onion-peeling*. Review of Scientific Instruments, 2009. **80**(5): p. 053104.

78. Zhao, K., Colvin, T., Hill, W.T., and Zhang, G., *Deconvolving two-dimensional images of three-dimensional momentum trajectories*. Review of Scientific Instruments, 2002. **73**(8): p. 3044.

79. *NIST: Atomic Spectra Database Line Form* 2012, National Institute of Standards and Technology.

80. *CRC Handbook of Chemistry and Physics*. 88 ed, ed. D. Lide. 2007-2008: CRC Press.

81. Wiley, W.C., and McLaren, I.H., *Time-of-Flight Mass Spectrometer with Improved Resolution*. Review of Scientific Instruments, 1955. **26**(12): p. 1150-1157.

82. Rulliere, C., ed. *Femtosecond Laser Pulses – Principles and Experiments*. Second ed. 2005, Springer.

83. Vasa, N.J., Tanaka, M., Okada, T., Maeda, M., and Uchino, O., *Comparative study of spectral narrowing of a pulsed Ti:Sapphire laser using pulsed and CW injection seeding*. Applied Physics B, 1996. **62**: p. 51-57.

84. Raghuramaiah, M., Sharma, A.K., Naik, P.A., Gupta, P.D., and Ganeev, R.A., *A second-order autocorrelator for single-shot measurement of femtosecond laser pulse durations*. Sadhana, 2001. **26**(2): p. 603-611.

85. Liu, J.M., *Simple technique for measurements of pulsed Gaussian-beam spot sizes*. Optics Letters, 1982. **7**(5): p. 196-198.

86. Kaminski, P., Wiehle, R., Renard, V., Kazmierczak, A., Lavorel, B., Faucher, O., and Witzel, B., *Wavelength dependence of multiphoton ionization of xenon*. Physical Review A, 2004. **70**: p 053413.

87. Schyja, V., Lang, T. and Helm, H., *Channel switching in above threshold ionization of xenon.* Physical Review A, 1998. **57**(5):p. 3692.

88. Liu, J., et al., *Fullerene Pipes*. Science, 1998. **280**(5367): p. 1253-1256

89. Nouri, N., and Ziaei-Rad, S., *Mechanical Property Evaluation of Carbon Nanotube Sheets*. Transaction F: Nanotechnology, 2010. **17**(2): p. 90-101.

90. L., J., van der Pauw, *A method of measuring specific resistivity and Hall effect of discs of arbitrary shape*. Philips Research Report, 1958. **13**(1): p. 1-9

91. H., Ko., S., Peleshanko and V., V., Tsukruk. *Combing and Bending of Carbon Nanotube Arrays with Confined Microfluidic Flow on Patterened Surfaces*. Journal of Physical Chemistry B, 2004. **108**: p 4385 – 4393

92. M., S., Dresselhaus., Dresselhaus, G., Saito, R., and Jorio, A., *Raman spectroscopy of carbon nanotubes*. Physics Reports, 2005. **409**(2): p. 47-99

93. Dunseith, D., *Fusion of Carbon Nanotubes With a Femtosecond Laser*. 2011. Masters report , University of Edinburgh.

94. C., V., Raman, *A new radiation*. Indian Journal of Physics, 1928. **2**.

95. S., Costa., Borowiak-Palen, E., Kruzynska, M., Bachmatiuk, A., and Kalenczuk, R.J., *Characterization of carbon nanotubes by Raman spectroscopy*. Materials Science Poland, 2008. **26**(2): p. 433-441

96. A., Jorio., Saito, R., Hafner, J.H., Lieber, C.M., Hunter, M., McClure, T., Dresselhaus, G., and Dresslehaus, M.S., *Structural (n, m) Determination of Isolated Single-Wall Carbon Nanotubes by Resonant Raman Scattering*. Physical Review Letters, 2001. **86**(6): p 1118.

97. Weber, J.M., Hansen, K., Ruf, M.W., and Hotop, H., *Penning ionization of C_{60} and C_{70}*. Chemical Physics, 1998. **239**: 271-286.

98. Weisskopf. V., *Statistics and nuclear reactions*. Physical Review A, 1937. **52**: p. 295-303.

99. Hansen, K., *Probing energy and time scales by thermionic emission. AIP Conference Proceedings*, 1997. **416**: 131-138.

100. Lin, Z., Zhigilei, L.V., and Celli, V., *Electron-phonon coupling and electron heat capacity of metals under conditions of strong electron-phonon nonequilibrium*. Physical Review B, 2008. **77**(7): p. 075133.

101. Moos, G., Fasel, R., and Hertel, T., *Temperature Dependence of Electron to Lattice Energy-Transfer in Single-Wall Carbon Nanotube Bundles*. Journal of Nanoscience and Nanotechnology, 2003. **3**(1/2): p. 145-149.

102. Orlandini, G., and Negri, F., *Electronic states and transitions in C_{60} and C_{70} fullerenes*. Photochemical & Photobiological Sciences, 2002. **1**(5): 289-308

103. Corkum, P.B., Burnett, N.H., and Brunel, F., *Above-Threshold Ionization in the Long-Wavelength Limit*. Physical Review Letters, 1989. **62**(11): p. 1259-1262.

104. Fedor, J., *Personal communication*, 2012.

105. Toma, E.S., Muller, H.G., Paul, P.M., Breger, P., Cheret, M., Agostini, P., Le Blanc, C, Mullot, G., Cheriaux, G., *Ponderomotive streaking of the ionization potential as a method for measuring pulse durations in the XUV domain with fs resolution*. Physical Review A, 2000. **62**: p. 061801.

106. Cooper, J., and Zare, R.N., *Angular Distribution of Photoelectrons*. Journal of Chemical Physics, 1968. **48**(2): p. 942-943.

107. White, M.G., Chupka, W.A., Seaver, M., Woodward, A., and Colson, S.D., *Resonant multiphoton ionization of NO via the $A^2\Sigma^+$ state: Photoelectron spectra and angular distributions*. The Journal of Chemical Physics, 1984. **80**(2): p. 678-686.

108. Dixit, S.N., and Lambropoulos, P., *Theory of photoelectron angular distributions in resonant multiphoton ionization*. Physical Review A, 1983. **27**(2): p. 861-874.

109. Brar, V.W., Samonidze, G.G., Santos, A.P., Chou, S.G., Chattopadhyay, D., Kim, S.N., Papadimitrakopoulos, F., Zheng, M., Jagota, A., Onoa, G.B., Swan, A.K., Unlu, M.S., Goldberg, B.B., Dresselhaus, G., and Dresselhaus, M.S., *Resonance Raman Spectroscopy Cahracterization of Single-Wall Carbon Nanotube Seperation by their Metallicity and Diameter*. Journal of Nanoscience and Nanotechnology, 2005. **5**(2): p. 209-228.

110. Deng, J-P., Ju, D.D., Har, G.R., Mou, C.Y., Chen, C.J., Lin, Y.Y., and Han, C.C., *Odd-Numbered Fullerene Fragment Ions from C_{60} Oxides*. Journal of Physical Chemistry, 1993. **97**(45): p. 11575-11577.

111. Johansson, O., *Personal communication*. 2011

Appendix A – Metastable fragmentation

In C_{60} mass spectra for some high laser power experiments, small peaks were present, between the peaks representing the even-numbered fullerene fragments, at positions where odd-numbered fullerene fragments would be expected were they to be produced in the experiment (Figure A.1). Production of odd-numbered fullerene fragments are unexpected as they do not have a closed structure and are therefore unstable although odd-numbered fullerene anions have been detected previously [110]. In previous studies of C_{60}, using nanosecond or picosecond laser pulses, peaks appear on the small mass side of even-numbered fullerene peaks due to the metastable fragmentation of the ion in the field-free region of a reflectron Time-of-Flight mass spectrometer [3]. Metastable fragmentation peaks have also been observed for shorter laser pulse durations, 35 fs, using a reflectron TOF mass spectrometer, where the position of the peaks can be tuned until they are clearly visible [25]. Calculations were carried out by Olof Johansson to determine if it is possible to observe peaks in the TOF spectra due to metastable fragments [111] and the calculations were compared to experimental results to determine whether the peaks were due to metastable fragments or promptly created odd-numbered fullerene ions.

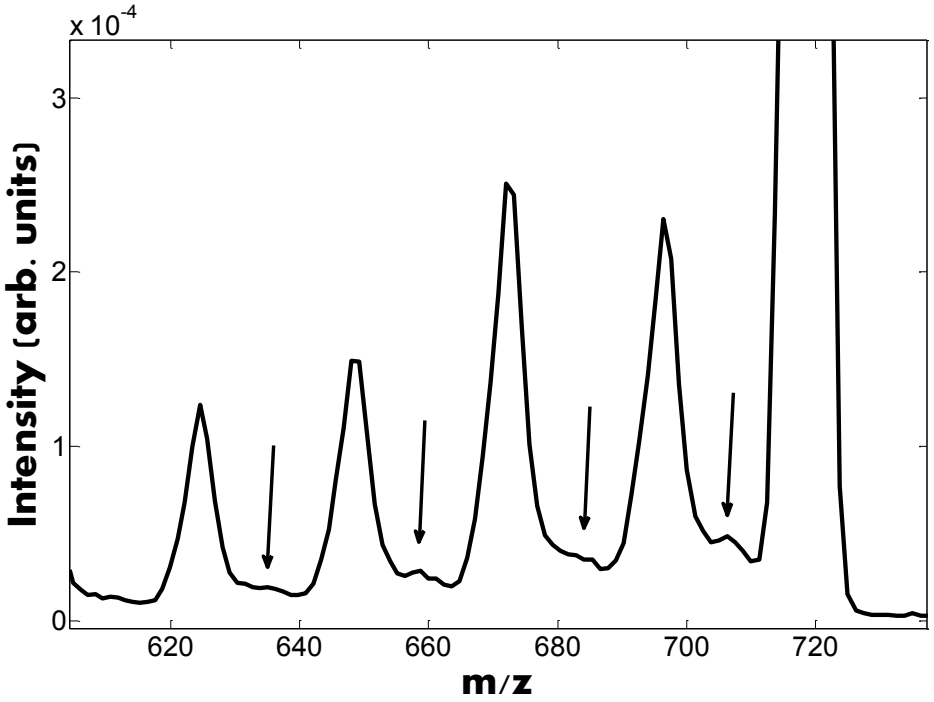

Figure A.1: Mass spectra of C_{60} ionised by 400 nm, 130 fs, 8.6 μJ pulses. Peaks appearing at m/z values corresponding to odd-numbered fullerenes are highlighted.

The calculation was based on determining the time-of-flight of a C_{60}^+ ion which decays to a C_{58}^+ ion, as a function of the distance travelled, from the point of origin, before fragmentation takes place. The following assumptions were made: Ions are created at the origin, equidistant between HV_1 and HV_2 electrodes. C_{60}^+ is produced promptly. The decay from C_{60}^+ to C_{58}^+ follows an exponential decay in time, $\exp(-kt)$. The time-of-flight of the fragment produced from a C_{60}^+ ion would not change significantly if it decayed in the drift region of the TOF. The potential energy as a function of distance from the origin in the extraction region of the TOF is shown in Figure A.2.

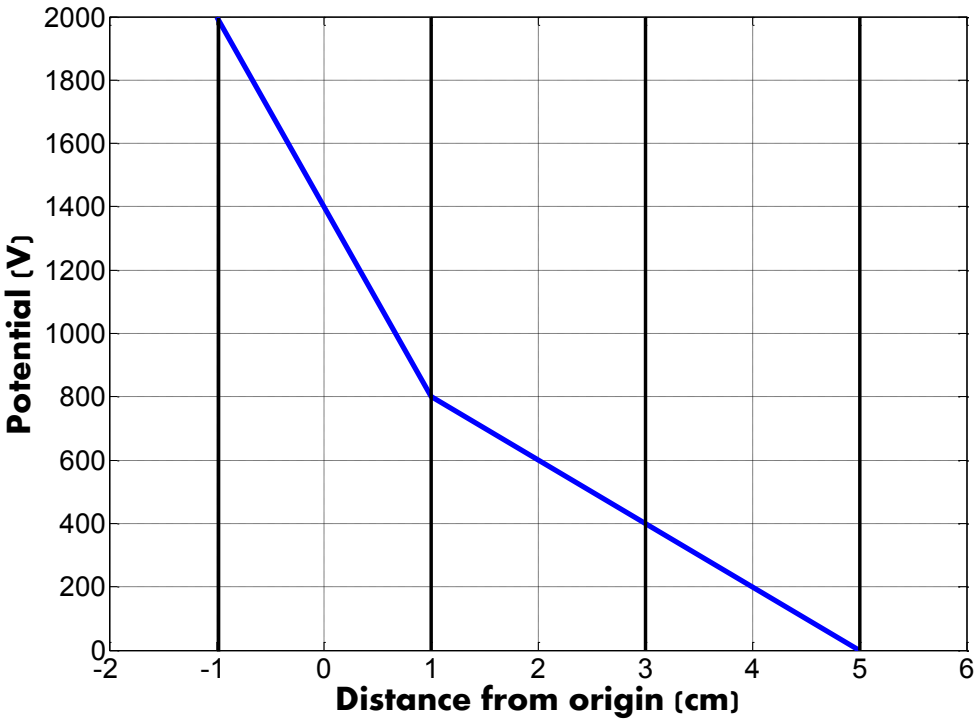

Figure A.2: Potential energy as a function of distance form the origin (0 cm) in the extraction region of the TOF mass spectrometer when HV_1 = 2000 V and HV_2 = 800 V. HV_1 sits at -1 cm from the origin, HV_2 at 1 cm, $HV_2/2$ at 3 cm, G_2 at 5 cm and beyond is the field-free region.

Figure A.3 shows the time-of-flight for a metastable ion as a function of the 'birth' distance from the origin, in a TOF mass spectrometer where HV_1 = 2000 V and HV_2 = 800 V. On the graph, times-of-flight for C_{60}^+, C_{59}^+ and, promptly created, C_{58}^+ are also shown. Since these ions do not decay between the point of 'birth' at the origin and the drift region, they have a well defined and unchanging time-of-flight. It can be seen, however, that the time-of-flight of the metastable C_{58}^+ ion does depend on where it is 'born' from the decay of the C_{60}^+ ion. The further from the origin it decays, the longer it's time-of-flight will be. This is because metastable C_{58}^+ ions which decay further from the origin will have spent more time as a heavier C_{60}^+ ion and therefore have undergone a lower acceleration, than ions which decayed closer to the origin.

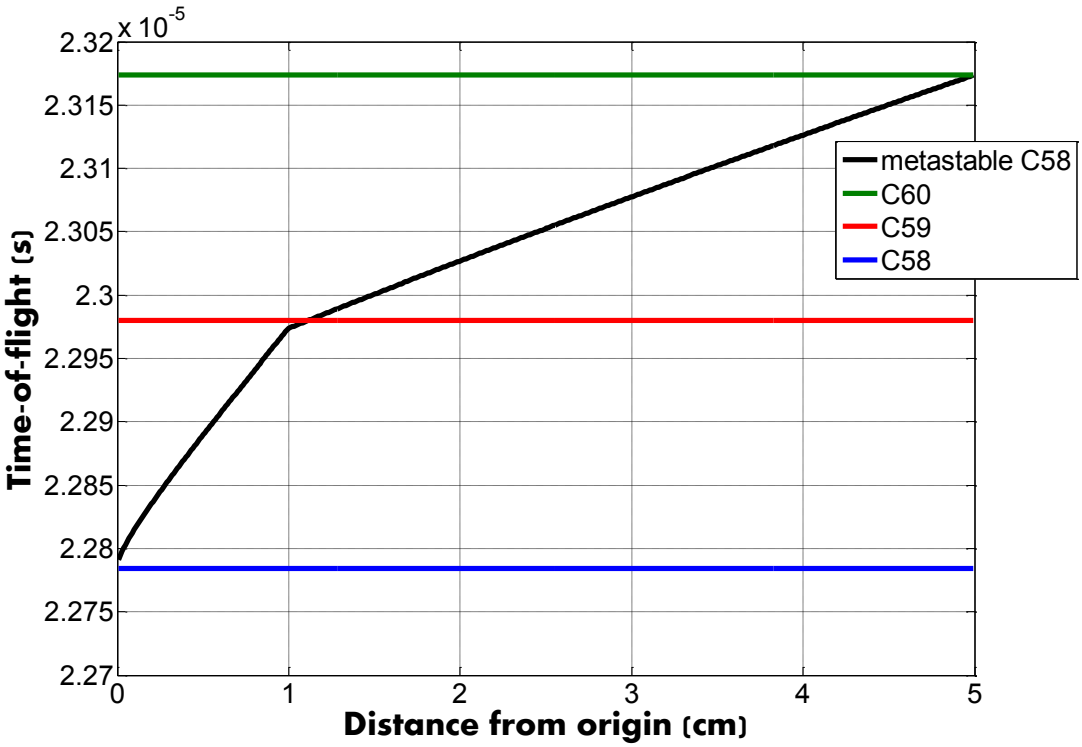

Figure A.3: Time-of-flight, as a function of birth distance from the origin, for metastable C_{58}^{+}.Time-of-flights for C_{60}^{+}, C_{59}^{+} and promptly created C_{58}^{+} are also shown.

There is a clear kink in the time-of-flight graph for metastable C_{58}^{+}. This coincides with the kink in the potential energy graph, situated at HV_2. This can be rationalised by pointing out that a metastable ion which decays before HV_2 will experience the higher potential energy in this region during its time as a lighter C_{58}^{+} ion. The graph also proves that it is possible for metastable C_{58}^{+} ions to have the same time-of-flight as C_{59}^{+} ions and it is also worth noting that the kink in the metastable C_{58}^{+} graph appears as it crosses the C_{59}^{+} graph. This does not necessarily mean that a peak in the mass spectrum will appear corresponding to the position of this kink. In order to investigate this, ion yields as a function of time-of-flight need to be investigated for metastable C_{58}^{+}.

C_{60}^{+} ions were assumed to undergo an exponential decay to C_{58}^{+} ions according to

$$I(t) = I_0 \exp(-kt). \quad \text{(A.1)}$$

The probability of a C_{60}^{+} ion decaying between times t_1 and t_2 then becomes

$$P = (t_2 - t_1)\exp(-kt_1) - \int_{t1}^{t2} \exp(-kt)t = (t_2 - t_1 - \frac{1}{k})\exp(-kt_1) + \frac{\exp(-kt_2)}{k}. \quad \text{(A.2)}$$

The ion yield, or peak intensity, is then plotted as a function of time-of-flight (Figure A.4). The graph has been binned in steps of a few tens of nanoseconds to reflect the typical resolution of the TOF. It is clear that there is a sudden increase in peak intensity when the C_{60}^{+} ions decay immediately after HV_2. This is because the ions slow down at that point, due to the change in potential energy, increasing the probability of metastable fragments being created. It happens that the sudden increase in metastable peak intensity occurred at the same time-of-flight as that of the prompt C_{59}^{+} ion. The calculation therefore shows that it is possible that a metastable peak can occur at the same position in the mass spectrum as a C_{59}^{+} ion.

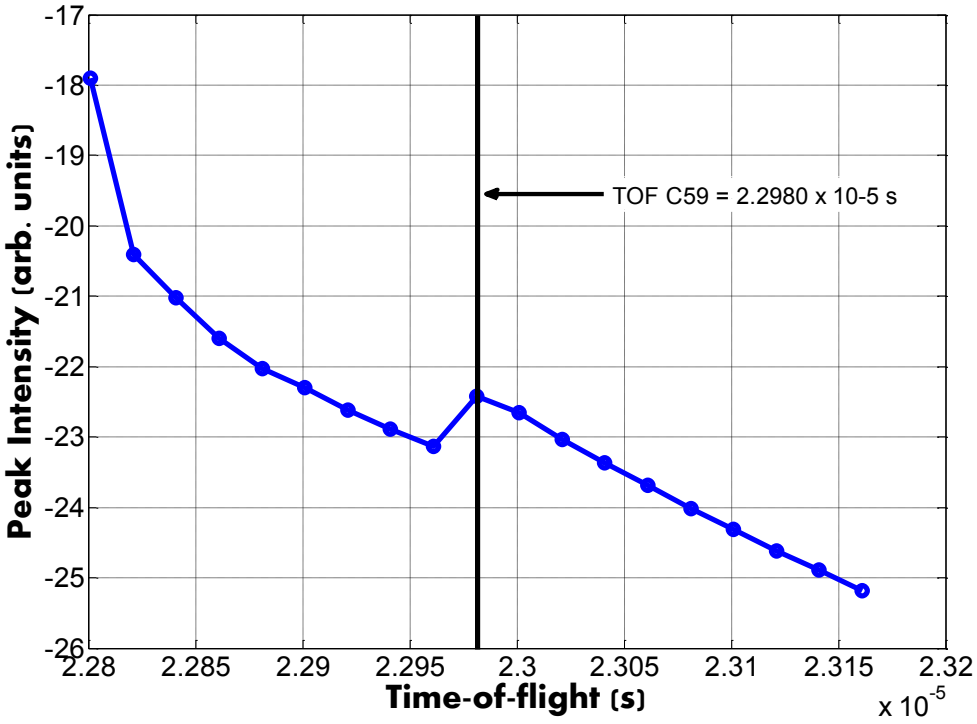

Figure A.4: Peak intensity as a function of time-of-flight for metastable C_{58}^{+} ions. A clear peak can be seen, overlapping with the calculated time-of-flight for C_{59}^{+} ions.

The calculations show that it is possible to observe a peak in the mass spectrum due to metastable C_{58}^{+} and that this peak would have a very similar time-of-flight to C_{59}^{+} ions. To determine which ion is responsible for the peak seen in the experimental spectra, the calculations are compared to experimental data as HV_1 is kept constant and HV_2 is varied. By varying the voltage across HV_2, the time-of-flight for all ions is changed. A smaller value means each ion will be subject to less potential energy, resulting in a smaller velocity. Also, a smaller voltage across HV_2 changes the shape of the potential energy function, inducing a more sudden or more gradual change in velocity as the ions pass HV_2. Since this change is crucial to how the metastable peak is formed, the behaviour of a peak due to metastable ions and one due to promptly created ions will differ according to the change in HV_2. Figure A.5 shows the calculated time-of-flight for metastable C_{58}^{+}, C_{60}^{+}, C_{59}^{+} and C_{58}^{+} as a function of the voltage across HV_2.

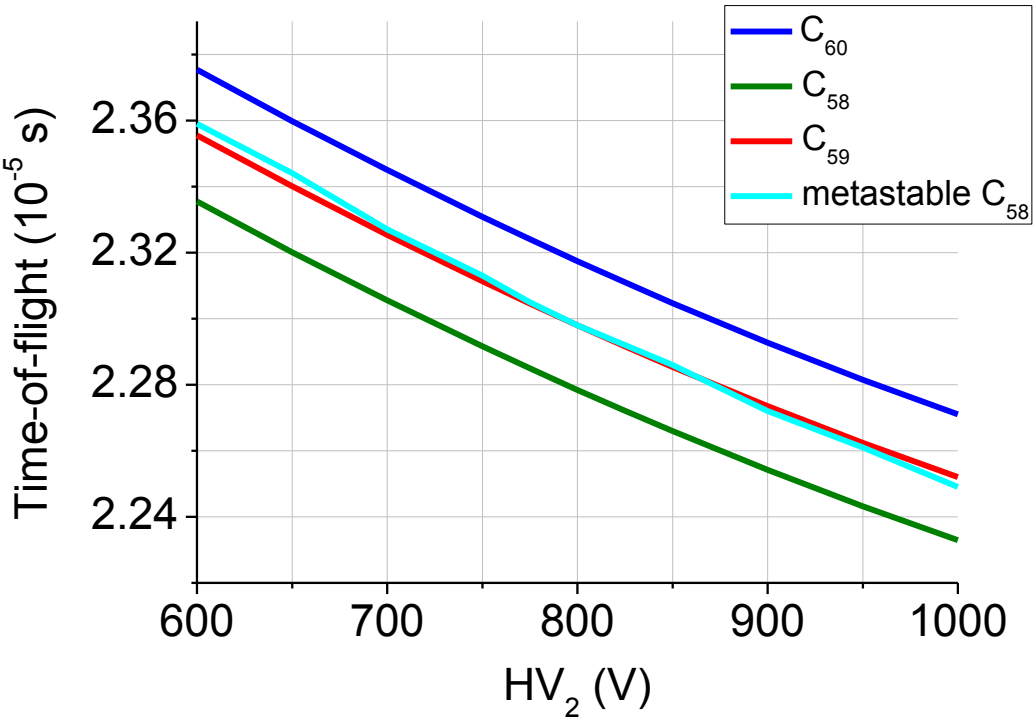

Figure A.5: Calculated time-of flight for promptly created ions C_{60}^{+}, C_{59}^{+}, C_{58}^{+} and metastable C_{58}^{+}, as a function of the voltage across electrode HV_2.

As can be seen in figure A.5, the calculated time-of-flight for each ion species follows a downward curve as the voltage across HV_2 is increased. The curves representing the promptly created ions have roughly similar slopes with regular spacing between each species. Metastable C_{58}^{+}, which lies in a similar position between the times-of-flight of C_{60}^{+} and C_{58}^{+} as the C_{59}^{+} ion, has a steeper, negative, gradient. Effectively, at smaller values of HV_2, it's time-of-flight is closer to that of C_{60}^{+} than C_{58}^{+} but as HV_2 is increased, it moves closer to C_{58}^{+} than to C_{60}^{+}. There should be no such movement with a peak due to prompt C_{59}^{+} and these slopes can be used to determine whether the peak observed is due to metastable C_{58}^{+} or prompt C_{59}^{+}.

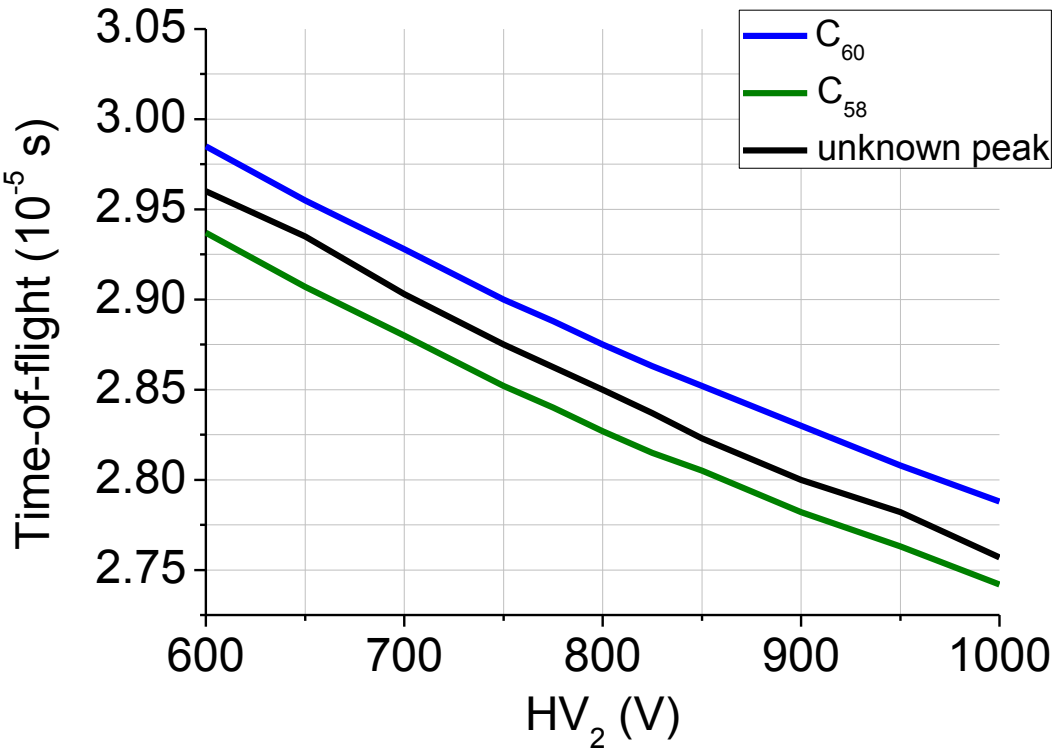

Figure A.6: Experimental time-of flight for promptly created ions C_{60}^+, C_{58}^+ and the unknown peak, as a function of the voltage across electrode HV_2.

Figure A.6 shows the experimental time-of-flight values for C_{60}^+, C_{58}^+ and the unknown peak as a function of the voltage across HV_2. The general trend is matched quite well to the calculated trends and it can already be seen, qualitatively, that the curve of the unknown peak seems to have a steeper gradient than the other two and move from a position relatively closer to the C_{60}^+ curve at low HV_2 values, to relatively closer to the C_{58}^+ curve at higher HV_2 values, indicating that the peaks in the spectra are due to metastable ions. To quantify this behaviour the relative position between the C_{60}^+ and C_{58}^+ curves is plotted for the calculated time-of-flight for metastable C_{58}^+, C_{59}^+ and the experimental time-of-flight of the unknown peak. As a measure of the relative position, the ratio

$$R = \frac{TOF_{C60} - TOF_{C58}}{TOF_{unknown} - TOF_{C58}}$$

is used where $TOF_{unknown}$ is the calculated time-of-flight for metastable C_{58}^+, C_{59}^+ or the unknown peak, respectively.

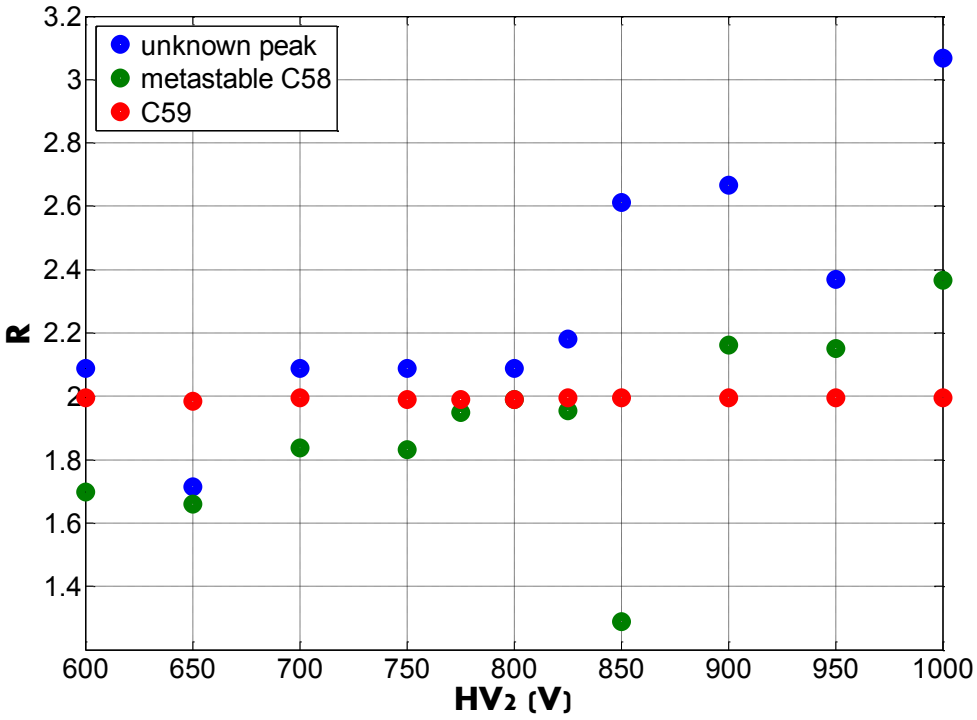

Figure A.7: Experimental ratio, R, as a function of the voltage across HV_2 for the unknown peak and calculated ratios of R for metastable C_{58}^+ and C_{59}^+.

A positive gradient, for the ratio, R, indicates that the unknown peak has a steeper gradient than that of C_{60}^+ and C_{58}^+ and is moving closer to C_{58}^+ with increasing HV_2. A gradient of zero, or close to zero, would indicate the unknown peak has a similar gradient to C_{60}^+ and C_{58}^+ and stays at a constant relative position between the two peaks as HV_2 changes. From the plots, it can clearly be seen that the unknown peak has a positive gradient, akin to the calculated plot for metastable C_{58}^+. Therefore, it is determined that the peaks seen in the mass spectra are due to metastable fragmentation of fullerene fragments in the extraction region of the TOF mass spectrometer.

Appendix B – Laser intensity calibration factors

Table A.1 shows the laser intensity calibration factors used for various laser pulse durations and wavelengths as described in section 4.4.7.

Table A.1: Laser intensity calibration factors.

Laser wavelength and pulse duration	**Calibration factor** $\left(\frac{W/cm^2}{\mu J}\right)$
800 nm, 130 fs	$(5.63 \pm 0.18) \times 10^{11}$
800 nm, 180 fs	$(4.34 \pm 0.10) \times 10^{11}$
800 nm, 1 ps	$(7.62 \pm 0.18) \times 10^{10}$
550 nm, 92 fs	$(6.10 \pm 0.26) \times 10^{11}$
625 nm, 50 fs	$(5.62 \pm 0.37) \times 10^{11}$
400 nm, 120 fs	$(3.19 \pm 0.51) \times 10^{11}$

Appendix C – GPOP inversion program

This section presents the *GPOP.m* MATLAB program used to invert raw VMI images. To run the program, the adj.m file, written by Paul Godfrey, is required (available from http://www.mathworks.com/matlabcentral/fileexchange/35-adj-m). Also the files, Pixels.LUT, Basis_Set.LUT and Ainc_LUT are required, available with the original POP program from http://www.dur.ac.uk/chemistry/lsd/groups/j.r.r.verlet/research/clusters/pop/.

```
%Polar Onion Peeling (POP) program for invertsing VMI images.
%Written by Gordon Henderson
%Adapted from the POP 8.5 program written in Labview and C
%Adapted to fit thi contribution with up to n=10 Legendre polynomials
%instead of n=4.

%To run this program requires the adj.m file to be in the same folder
and
%requires the Pixels.LUT, Basis_Set.LUT and Ainc.LUT txt files.
clear all
clc
display('------------------------------------------------------------')
display('GPOP inversion program')
display('------------------------------------------------------------')
%---------------------
%DATA INPUT
%---------------------
%load the raw image
folder = 'D:\Data\2012\06- June\20120610\';
file_name = 'El_2278_bg_smoothed0.50.5.txt';
file_name_s = 'El_2278_bg_smoothed0.50.5';
input_file = strcat(folder,file_name);
a = load(input_file);
%enter the centre coordinates of image
zzx = 741;
zzy = 531;
%If Data=0, the experimental h(r, theta) will be used to reconstruct
the
%image. If Data=1, the fitted h will be used. The choice does not
effect the
%ultimate radial spectrum produced. However, the latter smoothes
angular
%noise and presents very attractive images, however it also discards
real
%experimental noise.
Data = 1;
%Size of matrix
[n,m]=size (a);
%Defining maximal permitted radius
if zzx<=(m-zzx)
    gordonx=zzx;
else gordonx=(m-zzx);
end
```

```
if zzy<=(n-zzy)
    gordony=zzy;
else gordony=(n-zzy);
end

if gordonx<=gordony
    zz=gordonx;
else zz=gordony;
end
%Load the PIXELS LUT file
folder_pix = 'C:\Documents and Settings\s0233147\desktop\POP stuff\';
file_name_pix = 'Pixels_LUT.txt';

input_file = strcat(folder_pix,file_name_pix);
PIXELS = load(input_file);
%Load the Ainc LUT file
folder_ain = 'C:\Documents and Settings\s0233147\desktop\POP stuff\';
file_name_ain = 'Ainc_LUT.txt';
input_file = strcat(folder_ain,file_name_ain);
AINC = load(input_file);
%Load the Basis Set LUT file
folder_bs = 'C:\Documents and Settings\s0233147\desktop\POP stuff\';
file_name_bs = 'Basis_Set.txt';
input_file = strcat(folder_bs,file_name_bs);
LUT = load(input_file);

%---------------------
%CARTESIAN IMAGE FOLDING AND 4-WAY CENTRING
%---------------------

%Size and zero a4 matrix
a4=zeros(zz+1);
%Defining starting point of folded matrix
a4(1, 1) = a(zzy, zzx)*4;
%Defining the rest of the matrix
for i=1:(zz-1)
    a4(1,i+1) = (a(zzy,zzx+i)+a(zzy,zzx-i))*2;
    for j=1:(zz-1)
         a4(j+1,i+1)=a(zzy+j,zzx+i)+a(zzy+j,zzx-i)+a(zzy-
j,zzx+i)+a(zzy-j,zzx-i);
         a4(j+1,1)=(a(zzy+j,zzx)+a(zzy-j,zzx))*2;
     end
end

%---------------------
%CONVERSION FROM CARTESIAN TO POLAR COORDINATES
%---------------------
%Size and zero polar matrices
ira=zeros(((floor((zz+1)*pi/2))),zz);
iraraw = zeros(size(ira));
%Defining centre spot value
ira(1, 1) = a4(1,1);
%Building polar image
for rp=1:zz-1
    %nainc=number of polar pixles at given radius -1.
    %ainc = angular increment
    nainc=PIXELS(rp+1,2);
    ainc=AINC(rp+1);
```

```
    for qp=0:nainc

        %Calculating x,y coordinates of polar pixel
        xp=abs(rp*sin(ainc*qp))+1;
        yp=abs(rp*cos(ainc*qp))+1;

        xc=round(xp);
        yc=round(yp);

        xd=1-abs(xc-xp);
        yd=1-abs(yc-yp);

        %Determination of polar pixel intensity

        if ((xp>=xc) && (yp>=yc));
            pint=((xd*yd)*a4(yc,xc))+((xd*(1-yd))*a4(yc+1,xc))+(((1-
xd)*yd)*a4(yc,xc+1))+(((1-xd)*(1-yd))*a4(yc+1,xc+1));
        else

            if ((xp>=xc) && (yp<=yc));
                pint=((xd*yd)*a4(yc,xc))+((xd*(1-yd))*a4(yc-
1,xc))+(((1-xd)*yd)*a4(yc,xc+1))+(((1-xd)*(1-yd))*a4(yc-1,xc+1));
            else

                if ((xp<=xc) && (yp>=yc));
                    pint=((xd*yd)*a4(yc,xc))+((xd*(1-
yd))*a4(yc+1,xc))+(((1-xd)*yd)*a4(yc,xc-1))+(((1-xd)*(1-
yd))*a4(yc+1,xc-1));
                else

                    if ((xp<=xc) && (yp<=yc));
                        pint=((xd*yd)*a4(yc,xc))+((xd*(1-yd))*a4(yc-
1,xc))+(((1-xd)*yd)*a4(yc,xc-1))+(((1-xd)*(1-yd))*a4(yc-1,xc-1));
                    end
                end
            end
        end
        %Placing polar pixel intensity in polar pixel matrix "polar"
        ira(qp+1,rp+1)=ira(qp+1,rp+1)+pint;
    end
end

iraraw = ira;

%Generation of convoluted Photoelectron Spectrum
PESR = ira(1,:)-ira(1,:);
PESI = ira(1,:)-ira(1,:);
PESId = ira(1,:)-ira(1,:);
PESRd = ira(1,:)-ira(1,:);

for i = 1:1:zz
    nainc = PIXELS(i,2);
    PESR(i) = i-1;
    for j = 1:1:nainc+1
        PESI(i) = PESI(i) + ira(j,i);
    end
end

%---------------------
```

```
%OUTER RING FIT OF EXPERIMENTAL IMAGE (IRA) AT rp USING LINEAR
REGRESSION
%--------------------

%Zeroing deconcoluted polar image
iradecon = zeros(size(ira));
for rp = zz-1:-1:0
    %Zeroing matrices A and B before ring fit begins for given R
    B(1) = 0;
    B(2) = 0;
    B(3) = 0;
    B(4) = 0;
    B(5) = 0;
    B(6) = 0;
    for i = 1:1:6
        for j = 1:1:6
            A(j,i) = 0;
        end
    end

    %Calculation of matrices A and B
    nainc = PIXELS(rp+1,2);

   for  qp = 0:1:nainc

        y = ira(qp+1,rp+1);
        xa = 0.5*((3*(cos(AINC(rp+1)*qp)^2))-1);
        xb = (1/8)*((35*(cos(AINC(rp+1)*qp)^4))-
(30*(cos(AINC(rp+1)*qp)^2))+3);
        xe = (1/16)*((231*(cos(AINC(rp+1)*qp)^6))-
(315*(cos(AINC(rp+1)*qp)^4))+(105*(cos(AINC(rp+1)*qp)^2))-5);
        xf = (1/128)*((6435*(cos(AINC(rp+1)*qp)^8))-
(12012*(cos(AINC(rp+1)*qp)^6))+(6930*(cos(AINC(rp+1)*qp)^4))-
(1260*(cos(AINC(rp+1)*qp)^2))+35);
        xg = (1/256)*((46189*(cos(AINC(rp+1)*qp)^10))-
(109395*(cos(AINC(rp+1)*qp)^8))+(90090*(cos(AINC(rp+1)*qp)^6))-
(30030*(cos(AINC(rp+1)*qp)^4))+(3465*(cos(AINC(rp+1)*qp)^2))-63);

        B(1) = B(1)+y;
        B(2) = B(2)+(y*xa);
        B(3) = B(3)+(y*xb);
        B(4) = B(4)+(y*xe);
        B(5) = B(5)+(y*xf);
        B(6) = B(6)+(y*xg);

        A(1,1) = A(1,1)+1;
        A(2,1) = A(2,1)+xa;
        A(3,1) = A(3,1)+xb;
        A(4,1) = A(4,1)+xe;
        A(5,1) = A(5,1)+xf;
        A(6,1) = A(6,1)+xg;
        A(2,2) = A(2,2)+(xa^2);
        A(3,2) = A(3,2)+(xa*xb);
        A(4,2) = A(4,2)+(xa*xe);
        A(5,2) = A(5,2)+(xa*xf);
        A(6,2) = A(6,2)+(xa*xg);
        A(3,3) = A(3,3)+(xb^2);
        A(4,3) = A(4,3)+(xb*xe);
        A(5,3) = A(5,3)+(xb*xf);
        A(6,3) = A(6,3)+(xb*xg);
```

```
        A(4,4) = A(4,4)+(xe^2);
        A(5,4) = A(5,4)+(xe*xf);
        A(6,4) = A(6,4)+(xe*xg);
        A(5,5) = A(5,5)+(xf^2);
        A(6,5) = A(6,5)+(xf*xg);
        A(6,6) = A(6,6)+(xg^2);

    end

    A(1,2) = A(2,1);
    A(1,3) = A(3,1);
    A(2,3) = A(3,2);
    A(1,4) = A(4,1);
    A(2,4) = A(4,2);
    A(3,4) = A(4,3);
    A(1,5) = A(5,1);
    A(2,5) = A(5,2);
    A(3,5) = A(5,3);
    A(4,5) = A(5,4);
    A(1,6) = A(6,1);
    A(2,6) = A(6,2);
    A(3,6) = A(6,3);
    A(4,6) = A(6,4);
    A(5,6) = A(6,5);

    %inversion of matrix A
     d = det(A);
     A = A';
     A = adj(A);
     Ain = (1./d)*A;

     %Calculation of Beta coefficient matrix via multiplication of
matrix
     %Ain and B
     %Beta(1) = N(intensity factor)
     %Beta(2) = Beta2
     %Beta(3) = Beta4
     %Beta(4) = Beta6
     %Beta(5) = Beta8
     %Beta(6) = Beta10
     Beta(1) =
(B(1)*Ain(1,1))+(B(2)*Ain(1,2))+(B(3)*Ain(1,3))+(B(4)*Ain(1,4))+(B(5)
*Ain(1,5))+(B(6)*Ain(1,6));
     Beta(2) =
((B(1)*Ain(2,1))+(B(2)*Ain(2,2))+(B(3)*Ain(2,3))+(B(4)*Ain(2,4))+(B(5
)*Ain(2,5))+(B(6)*Ain(2,6)))./Beta(1);
     Beta(3) =
((B(1)*Ain(3,1))+(B(2)*Ain(3,2))+(B(3)*Ain(3,3))+(B(4)*Ain(3,4))+(B(5
)*Ain(3,5))+(B(6)*Ain(3,6)))./Beta(1);
     Beta(4) =
((B(1)*Ain(4,1))+(B(2)*Ain(4,2))+(B(3)*Ain(4,3))+(B(4)*Ain(4,4))+(B(5
)*Ain(4,5))+(B(6)*Ain(4,6)))./Beta(1);
     Beta(5) =
((B(1)*Ain(5,1))+(B(2)*Ain(5,2))+(B(3)*Ain(5,3))+(B(4)*Ain(5,4))+(B(5
)*Ain(5,5))+(B(6)*Ain(5,6)))./Beta(1);
     Beta(6) =
((B(1)*Ain(6,1))+(B(2)*Ain(6,2))+(B(3)*Ain(6,3))+(B(4)*Ain(6,4))+(B(5
)*Ain(6,5))+(B(6)*Ain(6,6)))./Beta(1);

     %Generation of Beta spectra
```

```
    Beta2(rp+1) = Beta(2);
    Beta4(rp+1) = Beta(3);
    Beta6(rp+1) = Beta(4);
    Beta8(rp+1) = Beta(5);
    Beta10(rp+1) = Beta(6);

    Na = abs(Beta(1));

%     if (Na == 0)
%
%          PESId(rp+1) = 0;
%          PESRd(rp+1) = rp;
%
%     end

%---------------------
%DECONVOLUTION
%(a) expand normalised LUT to obtain simulated image
%(b) select outer ring at rp to be used for iradecon (experiment or
%siimulated
%(c) subtract simulated image from experiment at eac pixel at each
radius
%(d) generation of deconvoluted PES
%---------------------

    PESRd(rp+1) = rp;

    for R = 0:1:rp

        pixels = PIXELS(R+1,1);
        it = (LUT(rp+1,R+1)*((nainc+1)./pixels));

        for qp = 0:1:pixels-1

            alpha = AINC(R+1)*qp;

            fact =
Beta(1)*it*(1+((Beta(2)*(1/2))*(3*(R/rp)^2*(cos(alpha)^2)-
1))+((Beta(3)*(1/8))*((35*(R/rp)^4*(cos(alpha)^4))-
(30*(R/rp)^2*(cos(alpha)^2))+3))+((Beta(4)*(1/16))*((231*(R/rp)^6*(co
s(alpha)^6))-
(315*(R/rp)^4*(cos(alpha)^4))+(105*(R/rp)^2*(cos(alpha)^2))-
5))+((Beta(5)*(1/128))*((6435*(R/rp)^8*(cos(alpha)^8))-
(12012*(R/rp)^6*(cos(alpha)^6))+(6930*(R/rp)^4*(cos(alpha)^4))-
(1260*(R/rp)^2*(cos(alpha)^2))+35))+((Beta(6)*(1/256))*((46189*(R/rp)
^10*(cos(alpha)^10))-
(109395*(R/rp)^8*(cos(alpha)^8))+(90090*(R/rp)^6*(cos(alpha)^6))-
(30030*(R/rp)^4*(cos(alpha)^4))+(3465*(R/rp)^2*(cos(alpha)^2))-63)));

            if (Data == 1) & (R == rp)
                PESId(R+1) = PESId(R+1)+fact*sqrt(R)*sin(alpha);
                iradecon(qp+1,R+1) = fact./sqrt(R);
                elseif (Data == 0) & (R == rp)
                     PESId(R+1) =
PESId(R+1)+ira(qp+1,R+1)*sqrt(R)*sin(alpha);
                     iradecon(qp+1,R+1) = ira(qp+1,R+1)./sqrt(R);
            end

            ira(qp+1,R+1) = ira(qp+1,R+1)-fact;
```

```
        end
    end
end

%Removing noise from deconvoluted image
iradecon(:,1) = 0;
iradecon(:,2) = 0;

%---------------------
%RECOVERING CARTESIAN IMAGES FROM POLAR IMAGES
%---------------------

%Recovering convoluted image (cart) from convoluted polar image
(iraraw)
polar2 = iraraw;
[m,n]=size(polar2);
if m<=n
    zz=m;
else
    zz=n;
end

polar=zeros(((floor(zz*pi/2))-1),2*zz);
polar(1:((floor(zz*pi/2))-1),1:zz-1)=polar2(1:((floor(zz*pi/2))-
1),1:zz-1);
cart=zeros(zz+1);

for x = 0:zz-2
    for y = 0:zz-2
        %Assigning values to centre and edge Cartesian pixels
        if ((x==0) && (y==0));
            cart(1,1) = polar(1,1);
        end
        if (x==0);
             cart(y+1,1) = polar(1,y+1);
        end
        if (y==0);
             i = PIXELS(x+1,1);
            cart(1,x+1) = polar(i,x+1);
        end
         end
end

for x = 1:zz-2
    for y = 1:zz-2
        %Conversion of all other pixels
        Rc = sqrt(x^2+y^2);

        if (y==0);
            ac = atan(0);
        else
            if(y~=0);
        ac = atan(x/y);
            end
        end

        Rp = round(Rc);
```

```
        if (AINC(Rp+1)==0);
            Qc = 0;
        else
            if (AINC(Rp+1)~=0);
                Qc = ac/AINC(Rp+1);
            end
        end

        Qp = round(Qc);
        Rd = 1-abs(Rp-Rc);
        QdA = 1-abs(Qp-Qc);

        cint = (Rd*QdA)*polar(Qp+1,Rp+1);

        if (Qc>=Qp);
            cint = cint+((Rd*(1-QdA))*polar(Qp+2,Rp+1));
        else
            if (Qc<=Qp);
                cint = cint+((Rd*(1-QdA))*polar(Qp,Rp+1));
            end
        end

        %Beginning of Move in the Radial position frame (i.e. move to
Rp +/- 1?)

        if (Rc>Rp);
           if (AINC(Rp+2)==0);
            Qc = 0;
        else
            if (AINC(Rp+2)~=0);
                Qc = ac/AINC(Rp+2);
            end
            end

        Qp = round(Qc);
        QdB = 1-abs(Qc-Qp)
        cint = cint+(((1-Rd)*QdB)*polar(Qp+1,Rp+2));
        if (Qc>=Qp);
            cint = cint+(((1-Rd)*(1-QdB))*polar(Qp+2,Rp+2));
        else
            if (Qc<=Qp);
                cint = cint+(((1-Rd)*(1-QdB))*polar(Qp,Rp+2));
            end
        end
        end

        if (Rc<Rp);
        if (AINC(Rp)==0);
            Qc = 0;
        else
            if (AINC(Rp)~=0);
                Qc = ac/AINC(Rp);
            end
        end

        Qp = round(Qc);
        QdB = 1-abs(Qc-Qp);
        cint = cint+(((1-Rd)*QdB)*polar(Qp+1,Rp));
```

```
        if (Qc>=Qp);
            cint = cint+(((1-Rd)*(1-QdB))*polar(Qp+2,Rp));
        else
            if (Qc<=Qp);
                cint = cint+(((1-Rd)*(1-QdB))*polar(Qp,Rp));
            end
        end
        end
         cart(y+1,x+1) = cint;
    end
end

%Recovering deconvoluted image (cart2) from deconvoluted polar image
%(iradecon)
polar2 = iradecon;
[m,n]=size(polar2);
if m<=n
    zz=m;
else
    zz=n;
end

polar=zeros(((floor(zz*pi/2))-1),2*zz);
polar(1:((floor(zz*pi/2))-1),1:zz-1)=polar2(1:((floor(zz*pi/2))-
1),1:zz-1);
cart2=zeros(zz+1);

for x = 0:zz-2
    for y = 0:zz-2
        %Assigning values to centre and edge Cartesian pixels
        if ((x==0) && (y==0));
            cart2(1,1) = polar(1,1);
        end

        if (x==0);
             cart2(y+1,1) = polar(1,y+1);
        end

        if (y==0);
             i = PIXELS(x+1,1);
            cart2(1,x+1) = polar(i,x+1);
        end
         end
end

for x = 1:zz-2
    for y = 1:zz-2
        %Conversion of all other pixels
        Rc = sqrt(x^2+y^2);
        if (y==0);
            ac = atan(0);
        else
            if(y~=0);
        ac = atan(x/y);
            end
        end

        Rp = round(Rc);

        if (AINC(Rp+1)==0);
```

```
        Qc = 0;
    else
        if (AINC(Rp+1)~=0);
            Qc = ac/AINC(Rp+1);
        end
    end

    Qp = round(Qc);
    Rd = 1-abs(Rp-Rc);
    QdA = 1-abs(Qp-Qc);
    cint = (Rd*QdA)*polar(Qp+1,Rp+1);

    if (Qc>=Qp);
        cint = cint+((Rd*(1-QdA))*polar(Qp+2,Rp+1));
    else
        if (Qc<=Qp);
            cint = cint+((Rd*(1-QdA))*polar(Qp,Rp+1));
        end
    end

    %Beginning of Move in the Radial position frame (i.e. move to
Rp +/- 1?)

    if (Rc>Rp);
       if (AINC(Rp+2)==0);
        Qc = 0;
    else
        if (AINC(Rp+2)~=0);
            Qc = ac/AINC(Rp+2);
        end
        end

    Qp = round(Qc);
    QdB = 1-abs(Qc-Qp);
    cint = cint+(((1-Rd)*QdB)*polar(Qp+1,Rp+2));

    if (Qc>=Qp);
        cint = cint+(((1-Rd)*(1-QdB))*polar(Qp+2,Rp+2));
    else
        if (Qc<=Qp);
            cint = cint+(((1-Rd)*(1-QdB))*polar(Qp,Rp+2));
        end
    end
    end

    if (Rc<Rp);
    if (AINC(Rp)==0);
        Qc = 0;
    else
        if (AINC(Rp)~=0);
            Qc = ac/AINC(Rp);
        end
    end

    Qp = round(Qc);
    QdB = 1-abs(Qc-Qp);
    cint = cint+(((1-Rd)*QdB)*polar(Qp+1,Rp));

    if (Qc>=Qp);
```

```
            cint = cint+(((1-Rd)*(1-QdB))*polar(Qp+2,Rp));
        else
            if (Qc<=Qp);
                cint = cint+(((1-Rd)*(1-QdB))*polar(Qp,Rp));
            end
        end
        end

         cart2(y+1,x+1) = cint;

    end
end

%---------------------
%UNFOLDING CARTESIAN IMAGES
%---------------------

%Unfolding convoluted image (cart)
a8 = zeros((zz*2)-1);

zzy=zz;
zzx=zz;
a8(zzy,zzx) = a4(1,1)/4;

%Defining the rest of the matrix
for i=1:(zz-1)
    a8(zzy,zzx+i) = a4(1,i+1)/4;
    a8(zzy,zzx-i) = a4(1,i+1)/4;
    for j=1:(zz-1)

    a8(zzy+j,zzx) = a4(j+1,1)/4;
    a8(zzy-j,zzx) = a4(j+1,1)/4;
    a8(zzy+j,zzx+i) = a4(j+1,i+1)/4;
    a8(zzy+j,zzx-i) = a4(j+1,i+1)/4;
    a8(zzy-j,zzx+i) = a4(j+1,i+1)/4;
    a8(zzy-j,zzx-i) = a4(j+1,i+1)/4;
     end
end

%Unfolding deconvoluted image (cart2)
decon = zeros((zz*2)-1);

zzy=zz;
zzx=zz;

decon(zzy,zzx) = cart2(1,1)/4;

%Defining the rest of the matrix
for i=1:(zz-1)
    decon(zzy,zzx+i) = cart2(1,i+1)/4;
    decon(zzy,zzx-i) = cart2(1,i+1)/4;
    for j=1:(zz-1)

    decon(zzy+j,zzx) = cart2(j+1,1)/4;
    decon(zzy-j,zzx) = cart2(j+1,1)/4;
    decon(zzy+j,zzx+i) = cart2(j+1,i+1)/4;
    decon(zzy+j,zzx-i) = cart2(j+1,i+1)/4;
    decon(zzy-j,zzx+i) = cart2(j+1,i+1)/4;
    decon(zzy-j,zzx-i) = cart2(j+1,i+1)/4;
```

```
    end
end

%saving files

%deconvoluted PES (PESId)
y_or_no = input('Save data: deconvoluted PES (y=yes; {Return} = no)?:
','s');
 if (y_or_no == 'y')

dlmwrite(strcat(folder,file_name_s,'_deconvoluted_PES.txt'),[PESId],
'delimiter','\t');
 end

 %averaged raw image (a8)
y_or_no = input('Save data: averaged raw image image (y=yes; {Return}
= no)?: ','s');
 if (y_or_no == 'y')

dlmwrite(strcat(folder,file_name_s,'_averaged_raw_image.txt'),[a8],
'delimiter','\t');
 end

 %inverted image (decon)
y_or_no = input('Save data: inverted image (y=yes; {Return} = no)?:
','s');
 if (y_or_no == 'y')

dlmwrite(strcat(folder,file_name_s,'_inverted_image.txt'),[decon],
'delimiter','\t');
 end
```

Appendix D – Sourcemeter LabVIEW program

This program controls two Keithley sourcemeters in order to carry out 4-probe resistance measurements. The part of the program on the second page follows on from the part in the first page and is inside a loop which can be cancelled by the user to terminate the measurement.

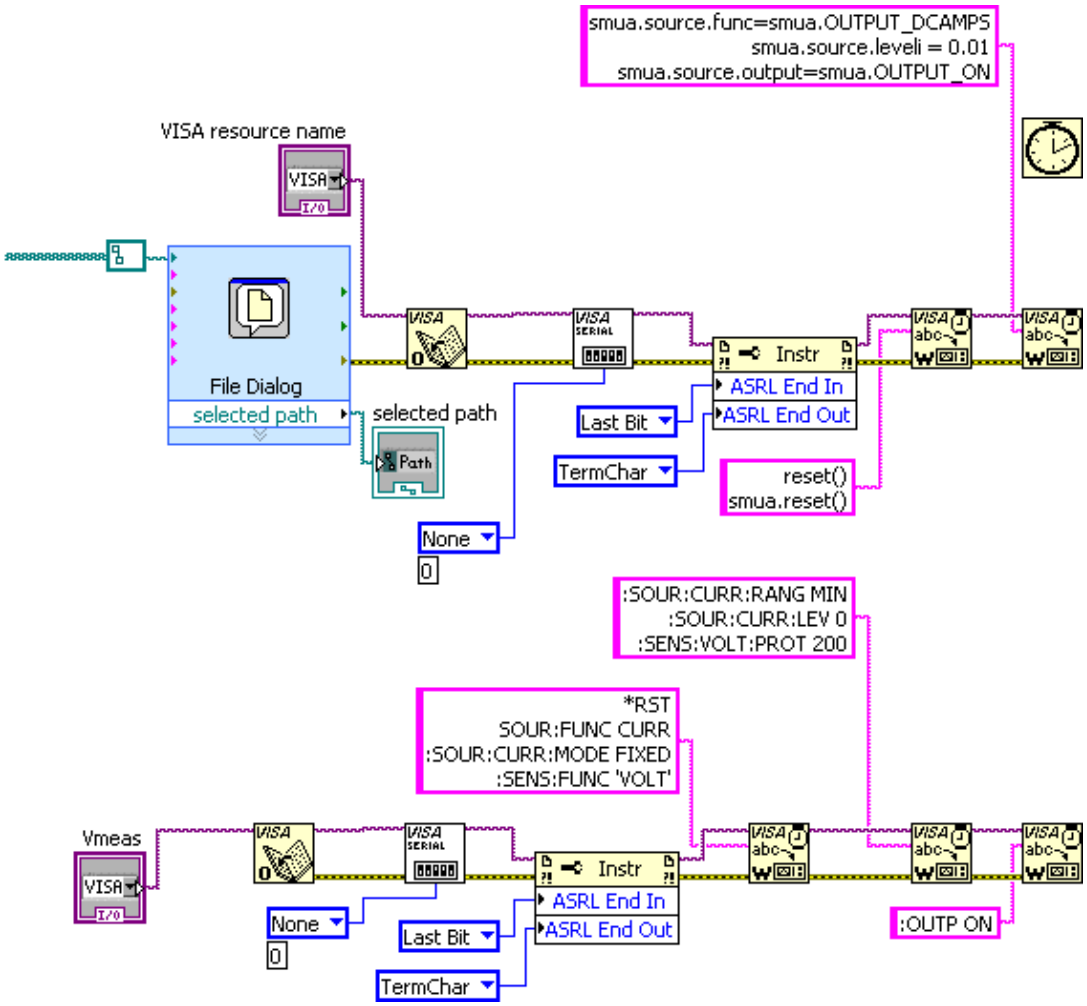

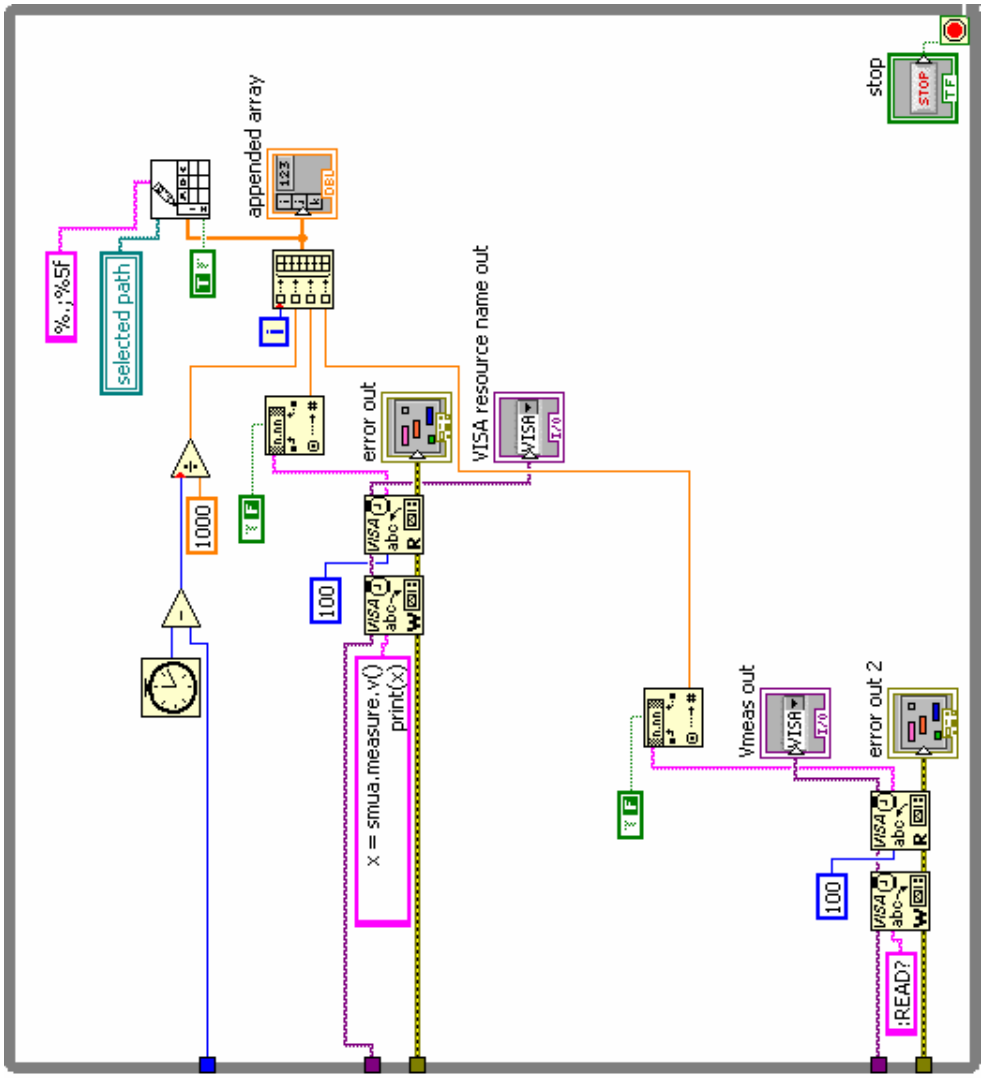

selected path